pg. 254

pg. 270

pg. 293

pg. 325

## About the Cover

*The lead article in this issue is an in-depth study on the geological formation and growth of Colombian trapiche emeralds. The cover photo shows a 58.83 ct crystal specimen (left) and a 22.74 ct cabochon (right), both displaying the material's signature six-rayed pattern, from the renowned Peñas Blancas emerald region. The host rock, seen in the background, is carbonaceous shale containing veins of calcite, pyrite, and minute crystals of low-grade emerald. Photo by Robert Weldon/GIA, courtesy of Jose Guillermo Ortiz and Colombian Emeralds Co.*

FSC
www.fsc.org
MIX
Paper from
responsible sources
FSC® C006300

# Trapiche and More…

Colombia's unique trapiche emeralds exert a fascination for many gemologists. In fine specimens, the combination of rich, gemmy green color with the six spokes' geometry is visually arresting.

In our lead article, we're delighted to present a comprehensive paper on these intriguing gems by a team of researchers headed by Isabella Pignatelli and Gaston Giuliani. They review the geology of trapiche emerald, provide 3-D petrographic examination of their crystals along with spectroscopic and chemical analyses, and propose a new formation model informed by their recent work. We hope this paper will serve as the primary reference on these one-of-a-kind gems for many years to come. Take a look at our cover photo and decide whether trapiche is a gemological curiosity or an object of beauty in its own right.

In our next paper, GIA's Ulrika D'Haenens-Johansson and her coauthors investigate the gemological properties of colorless to near-colorless HPHT-grown synthetic diamonds produced specifically for gem use by a Russian firm, New Diamond Technology. Their analysis of 44 faceted samples ranging up to 5.11 ct provides convincing evidence of the quality improvements—and increased size—of synthetics grown by this method.

Meanwhile, Lesotho's Letšeng-la-Terae mine is currently enjoying a renaissance. Rising prices for large, high-quality diamonds have overcome the twin challenges of this unique mine's remote location and low ore grade. In our third article, GIA's Russell Shor and Robert Weldon and their co-authors profile Letšeng to explain how the current owners have adapted their operations to promote recovery of the mine's biggest

*A gemological curiosity or an object of beauty in its own right?*

gems and increase profitability. Coauthors Bram Janse, Christopher "Mike" Breeding, and Steven Shirey offer insight into this mine's geology, its location on the Kaapvaal craton, and the distinctive characteristics of its diamonds.

Next, Zemin Luo, Mingxing Yang, and Andy Shen from the China University of Geosciences in Wuhan apply a statistical analysis method based on linear discriminant analysis (LDA) and LA-ICP-MS trace-element data to the provenance of dolomite-related white nephrite. The authors demonstrate the technique's high accuracy and potential for origin determination with many other gems.

We hope you enjoy our second Micro-World column. We had a fantastic response to the first installment and are extremely pleased to welcome several new contributors. We also want to thank our Lab Notes and Gem News International (GNI) contributors—these sections always refresh me with their diversity.

Finally, I'd like to welcome two new editors to our GNI section: Gagan Choudhary of the Gem Testing Laboratory in Jaipur, India, and GIA's own Dr. Mike Breeding—we thank them for their commitment and participation.

Welcome to our Fall issue!

Duncan Pay | Editor-in-Chief | dpay@gia.edu

# COLOMBIAN TRAPICHE EMERALDS: RECENT ADVANCES IN UNDERSTANDING THEIR FORMATION

Isabella Pignatelli, Gaston Giuliani, Daniel Ohnenstetter, Giovanna Agrosì, Sandrine Mathieu, Christophe Morlot, and Yannick Branquet

Colombia is the traditional source of the world's finest emeralds, including the famed trapiche crystals, with their distinctive texture resembling a wheel with six spokes. This gemological curiosity, found exclusively in the black shales of the country's western emerald zone, is linked to the peculiar structural geology of the deposits. The study presents a review and update on Colombian trapiche emeralds, followed by a three-dimensional examination of the crystals combined with spectroscopic and chemical analyses. The proposed formation model incorporates the structural geology of the deposits with the formation of trapiche and non-trapiche emeralds. The fluid accumulation at the faults' tip in the black shales leads to maximum fluid overpressure and sudden decompression and formation of the emerald-bearing vein system. The authors show that trapiche emerald growth starts at the beginning of the decompression that is responsible for local supersaturation of the fluid. The hydrothermal fluid comes in contact with the black shale matrix, favoring the formation of emerald seed crystals. During the growth of these seeds, textural sector zoning occurs, sometimes associated with chemical sector zoning, along with displacement of the matrix. Displacement growth occurs because the emeralds continue their growth, pushing the matrix material away from the growing faces. An overgrowth, generally of gem quality, can form after decompression, surrounding the core, the arms, and the dendrites, restoring the emeralds' euhedral habit.

Colombian emeralds continue to set the standard as the finest and most spectacular crystals unearthed (Ringsrud, 2013). Unique mineralogical curiosities include the emerald gastropods extracted from the Matecaña mine in Gachalá (Vuillet et al., 2002) and the famous gem-trapiche emeralds (figure 1) such as the 80.61 ct Star of the Andes (Ward, 1993).

The past 25 years have seen major advances in our understanding of the formation of Colombian emeralds (Ottaway et al., 1994; Cheilletz et al., 1994), but the genesis of trapiche emerald remains unresolved despite analytical and geological advances. This type of emerald is very rare and has been recovered only occasionally, from just a few mines on the western side of the Eastern Cordillera Basin. Named after the Spanish word for the cogwheels used in sugar mills, these mineral curiosities are prized by collectors. The texture on a section perpendicular to the c-axis is characterized by a central core, six arms, and *dendrites* between the arms and around the core (figure 1). An overgrowth may also be present. The trapiche texture can be observed in other minerals, such as rubies, tourmalines, chiastolites, and garnets (box A). Without a link between field observation and mineralogical studies, there is still no consensus on the causes of the growth mechanism and texture acquisition, or on the geological conditions necessary for the formation of trapiche emerald.

This article provides an update on Colombian trapiche emerald, with complete historical, geological, mineralogical, gemological, and crystallographic background. The review opens debate on the key question of the geological conditions necessary for the formation of gem-quality trapiche material. The
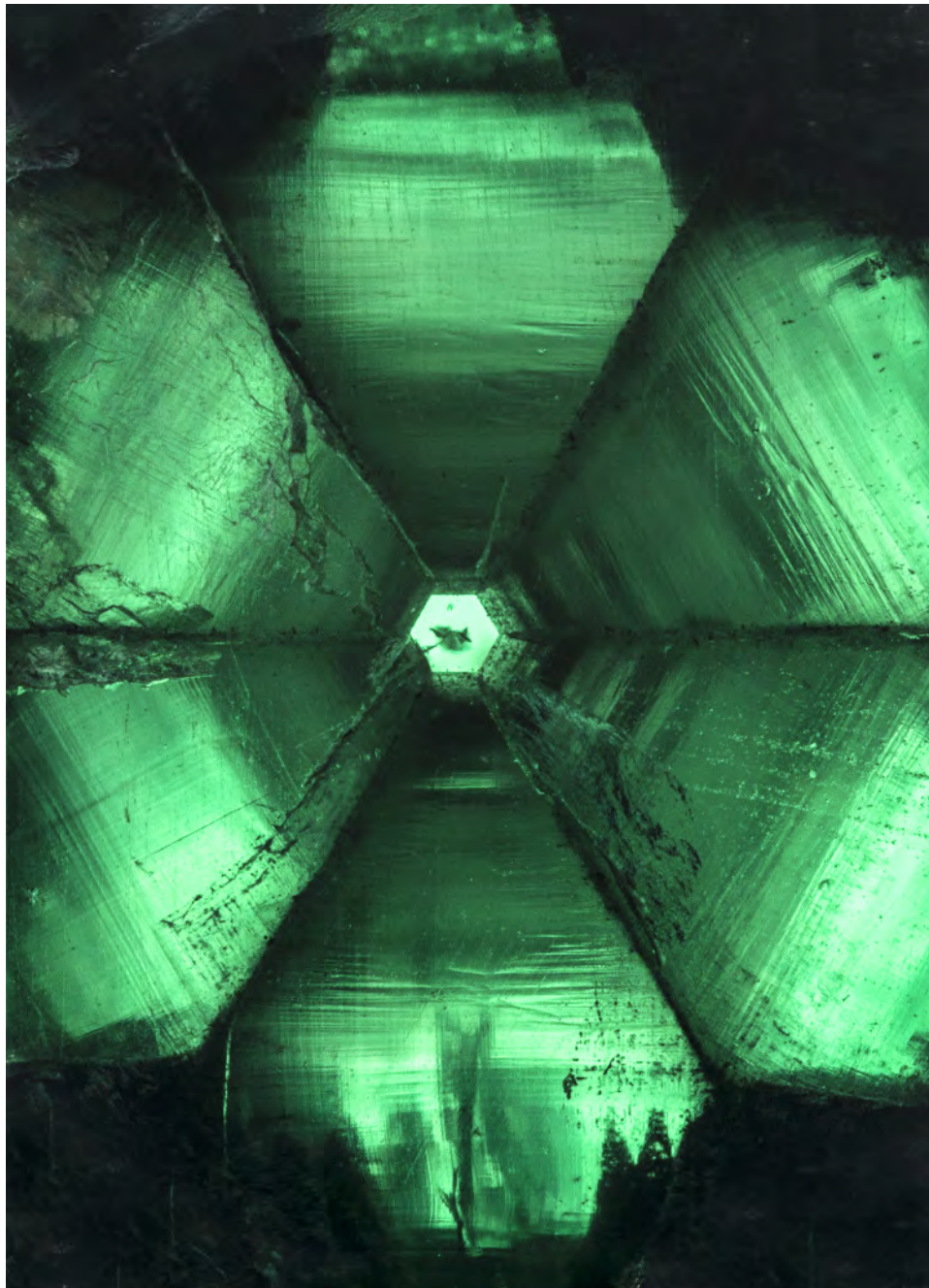
*Figure 1. Looking down the crystal axis of a backlit 58.83 ct trapiche emerald from Peñas Blancas (also featured on the cover of this issue). Photo by Robert Weldon/GIA, courtesy of Jose Guillermo Ortiz, Colombian Emerald Co.*

ongoing research into the mineralogy, chemical composition, and crystallography of trapiche emerald is connected with field expeditions conducted by French and Canadian research teams during the 1990s that proposed the hydrothermal sedimentary model now recognized by the scientific and exploration communities (Maya et al., 2004; Mantilla Figueroa et al., 2007). The scope is to propose a coherent mechanism for the formation of trapiche, linking it for the first time to the genetic model of Colombian emeralds. Colombia offers a unique case because other gem trapiches have not been studied intensively in connection with their geological setting. For the gemologist, this knowledge offers a better understanding of the mineralogy of trapiche emerald and a deeper appreciation of the complex geologic processes required to form such a peculiar mineral texture. Geologic terms that might be unfamiliar to the reader are defined in the glossary and italicized upon first mention within the text.

# BOX A: TRAPICHE VS. TRAPICHE-LIKE MINERALS

Win (2005) distinguished three types of trapiche minerals as a function of their appearance due to coloring elements, other mineral inclusions, or intergrowth of the same mineral. Schmetzer et al. (2011) improved this distinction, defining only two groups: "trapiche" minerals and "trapiche-like" minerals (figure A-1).

Trapiche minerals are characterized by crystallographically equivalent growth sectors that are separated by more or less sharp boundaries of inclusions (figure A-1, left). The boundaries intersect in a central point or extend from the edge of a central core. Gems that belong to this group include emeralds from Colombia, corundum (e.g., Müllenmeister and Zang, 1995; Schmetzer et al., 1996, 1998; Sunagawa, 1999; Garnier et al., 2002a, 2002b), tourmalines (Hainschwang et al., 2007; Schmetzer et al., 2011), chiastolites (Rice and Mitchell, 1991; Rice, 1993), and garnets (Harker, 1950; Atherton and Brenchley, 1972; Wilbur and Ague, 2006).

We also mention two examples of non-Colombian trapiche emerald crystals, one from the Brazilian state of Goiás (DelRe, 1994) and the other from the Mananjary area in Madagascar (Johnson and Koivula, 1998). The Brazilian crystal showed fibrous arms and a tapered core. The specimen from Madagascar presented the spoke-like texture associated with Colombian emerald. The core was limited to a center point, while the dendrites contained black material. These two gems refer more to trapiche than trapiche-like emeralds, but they cannot be compared with Colombian samples because their geological formation is unknown.

Two other features observed in trapiche crystals should be mentioned: symmetry and inclusions of organic matter. Trapiche minerals are always characterized by high symmetry: cubic for garnet, hexagonal for emerald, and trigonal for corundum and tourmaline. The only exception is chiastolite, which belongs to the orthorhombic system but is pseudotetragonal ($a \approx b$).

The symmetry affects the number of arms and dendrites in the trapiche texture, as well as the directions where the dendrites develop. Because high symmetry implies that a certain number of directions are equivalent, the positions of the dendrites can be predicted taking into account the crystal system. For example, in emerald there are six dendrites respectively along the positive and negative sides of the a-axis, whereas in chiastolite the four dendrites are along the a- and b-axes.

To the best of our knowledge, no trapiche texture has been reported in minerals with low symmetry (orthorhombic, monoclinic, or triclinic), even though the development of dendrites on the corners of minerals with euhedral morphology such as olivine is already known (Faure et al., 2003, 2007). This suggests that at least two of the three basic vectors $a$, $b$, and $c$ have to be equal (or, in the case of chiastolite, nearly equal) to obtain the trapiche texture, and thus the role of symmetry cannot be neglected.

The presence of transformed organic matter or graphite is observed in trapiche minerals formed in different geological environments—for instance, metamorphic deposits such as ruby (Garnier et al., 2002a,b), chiastolite, garnet (Rice and Mitchell, 1991), and tourmaline (Schmetzer et al., 2011). The role of carbonaceous materials in trapiche formation was raised by Rice and Mitchell (1991) and Rice (1993), referring to Burton (1986), who stated that graphite can control the fluid composition and dictate the mechanism and timing of mineral growth.

In trapiche-like minerals, the texture is caused by the distribution of color-inducing elements or of inclusions in alternating portions of the crystal (figure A-1, right). This is the case with sapphire (Koivula et al., 1994; Khotchanin et al., 2010; Kiefert, 2012), quartz (Win, 2005), and aquamarine (Koivula, 2008; Befi, 2012). Cordierite-indialite intergrowths also show a trapiche-like texture, as described by Rakovan et al. (2006).
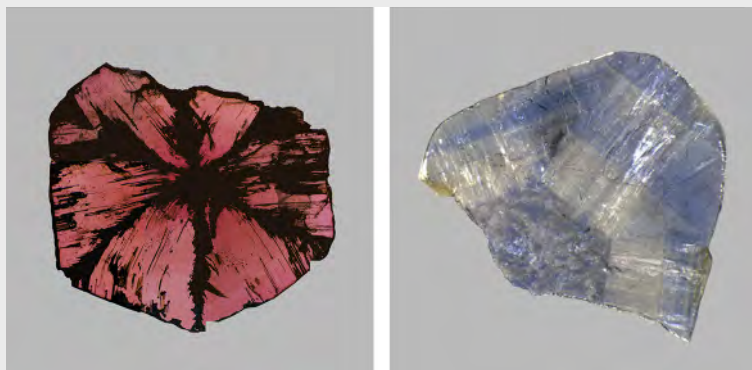


*Figure A-1. Trapiche vs. trapiche-like corundum. Left: Trapiche ruby originating from marble in Mong Hsu (Myanmar). The trapiche texture is characterized by dendrites and arms, though the specimen lacks a central core. Photo by V. Garnier. Right: A pinacoidal section of a trapiche-like blue sapphire from the Changle alkali basalt (China), showing a hexagonal core and outer zones with a fine oscillatory zoning. Photo by G. Giuliani.*
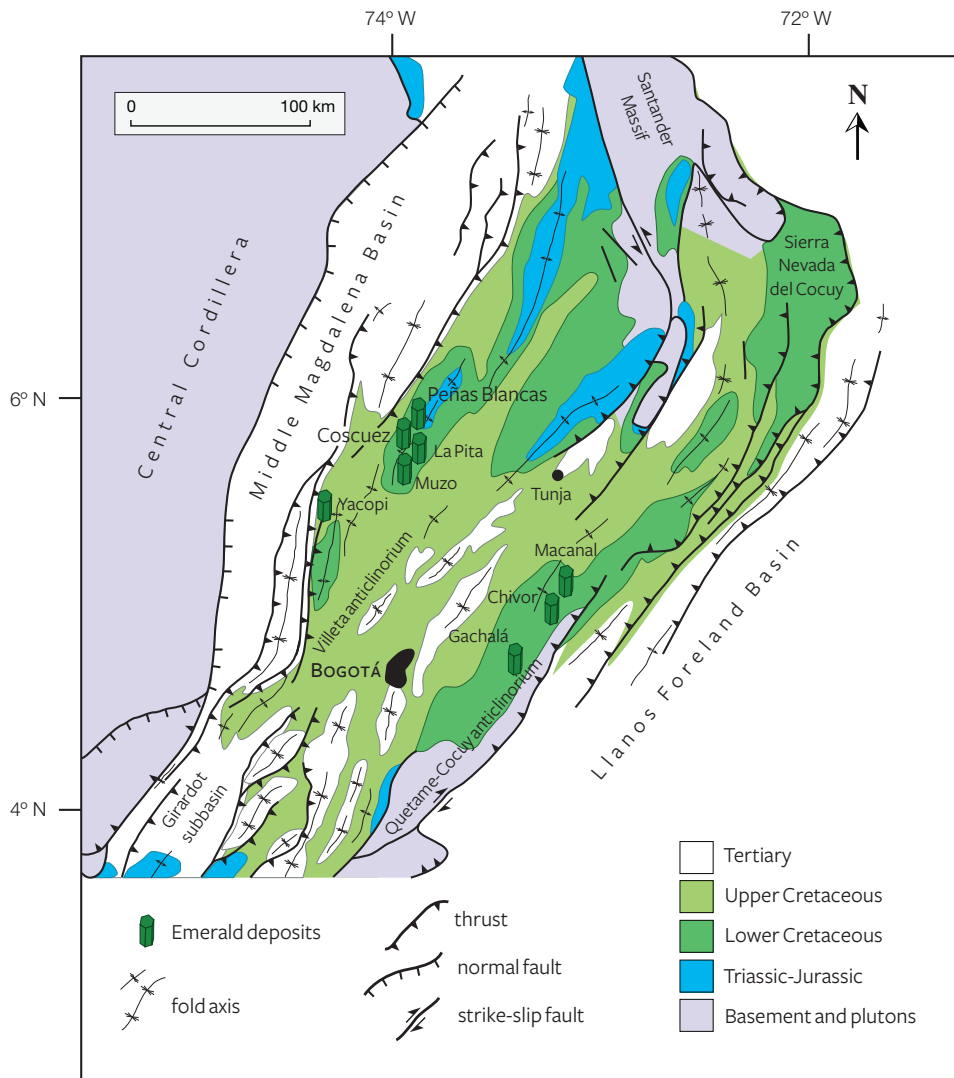
*Figure 2. Simplified geological map of the Eastern Cordillera Basin in Colombia. The emerald deposits are hosted by Lower Cretaceous sedimentary rocks forming two mineralized zones located on the eastern and western border of the basin, respectively. The western border contains the mining districts of La Glorieta–Yacopi, Muzo, Coscuez, La Pita, and Peñas Blancas, while Gachalá, Chivor, and Macanal lie on the eastern border.*

## GEOLOGY OF COLOMBIAN EMERALDS: AN UPDATE

**Geological Setting.** Located in the Eastern Cordillera Basin, the Colombian emerald deposits consist of two belts. On the western side lie the mining districts of Muzo, Coscuez, La Pita, Peñas Blancas, and La Glorieta–Yacopi. On the eastern side are Chivor, Gachalá, and Macanal (figure 2). The Eastern Cordillera is a slightly folded belt *overthrusting* the Llanos Foreland Basin to the east and the Middle Magdalena Basin to the west. The belt resulted from the tectonic inversion at the Middle Miocene (15 Ma), during the Andean tectonic phase, of the central part of the *subsiding marine basin*. The major part of the Eastern Cordillera is formed by thick folded and faulted Mesozoic sedimentary series. Emerald mineralization is hosted in the Neocomian series of

the Lower Cretaceous (135–116 Ma). The sediments are characterized by a succession of beds of sandstones, limestones, *black shales*, and *evaporites*.

The deposits from the eastern belt are contained in the Berriasian limestone–black shale horizon (135–130 Ma) of the Guavio Formation, which is overlain by siliceous black shales of the Valanginian Macanal Formation (130–122 Ma). In the Chivor mining district, the host rocks comprise the Guavio Formation shale sequences that contain intercalations of limestone lenses and gypsum beds, as suggested by phantom nodules, mesh and chevron textures, and *coquina limestone* grading to black shales intercalated with *olistostromes* (Branquet, 1999).

The deposits from the western belt are contained in the black shales and intercalated *dolomitic limestones* of Valanginian-Hauterivian age (130–116 Ma)

corresponding to the Rosablanca and Paja Formations. The lithostratigraphic column, from bottom to top, is formed by dolomitic limestones from the Rosablanca Formation, calcareous carbon-rich black shales from the Hauterivian that are the main emerald-bearing horizon, siliceous black shales (Hauterivian), and mudstones of the Barremian-Aptian Paja Formation (116–108 Ma).

The ages of emerald formation were obtained indirectly by argon-argon dating of syngenetic green muscovite. From this analysis, the first date was 65 Ma in the eastern zone, at the Cretaceous-Tertiary boundary when the dinosaurs disappeared (Cheilletz et al., 1997). The second date was between 38 and 32 Ma in the western zone, at the time of the Eocene-Oligocene boundary (Cheilletz et al., 1994).

**Emerald Mineralization**. In the two mineralized belts, emerald-bearing veins are spatially associated with stratiform *breccias* and white or black *albitites*, the latter resulting from the albitization of the black shales. The veins are parallel, *en echelon*, or conjugate arrays



Figure 3. Primary multiphase fluid inclusion trapped in an emerald from El Oriente mine in the Chivor district. The cavity, 180 µm long, contains (from right to left) two cubes of sodium chloride (halite), a rounded gas bubble, and two minute calcite crystals, with salt water occupying 75 vol.% of the cavity. The cavities usually contain only one cube of salt, but sometimes two or three cubes crystallize during fluid cooling. Photo by Hervé Conge.

> ## In Brief
> - Trapiche emeralds are found in the black shales of a few Colombian mines, in the western belt of the Eastern Cordillera Basin. They are characterized by a texture, visible perpendicular to the crystal's c-axis, that usually consists of a central core, six arms, and dendrites between the arms and around the core.
> - While trapiche emeralds are formed from the same fluid as gem-quality Colombian emeralds, their texture results from a complex growth history characterized by fluid pressure variations.
> - The formation of trapiche emeralds is controlled by the structural geology of the deposits and by the crystal's symmetry, which determines the number and the development of growth sectors.

forming two successive stages of extensional vein systems (Cheilletz and Giuliani, 1996). Stage 1 is accompanied by a bedding-parallel vein system filled by fibrous calcite, pyrite, and green muscovite. It is associated with the formation of *décollement* fault planes that focused the hydrothermal fluids and induced formation of albite and calcite in the black shales. The sodium *metasomatism* led to leaching of major (Si, Al, K, Ti, Mg), trace (Ba, Be, Cr, V), and rare-earth elements from the enclosing black shales (Beus and Mineev, 1972; Beus, 1979; Ottaway, 1991; Giu-

liani et al., 1993; Mantilla Figueroa et al., 2007). Stage 2 is characterized by faulting and folding associated with *extensional vein* sets and *hydraulic breccias* filled with calcite and dolomite, pyrite, muscovite, albite, bitumen, and the precipitation in *drusy cavities* of fluorite, apatite, parisite, dolomite, emerald, and quartz (Hall, 1993).

The Colombian emerald deposits were previously thought to be associated with mafic or granitic intrusions (Beus and Mineev, 1972; Ulloa, 1980). Detailed geochemical studies undertaken in the 1990s led to a hydrothermal model involving the circulation of hot *basinal brines* (Kozlowski et al., 1988; Ottaway, 1991; Giuliani et al., 1991; 1992; 1995; 2000; Cheilletz et al., 1994; Ottaway et al., 1994; Banks et al., 2000; Mantilla Figueroa et al., 2007). The fluids trapped by emerald are three-phase or multiphase fluid inclusions (figure 3) characterized by the presence of a cube (or occasionally two or three cubes) of halite (NaCl). At room temperature, the fluid inclusion cavities contain 75 vol.% salty water—in other words, a brine (liquid $H_2O$, 10 vol.% gas corresponding to the vapor bubble, and 15 vol.% halite *daughter mineral*). The mineralizing solutions are basinal brines that interacted with evaporites. The $H_2O$-NaCl-$CO_2$-(Ca-K-Mg-Fe-Li-$SO_4$) fluids (Banks et al., 2000) are NaCl-saturated [~40 wt.% equivalent NaCl] and were trapped at approximately 300–330°C (Roedder, 1984; Ottaway et al., 1994). The $CO_2$ densities of fluid inclusions range from 0.02 to 0.25 g/cm³ and indicate that emerald crystallized under variable fluid pressure. The increase of $CO_2$ pressure caused fluid *overpressure* in
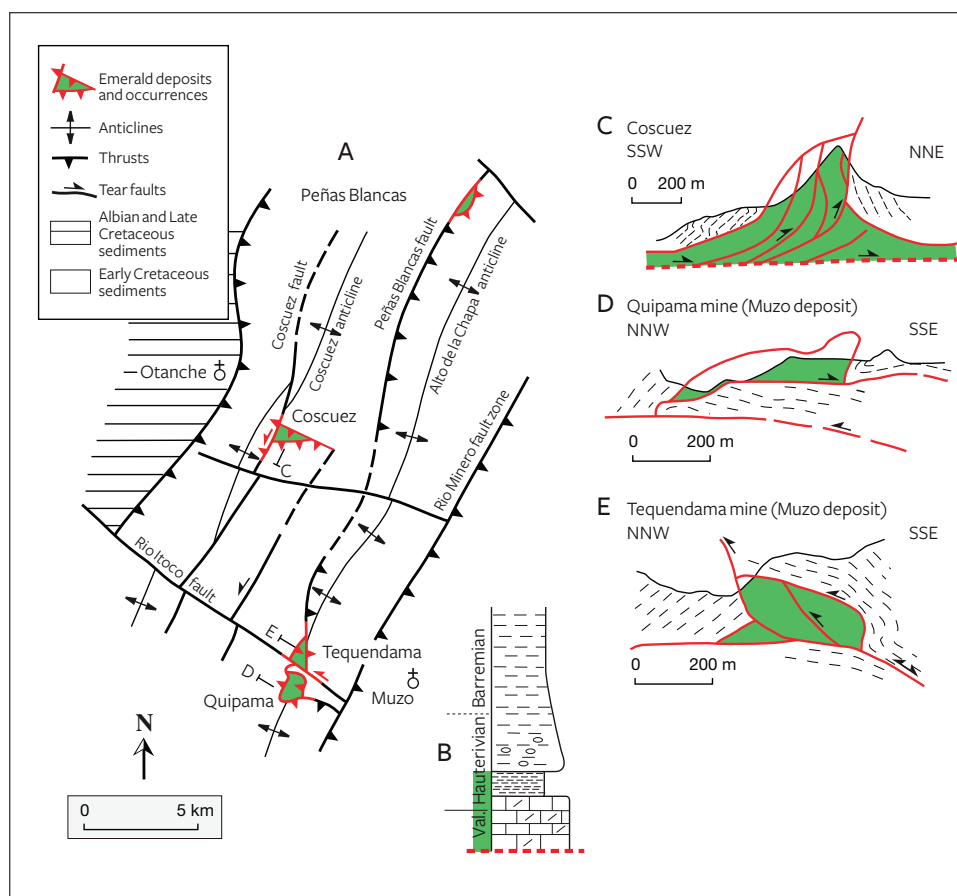
*Figure 4. Tectonic settings of Colombia's western emerald zone (modified from Branquet et al., 1999a). A: Structural location map of the emerald deposits and the regional structures, from Rodriguez and Ulloa (1994). B: Lithostratigraphic column of the emerald-bearing formations. From bottom to top: lowermost Cretaceous rocks, Valanginian-Hauterivian dolomitic limestone, Hauterivian calcareous carbon-rich black shale, Hauterivian siliceous black shale, and Barremian-Aptian mudstones. The red dotted line represents the décollement zone. C through E: Emerald deposits of Coscuez, Quipama, and Tequendama mines (Muzo district).*

the black shales and consequent fracturing and brecciation (Ottaway et al., 1994). The high-salinity brines interacted with calcareous shales rich with black organic matter. Sulfate ions ($SO_4^{2-}$) in minerals of evaporitic origin were reduced by organic matter in the black shale to form hydrogen sulfide ($H_2S$) and bicarbonate ($HCO_3^-$), which are responsible for the crystallization of pyrite and carbonates, respectively, with bitumen in the veins being derived from the organic matter.

The *thermal reduction of sulfate* by organic matter, at 300°C, released the chromium, vanadium, and beryllium in the black shale, which in turn enabled emerald formation (Ottaway et al., 1994; Cheilletz et al., 1994).

**Structural Setting and Type of Mineralization.** Detailed structural mapping and geometric analysis suggest that structural controls on mineralization are drastically different between the western and eastern sides of the Colombian emerald belt (Branquet, 1999; Branquet et al., 1999a,b). Muzo and Coscuez are characterized by compressive structures formed along *tear faults* (figure 4), whereas the eastern emerald deposits such as Chivor present extensional structures branched on a brecciated evaporitic level that acted as a local, gravity-driven *detachment* (Branquet et al., 2015). These tectonic structures are synchronous with the circulation of the hydrothermal fluids and emerald deposition.

On the western side, the deposits measure about 100 meters across and display numerous folds, *thrusts* (Pogue, 1916; Scheibe, 1926), and tear faults (Laumonier et al., 1996). At Muzo, thrusts are evidenced by the presence of calcareous black shales over siliceous black shales. All the tectonic contacts are marked by centimeter- to meter-thick hydrothermal breccias called "cenicero" (ashtray) by the local miners (Scheibe, 1926). These white or red breccias outline the thrust planes, which are associated with intense hydraulic fracturing due to overpressured fluids (Giuliani et al., 1990; Ottaway et al., 1994; Branquet et al., 1999b). The breccias are *cataclasites*, with clasts of calcareous black shales and white albitite within a carbonate-albite-pyrite cement. Multistage brecciation corresponds to successive fault-fluid flow pulses, and dilatant sites result from *shear*-fracturing synchronous to the thrust-fault propagation. Each

Figure 5. Geological map of the Muzo mines, with the height of each mining site reported in bold. Modified from Barriga Villalba (1948).

pulse is associated with (1) emerald-bearing banded carbonate vein-like structures present throughout the breccia; (2) emerald-bearing thrust-associated carbonate veins occurring in the wall rocks formed of calcareous black shales, called "cama" by the local miners; (3) emerald-bearing carbonate dykes escaping from the breccia zone and crosscutting the wall rocks; (4) en echelon sigmoidal *tension gashes*; and (5) *drag folds* indicating shearing in the roof of the breccia

zones. All these tectonic structures are associated with fluid circulation in the calcareous carbon-rich black shale, inducing intense albitization, carbonatization, and pyritization. The siliceous black shales, called "cambiado" by the local miners, have no mineralization (Oppenheim, 1948).

From a geological study in 1914–1915, Pogue (1916) described the trapiche texture but did not provide the precise location of the source. Scheibe (1926, 1933) identified the disseminations of trapiche emerald in the black shales from the Banco Amarillo. ("Banco" refers to a mineralized level, and "amarillo" is Spanish for yellow; here the yellowish color is due to pyrite alteration.) The geological map of Banco de la Republica (Barriga Villalba, 1948) indicates that Banco Amarillo was formed by the breccia zone, albitites, and the emerald-bearing veins (figure 5). The geological map by Laumonier et al. (1996) shows that a preserved remnant of the Banco Amarillo level (figure 6) is located under the administration building of the Muzo mine and corresponds to a *klippe* of the calcareous black shale that overthrust the siliceous black shale. Since 1948, this emerald-bearing formation has been exploited further to the southwest up to the Gallinazo, Zincho, and Malvinas mining workings (compare figures 5 and 6). Furthermore, Ottaway (1991) reported that "more recently trapiche have been found in the shale adjacent to larger bodies of Cenicero."

In the Coscuez deposit, the lithostratigraphic column is formed, from bottom to top (Branquet, 1999), by *dolomitic limestone* forming the peak of El Reten, calcareous carbon-rich black shale, and siliceous black shale. The folds and thrusts were guided by the Coscuez tear fault, which acted as a vertical conduit for the mineralizing fluids developed in the calcareous carbon-rich black shale (figure 4B). Breccia, formed by opening of dilatant sites related to fluid pressures and hydrothermal replacement, are similar to those described for the Muzo deposit (Branquet et al., 1999b). Trapiche emeralds have been found at Coscuez but have never been described by geologists.

In conclusion, the deposits on the western side formed as the consequence of a compressive phase characterized by folding and thrusting along tear faults at the time of the Eocene-Oligocene boundary. These complex structures imply the existence of a basal regional décollement fault at a level of evaporites (Branquet et al., 1999b). The fluid circulation is linked to the thrust-fault propagation.

On the eastern side, the mines are scattered along a regional white-brecciated level that contains emer-

ald (Branquet, 1999; Branquet et al., 1999a, 2015). The brecciated level in the Chivor area, more than 10 km long and 1–10 meters thick, is stratiform (i.e., parallel to the sedimentary strata) and largely made of hydrothermal breccia formed by fragments of the hanging wall (carbonated black shale, limestone, and whitish albitite), cemented by carbonates and pyrite. Its formation is related to the dissolution of an evaporitic horizon. All the mineralized structures are branched from the brecciated level. In the Chivor mines, emerald is located in centimeter- to decimeter-thick carbonate- and pyrite-bearing *listric faults*, meter-wide extensional fractures injected with hydrothermal breccia, and extensional sets of fractures in the calcareous carbon-rich black shales of the Macanal Formation. According to a member of the family that has owned the Chivor mines for many years, trapiche emeralds have never been found there or anywhere else in the eastern zone of the Eastern Cordillera (D. Oswaldo, pers. comm., 2014). Nevertheless, Nassau and Jackson (1970) claimed to have studied a thousand trapiche emeralds from these mines, and their article raised the question of Chivor origin. In conclusion, the brecciated level, the hydrothermal fluid circulation and emerald formation occurred at the same time, at the Cretaceous-Tertiary boundary (~65 Ma), during an extensional tectonic event linked to evaporite dissolution and driven by gravity (Branquet et al., 1999a, 2015).

Therefore, trapiche emeralds are only found in the deposits on the western side (Muzo, Coscuez, and Peñas Blancas) of the Eastern Cordillera Basin. The trapiche emerald–bearing deposits are formed along thrust and fault planes associated with fluid circulations, intense hydraulic fracturing of the enclosing black shales forming breccias, and carbonate veins. Trapiche and non-trapiche emeralds are associated with these compressive structures.

## EMERALD: STRUCTURE AND HABIT

Emerald is a gem variety of beryl, a cyclosilicate with the ideal formula $Be_3Al_2Si_6O_{18}$. Its structure is characterized by six-membered rings of silica tetrahedra lying in planes parallel to (0001). The rings are linked laterally and vertically by two kinds of coordination polyhedra, both distorted: $BeO_4$ tetrahedra and $AlO_6$ octahedra (figure 7). The stacking of these six-membered rings forms large open channels parallel to the c-axis with nonuniform diameter, consisting of cavities with a diameter around 5.1 Å separated by bottlenecks with a diameter of about 2.8 Å. The channels may be filled by alkali ions (such as $Na^+$,
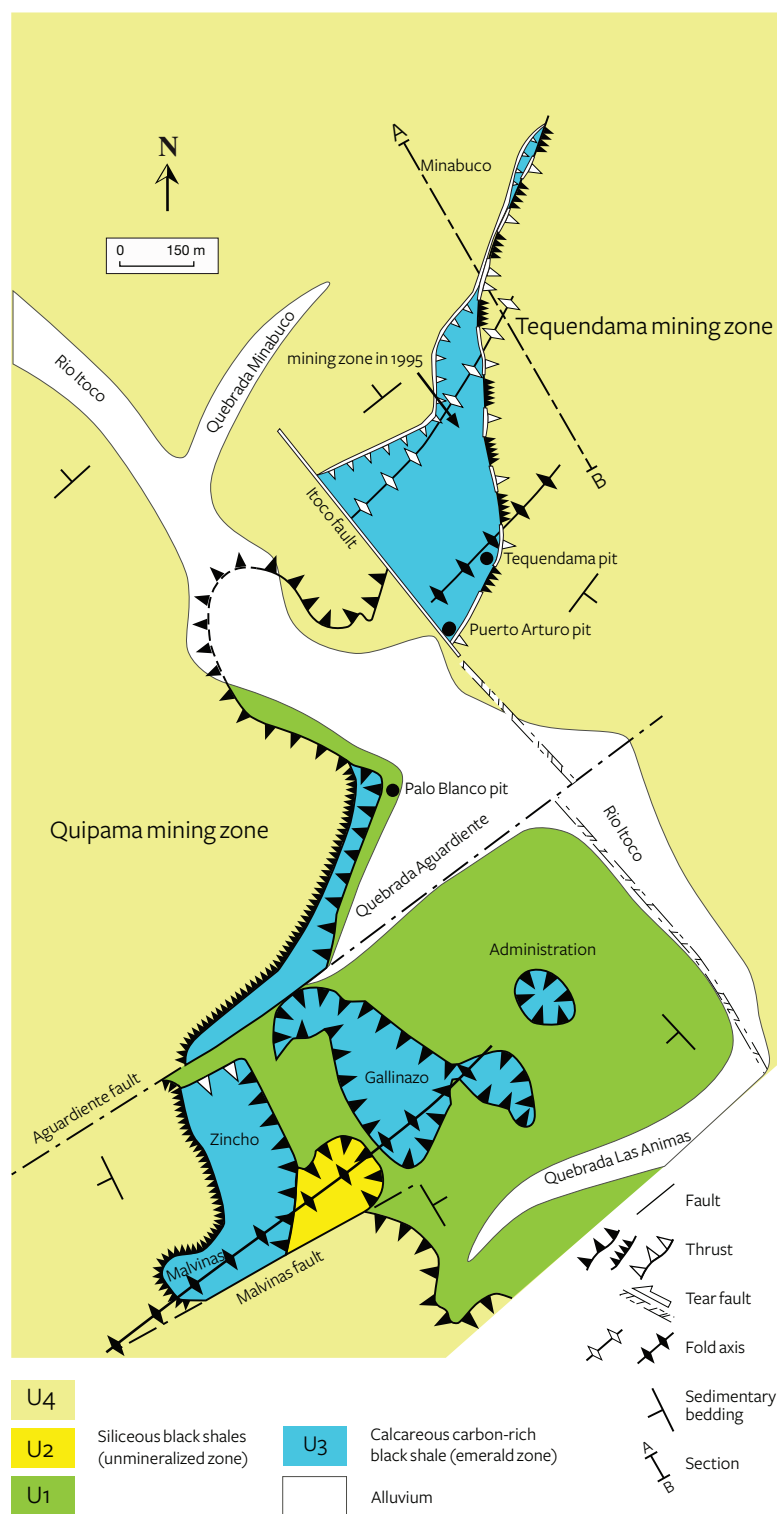


Figure 6. Geological map of the Muzo mines, where U1 through U4 represent the different tectonic units. U1, U2, and U4 are composed of barren siliceous black shales, while U3 consists of the emerald-bearing calcareous carbon-rich black shale. Modified from Laumonier et al. (1996).
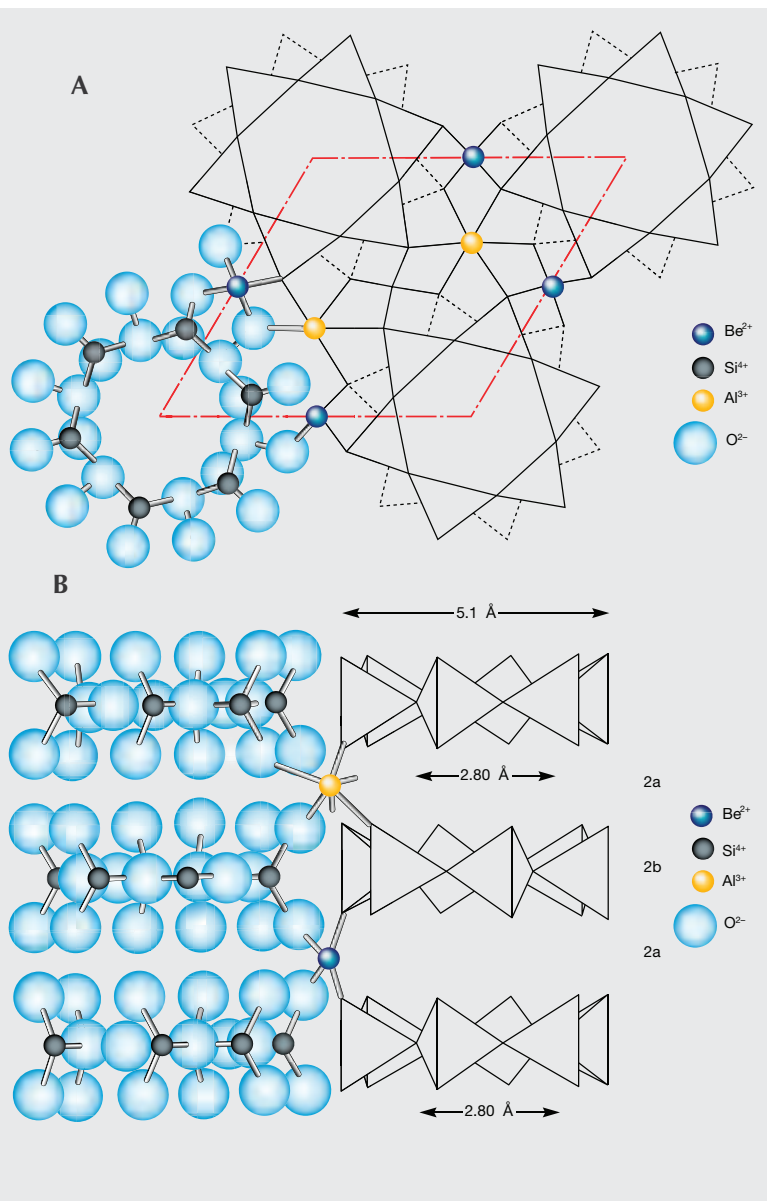
Figure 7. The structure of beryl, as seen in an apical view (A) and a lateral view (B). In the apical view, hexagonal silicate rings stacked parallel to the c-axis (normal to the drawing) are held together by $Al^{3+}$ (octahedral site) and $Be^{2+}$ (tetrahedral site). The lateral view, which is perpendicular to the apical view, shows the hexagonal silicate rings and the bottleneck (2b site) and open-cage (2a site) structures. From Charoy (1998).

$Li^+$, $K^+$, $Rb^+$, and $Cs^+$) that are needed to balance the positive charges when cation substitutions occur in the structure. For example, $Be^{2+}$ can be substituted with $Li^+$ (Aurisicchio et al., 1988), whereas $Al^{3+}$ is generally replaced by $Fe^{2+}$, ($Mg^{2+}$, $Mn^{2+}$), $Cr^{3+}$, $V^{3+}$, or

$Ti^{4+}$ (Groat et al., 2014). Variable amounts of neutral $H_2O$ and $CO_2$ molecules (Wood and Nassau, 1968) and noble gases such as argon, helium (Damon and Kulp, 1958), xenon, and neon (Giuliani et al., 2005) are also normally present in the channels.

Emerald is defined by Schwarz and Schmetzer (2002) as "the yellowish green, green or bluish green beryl which reveals distinct chromium and/or vanadium absorption bands in the red and blue violet ranges of their absorption spectra." The quantitative ranges of the Cr and V substitutions are between 25 ppm (Wood and Nassau, 1968) and 3.4 wt.% (Andrianjakavah et al., 2009) for $Cr_2O_3$, and between 34 ppm (Zwaan et al., 2012) and 2.44 wt.% (Rondeau et al., 2008) for $V_2O_3$. Emerald crystallizes in the hexagonal system with cell parameters $a$ = 9.218(2) Å, $c$ = 9.197(2) Å, $\alpha = \beta = 90°$, and $\gamma = 120°$, and its *space group* is $P6/mcc$ (Artioli et al., 1993). Its typical habit is prismatic (figure 8), characterized by eight faces and their corresponding growth sectors: six $\{10\bar{1}0\}$ first-order prismatic faces and two *pinacoidal* $\{0001\}$ faces. Small additional $\{10\bar{1}2\}$ and $\{11\bar{2}2\}$ faces may also be present in some crystals.

## TRAPICHE COLOMBIAN EMERALD: A REVIEW

Colombian trapiche emeralds were first described by the French mineralogist Emile Bertrand (1879), in a meeting at the Société Géologique de France, in which he presented "curious crystals of emerald… from Muso, New Granada." All 40 samples displayed a nearly colorless hexagonal center surrounded by a green portion. The latter is described as having striations parallel to the sides of the central hexagon and with "modifications" in the directions tangential to the sides of the hexagon. No further information was added about the composition or the nature of the "modifications." Bergt (1899) described a cut trapiche emerald from Muzo received by the geologist Stübel in 1868. Similar emeralds were reported by Codazzi (1915) in an accurate listing of Muzo's minerals. These emeralds were reported to have a cyclic twinning, as observed in aragonite. This contradicted the optical observations of Pogue (1916), who stated that these emeralds were not twinned. According to Pogue, the presence of re-entrant angles was due to "the effect of solution, the disposition of carbonaceous inclusions and the crystallizing forces, as shown also, for example, in chiastolite." It is worth noting that the Pogue study contained the first mention of inclusions of carbonaceous matter in the emeralds, "arranged in a six-rayed centering about a tapering hexagonal core."
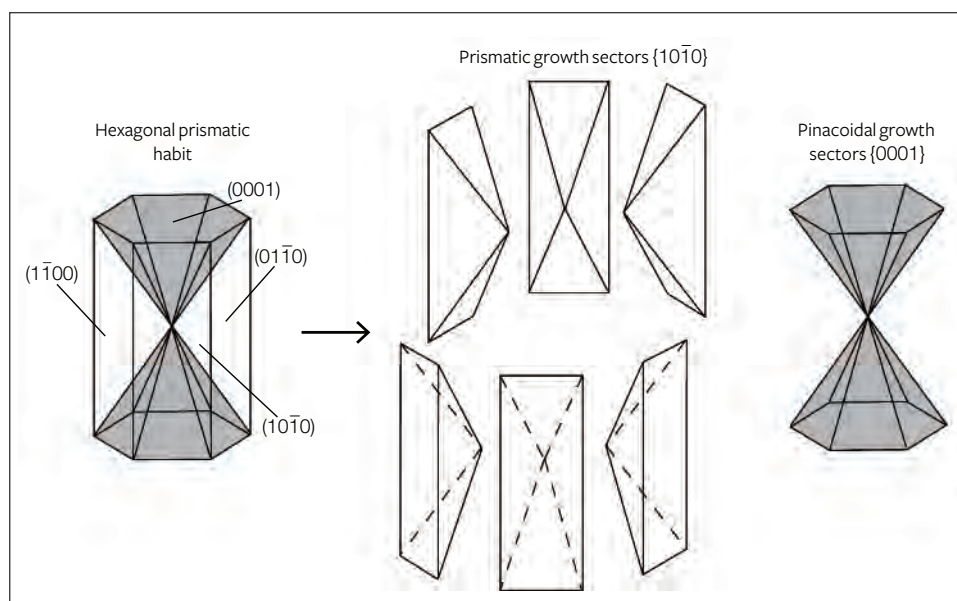
Figure 8. The habit of emerald crystals, characterized by eight main faces and their corresponding growth sectors: six {10$\bar{1}$0} first-order prismatic faces and two pinacoidal {0001} faces. Adapted from Rakovan et al. (2006).

During a geological study of Muzo in 1914–15, Scheibe (1926, 1933) collected several emeralds from the Banco Amarillo in the calcareous carbon-rich black shales of the Lower Cretaceous (again, see figure 5). These emeralds appeared very different from those usually found in the veins, and for this reason they were analyzed in detail by Bernauer (1933). Different morphologies were observed, as shown in figure 9: euhedral hexagonal prismatic emeralds (figure 9A), but also crystals with signs of corrosion along the edges of the prism (figures 9B to 9E). The emeralds showed dark, fibrous inclusions between the prismatic edges, starting from the middle of the crystal and enlarging toward the prism's corners. The inclusions, which seemed to be emphasized by the corrosion, were composed of quartz, muscovite, carbonates, pyrite, and a dark carbonaceous matter (probably with an organic or bituminous origin), sometimes with biotite and kaolin. Multiphase inclusions with liquid, vapor, and solid phases were

also observed. The core of the emeralds had the shape of two opposite hexagonal pyramids with their vertices located in the middle of the crystal. Sometimes these pyramids were so unevenly developed that the core resembled a column. The core was richer in inclusions, some of them more darkish to black, than the rest of the crystal. In fact, it can be surrounded by the dark inclusions (figure 9B), entirely composed of the dark inclusions (figure 9D), or formed by several parallel crystals separated by dark inclusions (figure 9C). In some emeralds the inclusions can be whitish instead of dark, due to the presence of albite and kaolin.

Although Bernauer (1933) suggested that these trapiche emeralds were due to cyclic twinning as in cordierite, chrysoberyl, aragonite, or other minerals, he emphasized that the growth rates in the different crystallographic directions played an important role in the incorporation of the dark inclusions and, thus, in the formation of these emeralds. Nevertheless,
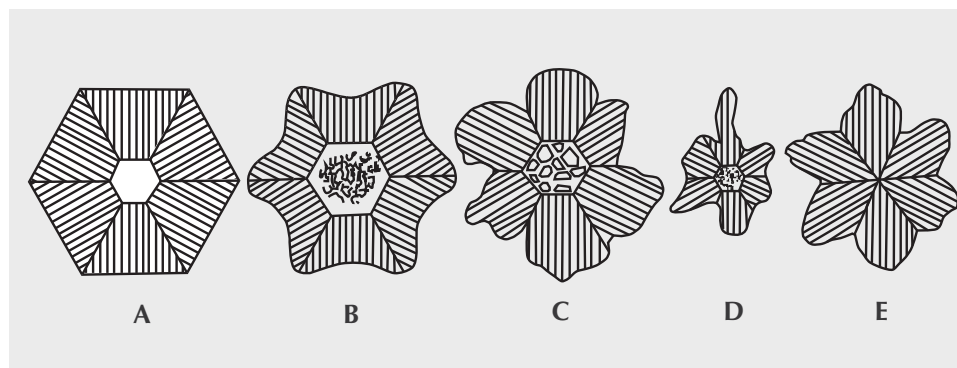


Figure 9. Different morphologies of trapiche emeralds from the Muzo mine, described by Bernauer (1933). A: Euhedral hexagonal prismatic crystals with no sign of corrosion. B through E: Crystals showing different degrees of corrosion along the prism's edges.

Barriga Villalba (1948) described the unusual trapiche emeralds from Muzo as aragonite-type twins of scientific interest but no gemological value. Studying the mineralogical features of Muzo emeralds, Barriga Villalba (1948) pointed out the special aspects of the core in crystals of different sizes. The gem core was formed by pyramidal and hexagonal cones presenting a three-dimensional geometric shape that tapered smoothly from the pinacoid to the vertex. These gem cones, sometimes of high quality, were extracted from the emerald crystal.

The 1960s saw further studies on Colombian trapiche emerald, with the discovery in 1963 of new material in the Peñas Blancas mines (Tripp and Hernandez, 1970). In 1964, McKague introduced the term "trapiche" to name the unusual Colombian emerald whose crystal habit was similar to the cane-crushing gears used by farmers. According to McKague, trapiche emerald was characterized by four morphological elements:

1. A central deep green hexagonal prism tapered toward one end and without inclusions

2. Six trapezoidal-shaped prisms extending from the $\{10\bar{1}0\}$ faces of the central prism and containing opaque inclusions

3. A colorless fine-grained beryl occurring between and within the six trapezoidal prisms but also in the central prism, with opaque minerals (probably altered in limonite) observed on and between the beryl grains

4. An overgrowth separated from the six prisms by scattered patches of opaque inclusions

McKague was the first to propose a genetic model for the formation of trapiche emeralds. In this model, the central prism formed first. A change in pressure, temperature, and chemical composition or a combination of these parameters caused the formation of the trapezoidal prisms. A further change in the system led to the overgrowth's formation. At the end, a more drastic change occurred and the trapezoidal prisms were partially converted into fine-grained beryl at the intersections of the $\{10\bar{1}0\}$ faces.

In 1967, Leiper examined unusual trapiche emeralds reportedly from the Chivor mine. The core and the six arms branching from it were emerald of good quality, while the material between the arms was a whitish-greenish beryl. This low-quality material was compared to the fine-grained beryl described by McKague, usually called "moralla" by the local miners.

In 1968, Schiffman analyzed trapiche crystals to identify them as natural or synthetic. The presence of channels, three-phase fluid inclusions, and solids (organic matter, possibly graphite, as well as quartz and albite) confirmed their natural origin. Chaudhari (1969) described the emeralds with the unusual gear-shaped pattern as composite crystals made of two distinct entities: a hexagonal pale green core and a dark green overgrowth on the prism faces. Around the core, the sectors were separated by a very fine-grained clay-like matrix (containing abundant quartz). Some of the sectors were irregular and formed by *stringers* that grew from the core to the faces. Small stringers of emeralds at 60° angles to each other in the matrix were also described, but only in the gaps between the sectors. According to Chaudhari, the sawtooth contact between the matrix and the sectors with the stringers indicated that several changes occurred in the chemical and physical conditions during trapiche growth.

Nassau and Jackson (1970) marked a real advance in the understanding of trapiche formation after Bernauer (1933). Nevertheless, this work raised a questionable point on the origin of trapiche material. The authors claimed to have studied a thousand trapiche emeralds from Chivor and only two from Muzo. Between 1963 and 1970, trapiche emeralds came only from the Peñas Blancas and Muzo mines. Leiper (1967) had not specified the provenance of his samples, leading to a series of misunderstandings in subsequent bibliographic citations. But Leiper's photos of the trapiche emeralds resembled those presented by Tripp and Hernandez (1970) for the Peñas Blancas mine. Samples from Peñas Blancas were given to Leiper by M. Anderton, manager of the Chivor emerald mine, and this is probably the source of the confusion over the origin of the stones studied by Nassau and Jackson. Finally, Sinkankas and Read (1985) clarified the provenance of the trapiche emeralds described by Nassau and Jackson, asserting that they were from Peñas Blancas.

Examinations of cross-sections of single crystals have shown considerable variation in the structure of trapiche emerald; see figure 10. Nassau and Jackson (1970) used the terms "core," "arms," and "two-phase region." The hexagonal core may or may not be present (figure 10C), and it is usually of good-quality emerald, but it is possible to find samples with one end as in figure 10B and the other as in figure 10C. The core usually has a taper, as previously noted by Pogue (1916), Barriga Villalba (1948), and McKague (1964). The emerald formed on the prism faces of the core are named "arms," because their
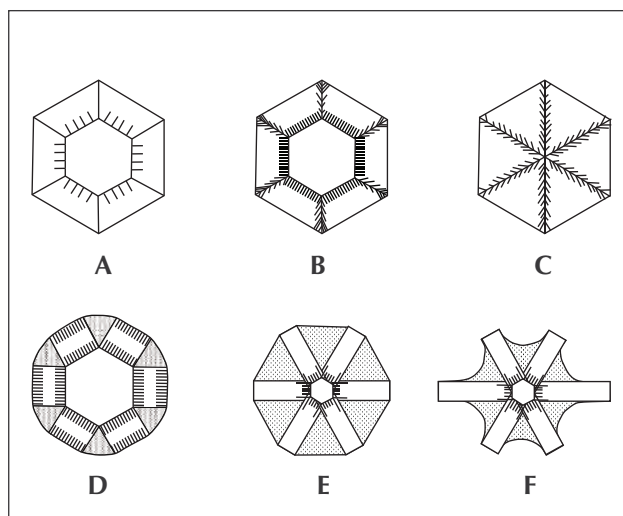
*Figure 10. Schematic cross-sections of different trapiche emeralds described by Nassau and Jackson (1970).*

shape is not always trapezoidal (as described in previous works). Moreover, the arms may be asymmetrical (figure 10F). The material observed between the arms as well as between the core and the arms can be white/gray or dark. The white to gray material is formed by a mixture of emerald and albite, while the dark material is carbonaceous, even if it contains albite. Trapiche emeralds with a core completely composed of this dark material have also been reported.

Nassau and Jackson (1970) rejected the hypothesis of twinning to explain trapiche formation. They proposed two mechanisms, one for the samples purportedly from Chivor and one for the Muzo samples. In the "Chivor" samples, the central core formed first, followed by beryl growth on its prism faces. Simultaneously, a dendritic growth of both beryl and albite under *eutectic* conditions occurred at the corners of the central core. The presence of beryl-albite can be also related to an abrupt increase in the growth rate of the arms. In fact, this favors the trapping of the foreign phase (albite in this case) at the interface between the growing "arms." According to the authors, all Chivor samples are grown "in the same time, in the same or similar environments, in a relatively small region." To explain the formation of Muzo samples, they suggested instead an abrupt decrease in the growth rate of the arms and/or an increased concentration of carbonaceous material in the growth medium.

In 1971, O'Donoghue synthesized the work of Nassau and Jackson (1970) and remarked that the whitish gray or dark inclusions are not randomly distributed but follow the "hexagonal axis," i.e., the <100> directions in the hexagonal system (a-axis).

Two decades later, Van der Giessen (1994) reported several Colombian trapiches, among them a special sample with two hexagonal cores surrounded by eight trapezoidal sectors (figure 11). This sample seems to be a rare case of contact twinning in trapiche emeralds. According to the author, the formation of the trapiche is related to sector zoning. This peculiar example is perhaps closer to the unusual double-trapiche emeralds from Muzo reported by Hsu (2013), which consist of twelve fine arms intersecting in a central point. These samples are described as "composed of two six-ray stars shifted slightly from each other," though one might think they are twinned.

Ohnenstetter et al. (1998) studied Colombian trapiche emeralds from Muzo, Coscuez, and Peñas Blancas. The cores were colorless, and the trapezoidal growth sectors were colored with vivid green overgrowths. Cathodoluminescence underlined the chemical zoning due to variations of vanadium (V) and chromium (Cr). The first published microprobe data on trapiche emerald confirmed that the green zones were V-rich ($0.5 < V_2O_3 < 0.79$ wt.%) and relatively Cr-poor ($0.35 < Cr_2O_3 < 0.39$ wt.%). The colorless hexagonal prism was a Cr- and V-free beryl. Scanning electron microscope observation of sections perpendicular to the c-axis showed streaks along the trapezoidal growth sectors and a feathery aspect to the inclusions in the arms of the crystals. The arms were formed mainly of albite and beryl, with some apatite and pyrite. The authors thought that trapiche emeralds resulted from a

*Figure 11. Schematic cross-section of an exceptional trapiche emerald examined by Van der Giessen (1994). The emerald is characterized by two hexagonal cores surrounded by eight trapezoidal sectors.*
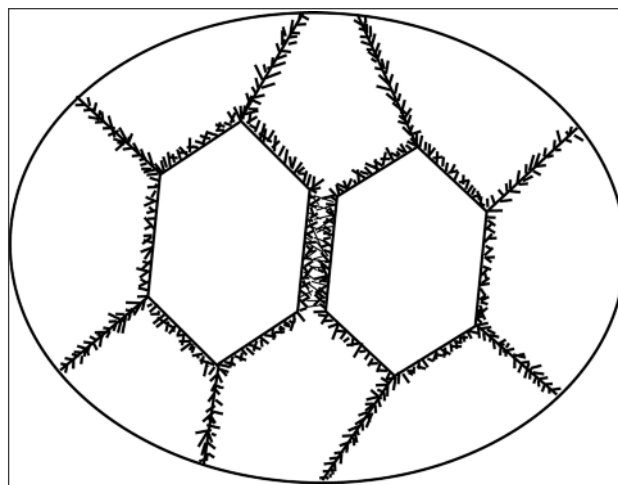
# BOX B: CRYSTAL NUCLEATION, GROWTH, AND TEXTURE

Sunagawa (1987, 1999) proposed that crystal morphology depends on the degree of supersaturation (also called undercooling) that conditioned the driving force and explained the evolution of crystal habit by changes in growth mechanism. Figure B-1 presents the driving force versus the growth rate anisotropy. The driving force is characterized by two critical points (X and Y) where the predominant growth mechanism changes: spiral growth for a low driving force, two-dimensional nucleation growth (2DNG) for an intermediate driving force, and an adhesive growth mechanism for a high driving force. The expected morphologies change from polyhedral to hopper or skeletal and then to fractal, spherulitic, and dendritic.

Crystals demonstrating rapid growth textures are found in many rock types and geological environments: pillow basalts (Bryan, 1972), granites and pegmatites (London, 2008), magmatic olivine (Faure et al., 2003), chiastolites and garnets in metamorphic environments (Burton, 1986; Rice, 1993), metasomatic tourmalines (Byerly and Palmer, 1991), and finally in trapiche emeralds and rubies (Sunagawa et al., 1999).

As stated by Nassau and Jackson (1970) for Colombian emerald, trapiche starts to grow as a beryl in the core, and then as coeval albite and beryl in the dendrites and stringers in the arms. Based on this mineralogical evidence with the simultaneous growth of both albite and beryl, the growth of trapiche emerald could be interpreted as a eutectic binary system (Nassau and Jackson, 1970), though

such a system of albite and beryl has not been investigated up to now. In the same way, Sunagawa et al. (1999) also considered the dendritic morphology and mineral composition (corundum and carbonate) of trapiche ruby that was formed under eutectic growth conditions.

Despite the fact that Colombian trapiche emerald is related to basinal fluid circulation, the association of albite-beryl in a $H_2O$-NaCl $\pm(CO_2)$ fluid seems to be similar to paragenesis in low-temperature $H_2O$-saturated pegmatites. In such a magmatic system, supersaturation is the driving force of the crystallization, and so the rate of nucleation and growth is driven by supersaturation in the solution. In a binary diagram of temperature and composition, the displacement of the liquidus (the temperature above which a magma is molten) may occur in response to changes in pressure, temperature, or composition (London, 2008). A decrease in pressure such as a drop in the $H_2O$ fluid pressure in an $H_2O$-saturated melt will provoke a decompression, providing the driving force of crystallization with dendritic textures (London, 2008). In the case of Colombian emerald, the decompression phenomena by a drop of $H_2O$ (and $CO_2$) fluid pressure at the tip of the faults induced a huge supersaturation that provided the driving force to initiate crystallization of the dendrites of trapiche emerald composed of albite and emerald. The predominance of albite over emerald in the dendrites indicates a great undercooling that promoted the crystallization first of albite and then emerald.
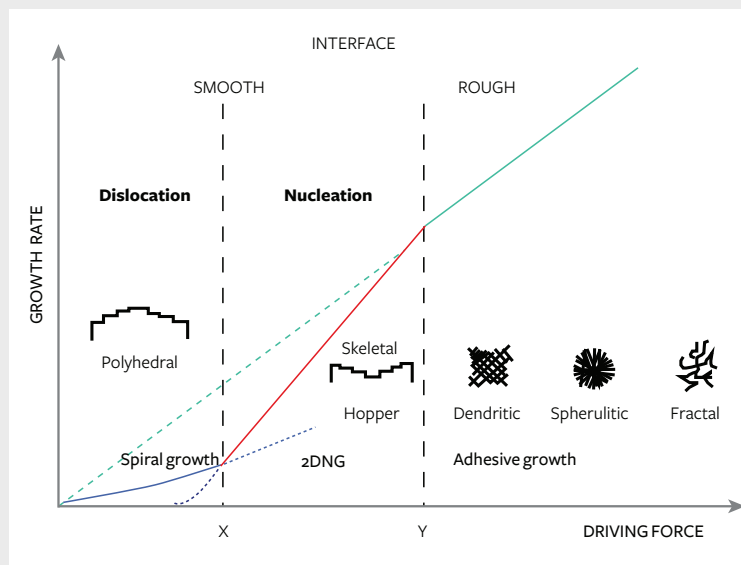


Figure B-1. This diagram shows the three types of crystal growth mechanisms (Sunagawa, 1999): spiral growth (blue curve), two-dimensional nucleation growth (2DNG; red curve), and adhesive growth (green curve). The nature of the interfaces is classified as either rough or smooth. The growth rates are determined by the state of the interfaces, which are classified as either rough or smooth. The increasing intensity of the driving force is presented between the critical points X and Y, where nucleation occurred. A rough interface is expected above Y and smooth interface below X, where dislocation occurred.

rapid and skeletal growth, complicated by interactions between the hydrothermal fluids and the black shales.

Sunagawa et al. (1999) compared the formation of trapiche emeralds to trapiche rubies in light of crystal

growth mechanisms, presenting evidence of many parallels (box B). Two main differences were pointed out: the typical absence of the core in rubies, and the dissimilar geological settings. However, the formation mechanism seems to be the same for both minerals: if a core is present, it is formed at first by *layer-by-layer* growth under small driving force conditions. When the driving force increases, a *dendritic* multiphase growth occurs around the core. Then, a decrease of the driving force leads to layer-by-layer growth and the formation of the ruby or emerald sectors. The contemporaneousness of the two last stages is not ruled out by Sunagawa et al. (1999).

In the past decade and a half, the main features of Colombian trapiche emeralds have been revisited in an exhaustive work by Hochleitner (2002); Giuliani et al. (2002) added that they are only found on the western side of the Eastern Cordillera Basin as material "disseminated in black shales or albitized black shales near emerald-bearing veins." Garnier et al. (2002) compared the geological setting of trapiche rubies from Mong Hsu in Myanmar with that of Colombian trapiche emeralds; the results underscored the differences in deposit type, fluid circulation, and *P-T* conditions of formation. Hainschwang et al. (2007) and Schmetzer et al. (2011) compared Zambian trapiche tourmalines to Colombian trapiche emeralds. Their studies suggested similar formation, depending on the growth rates of different sectors of the crystals. Both minerals contain dark carbonaceous inclusions along the a-axis, but the main visual difference is the tourmaline's three-sectored core due to the trigonal system of crystallization (space group *R3m*).

## NEW SCIENTIFIC ADVANCES ON THE COLOMBIAN TRAPICHE EMERALDS

**Material and Methods.** The twelve trapiche emeralds examined in this study were provided in 1998 by Omar Bustos Santana, manager of Sociedad Esmeralda Ltda. (figure 12; table 1). The samples came from three Colombian mines: Coscuez (figures 12A–12C), Peñas Blancas (figure 12D), and Muzo (figures 12E–12L). These samples were stubby and small; their diameters varied from approximately 4.0 mm to 1.2 cm, generally with lengths of a few millimeters, with the exception of one sample approximately 1.1 cm long (figure 12I). The habit of the trapiche emeralds could not be well defined owing to the presence of a whitish or dark material; nevertheless, the pinacoidal {0001} faces and first-order prism {10$\bar{1}$0} faces were recognizable in many of them. The color varied from one sam-

ple to another, but also within different portions of the same sample (from pale to deep green). The samples were prepared either as polished sections for electron microprobe analysis (EPMA), scanning electron microscopy (SEM), and cathodoluminescence analysis, or cut and polished on both sides to a thickness of 150–200 μm for microscopic examination. The main source and features of the crystals, and the different analytic methods applied for each trapiche emerald, are reported in table 1.

EPMA was performed at the University of Lorraine in Nancy's SCMEM laboratory on a fully automated Cameca SX100. The detection limits for trace elements in mass percentage were 715 ppm for Mn, 500 for Na and Si, 300 for Mg and Al, 110 for K, 40 for Ti, and 100 for V, Cr, and Fe. Data reduction was performed with the PAP program (Pouchou and Pichoir, 1991). Chemical formulas of emerald were calculated on the basis of 3 Be and 18 O apfu. BeO was determined by stoichiometry and $H_2O$ by the equation derived from experimental data (Giuliani et al., 1997): $H_2O$ (in wt.%) = (0.84958 × $Na_2O$ (in wt.%) + 0.8373).

Cathodoluminescence (CL) and back-scattered electron (BSE) images were recorded at the SCMEM laboratory using an FEG JEOL J7600F SEM with an accelerating voltage of 15 kV and a beam current of 10 to 20 nA for the X-ray analysis and 2 nA for the CL images. This SEM is equipped with a Gatan MonoCL2 system with three diodes measuring the intensity of light in different wavelength regions, so the observed colors correspond to those of the visible spectra. CL images were also obtained under a Technosyn cold CL device, where the electrons are generated by an electric discharge between two electrodes under low gas pressure.

Trapiche emeralds were investigated by X-ray diffraction topography (XRDT) at the University of Bari, Italy, to obtain the spatial distribution and full characterization of the crystal defects in the whole sample volume (Lang, 1959). Topographic images were taken in transmission geometry using a conventional Lang camera (Rigaku ME110ED) with monochromatic MoK$\alpha_1$ radiation (λ = 0.709 Å) and a micro-focus X-ray tube. To minimize the X-ray absorption according to the Beer-Lambert law, the optimum kinematic diffraction condition μt ≈ 1 (μ = linear absorption coefficient; t = crystal thickness) must be followed. Diffraction contrast was recorded on Kodak SR photographic film. The structural defects were characterized by applying the extinction criteria to their diffraction contrasts, ac-
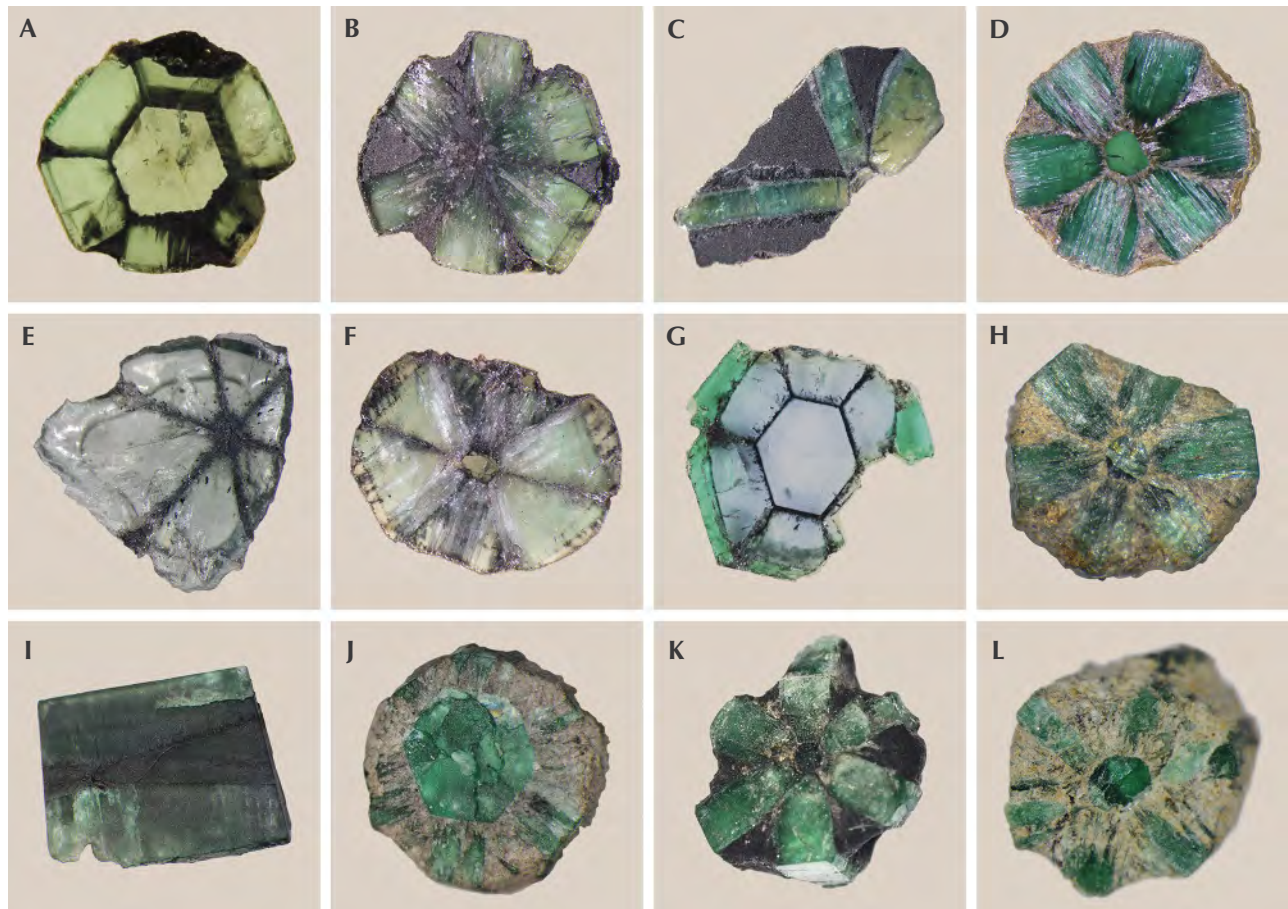
*Figure 12. The Colombian trapiche emeralds studied in this work originate from the Coscuez (A–C), Peñas Blancas (D), and Muzo (E–L) mines. The sample sizes are reported in table 1. Shown are samples T2 (A), T3 (B), T4 (C), T5 (D), T6 (E), T7 (F), T8 (G), T9 (H), T10 (I), T11 (J), T12 (K), and T13 (L).*

cording to kinematic and dynamic X-ray diffraction theories (Authier and Zarka, 1994).

X-ray computed tomography (CT) scanning is a non-destructive technique used in this study to reveal 3D interior details of trapiche emeralds. Images were made with a Phoenix Nanotom S scanner, using a resolution of 3.4 μm/voxel and a nanofocus X-ray tube tension value of 100 kV. Virtual cross-sections from all axes were extracted from the volume to observe the physical structure (e.g., inclusions and porosity) and to detect the presence of phases with different densities in the samples. The Nanotom scanner produces files with voxel (3D pixel) resolutions between 30.0 and 0.6 μm as a function of sample size. X-ray computed tomography has already been used for geoscience applications (Breeding et al., 2010; Tsuchiyama et al., 2005; Cnudde and Boone, 2013; Jia et al., 2014) but never previously for colored gems, because the X-ray exposure can strongly modify their colors. Here the technique was applied for the first time to ana-

lyze emeralds with satisfactory results and above all without color modification.

## RESULTS

In figure 13A, two sections of a trapiche emerald, perpendicular and parallel to the c-axis, are illustrated schematically: one can distinguish the central core, the arms, the dendrites, and the overgrowth. It is worth noting that the trapiche emeralds are more developed perpendicular to the c-axis rather than along the c-axis. For this reason, it is rare to observe a section parallel to the c-axis, such as the example shown in figure 12I. Such sections are usually not available for scientific study, as trapiches are cut as cabochons that display their particular texture for jewelry.

The spatial relationships between the core, arms, and dendrites are visible in three perpendicular sections obtained by X-ray computed tomography (figure 14). Each aspect of the trapiche texture is described in detail below.

**TABLE 1.** Features and properties of the 12 trapiche emeralds investigated in this study.

| Locality | Sample | Geometric pattern | Diameter (mm) | Section c-axis | Trapiche matrix | Composition (wt.%) $(V_2O_3)$ | $(Cr_2O_3)$ | Solid inclusions | Microscopy | SEM | EPMA | XRDT | CT | CL |
|---|---|---|---|---|---|---|---|---|---|---|---|---|---|---|
| Coscuez | T2 | Hexagonal crystal with core, arms, dendrites and small overgrowth | 8 | ⊥ | None | c: 0.13–0.15<br>d: 0.16–0.20<br>a: 0.22–0.62<br>og: 0.62–0.90 | 0.00–0.04<br>0.02–0.03<br>0.02–0.03<br>0.05–0.90 | Ab, Qtz, Brl, Ank, Dol | ✓ | ✓ | ✓ | ✓ | | ✓ |
| Coscuez | T3 | Center, arms | 6 | ⊥ | AbBS | | | Ab, Dol, Brl, Cal, Qtz, Fap, Fe(O,OH), Ank, Py | ✓ | ✓ | | | | |
| Coscuez | T4 | Small core, arms, dendrites | Arm up to 10 mm | ⊥ | AbBS | c: 0.12–0.14<br>d: 0.20–0.30<br>a: 0.20–0.30 | 0.12–0.14<br>0.18–0.19<br>0.15–0.20 | Ab, Cal, Brl, Tur, Rt, Mca, Fap, Po, Zrn, Dol, Kln | ✓ | ✓ | ✓ | | | ✓ |
| Peñas Blancas | T5 | Hexagonal green core with green arms, dendrites | 4 | ⊥ | AbBS + clays | c: 0.68–0.72<br>d: 1.17<br>a: 0.90–1.16 | 0.30–0.40<br>0.68<br>0.0–0.90 | Kln, Fe(O,OH), Ab, Rt, Brl, Zrn, Po, Cal, Dol, Fap, Mca | ✓ | ✓ | ✓ | | | ✓ |
| Muzo | T6 | Center, asymmetric arms | Arm up to 3.5 mm | ⊥ | None | | | | ✓ | | | ✓ | | |
| Muzo | T7 | Small core, arms, small overgrowth | 10 | ⊥ | None | | | Mca, Kln, Tur, Dol, Cal, Ank, Rt, Fe(O,OH), Qtz, Fl, Fap, Ab, Py | ✓ | ✓ | | | | |
| Muzo | T8 | Hexagonal crystal with hexagonal core and deep green overgrowth | 10 | ⊥ | None Clays in fractures | c: 0.02–0.03<br>a: 0.02–0.06<br>og: 0.62–0.64 | 0.00–0.02<br>0.00–0.06<br>0.31–0.72 | Ab, Qtz, Mca, Rt, Dol, Brl | ✓ | ✓ | ✓ | ✓ | | ✓ |
| Muzo | T9 | Hexagonal green core and green arms | 5 | ⊥ | AbBS + clays | | | Brl, Mnz, Qtz, Pt, Fap, Ab, Mca, Rt, Fe(O,OH), Po | ✓ | ✓ | | | ✓ | |
| Muzo | T10 | Bipyramidal core, arms | 10 | ∥ | None | c: 0.15–0.26<br>a: 0.15–0.23 | 0.02–0.12<br>0.02–0.09 | Ab, Kln, Fap | ✓ | ✓ | ✓ | | | |
| Muzo | T11 | Large green core, small arms | 8, with core ~3 mm | ⊥ | AbBS + clays | c: 0.59–0.75<br>d: 0.02–1.12<br>a: 0.91–1.09 | 0.49–0.62<br>0.02–0.99<br>0.73–0.89 | Brl, Qtz, Rt, Ab, Kln, Dol, Py | ✓ | ✓ | ✓ | | | ✓ |
| Muzo | T12 | Small hexagonal core, arms | 12 | ⊥ | AbBS | | | | | | | | | |
| Muzo | T13 | Core, arms | 5 | ⊥ | Ab | | | | | | | | | |

*c = core; d = dendrite; a = arm; og = overgrowth; AbBS = albitized black shale, Ab = albite; Cal = calcite; Qtz = quartz; Brl = beryl (emerald); Ank = ankerite; Dol = dolomite; Fap = F-apatite; Py = pyrite; Fe(O,OH) = iron oxides and hydroxides; Tur = tourmaline; Rt = rutile; Mca = muscovite; Po = pyrrhotite; Zrn = zircon; Kln = kaolinite; Fl = fluorite; Mnz = monazite; ∥ = section parallel to crystal's c-axis; ⊥ = section perpendicular to crystal's c-axis.*
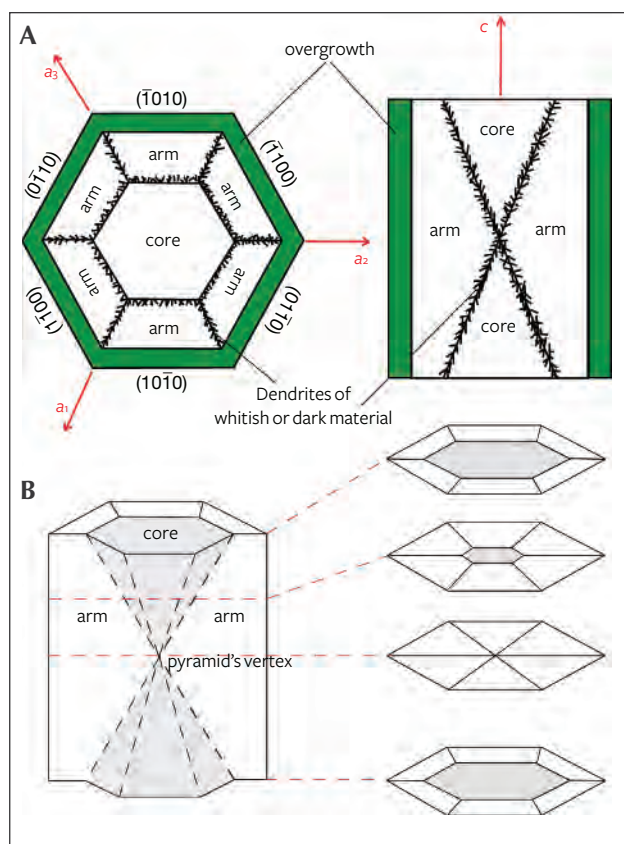
Figure 13. A: Schematic diagrams of trapiche emerald sections, perpendicular to the c-axis (top left) and parallel to it (top right). The sections show trapiche emerald's central core, arms, dendrites, and overgrowth zones. B: Aspect and variations of the core, which has a hexagonal bipyramidal shape. Its size varies as a function of the sections perpendicular to the c-axis: largest if the section is cut at the base of the pyramid, smallest near the pyramid's vertex.

**Core.** The central core may or may not be present in a trapiche emerald. The core is bounded by pinacoidal faces [0001] (see figures 12A, 12D, 12G, 12J, and 12L) and has the shape of two opposite hexagonal pyramids (figures 12I and 13) corresponding to the pinacoidal growth sectors. The presence and the size of the core depend on the position of the cross-section along the bipyramidal shape, as illustrated in figure 13B. If the trapiche's growth is homogeneous in both positive and negative directions of the c-axis, the two hexagonal pyramids will develop similarly. If the growth is inhomogeneous (due to limited space in the growth medium, for example), one pyramid will be more developed than the other, as in figure 12I. Moreover, in the sections perpendicular to the c-axis, the core is largest if the section is cut at the base of the pyramid, and smallest near
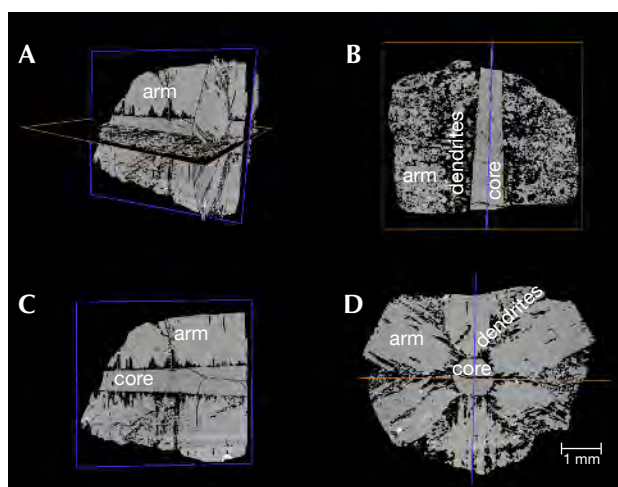


Figure 14. X-ray computed tomography images showing the spatial relationships between the core, arms, and dendrites in a trapiche emerald from Muzo.

the pyramid's vertex (figure 13B). This is confirmed by X-ray computed tomography: Figure 15A shows that the size of the core decreases from the top to the

Figure 15. X-ray computed tomography images of a trapiche emerald from Muzo. A: The size of the core decreases from the top toward the bottom of the crystal. B: The dendrites around the core develop laterally and penetrate into the arms. C: The spatial distribution and morphology of solid inclusions in the sample. D: The elevated porosity (in blue) of the whole sample in a section perpendicular to the c-axis.
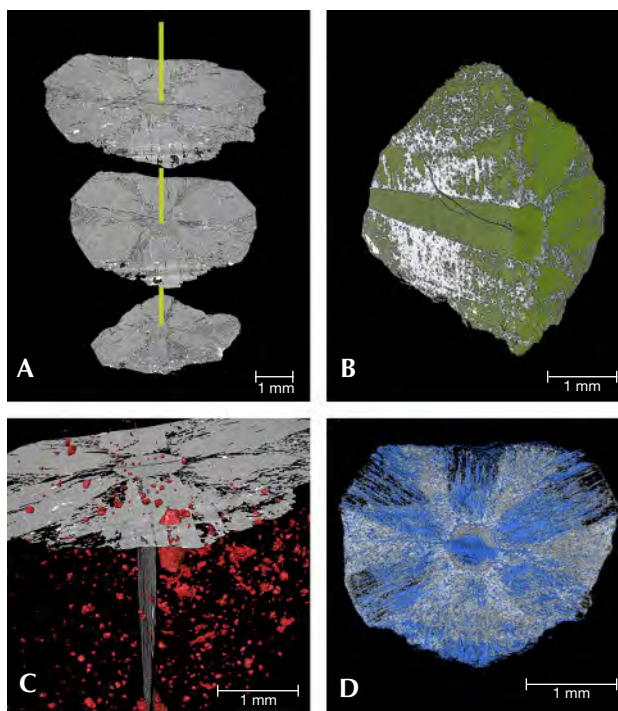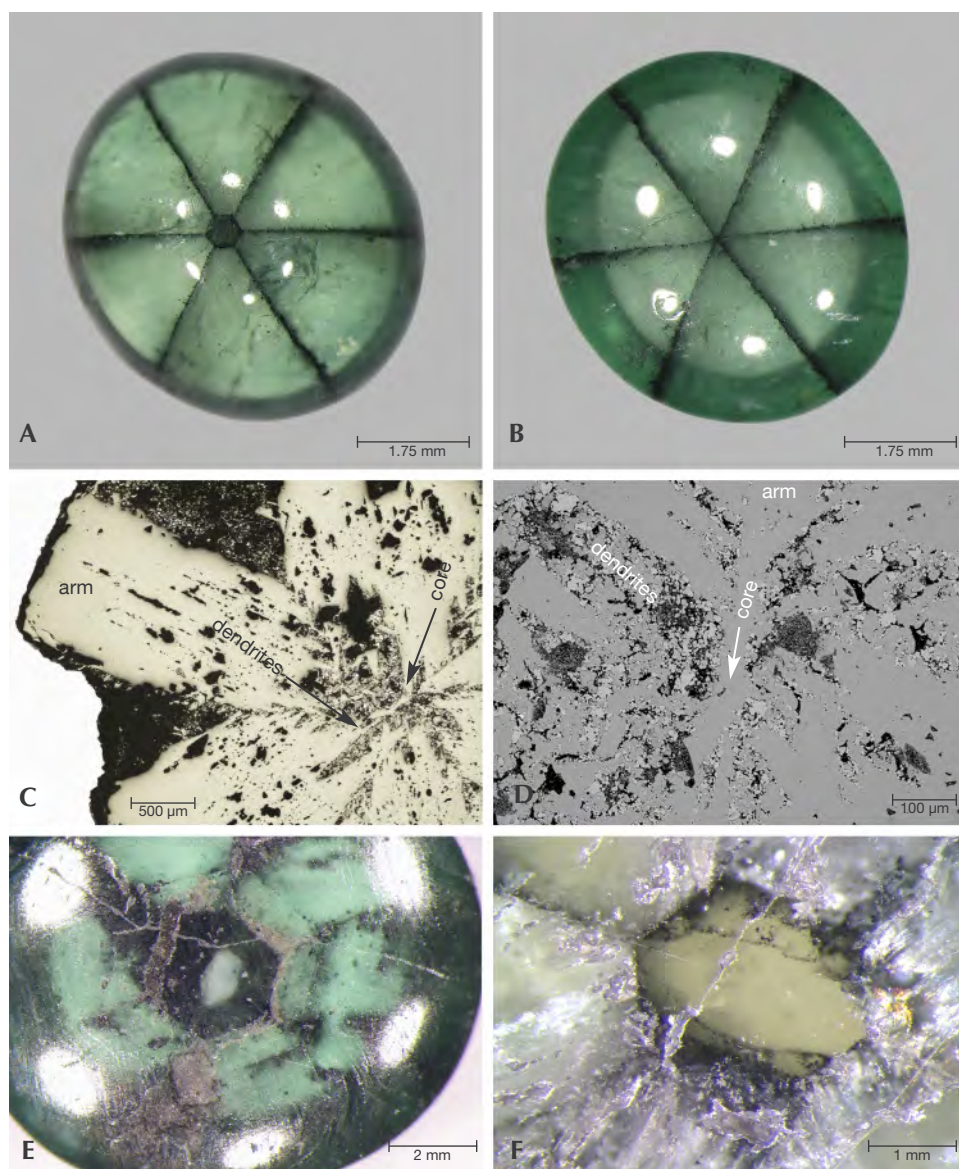
*Figure 16. Core images of several trapiche emeralds. Samples showing the upper part of the cabochon cut with the hexagonal core (A), and with only a central point (B); optical (C) and SEM (D) images of a sample with no core, the dendrites and arms crossing in the central point; an example of a hexagonal dark core (E); signs of fracturing and dissolution in a core, attesting to a complex growth history (F).*

bottom of the trapiche. When a section is cut between the vertices of two opposite pyramids, the core is absent and the arms and dendrites intersect in a central point, as in figures 12B, 12E, 16C, and 16D. This explains why some trapiche samples show a hexagonal core on one end (figure 16A) but no core on the other end (figure 16B). The color of the core can vary from very light to deep green, reflecting different quantities of the chromophores $V^{3+}$ and $Cr^{3+}$ (see the "Trace-Element Analysis" section below).

The core is surrounded by dendrites that can also replace it completely or partially, as described by Bernauer (1933). The replacement gives the core a dark aspect, as shown in figure 16E. The dendrites around the core develop laterally and penetrate into the arms,

as demonstrated by the density contrast in the tomographic images (figures 14 and 15B).

Optical observations of the sections perpendicular to the c-axis under cross-polarized light confirm that the core cannot be completely extinct, but a kind of wavy extinction, as in quartz, is made visible by turning the stage of the microscope. It follows that the core may be plastically deformed during or after its formation. This particular optical feature was mentioned by Bernauer (1933), who wrote of "listas onduladas," and Chaudhari (1969), who described "a sort of grating structure" in the core.

Signs of dissolution are observed in the core of two samples. For example, figures 17A and 17B show that the core's edges are not straight, due to
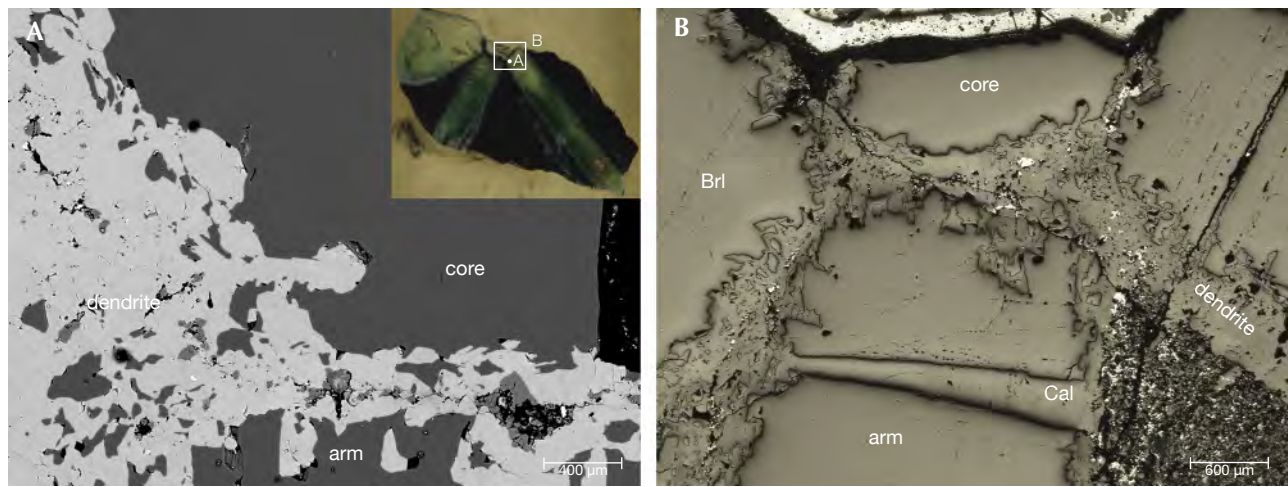
*Figure 17. A: An SEM image of the spatial relationship between the core, dendrites, and arms in the sample from figure 12C. The inset shows the whole sample, along with the locations of images A and B. The wavy contact between the core and the dendrites indicates a previous dissolution of the core by the fluids. The dendrites are formed mainly by calcite and albite sometimes associated with beryl. B: A microscopic image of the dendrites and the arms of emerald (Brl), which formed simultaneously, though the arms were affected by dissolution and fracturing (see the aspect of the core and arms). The microscopic image shows that the fracture crosscutting the arm is filled by calcite (Cal) and ± albite associated with tiny beryl crystals (around ten microns).*

etching, and are partially covered by the arms. In figure 16F, dissolution also occurred during the core's complex growth history. During its formation, the core underwent a deformational event marked by two main fractures coeval with the dendrites' development. The fractures are filled by the same minerals found in the dendrites: albite, pyrite, quartz, carbonates, fluorite, and *phyllosilicates*. Some of the fractures are filled by fluid inclusions, indicating fluid circulation and consequent dissolution of the edges and corners of the core. The effects of dissolution are marked by the modification of the core's shape from hexagonal to oval, and by the irregular etched borders. During a second stage, core
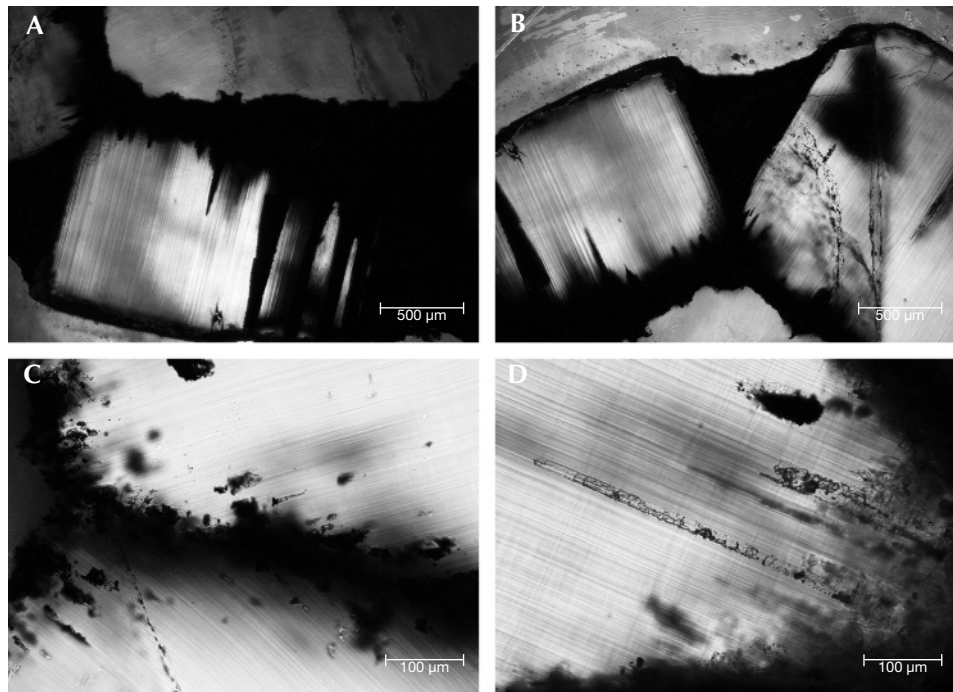


*Figure 18. Optical images of growth arms in trapiche emeralds. A and B: The arms are characterized by bundles of straight dislocations perpendicular to the {10$\bar{1}$0} faces. C: Direction of propagation of the dislocations in two adjacent growth sectors. Along these dislocation zones and at the contact of the dendrites, the crystals trap solids and cavities of fluid inclusions. D: Primary fluid inclusion trails are parallel to the dislocations.*
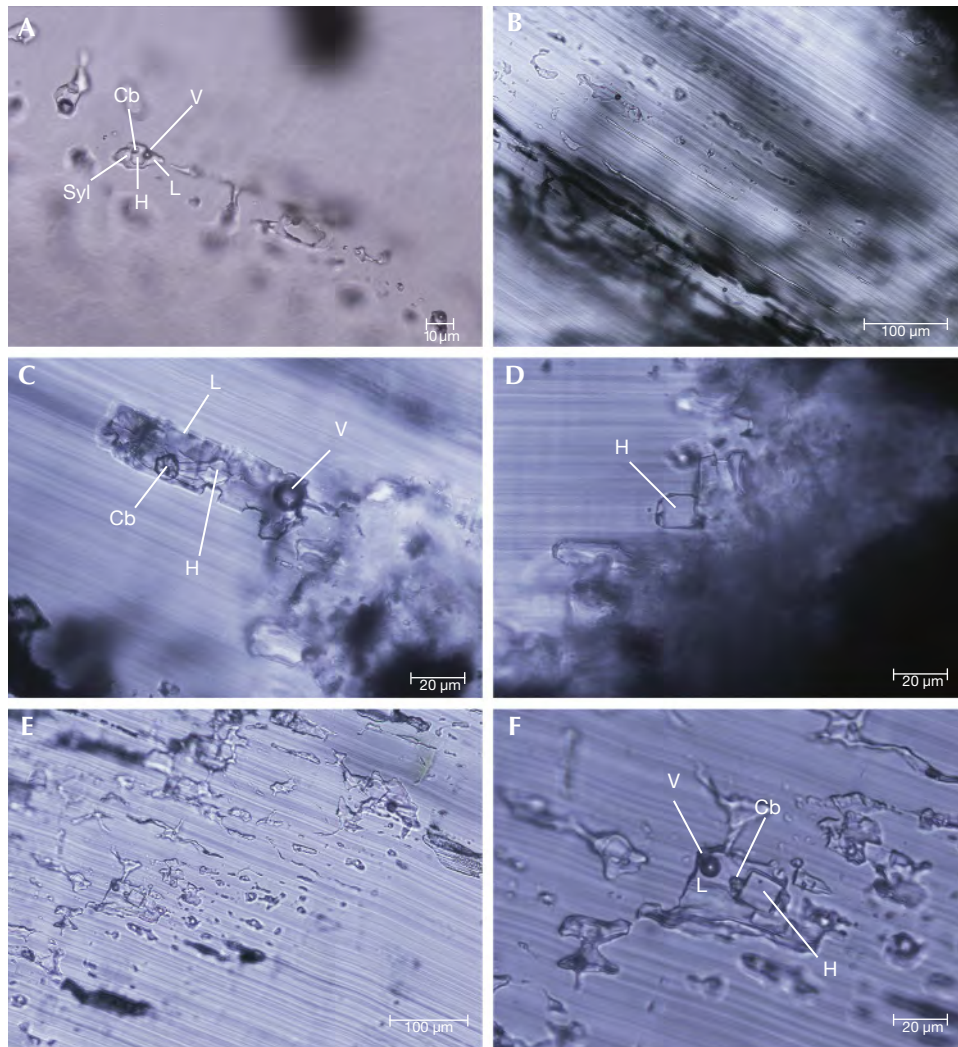
Figure 19. These multiphase fluid inclusions trapped in the arms of trapiche emeralds contain liquid (L) and vapor (V) phases as well as solid-phase daughter minerals (H = halite, Cb = carbonates, Syl = sylvite). A: This primary multiphase inclusion exhibits stretching and necking-down phenomena. B: Alignment of multiphase fluid inclusions along the dislocation plane of the arm. C: A multiphase fluid inclusion trapped at the end of a dendrite (on the right) and parallel to the dislocations. D: A large cube of halite in a fluid inclusion cavity formed at the edge of the dendrites. E: Trails of multiphase fluid inclusions affected by necking-down. Re-equilibration of the cavities occurred during cooling, and some of the primary fluid inclusions became monophase (L or V) or biphase (V + L or L + H) cavities. F: Typical primary multiphase fluid inclusion in trapiche emerald, similar to those trapped by non-trapiche emerald.

growth resumed and the pseudo-hexagonal shape was restored.

Rare multiphase fluid inclusions are observed in the core. They are similar to those found in the arms, indicating that the fluid composition was the same. However, multiphase fluid inclusions in the core are pseudo-secondary because they are often associated with fracturing.

**Arms.** Six arms with nearly identical size surround the core. They appear elongated in the $\langle 1\bar{1}0 \rangle$ directions and are bounded by the $\{10\bar{1}0\}$ faces. Sometimes a few arms are larger than others (figures 12E and 12F), making the trapiche asymmetric.

The color of the arms, like that of the core, can vary from pale (figures 12E and 12F) to intense green (figures 12D, 12H, 12K, and 12L) as a function of chemical composition (see "Trace-Element Analysis").

In each arm, bundles of straight dislocations develop perpendicular to the $\{10\bar{1}0\}$ faces (figures 18A and 18B). This indicates that they formed during the growth, in the direction of minimum elastic energy (Authier and Zarka, 1994). The direction of propagation of the dislocations in two adjacent growth sectors can be observed in figure 18C. Only in the trapiche of figure 12E do the dislocations appear slightly curved on the border of the largest arm. This is probably due to a change in the direction of minimum energy during the "anomalous" growth of this arm.

Solid and multiphase fluid inclusions are found in the arms. They are parallel to the dislocations (figures 18D, 19B, and 19E) and all located in proximity to the dendrites. The solid inclusions are similar to those found in the dendrites (see "Dendrites" below). The fluid inclusion cavities follow the extension of the dendrites in the arms. They are multiphase fluid inclusions containing daughter minerals, mainly halite
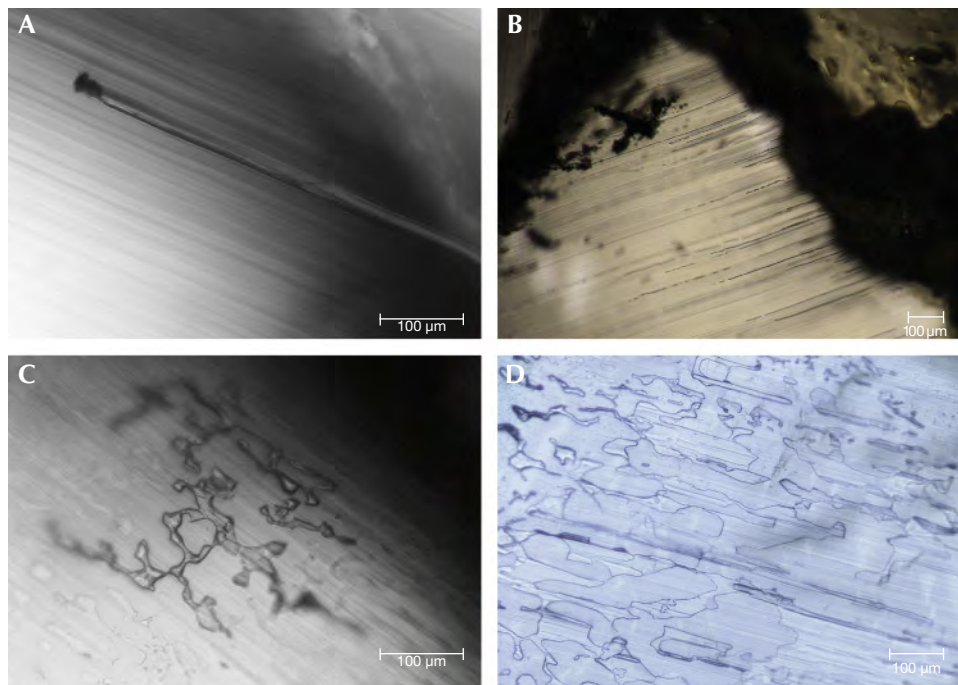
*Figure 20. Elongated voids observed in the arms, perpendicular to the growth front and parallel to the dislocations. A: An elongated fluid inclusion cavity that formed parallel to the dislocation plane and after subsequent trapping of a solid inclusion (the black solid on the upper part of the cavity). B: Trails of voids parallel to the dislocation planes. C: Monophase fluid inclusions with highly irregular dendritic morphologies in the arms. D: Flat monophase fluid inclusions that developed along the dislocation planes.*

but also carbonates and sylvite, liquid and vapor phases (figures 19A, 19C, and 19F). They belong to the $H_2O$-NaCl $\pm$ ($CO_2$) system already characterized for Colombian emerald-bearing veins (Roedder, 1963; Touray and Poirot, 1968; Kozlowski et al., 1988; Ottaway, 1991; Giuliani et al., 1991; Cheilletz et al., 1994). Sometimes, the multiphase fluid inclusions can be concentrated in certain portions of the arms, forming trails (figure 19E).

Evidence of heterogeneous trapping is observed in some multiphase fluid inclusions at the contact between dendrites and arms. This trapping is characterized by the presence of a large cubic crystal of halite (figure 19D) occupying more than 15 vol.% of the cavity and up to 70 vol.% (see "Emerald Mineralization" above).

Monophase fluid inclusions with highly irregular dendritic morphologies (figures 20C and 20D) are present in the arms. They do not contain solid or vapor phases. Similar inclusions were described in quartz crystals by Invernizzi et al. (1998) and interpreted as earlier-formed inclusions re-equilibrated at conditions of high *internal underpressure*. The dendritic morphology "results from the closure of the original inclusion void and preservation of fluid in long dendritic dissolution channels" (Invernizzi et al., 1998).

The arms contain elongated voids perpendicular to the growth front and thus parallel to the dislocations (figures 20A and 20B). Figure 20A shows that the formation of the elongated voids is related to the presence of solid inclusions. The voids resemble those described in Colombian emerald-bearing veins (Touray and Poirot, 1968) and in trapiche tourmaline (Schmetzer et al., 2011). Nevertheless, these voids may also have formed by dissolution along dislocation bundles if the *supersaturation* decreased after crystal growth (Scandale and Zarka, 1982; Authier and Zarka, 1994).

The arms are sometimes affected by fractures, filled by albite and small euhedral beryl crystals (figure 17B), that are synchronous with the arms' formation. The growth of the arms is not perturbed, because there is no discontinuity between the albite in the fractures and the albite in the dendrites on both sides of the arms.

In some emeralds, the arms have a fibrous texture like that of beryl in the dendrites (figure 21A), but in others they are not fibrous and appear similar to the core. Their different textures can reveal important information about the growth rates of the arms.

**Dendrites.** In trapiche emeralds, dendrites surround the core (figures 21B and 21F) and develop along the a-axis from the corners toward the outer edge with a herringbone texture (figure 21C). In particular, the dendrites may be larger near the edge, where they assume a characteristic fan shape (figures 21B and 21E). In some samples, the herringbone texture is not developed and the fan shape starts directly on the corners of the core. In this case, the dendrites are larger
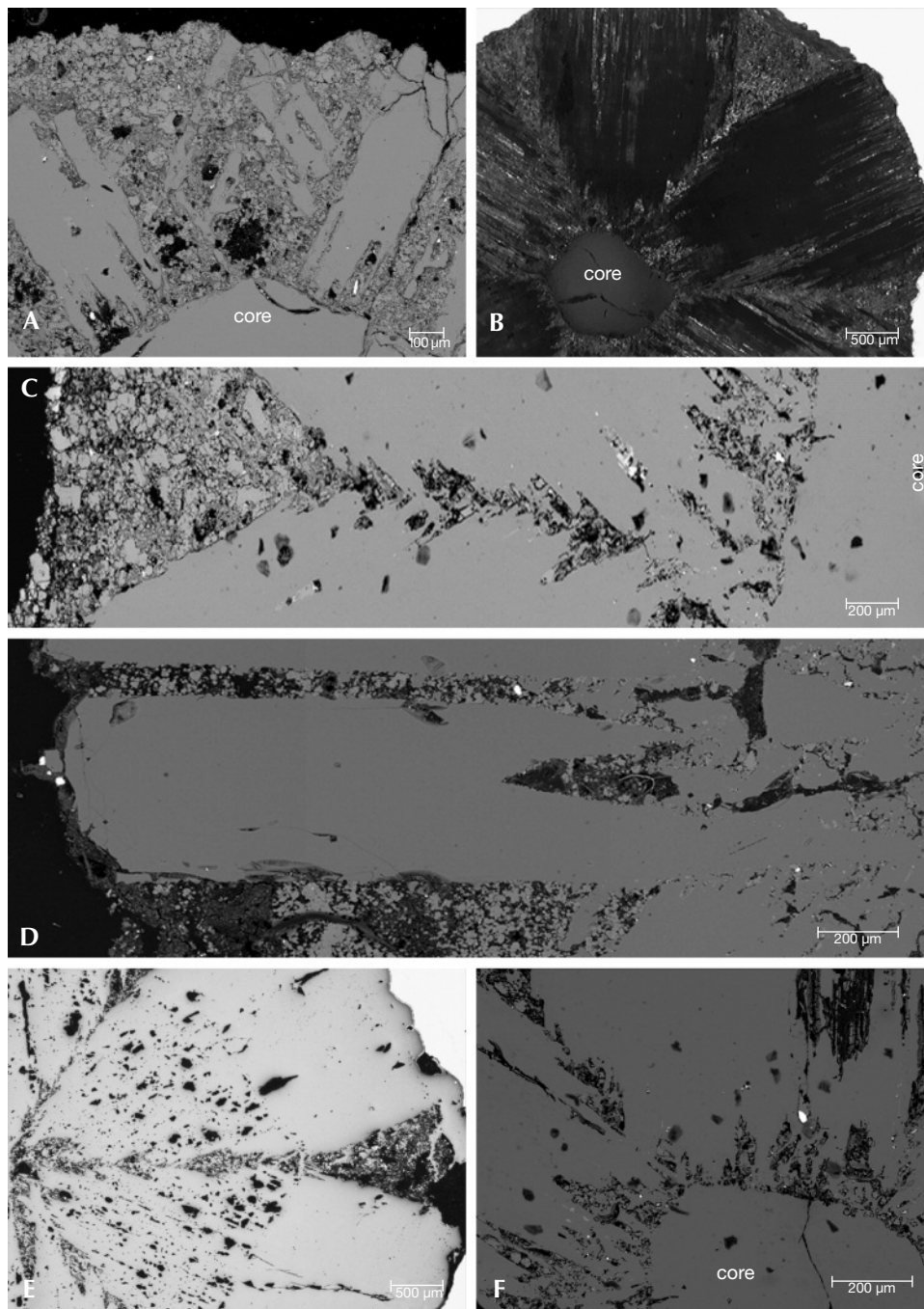
*Figure 21. A: An SEM image of dendrites containing stringers of beryl intersecting at 60° angles. B: The dendrites are enlarged near the edge of the crystal, where they assume a characteristic chevron shape (see also images C–E). C: An SEM image of the typical herringbone texture of dendrites. The crystal formed on an albitized black shale matrix (on the left side of the image). D: This SEM image shows the presence of dendrites in the arms. E: Aspect of the dendrites from the core to the edge of the emerald crystal in a special section where the core is represented by a central point. The arms include albitized black shale (right side of the image), part of the matrix that supports the emerald. F: An SEM image of dendrites surrounding the core.*

and contain stringers of emerald intersecting at 60° angles (figure 21A), as described by Chaudhari (1969). The dendrites may be present even in the arms (figures 12D and 12F) and parallel to the extension of the arms (figure 21D).

The dendrites are developed on albitized and calcitized black shales (figures 22A, 22B, 22D, and 22E), and sometimes rounded remnants of albitite are included in the calcite-bearing dendrites (figure 22C). In addition, variable quantities of organic matter are found in the

albitites as well as in the dendrites (figure 22D), explaining why they often appear dark (figures 12B, 12C, and 12K). The X-ray computed 3D tomography image (figure 15D) of the trapiche emerald from figure 12H permitted the calculation of the dendrites' volume. The sample's total volume is 64.75 mm³, of which 18% is occupied by the dendrites and 81% by the core and the arms, with the remaining 1% representing the porosity.

The dendrites contain mainly the albite and emerald assemblage, which explains why the den-
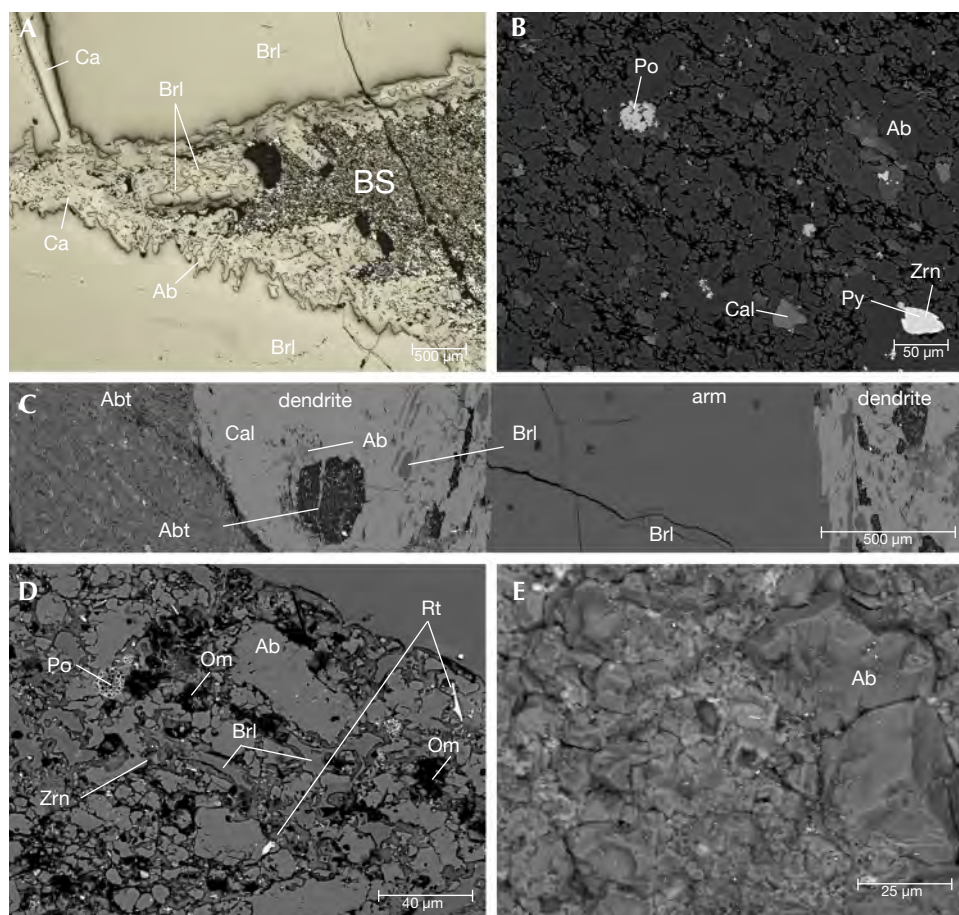
Figure 22. A: Microscopic image of dendrites formed on albitized (± calcitized) black shales (BS). The chevron-like habits characteristic of trapiche contain albite (Ab), emerald (Brl), and calcite (Cal). B: SEM image of the albitized black shale with albite, zircon (Zrn), calcite, pyrite (Py), and pyrrhotite (Po). C: SEM image of sample T4 showing the arm formed by emerald with dendrites on both sides. The dendrites are formed by calcite ± albite and emerald. The arm and the dendrites formed on albitite (Abt), a rounded remnant of which is included in the dendrite on the left side. D: SEM image of the albitite containing zircon, emerald, pyrrhotite with framboidal polycrystalline aggregates, rutile (Rt), and organic matter (Om). E: Morphology and size of albite crystals from the albitite, showing the rock's high porosity.

drite zones were also called "two-phase regions" by Nassau and Jackson (1970). The high quantity of albite (with or without calcite) makes the dendrites whitish, as shown in figures 12D and 12J. Quartz and dolomite complete the main paragenesis (figures 23A and 23B). Other solid inclusions characteristic of Colombian emeralds are found in minor amounts (figure 23C): rutile, carbonates (dolomite, ankerite, siderite), muscovite, fluorapatite, pyrite, pyrrhotite, zircon, fluorite, tourmaline, and minerals containing rare-earth elements such as monazite and parisite. Muscovite and rutile are V-bearing, and tourmaline usually shows complex zoning (figure 23D). The pyrrhotite forms *framboidal* polycrystalline aggregates typical of sedimentary sulfides.

Secondary alteration can affect the dendrites. The formation of clay minerals (mostly kaolin) and iron oxides/hydroxides modifies their original dark/whitish color to a brownish one (figures 12H and 12L). The typical evidence of alteration is the pseudomorphic replacement of framboidal sulfides by iron oxides/hydroxides. The alteration is favored by the elevated porosity of the dendrites, which is visible in the tomographic images of figure 15D.

**Overgrowth.** Overgrowth is not always present in trapiche emeralds. Its color is different from that of the adjacent arms, and it can be paler (figure 12F) or darker (figures 12A and 12G). The color difference indicates variations of $V_2O_3$ and $Cr_2O_3$ contents in the growth medium during the formation of the overgrowth (see "Trace-Element Analysis"). If many chemical changes occurred, the overgrowth becomes zoned, as in the trapiche shown in figure 12G. The contact between the overgrowth and the arms is often marked by the presence of inclusions.

**X-ray Diffraction Topography.** Even though X-ray diffraction topography is particularly suitable to investigate the strain associated with extended defects and to reconstruct the growth history of minerals (Agrosì et al., 2006; Agrosì et al., 2013), it has not been used until now to study trapiche emerald. This is probably because the technique requires the cutting of thin slices to minimize X-ray absorption, a drawback given the rarity of trapiche material. X-ray topographic images of trapiche emeralds are shown in figure 24. The samples' limited thickness kept us from preparing slices with different orientations, and only slices perpendicular to the c-axis were cut.
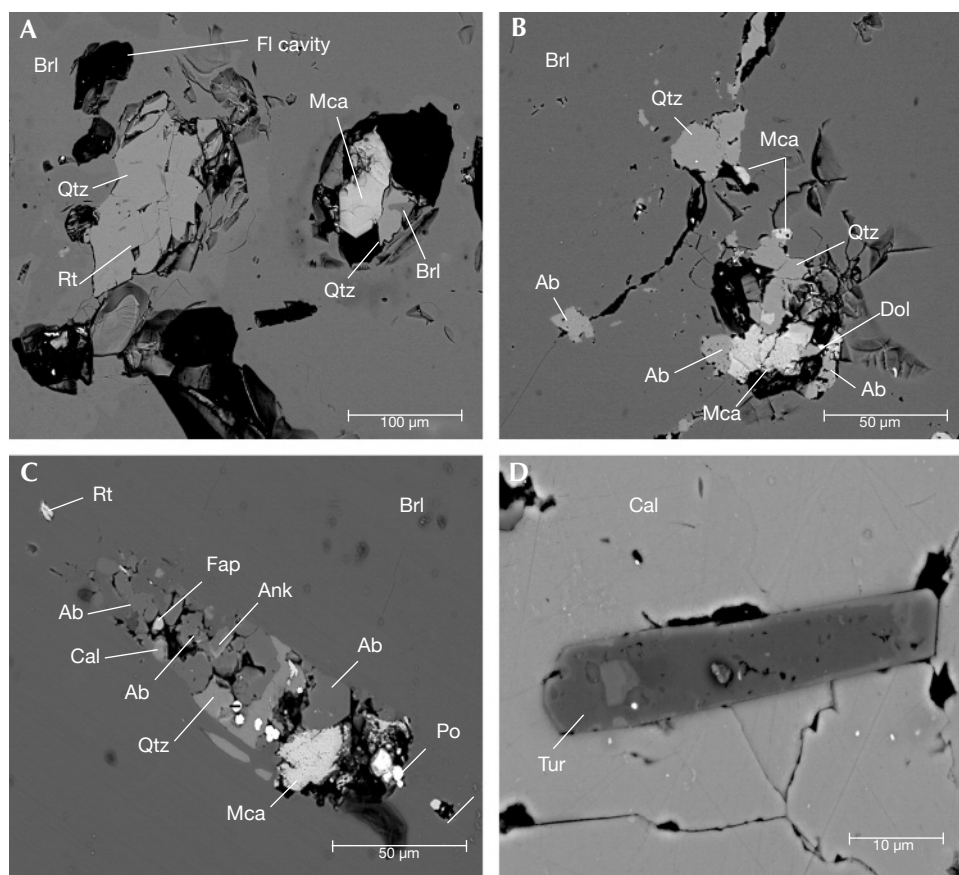
*Figure 23. SEM images of inclusions found in dendrites at the contact with trapiche emerald arms. A: Aspect of the cavities filled by solids in the dendrites. The assemblages are formed by rutile (Rt) + quartz (Qtz), and quartz + emerald (Brl) + muscovite (Mca). B: Other mineral assemblages formed by dolomite (Dol) + albite (Al) + quartz + muscovite (Mca). C: Aspect of a dendrite cavity filled by albite, calcite (Cal), ankerite (Ank), muscovite, quartz, pyrrhotite (Po), fluorapatite (Fap), and rutile. The different solids are coeval, and the limits of some minerals show the presence of small fluid inclusion cavities, indicating that a fluid was bathing the whole cavity during dendrite formation. D: An SEM image of a tourmaline (Tur) crystal included in calcite.*

Topographic images taken with *diffraction vectors* **g** of type *hki*0 show a strong diffraction contrast for the arms, while the core is almost invisible (figures 24A and 24C). In all arms, the presence of bundles of dislocations running perpendicular to the prismatic growth fronts is confirmed by the topographic images (figure 24). It was impossible to characterize these dislocations, because the orientation of the slices did not permit us to obtain topographic images with reflections suitable to determine the *Burgers vectors* applying the extinction criterion. The extinction criterion can be explained only referring to the diffraction contrast origin. The contrasts observed in the topographic images are due to the different intensities of diffraction between regions characterized by strain fields associated to the defects (kinematical effects) and almost perfect regions (dynamical effects). The diffraction contrasts can be extinct if the *scalar product* between the *diffraction vector* **g** and the vector representative of the strain field associated to the defect is equal to zero. In the case of dislocations, the extinction criterion is based on the scalar product **g** × **b** = 0, where **b** represents the Burgers vector. It follows that the dislocations are out of contrast when **g** is perpendicular to **b**.

No diffraction contrast corresponding to the growth sector boundaries can be seen in the topographic images. Thus, the boundaries between the adjacent arms can be recognized only by means of the lack of contrast corresponding to the dendrites or by the directions of propagation of the dislocations in each arm (for example figures 24E, 24F, and 18C). This indicates that in trapiche emeralds there is a good interconnection between the different arms.

Topographic images taken with diffraction vectors inclined with respect to the c-axis (e.g., **g** = 12$\bar{3}$1) show that the hexagonal core is also visible (figures 24B and 24D). The fact that both core and arms are visible in these topographic images indicates crystalline continuity between them, despite the presence of the dendrites.

The presence of dislocations in the core cannot be excluded, because the diffraction contrast observed (figure 24B) is not solely due to the fractures (slightly visible in figures 24A and 24C). It is worth noting that the contrast of these dislocations is always extinct on the topographic images with **g** = *hki*0. On the basis of the extinction criterion, the **b** vector should thus be parallel to the c-axis, and one may suppose that the dislocations in the core are of screw type. This could be verified by a topographic study of the sections par-
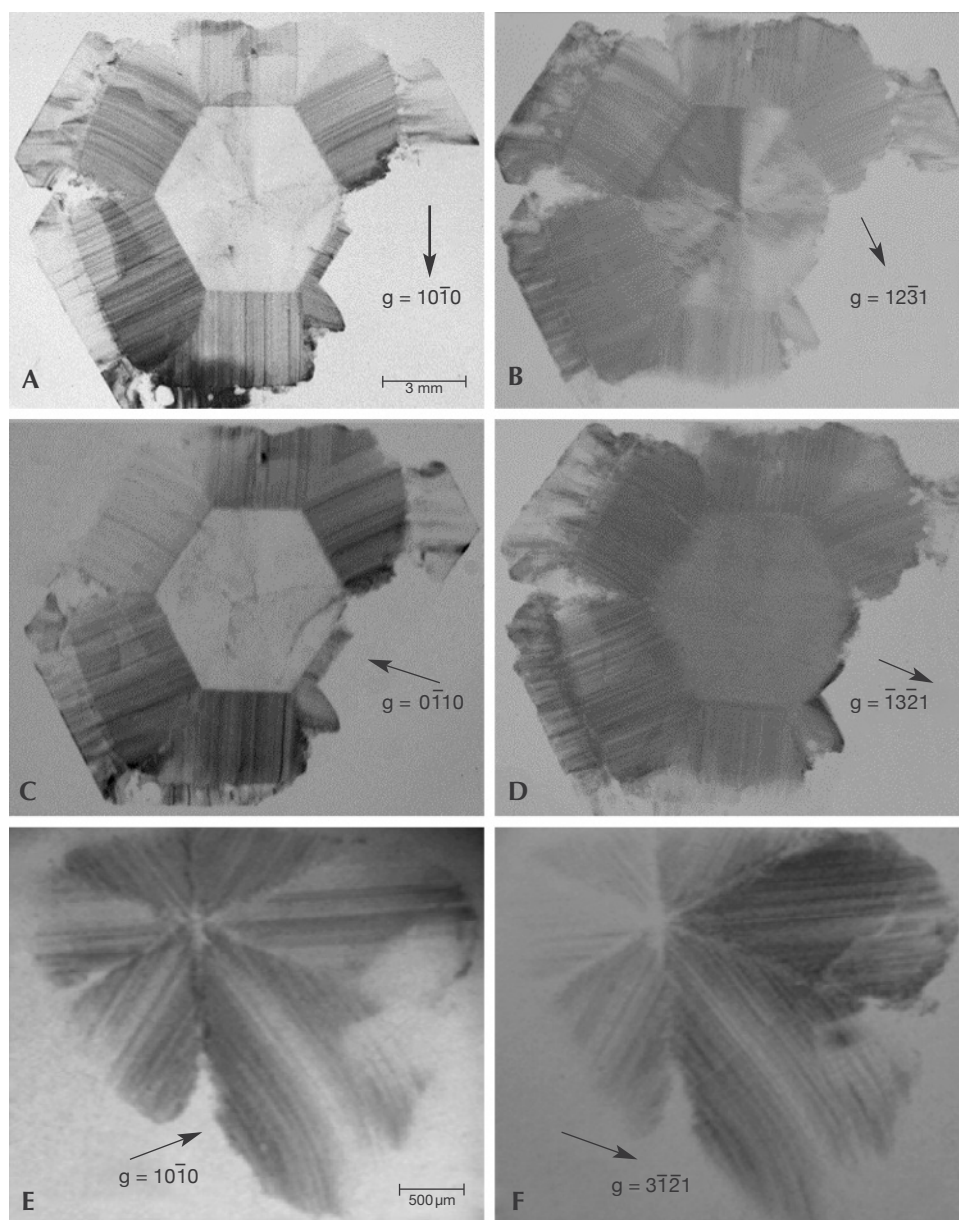
Figure 24. A to D: MoKα₁ X-ray topographic images of the trapiche emerald from figure 12G, taken with the diffraction vectors $g = 10\bar{1}0$ (A), $g = 12\bar{3}1$ (B), $g = 0\bar{1}10$ (C) and $g = \bar{1}3\bar{2}1$ (D). E to F: X-ray topographic images of the trapiche emerald from figure 13E, taken with the diffraction vectors $g = 10\bar{1}0$ (E) and $g = 3\bar{1}\bar{2}1$ (F).

allel to the c-axis, but unfortunately it was not possible to cut sections parallel and perpendicular to the c-axis from the same sample. For this reason, the presence of screw dislocations has not been confirmed.

**Cathodoluminescence.** CL images of the trapiche emerald samples exhibited several distinct features. The cold CL images obtained on the Peñas Blancas crystal (see figure 12D) show a crimson color due to the presence of $Cr^{3+}$ and $V^{3+}$ ions acting as the main CL activators (figure 25C). The cold CL image of the Muzo crystal (figure 25D) illustrates the color homogeneity of the core and the different textural and color aspect of the arms. These fibrous dendrites show variations in the reddish hue. Cold CL images obtained on the Coscuez crystal indicate that the core and arms have the same CL colors, but the dendrites formed by a fine intergrowth of albite, calcite, and emerald (figure 25D) have different CL colors for each: orange, yellow, and dark crimson for albite, calcite, and emerald, respectively. These CL colors could be explained by the presence of Mn in calcite (Ohnenstetter et al., 1998) and of Fe substituting Al in albite (Geake and Walker, 1975; White et al., 1986; Götze et al., 2000).

**Trace-Element Analysis.** Six sections of trapiche emerald from Coscuez, Peñas Blancas, and Muzo

**TABLE 2.** Representative chemical composition of trapiche emeralds from Coscuez, Muzo, and Peñas Blancas, obtained by electron microprobe analysis.

| Oxides (wt.%) | Coscuez | | | | | | Muzo | | | | Peñas Blancas | | |
|---|---|---|---|---|---|---|---|---|---|---|---|---|---|
| | T4-6 a | T4-1 d | T4-14 c | T11-1 a | T11-32 d | T11-23 c | T8-2 og | T8-11 og | T8-4 a | T8-13 c | T5-1 a | T5-10 d | T5-11 c |
| $SiO_2$ | 66.28 | 65.16 | 66.81 | 65.22 | 66.52 | 65.87 | 65.97 | 66.90 | 65.57 | 66.17 | 65.55 | 66.26 | 65.25 |
| $Al_2O_3$ | 17.26 | 17.27 | 17.61 | 15.19 | 17.18 | 16.77 | 16.62 | 17.69 | 17.56 | 17.80 | 16.28 | 15.22 | 15.77 |
| $Cr_2O_3$ | 0.17 | 0.18 | 0.12 | 0.80 | 0.95 | 0.62 | 0.29 | 0.72 | 0.05 | 0.02 | 0.90 | 0.68 | 0.30 |
| $Fe_2O_3$ | 0.20 | 0.12 | 0.08 | 0.37 | 0.08 | 0.12 | 0.07 | 0.04 | 0.03 | 0.03 | 0.19 | 0.56 | 0.16 |
| $V_2O_3$ | 0.27 | 0.27 | 0.14 | 1.08 | 0.82 | 0.67 | 0.64 | 0.30 | 0.05 | 0.03 | 0.87 | 1.17 | 0.68 |
| BeO calc.[a] | 13.79 | 13.56 | 13.90 | 13.57 | 13.84 | 13.71 | 13.73 | 13.92 | 13.64 | 13.77 | 13.64 | 13.79 | 13.58 |
| MgO | 0.58 | 0.53 | 0.55 | 1.28 | 0.33 | 0.65 | 0.99 | 0.29 | 0.73 | 0.69 | 0.71 | 1.40 | 1.47 |
| $Na_2O$ | 0.56 | 0.50 | 0.45 | 0.98 | 0.27 | 0.49 | 0.97 | 0.25 | 0.45 | 0.43 | 0.61 | 0.59 | 0.76 |
| $H_2O$ calc.[b] | 1.31 | 1.26 | 1.22 | 1.67 | 1.07 | 1.31 | 1.66 | 1.04 | 1.22 | 1.20 | 1.35 | 1.34 | 1.48 |
| Total | 100.42 | 98.85 | 100.88 | 100.16 | 101.06 | 100.21 | 100.94 | 101.15 | 99.30 | 100.14 | 100.10 | 101.01 | 99.45 |
| | | | | | | | | | | | | | |
| Si | 6.000 | 6.000 | 6.000 | 6.000 | 6.000 | 6.000 | 6.000 | 6.000 | 6.000 | 6.000 | 6.000 | 6.000 | 6.000 |
| Al | 1.841 | 1.874 | 1.864 | 1.647 | 1.826 | 1.800 | 1.782 | 1.870 | 1.894 | 1.902 | 1.756 | 1.624 | 1.709 |
| Cr | 0.012 | 0.013 | 0.009 | 0.058 | 0.068 | 0.045 | 0.021 | 0.051 | 0.004 | 0.001 | 0.065 | 0.049 | 0.022 |
| $Fe^{3+}$ | 0.014 | 0.008 | 0.005 | 0.026 | 0.005 | 0.008 | 0.005 | 0.003 | 0.002 | 0.002 | 0.013 | 0.038 | 0.007 |
| $V^{3+}$ | 0.020 | 0.020 | 0.010 | 0.080 | 0.059 | 0.049 | 0.047 | 0.022 | 0.004 | 0.002 | 0.064 | 0.085 | 0.050 |
| $Be^{2+ b}$ | 3.000 | 3.000 | 3.000 | 3.000 | 3.000 | 3.000 | 3.000 | 3.000 | 3.000 | 3.000 | 3.000 | 3.000 | 3.000 |
| Mg | 0.078 | 0.073 | 0.074 | 0.176 | 0.044 | 0.088 | 0.134 | 0.039 | 0.100 | 0.093 | 0.097 | 0.092 | 0.041 |
| Na | 0.098 | 0.089 | 0.078 | 0.175 | 0.047 | 0.087 | 0.171 | 0.043 | 0.080 | 0.076 | 0.108 | 0.104 | 0.135 |
| Total | 11.063 | 11.078 | 11.040 | 11.161 | 11.050 | 11.077 | 11.159 | 11.027 | 11.083 | 11.077 | 11.103 | 11.089 | 11.125 |
| | | | | | | | | | | | | | |
| V/Cr | 1.58 | 1.49 | 1.16 | 1.34 | 0.86 | 1.07 | 2.19 | 0.41 | 0.99 | 1.49 | 0.96 | 1.71 | 2.25 |

[a] Amount of Be inferred from stoichiometry zones of the trapiche emerald: a = arm; d = dendrite; c = core; og = overgrowth.
[b] Calculated following the equation $H_2O = (0.84958)(Na_2O) + 0.8373$ (Giuliani et al., 1997).

were analyzed by EPMA and with elemental compositional EDX maps in order to evaluate chemical composition, zoning, and color variations in the core, dendrites, arms, and overgrowths (tables 1–3). Overall, the emeralds contained relatively low concentrations of $Fe_2O_3$, from 200 to 5700 ppm. The $Na_2O$
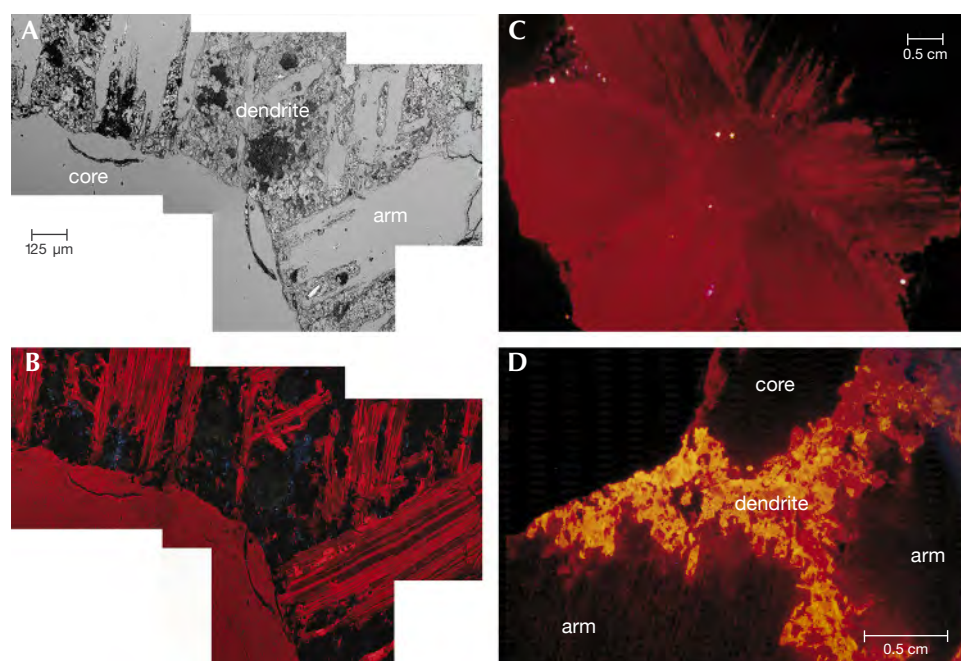


Figure 25. A and B: SEM and CL images of a Muzo sample show that under CL, the core is homogenous and appears crimson-colored due to the presence of $Cr^{3+}$ and $V^{3+}$ ions acting as the main CL activators. The arms, on the other hand, are fibrous and show variations in the reddish hue. C: The cold CL image of a Peñas Blancas sample shows the homogeneity of its red color due to the presence of the V and Cr chromophores. D: The cold CL image of a Coscuez sample reveals different CL colors: orange for albite, yellow for calcite, and dark crimson for emerald.

**TABLE 3.** Representative chemical composition of trapiche emeralds from Coscuez and Muzo[a], obtained by electron microprobe analysis.

| | Coscuez | | | | | | Muzo | | | | | | |
|---|---|---|---|---|---|---|---|---|---|---|---|---|---|
| Oxides (wt.%) | T11-25 c | T11-20 c | T11-33 d | T11-28 d | T11-1 a | T11-4 a | T10-1 center | T10-8 c S | T10-12 c N | T10-7 a S | T10-5 a S | T10-3 a S | T10-16 a N |
| $SiO_2$ | 66.36 | 65.37 | 66.07 | 65.59 | 65.22 | 65.34 | 66.50 | 65.50 | 66.21 | 66.38 | 66.57 | 65.71 | 66.29 |
| $Al_2O_3$ | 16.49 | 16.15 | 15.87 | 16.32 | 15.19 | 16.15 | 18.20 | 16.20 | 17.26 | 17.68 | 17.37 | 17.41 | 17.93 |
| $Cr_2O_3$ | 0.60 | 0.49 | 0.87 | 0.63 | 0.80 | 0.73 | 0.09 | 0.12 | 0.05 | 0.05 | 0.11 | 0.03 | 0.03 |
| $Fe_2O_3$ | 0.10 | 0.11 | 0.19 | 0.09 | 0.37 | 0.21 | 0.08 | 0.51 | 0.10 | 0.13 | 0.23 | 0.26 | 0.20 |
| $V_2O_3$ | 0.72 | 0.59 | 0.89 | 0.58 | 1.08 | 0.87 | 0.15 | 0.26 | 0.13 | 0.20 | 0.21 | 0.21 | 0.20 |
| BeO calc.[b] | 13.81 | 13.60 | 13.75 | 13.65 | 13.57 | 13.60 | 13.84 | 13.92 | 13.78 | 13.81 | 13.85 | 13.67 | 13.79 |
| MgO | 0.75 | 0.98 | 1.21 | 0.67 | 1.28 | 0.86 | 0.67 | 1.48 | 0.90 | 0.57 | 0.87 | 0.82 | 0.67 |
| $Na_2O$ | 0.66 | 0.78 | 0.86 | 0.55 | 0.98 | 0.64 | 0.56 | 1.13 | 0.63 | 0.39 | 0.69 | 0.67 | 0.56 |
| $H_2O$ calc.[c] | 1.39 | 1.49 | 1.56 | 1.30 | 1.67 | 1.38 | 1.31 | 1.79 | 1.87 | 1.10 | 1.42 | 1.40 | 1.31 |
| Total | 100.88 | 99.56 | 101.27 | 99.38 | 100.16 | 99.78 | 101.40 | 100.91 | 100.93 | 100.31 | 101.32 | 100.18 | 100.98 |
| | | | | | | | | | | | | | |
| Si | 6.000 | 6.000 | 6.000 | 6.000 | 6.000 | 6.000 | 6.000 | 6.000 | 6.000 | 6.000 | 6.000 | 6.000 | 6.000 |
| Al | 1.757 | 1.747 | 1.699 | 1.760 | 1.647 | 1.748 | 1.935 | 1.749 | 1.843 | 1.883 | 1.845 | 1.874 | 1.913 |
| Cr | 0.043 | 0.036 | 0.062 | 0.046 | 0.058 | 0.053 | 0.006 | 0.009 | 0.004 | 0.004 | 0.008 | 0.002 | 0.014 |
| $Fe^{3+}$ | 0.007 | 0.008 | 0.013 | 0.006 | 0.026 | 0.015 | 0.005 | 0.035 | 0.007 | 0.009 | 0.016 | 0.018 | 0.014 |
| $V^{3+}$ | 0.052 | 0.043 | 0.065 | 0.043 | 0.080 | 0.064 | 0.011 | 0.019 | 0.009 | 0.014 | 0.015 | 0.015 | 0.015 |
| $Be^{2+}$ [b] | 3.000 | 3.000 | 3.000 | 3.000 | 3.000 | 3.000 | 3.000 | 3.000 | 3.000 | 3.000 | 3.000 | 3.000 | 3.000 |
| Mg | 0.101 | 0.134 | 0.164 | 0.091 | 0.176 | 0.118 | 0.090 | 0.202 | 0.122 | 0.077 | 0.117 | 0.112 | 0.090 |
| Na | 0.116 | 0.139 | 0.151 | 0.098 | 0.175 | 0.114 | 0.098 | 0.201 | 0.111 | 0.068 | 0.121 | 0.119 | 0.098 |
| Total | 11.076 | 11.107 | 11.154 | 11.043 | 11.161 | 11.111 | 11.146 | 11.215 | 11.096 | 11.056 | 11.121 | 11.139 | 11.144 |
| | | | | | | | | | | | | | |
| V/Cr | 1.19 | 1.20 | 1.02 | 0.91 | 1.34 | 1.18 | 1.66 | 2.15 | 2.58 | 3.97 | 1.90 | 6.95 | 6.62 |

[a] Analyses on Coscuez samples were performed on a section perpendicular to the c-axis. Analyses on Muzo samples were conducted on a section parallel to the c-axis.
[b] Amount of Be inferred from stoichiometry zones: a = arm; c = core; d = dendrite; S = southern part of the crystal; N = northern part of the crystal.
[c] Calculated following the equation $H_2O = (0.84958)(Na_2O) + 0.8373$ (Giuliani et al., 1997).

concentrations were between 1400 and 15,500 ppm, which corresponds to a calculated $H_2O$ in the channels between 0.95 and 2.15 wt.%, following the equation proposed by Giuliani et al. (1997). In terms of chromophores, V was the main element; the highest concentrations in $V_2O_3$ and $Cr_2O_3$ were 11,700 and 9,700 ppm, respectively. The V/Cr ratio was between 0.42 and 6.9 (tables 2 and 3). Some of the emeralds were Cr-free, with $V_2O_3$ content up to 1.17 wt.% (sample in figure 12D; table 2). The Mg contents were between 2,300 and 14,800 ppm.

Chemical compositional EDX maps of trapiche from Muzo (sample T8 in figure 12G) were obtained on a section perpendicular to the c-axis (figure 26A). This sample contained a colorless to very light green core rimmed by dendrites and six colorless arms (figure 12G). The arms were rimmed by deep green overgrowth zones. All the chemical elements of emerald were distributed homogenously in the EDX-map of the core and arms. The dendrites were characterized by Na anomalies that correspond to minute crystals of albite formed during their growth. The overgrowth zones were richer in Mg and Na, with important Cr and V anomalies, than the core and arms. The con-

tact zone between the arm and the overgrowth was sharp and distinguished by a Cr-rich zone (figure 26F). The Al anomalies detected at the border and within the fractures of the crystal were due to argillites that formed during a late *meteoric water* stage.

The distribution of the different chemical elements in the various maps were coupled to the chemical distribution of Cr and V (in wt.%). EPMA analyses presented in table 2 show that the arms were richer in Cr and V than the core. The contact zone between the arms and the overgrowth was sharp and indicated by a Cr-rich zone in the EDX image (figure 26F). The $Cr_2O_3$ and $V_2O_3$ contents calculated by EDX reached 0.72 and 0.64 wt.%, respectively.

Sample T10 is a section parallel to the c-axis of a V-rich greenish trapiche emerald from Muzo (figure 27A). The chemical composition of the center, the core, and the rims are reported in table 3. The spatial distribution of V and Cr in the longitudinal section showed a positive correlation between these two elements for the center and the core (figure 27B). The arms from both sides of the crystal had a restricted $V_2O_3$ range (table 3).
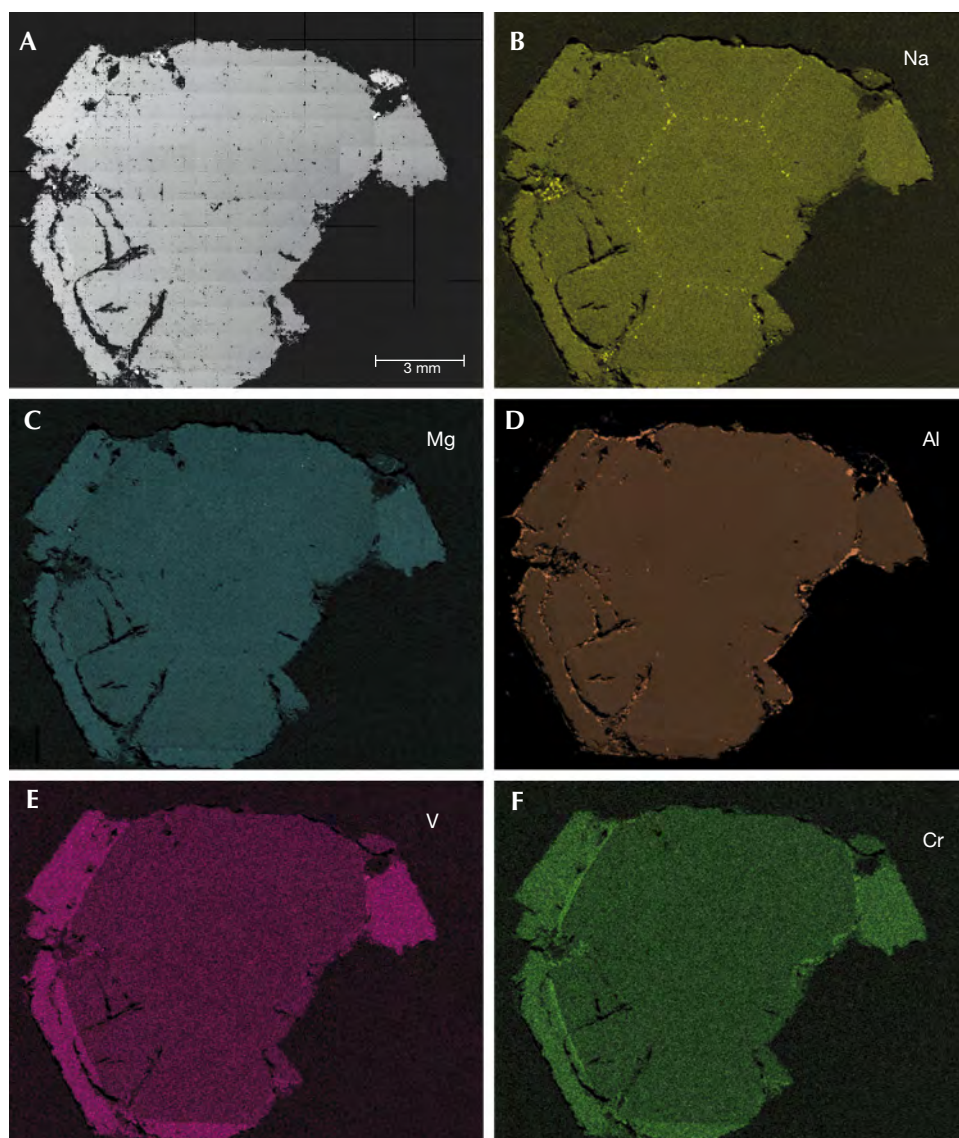
Figure 26. A: An SEM view of sample T8 from Muzo (shown in figure 12G). B–F: EDX elemental maps show the distribution of sodium (B), magnesium (C), aluminum (D), vanadium (E), and chromium (F). Brighter color corresponds to a higher concentration of the element being imaged. Image B shows a very high concentration of Na in the dendrites where albite is present. Image C shows a slight increase of Mg in the overgrowth zone. Image D shows important concentrations of Al in the fractures filled by clay minerals during late meteoric fluid circulation. Images E and F show that there is no chemical difference in the distribution of V and Cr between the core and the arms: Both areas are very poor in chromophores (Cr and V <600 ppm), although the overgrowth zone is very rich in V and Cr: This area has the "green grass" color of Muzo emeralds. The emerald zone in contact with the arms is Cr-rich (up to 7200 ppm), while the outer zone is V-rich (up to 6400 ppm).

## DISCUSSION

The formation of trapiche emerald was approached by a combination of previous and new experimental data on the trapiche texture with the constraints of tectonics and basinal fluid circulation in a sequence of black shales of the western emerald zone in Colombia's Eastern Cordillera.

**Growth History.** While many hypotheses have been proposed, how and why trapiche emeralds formed will be elucidated on the basis of new experimental data presented in this work. These data further confirm that trapiche emeralds are neither composite (Chaudhari, 1969) nor twinned crystals (Codazzi, 1915; Bernauer, 1933). The possibility that trapiche emeralds are made of three intersecting crystals elongated in the <1$\bar{1}$0> directions and that the spaces between them are filled by dendrite material is excluded by the presence of the dendrites around the core (see, for example, figures 14 and 15). Moreover, X-ray topographic images show crystalline continuity between the arms and the core, indicating they are not several crystals but portions of the same emerald. The trapiche emerald is thus a unique crystal formation, as already stated by Nassau and Jackson (1970). Furthermore, the presence of multiphase fluid inclusions in the trapiche emeralds similar to those observed in non-trapiche Colombian emeralds suggests that they formed from the same fluid in the system, $H_2O$-$NaCl$ ± ($CO_2$).

The chemical composition of the interstitial fluid, the temperature (approximately 300–330°C), and the bulk composition of the rocks (i.e., albitized black shales) are the same for trapiche emerald and emerald-
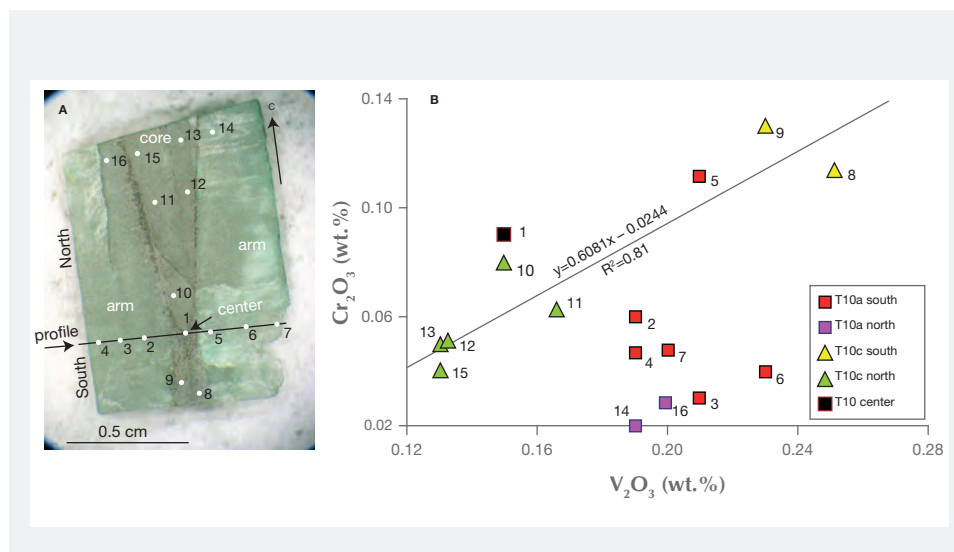
*Figure 27. Variation of vanadium ($V_2O_3$) and chromium ($Cr_2O_3$) contents (in wt.%) in the trapiche emerald from Muzo presenting a section parallel to the c-axis (see table 3). A: The different points of analyses are reported from 1 to 16 in the core (pts. 1, 8–10, 11–13, and 15) and the two arms (pts. 2–7, 14, and 16). B: Variation of the $V_2O_3$ and $Cr_2O_3$ contents in the core and the arms of the sample.*

bearing veins. The difference in the texture between these two is due to extreme variation of pressure in the history of their formation. That trapiche formed before regular emerald is evidenced by field observation. Trapiche emerald developed on albitized black shale that is crosscut by regular-emerald-bearing veins and tension gashes. Some of the trapiche have an overgrowth zone that undoubtedly grew during the formation of non-trapiche emerald. The tectonic decompression increased the degree of supersaturation, allowing the formation of trapiche emeralds, whereas emerald overgrowths occurred at a lower degree of supersaturation, until finally, at equilibrium conditions, euhedral non-trapiche emerald grew in the veins.

The trapiche emeralds started growing at the beginning of the local decompression. The hydrothermal fluid came in contact with the albitized black shale matrix, favoring the formation of seed crystals of emerald. During the growth of these seeds, textural sector zoning—i.e., the accumulation of inclusions derived from the matrix along the interfaces of growth sectors (Andersen, 1984)—took place. This is proved by the presence of dendrites all around the core (pinacoidal growth sectors) and between the arms (prismatic growth sectors).

Textural zoning can also occur with chemical sector zoning, in which the growth sectors have different chemical compositions. In both cases, the growth sectors can be easily recognized. They are separated by inclusions in textural sector zoning, and by composition and color differences in chemical zoning. This is the case with some trapiche samples analyzed in this study showing different concentrations of V

and Cr in the core and the arms (tables 2 and 3). Different amounts of chromophore elements can result in different colors of various sectors, as in sample T4 (figure 12C), where the core is very pale green and the arms are green (richer in both Cr and V). The higher quantity of V and Cr also suggests that the arms grow faster than the core. The faster growth causes the de-

*Figure 28. Schematic representation of trapiche texture in Colombian emeralds, formed by textural sector zoning and displacement growth.*
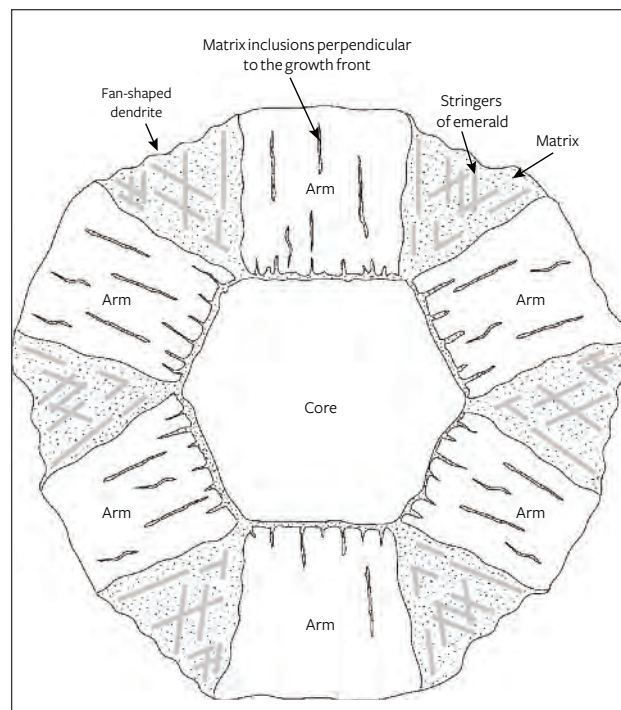
pletion of Al in the fluid near the prismatic growth fronts, allowing the incorporation of metal elements in the octahedral site to allow the growth's front to advance. The faster growth of arms is supported by the higher quantity of defects perpendicular to the growth fronts such as bundles of dislocations and solid and multiphase fluid inclusions (figures 20 and 24).

The overpressure and associated fluid supersaturation allow emerald to continue its growth and favor the displacement growth pushing the matrix material from the growing faces (Yardley, 1974; Carstens, 1986; Riche and Mitchell, 1991). Two factors are necessary for displacement growth: high fluid pressures and slow growth (Yardley, 1974). Because the core grows slower than the arms, it pushes away the matrix material that accumulates around it as dendrites (figure 28).

The matrix material is also displaced by the prismatic growth sectors. Nevertheless, the matrix cannot be moved away as fast as these sectors grow. Thus the matrix is trapped, forming dendrites within and/or along the arms and perpendicular to the growth fronts (i.e., parallel to the elongation direction of the arms; see figures 12D and 21D). It should be noted that the matrix material is trapped primarily along the a-axis, forming dendrites whose size is a function of the quantity of displaced material (figure 12). The crystallographic orientation of the dendrites can be explained by the Berg effect (1938). Because the driving force is higher on the corners than on the faces, the emerald can grow so fast as to trap most of the matrix material along the a-axis. The fan-shaped dendrites observed in some trapiche emeralds are common in trapiche chiastolites and garnets (Riche and Mitchell, 1991; Rice, 1993) and are also known as "re-entrants" (Pogue, 1916). Fan-shaped dendrites are also considered nucleation zones for minor growth (Rice, 1993), explaining why in some dendrites the stringers of emerald develop parallel to the edges of prismatic sectors and intersect at 60° angles (figure 21A). This 60° angle is not arbitrary and indicates that the emerald grows parallel to the two prismatic sectors delimiting the fan-shaped dendrite. The rapid growth along the a-axis is also proved by the fact that the stringers of emerald have a tree-like, fibrous texture (figures 25A and 25C).

During displacement growth, the black shales played a key role in the thermal reduction of sulfate by oxidizing the organic matter. Oxidation generated $CO_2$, creating fluid overpressure in the black shale. Such exothermic reactions produced hydrothermal carbon (bitumen), which can float in the fluid as a syngenetic material and concentrate in the dendrites.

Overpressure can explain the presence of fractures in the core and arms (see "Results" for details) filled with the same materials observed in the matrix. It can also account for the plastic deformation of the core that results in an *undulatory extinction* under cross-polarized light in some samples.

Overpressure can also cause a change in the chemical composition of the growth medium, leading to the dissolution of the emerald not yet in equilibrium with these new conditions. Consequently, partial dissolution affects some portions of growing crystals. This kind of "selective" dissolution (etching) has been described by Bernauer (1933) on some trapiche emeralds from Muzo. It has been observed by Lyckberg (2005a,b) on the prismatic faces of heliodor from Karelian, Russian, and Ukrainian pegmatites, and by Tempesta et al. (2011) on beryl crystals from Minas Gerais, Brazil.

After decompression and hydraulic fracturing, the degree of supersaturation of the fluid decreased considerably. This can favor the formation of an overgrowth surrounding the core, the arms, and the dendrites. The lower degree of supersaturation can also explain the formation of elongated voids in the arms by dissolution along the dislocation bundles (Scandale and Zarka, 1982; Authier and Zarka, 1994).

**Geological History.** The emerald-bearing veins in Colombia's western emerald zone formed in a context of fluid pressure variations in tear faults and thrusts affecting the Lower Cretaceous black shales. Formed along tear faults were numerous veins and hydraulic breccias. They resulted from the fracturing of the wall rocks during a tear fault increment (a displacement along the fault plane, likely inducing a seismic event). This increment is responsible for development of dilational *jogs* along several fault segments. As a result, the jogs caused a large fluid pressure gradient and "pumped" the surrounding hydrothermal fluids. Blocks of black shales, white albitite, and albitized and/or carbonatized black shales simultaneously collapsed into the jog and were cemented by carbonates and albite.

Along the thrust, the fault propagation is achieved by shear-tensional failure caused by hydraulic fracturing under supra-lithostatic fluid pressure and small differential effective stresses (box C). The polygenetic nature of the fragments of the breccia such as in the tear faults, and the rotations and partial dissolution of the elements, clearly indicate bulk transport of mate-

# BOX C: GEOLOGICAL MODEL FOR THE PROPOSED MECHANISM OF TRAPICHE EMERALD FORMATION
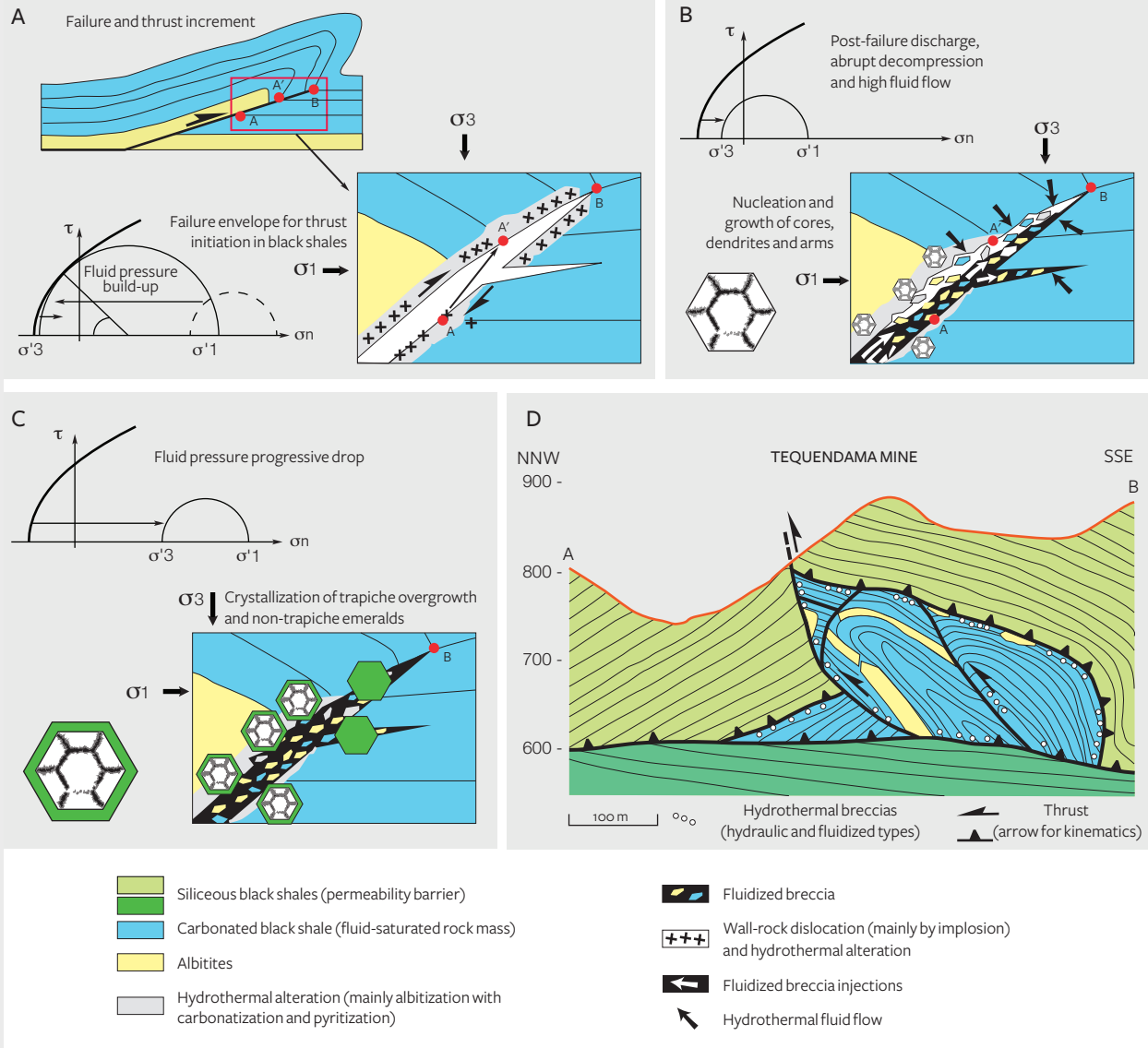


Figure C-1. Geological model for the proposed mechanism of the trapiche emerald formation from the western emerald zone. A: Thrust propagation and failure. B: Nucleation and growth of core, dendrites, and arms of trapiche emerald. C: Formation of trapiche overgrowths and regular emerald in veins. D: Cross-section of the Tequendama mine. In the Mohr's circle diagrams in A, B, and C, $\tau$ = shear stress; $\sigma n$ = normal stress; $\sigma 1$ and $\sigma 3$ = the main stresses.

rial during fluid flow (*fluidization phenomena*). The cement is formed by carbonates, pyrite, and albite, creating the hydrothermal breccia called "cenicero." The fluidized breccias are associated with emerald-bearing thrust veins, which are horizontal tension gashes in this compressive tectonic context. The sealing of faults by carbonate deposition and cementation of the fluidized breccia depends on the elapsed time between

The formation of Colombian trapiche emerald is closely related to the structural geology history in the western zone. The correlation between the formation of tear faults under compressional stress and the growth of trapiche emerald can be elucidated in the following three steps (figure C-1: A, B and C):

- A: Thrust propagation and failure. The *incremental thrust propagation* is related to the highest fluid pressures, which caused the failure and propagation of the fault (from point A to point A'). The failure occurred in the hybrid-shear-extensional mode, the thrust presenting a dilatant component. Physically, the *Mohr's circle* moved to the left and touched the failure envelope of the black shale material.

- B: Abrupt decompression of fluid pressure is related to the opening of dilatant sites (i.e., high permeability and porosity zones) along the thrust. Hypersaline Na-bearing fluids responsible for strong albitization of the hosting carbon-rich black shales are "pumped" into those dilatant zones with high flow rates. As a result, high fluid pressure gradients also triggered fluidization processes responsible for the formation of polygenic breccia. Physically, the Mohr's circle describes an incipient rightwards motion. This decompression caused an increase of the driving force of the emerald crystal growth. The emerald seed crystals grew on albitized black shales. During the growth of these seeds, textural sector zoning of trapiche emerald took place with the dendrites all around the core and between the arms.

- C: Formation of trapiche overgrowths and non-trapiche emeralds during a progressive decrease of pressure and flow (i.e., lower fluid pressure gradient than in B). Non-trapiche emeralds are mainly hosted within sub-horizontal extensional veins and fluidized hydrothermal breccias.

In diagram D in figure C-1, a cross-section of the Tequendama mine following the geological map in figure 6 illustrates the relationship between structures and trapiche growth. The cross-section shows the different lithologies and tectonic structures described in the text. The thrusts and tear faults (represented in figure 6) are associated with the breccias, sub-horizontal extensional veins, and potential zones related to trapiche emerald.

the drop and the following build-up of fluid pressure. The thrusts propagate in a succession of faulting, fluid flow (multistage events), hydrothermal alteration, and emerald deposition (Branquet et al., 1999b).

Trapiche emerald (figure 29) formed when the fluid pressure exceeded the *lithostatic pressure* (box C). The local decompression induced the supersaturation of the hydrothermal fluid and an increase of the driving force of the emerald crystal growth (stage 1 under "Emerald Mineralization"). The emerald seed crystals grew on albitized carbon-rich black shale (see box C, figure C-1) or albitite (the type seen at Peñas Blancas; Vuillet et al., 2002), as argued by the presence of solid inclusions and matrix around the trapiche cores (Bernauer, 1933; Nassau and Jackson, 1970). Stage 1 is also associated with the formation of tension gashes and thrust-fluidized breccias ("cenicero") and thrust veins.

The hydrothermal fluid bathed each whole cavity, and the precipitation of carbonates, pyrite, and albite sealed the fault open spaces (hydrothermal breccia), and emerald deposition occurred with its carbonate-pyrite assemblage in the thrust veins (stage 2). During this last episode of emerald crystallization in the veins, the degree of supersaturation of the fluid decreased considerably up until chemical equilibrium. During this time, the trapiche emeralds probably acquired their final deep-green overgrowths, also found in non-trapiche emerald-bearing thrust veins.

## CONCLUSIONS

Trapiche emeralds occur in association with black shales in the western emerald zone of Colombia's Eastern Cordillera Basin. They formed in a geological context of fluid pressure variations along faults and thrusts affecting the Lower Cretaceous sedimentary series. The fluid accumulation at the faults' tip led to maximum fluid overpressure and subsequent decompression. The rocks failed, and trapiche emerald formed in the albitized black shale host rock, followed by the crystallization of emerald in carbonate veins.

Trapiche emeralds from Muzo, Coscuez, and Peñas Blancas were investigated by several analytical techniques in order to propose a model of formation for trapiche texture linked to the structural geology of the deposits. Petrographic and SEM observations combined with X-ray topography and tomography images confirmed that trapiche emerald is a single crystal formed by different zones: a core (pinacoidal growth sectors), dendrites, and arms (prismatic growth sectors), sometimes surrounded by an overgrowth. The color of these zones is due to the presence of V and lower concentrations of Cr, although both elements were detected by EPMA even in colorless zones such as some of the cores.

*Figure 29. These trapiche emeralds, all from Peñas Blancas, range from 5.09 to 22.74 ct. Photo by Robert Weldon/GIA. Courtesy of Jose Guillermo Ortiz, Colombian Emerald Co.*

The formation of the trapiche texture in Colombian emeralds is controlled both by the peculiar "structurally controlled" genesis of the deposits and by the crystal symmetry, determining which growth sectors develop and how many of them. From this, a few crucial points on trapiche formation can be summarized:

1. The growth of trapiche emerald started during the local decompression responsible for the supersaturation of the fluid. The hydrother- mal fluid came in contact with the black shale matrix, favoring the formation of emerald crystal seeds.

2. Textural sector zoning, sometimes associated with chemical sector zoning, took place during the growth of these seeds. The inclusions of black shale matrix were incorporated between the growth sectors, forming the dendrites around the core and between the arms.

3. The emeralds continued their growth, displac- ing the matrix material from the growing faces. As a result, the matrix may also be trapped in the arms perpendicular to their growth fronts, even if it is preferentially incorporated along the a-axis. The dendrites between the arms have a typical fan-shape near the borders of the samples, because the emerald grows faster along the a-axis than along $\langle 1\bar{1}0 \rangle$ (see again fig- ure 13), and thus a higher quantity of matrix material can be trapped.

4. An overgrowth, generally of gem quality, may be formed after decompression. This over- growth surrounding the core, arms, and den- drites and restoring the emeralds' euhedral habit. During overgrowth formation, non- trapiche emerald formed in the carbonate veins.

For the first time, the development of the trapiche texture has been related to the geological conditions of Colombian emerald deposits. Al- though some formation models were previously pro- posed for trapiche minerals, they were extrapolated from the deposit context and were not supported by geological events responsible for the supersaturation of the mineralizing fluids.

ABOUT THE AUTHORS
*Dr. Pignatelli, a geologist and expert in mineralogy and crystal- lography, is currently a postdoctoral researcher at the University of California, Los Angeles. Dr. Giuliani is director of research at the Institute of Research for Development (IRD) in Toulouse (GET) and the French National Center of Research (CRPG/CNRS) in Vandœuvre. He is recognized for his work on the geology, geochemistry, and genesis of several colored stone deposits. Dr. Ohnenstetter is a retired geologist based in Mar- inville-sur-Madon, France, formerly with CRPG/CNRS, who spe- cializes in petrology and cathodoluminescence spectroscopy and mineralogy. Dr. Agrosì is a researcher with the Department of Earth and Geo-environmental Sciences at the University of*

*Bari, Italy. Ms. Mathieu specializes in quantitative analyses using EDX and WDX spectrometry in complex systems at GéoRes- sources 7359 research unit, Vandœuvre, France. Mr. Morlot is responsible for X-ray tomography applied to Geosciences at GéoRessources 7359 unit, Vandœuvre, France. Dr. Branquet is an assistant professor of earth sciences at the University of Or- léans in France.*

# GLOSSARY

**Albitite:** a magmatic or metasomatic (see *metasomatism*) rock composed almost wholly of coarse- to fine-grained crystals of albite.

**Basinal brine:** fluids in basins that are enriched Na, Ca, and Mg sulfates. In basins, processes of sediment or basin dewatering give rise to large volumes of fluids moving through different types of rocks (generally sedimentary). The temperature increases to 80°–200°C or higher based on the depth of fluid circulation in the basin. After reacting with different rocks, the fluids are enriched in Na, Ca, and Mg sulfates, and their salinity can increase tremendously.

**Black shale:** a fine-grained clastic sedimentary mudrock composed of clay mineral flakes and other fragments, mainly quartz and calcite.

**Breccia:** a rock composed of broken fragments of minerals or rock cemented together by a fine-grained matrix.

**Burgers vectors:** a quantity, usually represented by an arrow, describing the magnitude and the direction of the lattice distortion resulting from a dislocation.

**Cataclasite:** a rock consisting of angular *clasts* in a fine-grained matrix that formed by fracturing and pulverization of the rock during faulting.

**Clast:** a fragment of pre-existing mineral or rock.

**Coquina limestone:** slightly cemented sedimentary rock formed almost completely of sorted fossils, generally shell and shell fragments.

**Daughter mineral:** the new phases formed in a fluid inclusion cavity that have precipitated from the solution within.

**Décollement plane:** a low-angle dipping fault or shear zone corresponding to a gliding plane between two rock masses. These planes are developed in compressional tectonic settings (involving folding and overthrusting) and extensional settings. Also known as a basal detachment fault.

**Dendrite:** A portion of the trapiche texture having saw-tooth contact with the core and the arms and formed by dendritic growth (i.e., a high degree of supersaturation, see box B). In agreement with the literature, the word can also be used to refer to feather-edge morphologies due to the incorporation of matrix material (as in this study).

**Detachment:** see *décollement plane*

**Diffraction vector g:** In a crystal of any structure, vector **g** is normal to the planes (*hkl*) and has a length inversely proportional to the distance between the planes.

**Dolomitic limestone (or dolomite):** an anhydrous carbonate mineral with the formula $(Ca, Mg)(CO_3)_2$.

**Drag folds:** curvature that represents the bending of rocks before they break. Drag folds occur in conjunction with faults.

**Drusy cavity:** a hollow space within a rock with a crust of tiny crystals.

**En echelon vein:** also known as *tension gash* arrays, these veins are characteristic of ductile-brittle shear zones. They are sets of short, parallel planar lenses on the surface of a rock. En echelon veins originate as tension fractures and are subsequently filled through the precipitation of a mineral, most commonly calcite or quartz.

**Eutectic system:** a mixture of two species that melt and solidify at constant temperature. The eutectic system behaves in fact as a pure body from the standpoint of fusion.

**Evaporites:** any sedimentary rock such as gypsum, anhydrite, or rock salt (such as halite or sylvite) that is formed by precipitation from evaporating seawater.

**Extensional vein:** equivalent of *tension gash*.

**Fluidization phenomena:** transport of rock fragments and breccia by a fluid (liquid or gas) in a fault structure. During fluid flow, the heavier fragments of the breccia are transported, suspended, rotated, sorted, and cemented by the matrix. The fragments and matrix are suspended and transported as a fluid-supported pulp.

**Framboidal:** Referring to a texture of roughly spherical aggregates of discrete rounded equi-angular euhedral microcrystallites approximately 0.5 μm in diameter, with an average aggregate size ranging from 5 to 20 μm.

**Hydraulic breccia:** a rock formation resulting from hydraulic fracturing, in which the hydrostatic pressure is greater than lithostatic pressure. Hydraulic fracturing may create a *breccia* that is filled with vein material. Such vein systems may be quite extensive, and can form in the shape of tabular dipping sheets, diatremes, or laterally extensive mantos controlled by boundaries such as *thrust* faults, competent sedimentary layers, or cap rocks.

**Incremental thrust propagation:** the propagation of a dislocated part of the terrane over an area in relatively small overlapping increments.

**Internal over- and underpressure:** When trapped by a mineral, pressure and temperature conditions preserved by fluid inclusion cavities can sometimes suffer re-equilibration during growth. As a result, the cavities can suffer internal overpressure when the internal pressure in the inclusion exceeds the external confining pressure, or internal underpressure when the internal pressure is lower than the external confining pressure.

**Jogs (or bends):** a gap or segment between two fault plane with the same strike and slip direction. Jogs offset perpendicular to the slip direction.

**Klippe:** in *thrust fault* terrains, the remnant of a nappe after erosion has removed the connecting portions.

**Layer-by-layer growth:** a growth mechanism based on two-dimensional nucleation.

**Listric faults:** faults in which the fault plane curves; the dip is steeper near the surface and shallower with increased depth.

**Lithostatic pressure:** the pressure or stress imposed on a layer of soil or rock by the weight of material. It is also called overburden pressure, confining pressure, or vertical stress.

**Metasomatism:** the chemical alteration of a rock by hydrothermal and/or other fluids. The chemical elements of the mother rock undergo fluid transport, accompanied by a modification (metasomatic process) of chemical composition to form a daughter rock.

**Meteoric water:** the water derived from precipitation that forms ice melts and bodies of water such as rivers and lakes.

**Mohr's circle:** A diagram that graphically illustrates in two dimensions the complex relationships between components of normal and shear stress.

**Nappe:** a large sheetlike body that moved more than two kilometers above the thrust fault from its original location.

**Necking-down:** a re-equilibration process of the morphology of a fluid cavity during cooling. This post-entrapment phenomenon changes the shape of the cavity by splitting it into smaller fluid inclusions. Necking-down leads to a distribution of the phases (vapor, liquid, solid) that is different from the original fluid inclusion assemblage.

**Olistostrome:** a sedimentary deposit composed of a chaotic mass of heterogeneous material, such as blocks and mud. The mass accumulates as a semi-fluid body via submarine gravity sliding or slumping of the loose materials.

**Overthrusting:** large total displacement of *thrust faults*.

**Phyllosilicates:** silicate minerals with sheet-like structures.

**Pinacoidal faces:** two equivalent faces related by an inversion center.

**Scalar product:** the product of the magnitudes of two vectors and the cosines of the angles between them.

**Shear zone:** a zone of strong deformation with a high strain rate surrounded by rocks with a lower state of finite strain. It is characterized by a length-to-width ratio of more than 5:1. Shear zones form a continuum of geological structures, ranging from brittle to brittle-ductile (or semi-brittle), ductile-brittle, and ductile shear zones.

**Space group:** A set of symmetry operations of a three-dimensional crystal pattern.

**Stringers:** oblique growth of emeralds at 60° to each other occurring in the dendrites. They are also observed in other trapiche minerals such as chiastolite and garnet, where they form at 90° and 60°, respectively (Rice, 1993).

**Subsiding marine basin:** areas generally characterized by thick accumulation of marine sediments. Subsidence is controlled by tectonic (e.g. normal faults as in passive margin or rift basin) and thermal re-equilibration of thinned crust.

**Supersaturation (or undercooling):** the difference between the concentration $C_\infty$ at the equilibrium temperature $T_E$ of a saturated solution and the concentration $C$ at the growth temperature $T_G$ (Sunagawa, 2005). Supersaturation is critical because it is the driving force for crystal nucleation and growth.

**Tear faults:** small-scale local strike-slip faults. Strike-slip faults with left-lateral motion are known as sinistral faults, those with right-lateral motion are known as dextral faults. Each is defined by the direction of movement of the ground on the opposite side of the fault from an observer. Tear faults are associated with other structures such as folds, thrust faults, and normal faults. In a thrust belt, the tear faults strike perpendicular to the thrust front and fold axis. As the thrust sheet propagates into the foreland, the tear faults start to segment the thrust sheets, eventually acting as lateral boundaries that separate the thrust units.

**Tension gash:** veins characteristic of ductile-brittle shear zones, classically disposed en echelon when non-coaxial strain is applied to rocks (see *en echelon vein*). Also called *extensional veins*.

**Thermal reduction of sulfate:** redox reactions in which sulfate is reduced by hydrocarbons, either bacterially (bacterial sulfate reduction) or inorganically (thermochemical sulfate reduction).

**Thrust fault:** a fault with a very low dip angle and a very large total displacement of the terranes, called *overthrust* or detachment. Thrust faults are characteristic of compressive tectonics. This process results in an outlier of exotic, often nearly horizontally translated strata called "nappe" overlying autochthonous strata.

**Undulatory extinction:** the consequence of tectonic constraints, seen as a darker zone during the rotation of the microscope stage. Also called wavy extinction.

## REFERENCES

Agrosì G., Bosi F., Lucchesi S., Melchiorre G., Scandale E. (2006) Mn-tourmaline from island of Elba (Italy): Growth history and growth marks. *American Mineralogist*, Vol. 91, Nos. 5–6, pp. 944–952, http://dx.doi.org/10.2138/am.2006.1978

Agrosì G., Tempesta G., Scandale E., Harris J. W. (2013) Growth and post-growth defects in a diamond from Finsch mine (South Africa). *European Journal of Mineralogy*, Vol. 25, No. 4, pp. 551–559, http://dx.doi.org/10.1127/0935-1221/2013/0025-2301

Andersen T.B. (1984) Inclusion patterns in zoned garnet from Magerøy, north Norway. *Mineralogical Magazine*, Vol. 48, No. 346, pp. 21–26, http://dx.doi.org/10.1180/minmag.1984.048.346.03

Andrianjakavah P.R., Salvi S., Béziat D., Rakotondrazafy A.F.M., Giuliani G. (2009) Proximal and distal styles of pegmatite-related metasomatic emerald mineralization at Ianapera, southern Madagascar. *Mineralium Deposita*, Vol. 44, No. 7, pp. 817–835, http://dx.doi.org/10.1007/s00126-009-0243-5

Artioli G., Rinaldi R., Ståhl K. (1993) Structure refinements of beryl by single-crystal neutron and X-ray diffraction. *American Mineralogist*, Vol. 78, pp. 762–768.

Atherton M.P., Brenchley P.J. (1972) A preliminary study of the structure, stratigraphy and metamorphism of some contact rocks of the Western Andes, near the Quebrada Venado Muerto, Peru. *Geological Journal*, Vol. 8, pp. 161–178, http://dx.doi.org/10.1002/gj.3350080114

Aurisicchio C., Fioravanti G., Grubessi O., Zanazzi P.F. (1988) Reappraisal of the crystal chemistry of beryl. *American Mineralogist*, Vol. 73, Nos. 7–8, pp. 826–837.

Authier A., Zarka A. (1994) X-ray topographic study of the real structure of minerals. In A.S. Marfunin, Ed., *Composition, Structure and Properties of Mineral Matter*, Springer-Verlag, Berlin, pp. 221–233.

Banks D.A., Giuliani G., Yardley B.W.D., Cheilletz A. (2000) Emerald mineralisation in Colombia: fluid chemistry and the role

of brine mixing. *Mineralium Deposita*, Vol. 35, No. 8, pp. 699–713, http://dx.doi.org/10.1007/s001260050273

Barriga Villalba A.M. (1948) Estudio cientifico de la Esmeraldas de Colombia. In *Esmeraldas de Colombia*, Banco de la Republica Publisher, Bogotá, Colombia Parte II, pp. 97–133 [in Spanish].

Befi R. (2012) Gem News International: Trapiche aquamarine from Namibia. *G&G*, Vol. 48, No. 2, pp. 143–144.

Berg W.F. (1938) Crystal growth from solutions. *Proceedings of the Royal Society*, Vol. 164, No. 916, pp. 79–95, http://dx.doi.org/10.1098/rspa.1938.0006

Bergt W. (1899) Die älteren Massengesteine, kristalli nen Schiefer und Sedimente, p. 46. In F. Bernauer Ed., *Compilación de los Estudios Geológicos Oficiales en Colombia -1917 a 1933*, No. 4, pp. 199–221 (in German).

Bernauer F., Ed. (1933) Las llamadas maclas multiples de esmeralda de Muzo y sus anomalias opticas. *Compilación de los Estudios Geológicos Oficiales en Colombia -1917 a 1933*, No. 4, pp. 199–221 (in Spanish).

Bertrand E. (1879) Compte-rendu de la séance du 13 Février 1879 [Report of the meeting of February 13, 1879]. *Bulletin de la Société Minéralogique de France*, Vol. 2, p. 31.

Beus A.A. (1979) Sodium - a geochemical indicator of emerald mineralization in the Cordillera oriental, Colombia. *Journal of Geochemical Exploration*, Vol. 11, No. 2, pp. 195–208, http://dx.doi.org/10.1016/0375-6742(79)90023-2

Beus A.A., Mineev D.A. (1972) *Some geological and geochemical features of the Muzo and Coscuez emerald zone, Cordillera oriental, Colombia.* INGEOMINAS, Informe 1689, 50 pp.

Branquet Y. (1999) Etude structurale et métallogénique des gisements d'émeraude de Colombie: contribution à l'histoire tectono-sédimentaire de la cordillère orientale de Colombie. PhD Thesis, Université de Lorraine, Nancy, France [in French].

Branquet Y. Laumonier B., Cheilletz A., Giuliani G. (1999a) Emeralds in the eastern Cordillera of Colombia: two tectonic settings for one mineralisation. *Geology*, Vol. 27, No. 7, pp. 597–600, http://dx.doi.org/10.1130/0091-7613(1999)027%3C0597:EITECO%3E2.3.CO;2

Branquet Y., Cheilletz A., Giuliani G., Laumonier B., Blanco O. (1999b) Fluidized hydrothermal breccia in dilatant faults during thrusting: The Colombian emerald deposits. In *Fractures, Fluid and Mineralization*. Geological Society, London, 1999, Special Publication 155, pp. 183–195.

Branquet Y., Giuliani G., Cheilletz A., Laumonier B. (2015) Colombian emeralds and evaporites: tectono-stratigraphic significance of a regional emerald-bearing evaporitic breccia level. *13th SGA Biennial Meeting*, Nancy, France, Proceedings Vol. 4, pp. 1291–1294.

Breeding C.M., Shen A.H., Eaton-Magaña S., Rossman G.R., Shigley J.E., Gilbertson A. (2010) Developments in gemstone analysis techniques and instrumentation during the 2000s. *G&G*, Vol. 46, No. 3, pp. 241–257, http://dx.doi.org/10.5741/GEMS.46.3.241

Bryan W.B. (1972) Morphology of quench crystals in submarine basalts. *Journal of Geophysical Research*, Vol. 77, No. 29, pp. 5812–5819, http://dx.doi.org/10.1029/JB077i029p05812

Burton K.W. (1986) Garnet-quartz intergrowths in graphitic pelites: the roles of the fluid phase. *Mineralogical Magazine*, Vol. 50, pp. 611–620, http://dx.doi.org/10.1180/minmag.1986.050.358.06

Byerly G.R., Palmer M.R. (1991) Tourmaline mineralization in the Barberton greenstone belt, South Africa: early Archean metasomatism by evaporite-derived boron. *Contributions to Mineralogy and Petrology*, Vol. 107, No. 3, pp. 387–402, http://dx.doi.org/10.1007/BF00325106

Carstens H. (1986) Displacive growth of authigenic pyrite. *Journal of Sedimentary Petrology*, Vol. 56, No. 2, pp. 252–257.

Charoy B. (1998) Cristallochimie du béryl: l'état des connaissances. In *L'émeraude*, Association Française de Gemmologie-CNRS-ORSTOM, Groupe Rosay, Paris, France, pp. 47–54 (in French).

Chaudhari M.W. (1969) An unusual emerald. *Schweizerische Mineralogische und Petrographische Mitteilungen*, Vol. 49, No. 3, pp. 569–575.

Cheilletz A., Giuliani G. (1996) The genesis of Colombian emeralds: a restatement. *Mineralium Deposita*, Vol. 31, No. 5, pp. 359–364, http://dx.doi.org/10.1007/BF00189183

Cheilletz A., Féraud G., Giuliani G., Rodriguez C.T. (1994) Time-pressure and temperature constraints on the formation of Colombian emeralds; an $^{40}Ar/^{39}Ar$ laser microprobe and fluid inclusion study. *Economic Geology*, Vol. 89, No. 2, pp. 362–380, http://dx.doi.org/10.1180/10.2113/gsecongeo.89.2.361

Cheilletz A., Giuliani G., Branquet Y., Laumonier B., Sanchez A.J., Féraud G., Arthan T. (1997) Datation K-Ar et $^{40}Ar/^{39}Ar$ à 65 ± 3 Ma des gisements d'émeraude du district de Chivor-Macanal: argument en faveur d'une déformation précoce dans la Cordillère Orientale de Colombie. *Comptes Rendus de l'Académie des Sciences*, Paris, Sér. IIa, Vol. 324, pp. 369–377 (in French).

Cnudde V., Boone M.N. (2013) High-resolution X-ray computed tomography in geosciences: a review of the current technology and applications. *Earth-Science Reviews*, Vol. 123, pp. 1–17, http://dx.doi.org/10.1016/j.earscirev.2013.04.003

Codazzi R.L. (1915) Los minerales de Muzo. *Contribución al Estudio de los Minerales de Colombia*, Bogotá, pp. 3–7 (In Spanish).

Damon P.E., Kulp J.L. (1958) Excess helium and argon in beryl and other minerals. *American Mineralogist*, Vol. 43, Nos. 5–6, pp. 433–459.

DelRe N. (1994) Lab Notes: Emerald, trapiche from a new locality. *G&G*, Vol. 30, No. 2, pp. 116–117.

Faure F., Trolliard G., Nicollet C., Montel J.M. (2003) A development model of olivine morphology as a function of the cooling rate and the degree of undercooling. *Contributions to Mineralogy and Petrology*, Vol. 145, No. 2, pp. 251–263, http://dx.doi.org/10.1007/s00410-003-0449-y

Faure F., Schiano P., Trolliard G., Nicollet C., Soulestin B. (2007) Textural evolution of polyhedral olivine experiencing rapid cooling rates. *Contributions to Mineralogy and Petrology*, Vol. 153, No. 4, pp. 369–492, http://dx.doi.org/10.1007/s00410-006-0154-8

Garnier V., Ohnenstetter D., Giuliani G., Blanc P., Schwarz D. (2002a) Trace-element contents and cathodoluminescence of "trapiche" rubies from Mong Hsu, Myanmar (Burma): geological significance. *Mineralogy and Petrology*, Vol. 76, Nos. 3–4, pp. 179–193, http://dx.doi.org/10.1007/s007100200040

Garnier V., Ohnenstetter D., Giuliani G., Schwarz D. (2002b) Rubis trapiches de Mong Hsu, Myanmar. *Revue de Gemmologie AFG*, Vol. 144, pp. 5–12 (in French).

Geake J.E., Walker G. (1975) *Luminescence of Minerals in the Near Infrared and Raman Spectroscopy of Lunar and Terrestrial Minerals*. Academic Press, New York, pp. 73–89.

Giuliani G., Rodriguez C.T., Rueda F. (1990) Les gisements d'émeraude de la Cordillère Orientale de la Colombie: nouvelles données métallogénies. *Mineralium Deposita*, Vol. 25, pp. 105–111 (in French).

Giuliani G., Cheilletz A., Dubessy J., Rodriguez C.T. (1991) $H_2O$-NaCl-CaCl$_2$-bearing fluids in emeralds from the Vega San Juan mine, Gachalá district, Colombia. *Plinius*, No. 5, p. 90.

Giuliani G., Sheppard S.M.F., Cheilletz A., Rodriguez C.T. (1992) Fluid inclusions and $^{18}O/^{16}O$, $^{13}C/^{12}C$ isotope geochemistry: contribution to the genesis of emerald deposits from the Oriental Cordillera of Colombia. *Comptes Rendus de l'Académie des Sciences*, Paris, Vol. 314, pp. 269–274.

Giuliani G., Cheilletz A., Dubessy J., Rodriguez C.T. (1993) Emerald deposits from Colombia: chemical composition of fluid inclusions and origin. *Proceedings of the 8th IAGOD Symposium*, Ottawa, pp. 159–168.

Giuliani G., Cheilletz A., Arboleda C., Carrillo V., Rueda F., Baker J. (1995) An evaporitic origin of the parent brines of Colombian emeralds: fluid inclusion and sulphur isotope evidence. *European Journal of Mineralogy*, Vol. 7, pp. 151–165.

Giuliani G., France-Lanord C., Zimmermann J-L., Cheilletz A. (1997) Fluid composition, δD of channel H$_2$O, and δ$^{18}$O of lattice oxygen in beryls: Genetic implications for Brazilian, Colombian, and Afghanistani emerald deposits. *International Geology Review*, Vol. 39, No. 5, pp. 400–424, http://dx.doi.org/10.1080/00206819709465280

Giuliani G., France-Lanord C., Cheilletz A., Coget P., Branquet Y., Laumonier B. (2000) Sulfate reduction by organic matter in Colombian emerald deposits: chemical and stable isotope (C, O, H) evidence. *Economic Geology*, Vol. 95, No. 5, pp. 1129–1153, tp://dx.doi.org/10.2113/95.5.1129

Giuliani G., Jarnot M., Neumeier G., Ottaway T., Sinkankas J., Staebler G. (2002) *Emeralds of the World*. ExtraLapis English No. 2: The Legendary green beryl. Lapis International Publisher, LLC, East Hampton, CT.

Giuliani G., Marty B., Banks D. (2005) Noble gases in fluid inclusions from emeralds: Implications for the origins of fluids and constraints on fluid-rock interactions. Abstract, *18th Biennial Meeting of European Current Research on Fluid Inclusions*, Siena, Italy, CD-ROM.

Götze J., Krbetschek M.R., Habermann D., Wolf D. (2000) High-resolution cathodoluminescence studies of feldspar minerals. In *Cathodoluminescence in Geosciences*. Springer Verlag, Berlin, pp. 245–270.

Groat L., Giuliani G., Marshall D., Turner D. (2014) Emerald. In *Geology of Gem Deposits*, Mineralogical Association of Canada, Short Course Series 44, Tucson, pp. 135–174.

Hainschwang T., Notari F., Anckar B. (2007) Trapiche tourmaline from Zambia. *G&G*, Vol. 43, No. 1, pp. 36–46, http://dx.doi.org/10.5741/GEMS.43.1.36

Hall M. (1993) Mineralogía y geoquímica de las vetas esmeraldíferas de Muzo, Departamento de Boyacá con implicaciones en la prospección futura de esmeraldas en otras partes de Colombia. *Compilación de los estudios geológicos oficiales en Colombia*. Tomo XIII, pp. 1–326 (In Spanish).

Harker A. (1950) *Metamorphic Textures*. Methuen and Co., London.

Hochleitner R. (2002) The emerald: mineralogically a beryl! In *Emeralds of the World*, ExtraLapis English No. 2: The Legendary green beryl. Lapis International, LLC, East Hampton, CT, pp. 11–17.

Hsu T. (2013) Gem News International: Rare double-trapiche emerald. *G&G*, Vol. 49, No. 1, p. 53.

Invernizzi C., Vityk M., Cello G., Bodnar R. (1998) Fluid inclusions in high pressure/low temperature rocks from the Calabrian Arc (Southern Italy): the burial and exhumation history of the subduction-related Diamante-Terranova unit. *Journal of Metamorphic Geology*, Vol. 16, No. 2, pp. 247–258, http://dx.doi.org/10.1111/j.1525-1314.1998.00138.x

Jia L.C., Chen M., Jin Y. (2014) 3D imaging of fractures in carbonate rocks using X-ray computed tomography technology. *Carbonates and Evaporites*, Vol. 29, No. 2, pp. 147–153.

Johnson M.L., Koivula J.I., Eds. (1998) Gem News: Beryl from Madagascar…and trapiche beryl. *G&G*, Vol. 34, No. 2, pp. 137–138.

Khotchanin K., Thanasuthipitak P., Thanasuthipitak T. (2010) Characteristics of trapiche blue sapphire from Southern Vietnam. *Chiang Mai Journal of Science*, Vol. 37, No. 1, pp. 64–73.

Kiefert L. (2012) Gem News International: Unusual trapiche sapphire. *G&G*, Vol. 48, No. 3, p. 229.

Koivula J.I. (2008) Gem News International: Two unusual aquamarines. *G&G*, Vol. 44, No. 3, pp. 275–276.

Koivula J.I., Kammerling R.C., Fritsch E., Eds. (1994) Gem News: "Trapiche" purple-pink sapphire. *G&G*, Vol. 30, No. 3, p. 197.

Kozlowski A., Metz P., Jaramillo H.A.E. (1988) Emeralds from Somondoco, Colombia: chemical composition, fluid inclusion and origin. *Neues Jahrbuch für Mineralogie Abhandlungen*, Vol. 59, pp. 23–49.

Lang A.R. (1959) The projection topograph: a new method in X-ray diffraction microradiography. *Acta Crystallographica*, Vol. 12, No. 3, pp. 249–250, doi:10.1107/S0365110X59000706.

Laumonier B., Branquet Y., Cheilletz A., Giuliani G., Rueda F.

(1996) Mise en évidence d'une tectonique compressive Eocène-Oligocène dans l'Ouest de la Cordillère orientale de Colombie, d'après la structure en duplex des gisements d'émeraude de Muzo et Coscuez. *Comptes Rendus de l'Académie des Sciences, Paris, Série IIa*, Vol. 323, pp. 705–712 (in French).

Leiper H. (1967) Rare trapiche emerald crystals show unique twinning evidence. *Lapidary Journal*, Vol. 21, No. 4, pp. 565.

London D. (2008) *Pegmatites*. The Canadian Mineralogist, special publication No. 10, Mineralogical Association of Canada, Québec.

Lyckberg P. (2005a) Le béryl héliodore de Karélie (Finlande). *Le Règne Minéral*, Vol. 62, pp. 33–39 [in French].

——— (2005b) Gem beryl from Russia and Ukraine. In *Beryl and Its Color Varieties*, Lapis International Publishing, East Hampton, CT, pp. 49–57.

Mantilla Figueroa L.C., Silva A., Serrano J., Gomez J., Ramirez J., Meza J., Pelayo Y., Ortega L., Plata L., Peña E. (2007) *Investagación petrográfica y geoquímica de las sedimentitas del Cretácico inferior (K1) y sus manifestaciones hidrotermales asociadas; Planchas 169, 170, 189, 190 (Cordillera oriental): imlicacions en la búsqueda de Esmeraldas*. INGEOMINAS informe, Bogotá, Colombia, 330 pp. (In Spanish).

Maya M., Buenaventura J., Salinas R. (2004) *Estado del conocimiento de la exploracion de Esmeraldas en Colombia*. INGEOMINAS informe, Bogotá, Colombia, 89 pp. (In Spanish).

McKague H.L. (1964) Trapiche emeralds from Colombia. *G&G*, Vol. 11, No. 7, pp. 210–223.

Müllenmeister H.J., Zang J. (1995) Ein Trapiche-Rubin aus Myanmar (Burma). *Lapis*, Vol. 20, No. 12, p. 50 (in German).

Nassau K., Jackson K.A. (1970) Trapiche emeralds from Chivor and Muzo, Colombia. *American Mineralogist*, Vol. 55, Nos. 3–4, pp. 416–427.

O'Donoghue M.J. (1971) Trapiche emerald. *The Journal of Gemmology*, Vol. 12, No. 8, pp. 329–332.

Ohnenstetter D., Giuliani G., Bustos O. (1998) Emeraudes trapiches colombiennes. In *L'émeraude*. Connaissances actuelles et prospective. Association Française de Gemmologie, pp. 119–124 (in French).

Oppenheim V. (1948) The Muzo emerald zone, Colombia. *Economic Geology*, Vol. 43, No. 1, pp. 31–38, http://dx.doi.org/10.2113/gsecongeo.43.1.31

Ottaway T.L. (1991) The geochemistry of the Muzo emerald deposit, Colombia. Master's thesis, University of Toronto, Canada.

Ottaway T.L., Wicks F.J., Bryndzia L.T., Kyser T.K., Spooner E.T.C. (1994) Formation of the Muzo hydrothermal emerald deposit in Colombia. *Nature*, Vol. 369, No. 6481, pp. 552–554, http://dx.doi.org/10.1038/369552a0

Pogue J.E. (1916) The emerald deposits of Muzo, Colombia. *Transactions of the American Institute of Mining Engineers*, Vol. 55, pp. 383–406.

Pouchou J.L., Pichoir F. (1991) Quantitative analysis of homogeneous or stratified microvolumes applying the model "PAP." In K.F.J. Heinrich and D.E. Newbury, Eds., *Electron Probe Quantitation*, Springer Science-Business Media, New York, pp. 31–76.

Rakovan J., Kitamura M., Tumada O. (2006). Sakura ishi (cherry blossom stones): Mica pseudomorphs of complex cordierite-indialite intergrowths from Kameoka, Kyoto Prefecture, Japan. *Rocks and Minerals*, Vol. 81, No. 4, pp. 284–292, http://dx.doi.org/10.3200/RMIN.81.4.284-292

Rice A.H.N. (1993) Textural and twin sector-zoning and displacement of graphite in chiastolite and -pyralspite and grandite garnets in the variscides of South-West England. *Read at the Annual Conference of the Ussher Society*, pp. 129–131.

——— (2007) Chemical disequilibrium during garnet growth: Monte Carlo simulations of natural morphologies: Comment. *Geology*, Vol. 35, No. 1, pp. 124–125, http://dx.doi.org/10.1130/G23441C.1

Rice A.H.N., Mitchell J.I. (1991) Porphyroblast textural sector-zoning and matrix displacement. *Mineralogical Magazine*, Vol. 55,

No. 380, pp. 379–396, http://dx.doi.org/10.1180/minmag.1991.055.380.08

Ringsrud R. (2013) *Emeralds: A Passionate Guide*. GVP Publishing, Oxnard, CA.

Rodríguez E.M., Ulloa C.M. (1994) *Plancha 189-La Palma, Bogotá*, Ingeominas, scale 1:1000000.

Roedder E. (1963) Studies of fluid inclusions II: freezing data and their interpretation. *Economic Geology*, Vol. 58, No. 2, pp. 163–211, http://dx.doi.org/10.2113/gsecongeo.58.2.167

Roedder E. (1984) *Fluid Inclusions*. Mineralogical Society of America. Reviews in Mineralogy, Vol. 12, BookCrafters Publisher, Chelsea, MI.

Rondeau B., Fritsch E., Peucat J.-J., Nordrum F.S., Groat L. (2008) Characterization of emeralds from a historical deposit: Byrud (Eidsvoll), Norway. *G&G*, Vol. 44, No. 2, pp. 108–122, http://dx.doi.org/10.5741/GEMS.44.2.108

Scandale E., Zarka A. (1982) Sur l'origine des canaux dans les cristaux. *Journal of Applied Crystallography*, Vol. 15, No. 4, pp. 417–422, http://dx.doi.org/10.1107/S0021889882012291.

Scheibe R. (1926) Die Smaragdlagerstätte von Muzo (Kolombien) und ihre nähere Umberbung. *Neues Jahrbuch für Mineralogie Abhandlungen*, Vol. 54, pp. 419–447 (in German).

Scheibe R. (1933) Informe geológico sobre la mina de esmeraldas de Muzo. *Compilación de los Estudios Geológicos Oficiales en Colombia*, No. 1, pp. 169–198 (in Spanish).

Schiffman C.A. (1968) Unusual emeralds. *Journal of Gemmology*, Vol. 11, No. 4, pp. 105–114.

Schmetzer K., Hänni H.A., Bernhardt H.J., Schwarz D. (1996) Trapiche rubies. *G&G*, Vol. 32, No. 4, pp. 242–250, http://dx.doi.org/10.5741/GEMS.32.4.242

Schmetzer K., Beili Z., Yan G., Bernhardt H.J., Hänni H.A. (1998) Element mapping of trapiche rubies. *Journal of Gemmology*, Vol. 26, No. 5, pp. 289–301.

Schmetzer K., Bernhardt H.J., Hainschwang T. (2011) Chemical and growth zoning in trapiche tourmaline from Zambia – a re-evolution. *Journal of Gemmology*, Vol. 32, No. 5-8, pp. 151–173.

Schwarz D., Schmetzer, K. (2002) The definition of emerald: the green variety of beryl colored by chromium and/or vanadium. In *Emeralds of the World*, ExtraLapis English No. 2: The Legendary green beryl. Lapis International, LLC, East Hampton, CT, pp. 74–78.

Sunagawa I. (1987) Morphology of minerals. In I. Sunagawa, Ed., *Morphology of Crystals, Part B*. Terra Scientific Publishing Company, Tokyo, pp. 509–587.

Sunagawa I. (1999) Growth and morphology of crystals. *Forma*, Vol. 14, pp. 147–166.

Sunagawa I. (2005) *Crystals: Growth, Morphology and Perfection*. Cambridge University Press, Cambridge, UK.

Sunagawa I., Bernhardt H.J., Schmetzer K. (1999) Texture formation and element partitioning in trapiche ruby. *Journal of Crystal Growth*, Vol. 206, No. 4, pp. 322–330, http://dx.doi.org/10.1016/S0022-0248(99)00331-0

Tempesta G., Scandale E., Agrosì G. (2011) Striations and hollow channels in rounded beryl crystals. *Periodico di Mineralogia*, Vol. 79, No.1, pp. 75–87.

Touray J.C., Poirot J.P. (1968) Observations sur les inclusions fluides primaires de l'émeraude et leurs relations avec les inclusions solides. *Comptes Rendus de l'Académie des Sciences*, Paris, Sér. D, Vol. 266, pp. 305–308 (in French).

Tripp E.J., Hernandez L.H. (1970) The complete trapiche emerald picture. The cutting of gems from trapiche crystals. *Lapidary Journal*, Vol. 24, No. 1, pp. 97–104.

Tsuchiyama A., Uesugi K., Nakano T., Ikeda S. (2005) Quantitative evaluation of attenuation contrast of X-ray computed tomography images using monochromatized beams. *American Mineralogist*, Vol. 90, No. 1, pp. 132–142, http://dx.doi.org/10.2138/am.2005.1552

Ulloa C. (1980) Ambiente geológico de los yacimientos esmeraldíferos en Colombia. *Boletín Sociedad Geológica Perú*, Vol. 65, pp. 157–170.

Vuillet P., Giuliani G., Fischer J.C., Chiappero P.J. (2002) Emeraudes de Gachala, Colombie: historique, genèse et découvertes paléontologiques. *Le Règne Minéral*, No. 46, pp. 5–18 (in French).

Ward F. (1993) *Emeralds*. Gem Book Publishers, Bethesda, MD.

White W.B., Masako M., Linnehan D.G., Furukawa T., Chandrasekhar B.K. (1986) Absorption and luminescence of $Fe^{3+}$ in single-crystal orthoclase. *American Mineralogist*, Vol. 71, Nos. 11–12, pp. 1415–1419.

Wilbur D.E., Ague J.J. (2006) Chemical disequilibrium during garnet growth: Monte Carlo simulations of natural crystal morphologies. *Geology*, Vol. 34, No. 8, pp. 689–692, http://dx.doi.org/10.1130/G22483.1

Win K.K. (2005) Trapiche of Myanmar. *Australian Gemmologist*, Vol. 22, No. 6, pp. 269–270.

Wood D.L., Nassau K. (1968) Characterization of beryl and emerald by visible and infrared absorption spectroscopy. *American Mineralogist*, Vol. 53, Nos. 5–6, pp. 777–800.

Yardley B.W.D. (1974) Porphyroblasts and "crystallization force": Discussion of some theoretical considerations. *Geological Society of America Bulletin*, Vol. 85, No. 1, pp. 61–62, http://dx.doi.org/10.1130/0016-7606(1974)85<61:PACFDO>2.0.CO;2

Zwaan J.C., Jacob D.E., Häger T., Cavalcanti Neto M.T.O., Kanis J. (2012) Emeralds from the Fazenda Bonfim region, Rio Grande do Norte, Brazil. *G&G*, Vol. 48, No. 1, pp. 2–17, http://dx.doi.org/10.5741/GEMS.48.1.2

# LARGE COLORLESS HPHT-GROWN SYNTHETIC GEM DIAMONDS FROM NEW DIAMOND TECHNOLOGY, RUSSIA

Ulrika F.S. D'Haenens-Johansson, Andrey Katrusha, Kyaw Soe Moe, Paul Johnson, and Wuyi Wang

The Russian company New Diamond Technology is producing colorless and near-colorless HPHT-grown synthetic diamonds for the gem trade. Forty-four faceted samples synthesized using modified cubic presses were analyzed using a combination of spectroscopic and gemological techniques to characterize the quality of the material and determine the means of distinguishing them from natural, treated, and alternative laboratory-grown diamonds. These samples, with weights ranging from 0.20 to 5.11 ct, had color grades from D to K and clarity grades from IF to $I_2$. Importantly, 89% were classified as colorless (D–F), demonstrating that HPHT growth methods can be used to routinely achieve these color grades. Infrared absorption analysis showed that all were either type IIa or weak type IIb, and photoluminescence spectroscopy revealed that they contained Ni-, Si-, or N-related defects. Their fluorescence and phosphorescence behavior was investigated using ultraviolet excitation from a long-wave/short-wave UV lamp, a DiamondView instrument, and a phosphorescence spectrometer. Key features that reveal the samples' HPHT synthetic origin are described.

I n the last few years, available colorless and near-colorless gem-quality synthetic diamonds have improved dramatically with advances in growth technologies and a heightened understanding of the underlying processes. Although the majority of these products have been grown using the well-established chemical vapor deposition (CVD) technique (see Martineau et al., 2004; Wang et al., 2007; 2012), the high-pressure, high-temperature (HPHT) method, associated more with attractive fancy color samples, has recently emerged as a method for producing sizable colorless and near-colorless synthetic diamonds (D'Haenens-Johansson et al., 2014). The commercial viability of synthetic diamonds depends on a variety of factors, such as desirable colors (or, in this case, the absence of color), clarities, and sizes. Additionally, producers must be able to manufacture a high enough volume to satisfy demand at a price point that makes them competitive with natural diamond and alternative diamond products.

New Diamond Technology (NDT), which together with Inreal and Nevsky Brilliant is part of a Russian diamond group, has grown synthetic diamonds for industrial and technological uses. In the past year, the company has produced large high-quality, colorless samples for the gem trade. NDT says it has developed HPHT technology that enables the growth of multiple synthetic diamonds in different reaction layers within the same cell, resulting in much larger production runs compared to other known methods, reaching up to 200 samples (with cross-sectional sizes of 2.5–3.0 mm) across two layers in a single run. At present, NDT can simultaneously grow up to 16 colorless "rough" crystals approaching 10 ct apiece.
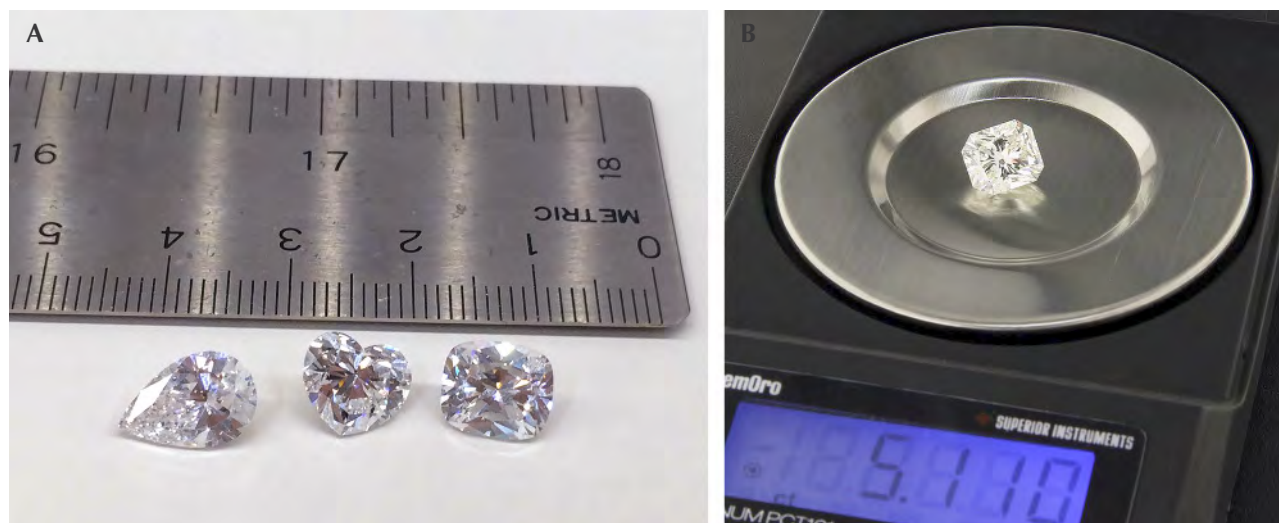
Figure 1. A: These three colorless HPHT-grown synthetic diamonds demonstrate some of the sizes achieved by New Diamond Technology. From left to right, samples NDT04, NDT02, and NDT01 weigh 2.02, 2.20, and 2.30 ct, respectively. Photo by Ulrika D'Haenens-Johansson. B: Sample NDT-A, a 5.11 ct specimen with K color, is the largest faintly colored synthetic diamond studied by GIA to date. The visual characteristics of these samples are summarized in table 1. Photo courtesy of New Diamond Technology.

It was reported in May 2015 that NDT had produced a 32.26 ct "rough" synthetic diamond, which was subsequently faceted into a 10.02 ct square-cut emerald shape and graded by the IGI Hong Kong laboratory as E color and $VS_1$ clarity (International Gemological Institute, 2015). This is believed to be the largest colorless synthetic diamond to date from either HPHT or CVD growth. New Diamond Technology's crystals have the potential to be faceted and polished into gems that are significantly larger than those currently available from other HPHT synthetic producers such as AOTC, which limit their polished sizes to less than 1 ct, usually about 0.5 ct (D'Haenens-Johansson et al., 2014; AOTC, 2015).

In October 2014, NDT loaned GIA a suite of 44 colorless to faintly colored polished gem-quality HPHT-grown synthetic diamonds ranging from 0.20 to 5.11 ct, representative of their 2014 production (see figure 1). The largest of these was reported in February 2015 by *JCK* magazine and by GIA researchers the following month (Bates, 2015; Poon et al., 2015). The 44 samples were comprehensively investigated using both gemological and spectroscopic techniques. Based on the results presented in this study, NDT's lab-grown samples, though often included, achieved excellent colors and could visually match high-quality natural diamonds. Nevertheless, the samples could be readily separated from natural stones by characteristics that arise from their artificial growth conditions.

## BACKGROUND ON HPHT SYNTHETIC DIAMOND GROWTH

Most HPHT growth of single-crystal diamond, irrespective of the press design, is based on the temperature-gradient method first developed by Bovenkerk et al. (1959) for General Electric. The growth capsule is filled with the ingredients necessary for laboratory diamond growth: a source of carbon (such as graphite), a sacrificial diamond "seed" that acts as a template for diamond formation, and a metallic solvent/catalyst (usually Fe, Ni, Co, or their alloys). The catalyst enables diamond growth at lower temperatures and pressures than would be otherwise possible, alleviating some of the technological requirements. The capsule is then exposed to pressures of 5–6 GPa and temperatures of 1300–1600°C. The design of the system creates a temperature gradient, with the source carbon area hotter than the area where the seed is located. Consequently, the carbon is dissolved into the hot molten metal and transferred into the cooler region, where it recrystallizes in the form of synthetic diamond on the seed.

The main focus of HPHT technology development has been to create systems that can reliably produce large volumes of synthetic diamonds with desirable properties for specific technological and industrial needs. Although HPHT diamond synthesis was first achieved in the 1950s, it was only in the 1990s that certain manufacturers started growing samples for the gem and jewelry trade (e.g., Shigley

et al., 1997). Since color-producing dopants such as nitrogen (yellow) or boron (blue) are so easily introduced, these were typically fancy-color synthetics.

Creating colorless HPHT synthetics has been significantly more challenging, as costly modifications to the capsule design are necessary and additional constraints must be placed on the chemical components to minimize dopant uptake, particularly nitrogen. Eliminating contamination in the growth cell is impossible, as trace amounts of nitrogen will likely remain. Thus, growers have to adapt the growth chemistry to intentionally include elements with a strong affinity to nitrogen, termed "nitrogen getters," effectively trapping the nitrogen so it does not disperse through the diamond lattice. Finally, growth rates for high-purity colorless diamond (type IIa or weak type IIb) are significantly lower than for standard type Ib (containing isolated nitrogen) synthetic diamond, necessitating longer growth times and greater control over the temperature and pressure conditions. Consequently, successful near-colorless diamond synthesis depends on the careful design of the HPHT press and its components, the quality and chemical composition of the solvent/catalyst melt,



Figure 2. The anvil arrangement and sample cell for a standard cubic press. Illustration by M. Toosi and U. D'Haenens-Johansson, adapted from Sumiya (2009).

## In Brief

- The Russian company New Diamond Technology (NDT) is producing faceted colorless and near-colorless HPHT-grown synthetic diamonds for the gem trade.
- Eighty-nine percent of the 44 faceted samples, weighing up to 5.11 ct, were classified as colorless. Color and clarity grades ranged from D to K and IF to $I_2$.
- The quality of NDT-produced material is on par with, or surpasses, that by other synthetic diamond growers.
- The samples were conclusively identified as HPHT synthetics using a combination of gemological observations and spectroscopic analysis.

the choice of nitrogen getters, and the ability to control the chemical and thermodynamic conditions across the reaction layer. Further complications result from the need for high crystal quality and minimal inclusion uptake.

### HPHT GROWTH CONSIDERATIONS BY NEW DIAMOND TECHNOLOGY

NDT uses modified cubic HPHT presses to grow gem-quality colorless synthetics, with custom-made

systems designed to stabilize the thermodynamic parameters (pressure and temperature distribution across the sample cell). Figure 2 illustrates the main components of a standard cubic press, which consists of six anvils coupled to independent hydraulic cylinders surrounding a cubic sample cell. Although this design is complicated by the requirement for synchronized motion of separate anvils, it does allow the application of hydrostatic pressure across a relatively large volume cell compared to other press types.

When selecting materials for the cell components of a multi-anvil apparatus, such as a cubic HPHT press, it is necessary to consider their ability to withstand the high-pressure and high-temperature conditions necessary to synthesize diamond with the desired properties. This will depend on both the compressive strength of the materials and component geometries. Generally, the choice of materials is limited to either complex ceramics (Al, Zr, or Mg oxides) or salt-based materials (iodides and chlorides) (Strong, 1977; Satoh et al., 2000; Zhu et al., 2012). Their properties, coupled with the press design, determine the producer's ability to apply long-lasting hydrostatic
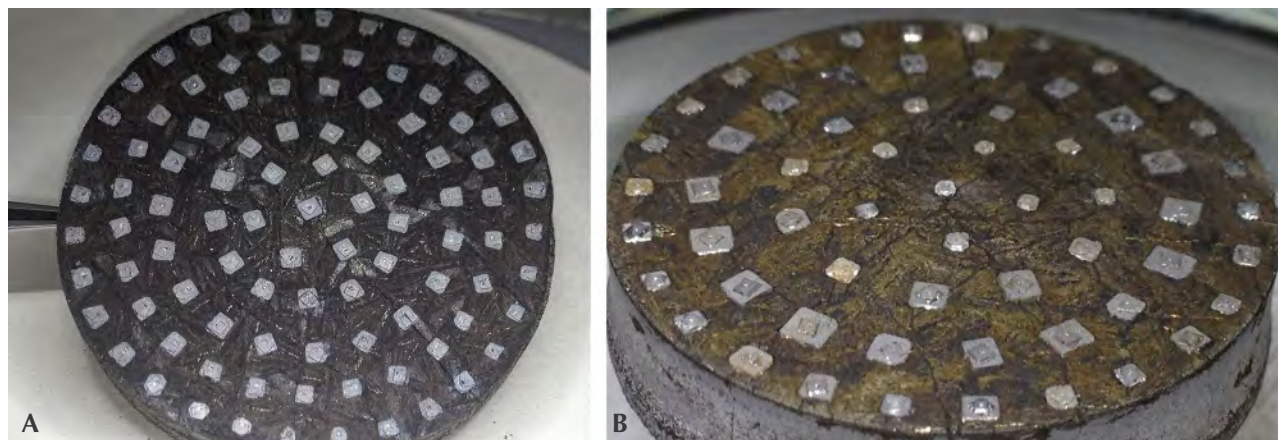
*Figure 3. A: In the multi-seed diamond growth layout on the left, the distribution of the temperature field was ideally controlled across the reaction layer, resulting in even growth sizes for all the samples. B: In the growth layout on the right, the temperature distribution was not optimized. The crystal edge sizes are less than 2 mm. Photos courtesy of New Diamond Technology.*

pressure to the sample cell. If the designs for the cell components are not optimized, they may deteriorate during the HPHT run, hindering the stability of the growth parameters and in turn the synthesis quality. In the worst case, there may be catastrophic failure, with a component breaking. This may lead to costly damage to the equipment in addition to the cost associated with an unsuccessful growth run.

Another prerequisite for successful diamond growth is the precise control of the carbon concentration field, which is determined mostly by the temperature distribution field within the reaction volume of the cell (liquid solvent volume). Computer simulation methods such as FEM (the finite element method) are widely used to model the carbon concentration field, which defines the carbon flow direction, at different thermodynamic conditions as well as for different growth cell designs (Zhan-Chang et al., 2013). It is important to note that the correct prediction of material properties inside the reaction volume, in particular for composites, is greatly complicated by the high pressures and temperatures they are subjected to. Correct control of the temperature distribution (isotherms) inside the cell is also important, especially for layouts containing multiple seeds and/or growth layers. Examples of two separate multiple-seed growth layouts tested by NDT are shown in figure 3. These trials demonstrated that the arrangement in figure 3A resulted in a more even temperature distribution across the reaction volume,

producing higher-quality crystals with more uniform size.

Care must also be taken when selecting the solvent/catalyst constituents contained within the growth cell. The chemical properties of the interaction boundary at the surface of the growing diamond crystal can determine the crystal's morphology, crystalline quality, impurity concentrations, and propensity to trap inclusions. Iron-based solvents, which include Ni and/or Co, are often used for HPHT diamond growth (Strong and Chrenko, 1971). For colorless diamond growth, it is important to suppress the introduction of boron and nitrogen impurities, which generally form color-producing substitutional defects. Traces of boron can be present in either the carbon source or the solvent/catalyst, yet careful selection of high-purity materials (with boron concentrations less than 0.1 ppm) may reduce the boron uptake to the extent that it no longer produces a discernible blue color (Sumiya and Satoh, 1996). Most diamonds will readily incorporate nitrogen present within the growth cell, which can originate from the carbon source, the solvent/catalyst, and gas found in empty spaces or pores of the capsule. This results in a high concentration of isolated nitrogen defects, which impart a yellow color. To produce a colorless diamond, nitrogen getters such as Al, Ti, Zr, or Hf are used (Sumiya and Satoh, 1996). These additives will also influence the growth properties of the material.

Using an Fe-based solvent/catalyst with the addi-

Figure 4. As-grown HPHT diamond single crystals produced using a simple Fe-based solvent with Al as a nitrogen getter. The sample on the far right is the largest, weighing 1.40 ct. Photo courtesy of New Diamond Technology.

tion of only Al results in crystal growth dominated by (100) and (111) faces, as shown in figure 4. While these are simple to facet into gems, NDT says the color grade of material produced through these methods is generally limited to G or poorer. Conversely, adding Co and Ti/Zr to the growth medium stimulates the formation of high-index growth planes such as (113), (110), and (115), yet this material benefits from being colorless (D–F color grades). Unfortunately, the nitrogen getters may react with the carbon source to form carbides, which affect the carbon transport and diffusion properties of the system, decreasing the carbon available for crystal growth. These conditions may result in trapped traces of the metal/catalyst melt, forming visible inclusions. To suppress the development of such inclusions, it may be necessary to (1) introduce additional chemicals such as Cu or (2) decompose the carbides otherwise created by the nitrogen getters (Sumiya and Satoh, 1996; Sumiya et al., 2002). Obtaining sufficiently

pure constituent metals for the solvent/catalyst may be challenging, necessitating additional purification steps by the manufacturer. The identities and incorporation methods for the nitrogen getters and other additives vary for different manufacturers and research teams, and the ultimate mix of solvent/catalyst and getter is often proprietary. NDT claims to have determined the optimal balance of chemical constituents needed to routinely produce gem-quality colorless synthetic diamonds, divulging that their solvent is based on Fe, Co, or a combination of the two.

Orientation of the seed initiation surface also significantly affects the morphology of the grown crystals (figure 5). Using differently oriented seeds—with (110)- or (113)-oriented initiation surfaces, for example—may optimize the growth morphology. To grow a crystal whose top face is (110)- or (113)-oriented, it is not strictly necessary to have a seed with a similarly oriented face, only to have the [110] or [113] di-

Figure 5. The morphology of synthetic diamonds depends largely on the orientation of the seed surface. Photo A shows a reaction layer where the sample in the center and the two outer rings of samples were grown on (100)-oriented seeds. Meanwhile, the samples with triangular outlines (the two inner rings) were grown using (111)-oriented surfaces. The samples shown here are yellow due to the presence of isolated nitrogen. The blue samples shown in (B) and (C) are boron-doped and were grown on (100)- and (111)-oriented substrates, respectively. The samples shown in (B) weigh 0.92 and 0.23 ct, while those in (C) weigh 0.29 and 0.88 ct. Photos courtesy of New Diamond Technology.
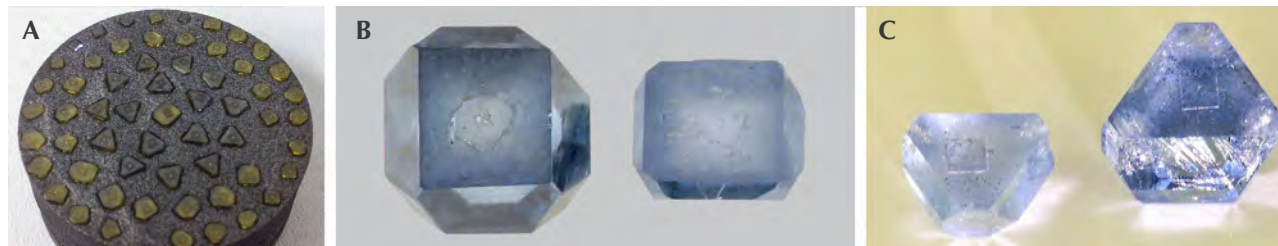
rection vertical in the growth chamber. Since seed crystals are typically cuboctahedral, however, it is easier to orient them in the chamber with either a (100) or (111) face on the top. Consequently, most HPHT diamond growth is conducted on (100)- or (111)-oriented seeds. NDT generally uses the former, which produce crystals with higher cutting yields and more easily polished surfaces.

The growth rate of individual diamond crystals depends on a combination of parameters: the identities and ratios of the chemical constituents used for growth; the thermodynamic conditions; the seed quantity, size, and orientation; the carbon flow rate; and temperature gradient. The quantity of the seeds in a run can greatly impact the growth rate of individual crystals if no additional changes are made to the cell, with an increase in the number of crystals leading to a slower rate. The latter parameter is adjusted by modifying the growth cell layout. When evaluating growth rates quoted by manufacturers, it is important to note that the rate increases nonlinearly with crystal mass. As the crystal grows, the surface area (and hence the deposition area) increases. Yet the deposition rate per unit area (mm/hour) is approximately constant. Consequently, the crystal growth rate (mg/hour) for a given area will rise (Sumiya et al., 2005). Colorless type IIa diamond growth rates as high as 8–10 mg/hour can be achieved using HPHT technology, though such material is generally plagued by metallic inclusions (Sumiya et al., 2005). Limiting the maximum stable growth rate to 6–7 mg/hour has been reported to produce higher-quality growth (Sumiya et al., 2005).

NDT systems can support growth for 200–250 hours, simultaneously yielding up to 16 crystals weighing up to 10 ct each. Further modifications have enabled growth rates up to 30–50 mg/hour—up to five times higher than commonly reported—though maintaining this rate for extended periods is challenging due to the higher pressure and temperature conditions required.

## MATERIALS AND METHODS

For this investigation, NDT loaned GIA 44 colorless to faintly colored HPHT-grown specimens. These samples had been faceted into round brilliant (26) or fancy shapes (18) and weighed 0.20–5.11 ct (table 1; see again figure 1). According to NDT, these samples were grown separately using cubic presses in single-layer runs, and are representative of their 2014 production methods. Because of limited access times, the two largest samples, labeled NDT-A (5.11 ct) and

NDT-B (4.30 ct), underwent fewer tests than the rest of the samples, as specified below.

Color and clarity grading was performed by GIA using standard diamond grading nomenclature. Samples and their internal features were further examined using a standard Gem Instruments binocular microscope system and a Nikon SMZ1500 research microscope under darkfield and fiber-optic illumination. The presence of anomalous birefringence patterns, attributed to strain in the diamond lattice, was evaluated by viewing each sample between crossed polarizing filters using brightfield illumination.

The specimens' fluorescence and phosphorescence response to ultraviolet (UV) light from a conventional four-watt combination long-wave (365 nm) and short-wave (254 nm) lamp was tested in a dark room. The emission intensities were visually compared to the fluorescence of a GIA fluorescence master set. Fluorescence and phosphorescence imaging was conducted using a DTC DiamondView instrument (illumination wavelengths <230 nm), revealing the samples' internal growth structures. An in-house custom-built phosphorescence spectrometer consisting of an Ocean Optics HR4000 spectrometer coupled by fiber optics to an Avantes-DH-S deuterium-halogen light source (operating with only the deuterium light, 215–400 nm) was used to further investigate the samples' phosphorescence at room temperature (see Eaton-Magaña et al., 2007, 2008). Consecutive spectra, each with a one-second integration time, were collected for up to five minutes following 30 seconds of illumination. Samples NDT-A and NDT-B were investigated with the UV lamp and the DiamondView, but phosphorescence spectra were not recorded for them.

To gain an understanding of the impurities present in the samples, Fourier-transform infrared (FTIR) absorption spectra covering the 400–6000 cm$^{-1}$ range were taken using a Thermo Nicolet Nexus 6700 spectrometer furnished with KBr and quartz beam splitters and a diffuse-reflectance infrared Fourier transform (DRIFT) accessory. The instrument and sample chambers were purged with dried air to minimize absorption features stemming from atmospheric water. Spectra were normalized based on the height of the two-phonon absorption in diamond (Palik, 1985), enabling us to calculate the absorption coefficient for comparison and quantitative impurity concentration analysis without having to know the light path length through the samples.

Supplementary analysis of impurity content was provided by photoluminescence (PL) spectra acquired

**TABLE 1.** Gemological properties and calculated bulk concentrations of neutral boron ($B^0$) impurities for 44 HPHT synthetic diamonds produced by New Diamond Technology.

| Sample | Carat weight (ct) | Color | Clarity | Cut | Dimensions (mm) | Type | $B^0$ bulk concentration (ppb) |
|---|---|---|---|---|---|---|---|
| NDT-A | 5.11 | K | $I_1$ | Cut-corner rectangular modified brilliant | 10.05 × 8.74 × 7.01 | IIb | 1.2 ± 0.2 |
| NDT-B | 4.30 | D | $SI_1$ | Cushion | 10.29 × 9.76 × 5.39 | IIb | 7 ± 1 |
| NDT01 | 2.30 | E | $SI_1$ | Cushion | 7.30 × 8.48 × 4.85 | IIa | nd [a] |
| NDT02 | 2.20 | E | $VVS_2$ | Heart | 8.53 × 7.55 × 5.41 | IIb | 20 ± 3 |
| NDT03 | 2.03 | F | $SI_2$ | Heart | 7.73 × 8.41 × 5.07 | IIb | 5 ± 1 |
| NDT04 | 2.02 | D | $I_1$ | Pear | 7.14 × 10.80 × 4.45 | IIb | 6 ± 1 |
| NDT05 | 1.90 | F | $VS_1$ | Octagonal | 7.65 × 7.68 × 4.58 | IIa | nd |
| NDT06 | 1.53 | D | $SI_1$ | Round | 7.18 × 7.26 × 4.60 | IIb | 2.0 ± 0.5 |
| NDT07 | 1.53 | D | $I_1$ | Round | 6.49 × 9.33 × 4.08 | IIb | 13 ± 2 |
| NDT08 | 1.50 | E | $SI_1$ | Round | 7.14 × 7.17 × 4.44 | IIb | 2.6 ± 0.5 |
| NDT09 | 1.41 | D | $VS_2$ | Square emerald | 6.25 × 6.49 × 4.26 | IIa | nd |
| NDT10 | 1.20 | E | $SI_2$ | Round | 6.73 × 6.75 × 4.23 | IIb | 2.5 ± 0.5 |
| NDT11 | 1.13 | D | IF | Round | 6.57 × 6.62 × 4.10 | IIb | 0.8 ± 0.2 |
| NDT12 | 1.04 | E | $SI_2$ | Oval | 5.58 × 7.92 × 3.40 | IIb | 13 ± 2 |
| NDT13 | 1.03 | D | $SI_2$ | Round | 6.39 × 6.47 × 3.99 | IIb | 9 ± 1 |
| NDT14 | 1.02 | F | $SI_1$ | Round | 6.45 × 6.49 × 4.06 | IIb | 58 ± 9 |
| NDT15 | 1.01 | D | $VS_2$ | Oval | 5.64 × 7.79 × 3.35 | IIb | 0.5 ± 0.3 |
| NDT16 | 1.00 | G | I2 | Round | 6.50 × 6.53 × 3.79 | IIb | 6 ± 1 |
| NDT17 | 0.92 | E | $VS_2$ | Round | 6.04 × 6.07 × 3.96 | IIb | 1.6 ± 0.5 |
| NDT18 | 0.90 | D | $VS_1$ | Pear | 5.38 × 7.78 × 3.38 | IIa | nd |
| NDT19 | 0.90 | D | $SI_1$ | Round | 6.15 × 6.18 × 3.78 | IIb | 5 ± 1 |
| NDT20 | 0.81 | D | $VVS_2$ | Round | 5.92 × 5.96 × 3.79 | IIb | 2.5 ± 0.5 |
| NDT21 | 0.80 | D | $VVS_2$ | Round | 6.07 × 6.09 × 3.57 | IIa | nd |
| NDT22 | 0.80 | D | $SI_2$ | Pear | 5.34 × 7.78 × 3.17 | IIb | 9 ± 1 |
| NDT23 | 0.71 | D | $VS_1$ | Round | 5.75 × 5.80 × 3.42 | IIb | 8 ± 1 |
| NDT24 | 0.71 | D | $VVS_1$ | Pear | 5.08 × 7.29 × 2.99 | IIb | 6 ± 1 |
| NDT25 | 0.64 | E | $SI_2$ | Round | 5.43 × 5.46 × 3.53 | IIa | nd |
| NDT26 | 0.58 | H | $I_1$ | Round | 5.43 × 5.46 × 3.53 | IIb | 2.5 ± 0.5 |
| NDT27 | 0.58 | E | $SI_2$ | Oval | 4.89 × 6.49 × 2.75 | IIa | nd |
| NDT28 | 0.54 | E | $SI_1$ | Pear | 4.62 × 6.63 × 2.92 | IIb | 13 ± 2 |
| NDT29 | 0.52 | E | $VS_2$ | Round | 5.09 × 5.11 × 3.31 | IIb | 9 ± 1 |
| NDT30 | 0.51 | D | $VVS_1$ | Round | 5.15 × 5.17 × 3.90 | IIb | 6 ± 1 |
| NDT31 | 0.50 | E | $SI_2$ | Round | 5.08 × 5.12 × 3.10 | IIa | nd |
| NDT32 | 0.48 | D | $VVS_2$ | Round | 5.11 × 5.14 × 3.06 | IIa | nd |
| NDT33 | 0.47 | H | IF | Emerald | 3.93 × 4.71 × 2.67 | IIb | 33 ± 5 |
| NDT34 | 0.43 | F | $I_1$ | Round | 4.78 × 4.80 × 2.99 | IIb | 3.7 ± 0.5 |
| NDT35 | 0.43 | D | $VS_1$ | Pear | 4.38 × 6.22 × 2.66 | IIb | 20 ± 3 |
| NDT36 | 0.38 | F | $I_1$ | Round | 4.70 × 4.73 × 2.83 | IIb | 1.8 ± 0.5 |
| NDT37 | 0.37 | D | $I_1$ | Marquise | 3.90 × 7.64 × 2.24 | IIb | 25 ± 4 |
| NDT38 | 0.31 | E | $VS_2$ | Round | 4.35 × 4.37 × 2.63 | IIb | 18 ± 3 |
| NDT39 | 0.30 | E | $I_2$ | Round | 4.34 × 4.36 × 2.59 | IIb | 1.6 ± 0.5 |
| NDT40 | 0.28 | F | $VVS_2$ | Round | 4.15 × 4.17 × 2.60 | IIb | 13 ± 2 |
| NDT41 | 0.24 | D | $SI_1$ | Round | 4.09 × 4.11 × 2.41 | IIb | 3.3 ± 0.5 |
| NDT42 | 0.20 | G | $VS_1$ | Round | 3.70 × 3.69 × 2.33 | IIb | 33 ± 5 |

[a] "nd" indicates that boron was not detected.

with the samples submerged in liquid nitrogen (77 K, or –196°C) using a Renishaw InVia Raman confocal microspectrometer (Hall et al., 2010). To maximize the effectiveness of stimulating different luminescent defect centers across a wide range of wavelengths, the system was equipped with four laser sources producing six different excitation wavelengths: He-Cd metal vapor (324.8 nm), Ar-ion (457.0, 488.0 and 514.5 nm), He-Ne (632.8 nm), and a diode laser (830.0 nm). Spectra with the 324.8 and 488.0 nm excitations were not collected for samples NDT-A and NDT-B, because of limited access to the instrument.

## RESULTS AND ANALYSIS

**Visual Appearance.** The grading characteristics of NDT's faceted HPHT-grown diamonds are presented in table 1. The samples had carat weights ranging from 0.20 to 5.11 ct, with average and median weights of 1.08 ct and 0.81 ct. There was no clear trend between the cut shapes and sample weights, though it was noted that the six stones weighing over 2 ct were all faceted into fancy shapes. Thirty-nine (89%) of the samples were found to be colorless (D–F), while four attained near-colorless (G or H) grades and the remaining (and largest) sample was a faintly colored K grade. Remarkably, five of the six 2+ ct stones were colorless, and the color zoning often seen in HPHT-grown diamonds was not apparent. There was a wide clarity range for this set of samples: internally flawless (2, or 5%); very, very slightly included (7, or 16%); very slightly included (10, or 23%); slightly included (16, or 36%); and included (9, or 20%). No correlation was observed between sample weight, color, and clarity grade. NDT11 weighed 1.13 ct and achieved D color and IF

clarity grades, marking a major breakthrough in laboratory growth.

Poorer clarity grades generally stemmed from the presence of inclusions, which appeared dark and opaque in transmitted light and gray and metallic in reflected light. These inclusions took a variety of shapes (as demonstrated in figure 6), sometimes within the same sample. Rod-like inclusions were noted to have lengths of up to approximately 1.5 mm, and could be observed singly or in clusters with the inclusions aligned in one direction. Three of the synthetics contained flat plate inclusions with approximately triangular geometry, with thicknesses of about 30 µm and edge dimensions up to approximately 600 µm. Some of the metallic inclusions were irregular in shape. Sufficiently included samples ($VS_2$–$I_2$) were attracted to a strong magnet, depending on the magnet's placement relative to the position of the inclusion. The presence of feathers, occasionally combined with metallic inclusions, also reduced the clarity grades of some samples. The inclusions likely result from entrapped traces of the metallic

*Figure 6. Inclusions observed in some of New Diamond Technology's HPHT synthetic diamonds had a dark metallic appearance, suggesting they were remnants of the metallic solvent/catalyst melt used for growth. The inclusions took a variety of morphologies, including rods (A–D), thin plates (E), and irregular shapes (F). Images A, B, C, D, E, and F were taken for samples NDT16, NDT25, NDT13, NDT12, NDT26, and NDT37, respectively. Photomicrographs by Ulrika D'Haenens-Johansson.*
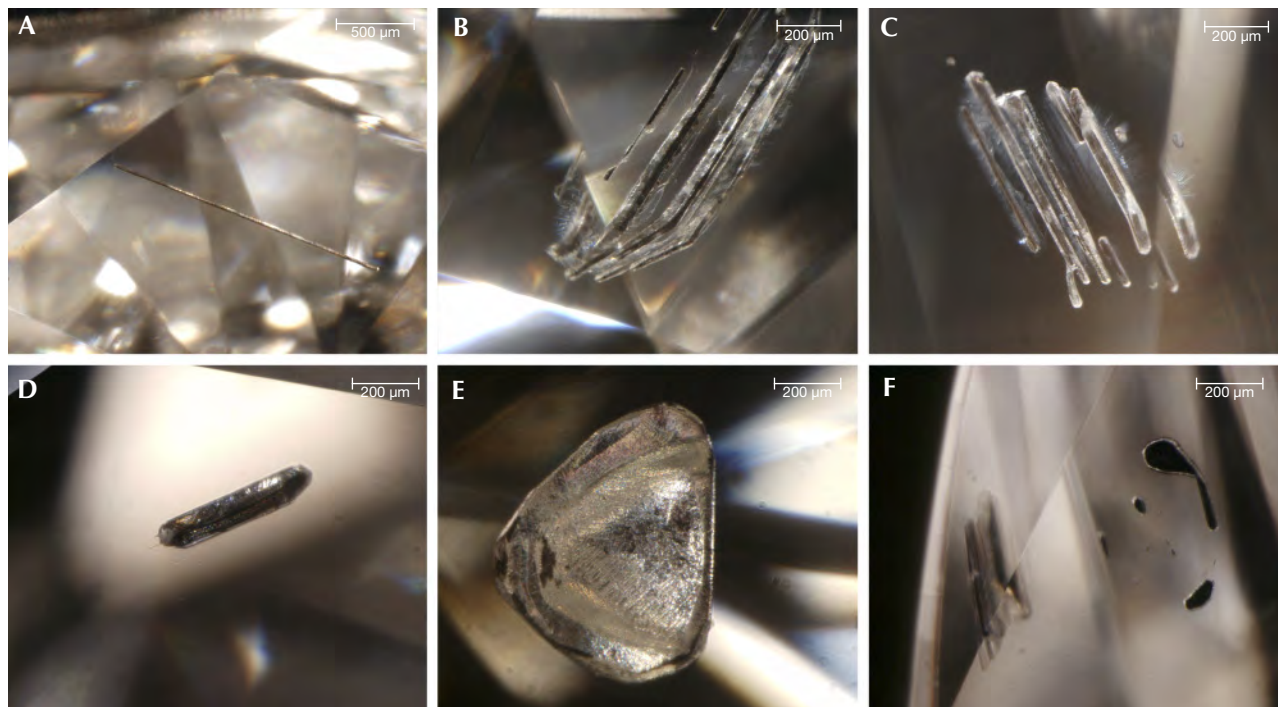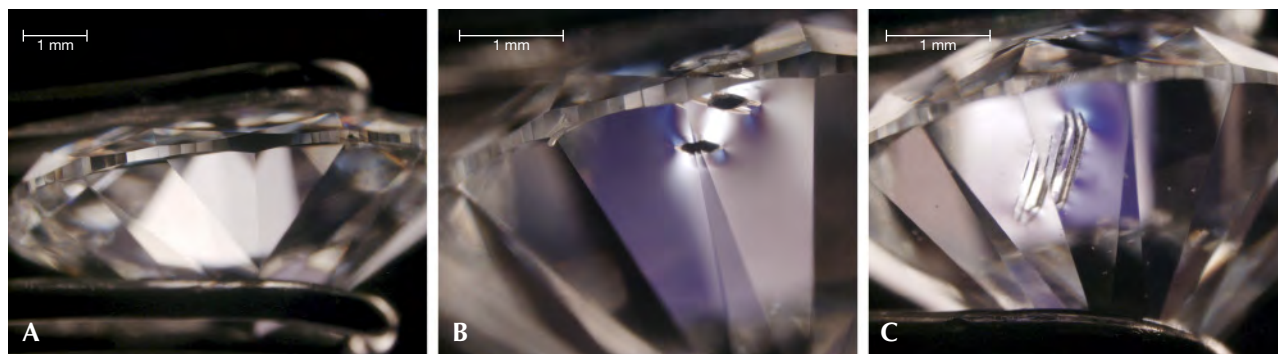
*Figure 7. A: Unincluded sections of the HPHT synthetic samples did not show birefringence patterns when viewed under crossed-polarized light, instead showing smooth gradations in subdued low-order interference colors (grays, purples, and blues), indicating low levels of strain. B and C: Localized distortions in the diamond lattice were only apparent adjacent to inclusions or feathers. These images were taken for samples NDT27, NDT13, and NDT25, respectively. Photomicrographs by Ulrika D'Haenens-Johansson.*

solvent/catalyst melt. Graining, an optical phenomenon whereby a series of transparent, tightly spaced lines can be observed in the sample when viewed from certain directions, has been reported in fancy-color HPHT-grown synthetic diamonds (Shigley et al., 2004) but was not detected in any of the samples in this study.

**Birefringence.** When viewed between crossed polarizers, the samples only showed subdued low-interference colors (grays, blues, and purples) without forming any patterns. This was in stark contrast with natural diamonds in general, which show mottled, banded, or cross-hatched "tatami" patterns in a wider range of colors. These colors, and the absence of a clear pattern, indicate that the synthetic material was characterized by low strain levels, in agreement with previously reported observations (Crowningshield, 1971; Shigley et al., 1997; D'Haenens-Johansson et al., 2014). Localized areas of higher strain were only observed adjacent to inclusions or feathers, where the diamond lattice was distorted to accommodate the clarity feature. Characteristic birefringence effects are shown in figure 7.

**Fluorescence and Phosphorescence Behavior.** The samples' fluorescence and phosphorescence responses to long-wave (365 nm) and short-wave (254 nm) UV illumination from a gem-testing lamp were investigated, with the results summarized in table 2. The majority (38, or 86%) were inert to long-wave UV light, with the remaining samples only emitting very faint yellow-orange fluorescence. The sample set had a stronger response to short-wave (254 nm)

UV illumination, with 41 of them (93%) fluorescing yellow, orangy yellow, or green-yellow, with intensities that were very weak (22), weak (15), medium (2), or strong (1). The remaining three samples (7%) did not fluoresce. After short-wave UV illumination, 43 (98%) of the samples, including two that did not show fluorescence, displayed varying degrees of persistent green, yellowish green, greenish yellow, yellow, or orangy yellow phosphorescence, which could be observed for up to approximately six minutes. Only one sample, NDT30, showed neither fluorescence nor phosphorescence when exposed to either UV emission wavelength from the gem testing lamp. The stronger fluorescence following short-wave UV illumination is characteristic of colorless and near-colorless HPHT synthetic diamonds, the opposite of the behavior seen for natural stones (Crowningshield, 1971; Rooney et al., 1993; Shigley et al., 1997; D'Haenens-Johansson et al., 2014).

The above band-gap energy UV source (<230 nm) from a DiamondView was able to induce blue fluorescence and phosphorescence in all the samples, as illustrated in figure 8. It was crucial to view the samples along several different directions in order to perceive the cuboctahedral growth patterns characteristic of HPHT synthetic diamonds (Welbourn et al., 1996; D'Haenens-Johansson et al., 2014). The patterns were usually most clear when viewed along the pavilion, rather than with the sample oriented face-up. The patterns, which arose from the different impurity uptake efficiencies for the separate growth sectors, showed poor contrast due to the high purity levels of the samples.

**TABLE 2.** Fluorescence and phosphorescence behavior of the HPHT synthetics under different excitation sources.

| Sample | Long-wave (365 nm) UV gem lamp illumination response | | Short-wave (254 nm) UV gem lamp illumination response | | Phosphorescent emission following broadband illumination | |
|---|---|---|---|---|---|---|
| | Fluorescence | Phosphorescence | Fluorescence | Phosphorescence | 500 nm | 575 nm |
| NDT-A | None | None | Strong yellow-green | Medium green-yellow | N/A* | N/A |
| NDT-B | None | None | Strong yellow-green | Strong green-yellow | N/A | N/A |
| NDT01 | None | None | Weak green | Weak yellow | ✓ | ✕ |
| NDT02 | None | None | Weak green | Weak yellow | ✓ | ✕ |
| NDT03 | Very weak yellow-orange | Very weak yellowish orange | Weak green | Weak yellow | ✓ | ✓ |
| NDT04 | None | None | Weak green | Very weak yellow | ✓ | ✕ |
| NDT05 | None | None | Weak green | Weak yellow | ✓ | ✕ |
| NDT06 | Very weak yellow-orange | Very weak yellowish orange | Weak yellowish green | Weak yellow | ✓ | ✓ |
| NDT07 | None | Weak yellowish orange | Weak green | Weak yellow | ✓ | ✕ |
| NDT08 | Very weak yellow-orange | Weak yellowish orange | Weak yellowish green | Weak yellow | ✓ | ✓ |
| NDT09 | None | None | Weak green | Very weak yellow | ✓ | ✕ |
| NDT10 | Very weak yellow-orange | Weak green | Weak green | Weak yellow | ✓ | ✓ |
| NDT11 | None | None | Weak green | Very weak yellow | ✓ | ✕ |
| NDT12 | None | Weak yellowish orange | Weak green | Weak yellow | ✓ | ✕ |
| NDT13 | None | None | Weak green | Very weak yellow | ✓ | ✕ |
| NDT14 | None | Very weak yellowish orange | Weak green | Very weak yellow | ✓ | ✓ |
| NDT15 | None | None | Very weak yellowish green | Very weak yellow | ✓ | ✕ |
| NDT16 | Very weak yellow-orange | Very weak yellowish orange | Weak yellowish green | Weak yellow | ✓ | ✓ |
| NDT17 | None | Weak yellowish orange | Weak green | Weak yellow | ✓ | ✓ |
| NDT18 | None | None | Weak green | Very weak yellow | ✓ | ✕ |
| NDT19 | Very weak yellow-orange | None | Weak green | Very weak yellow | ✓ | ✕ |
| NDT20 | None | Very weak yellowish orange | Very weak green | Very weak yellow | ✓ | ✓ |
| NDT21 | None | None | Weak green | Very weak yellow | ✓ | ✕ |
| NDT22 | None | None | Weak green | Very weak yellow | ✓ | ✕ |
| NDT23 | None | None | Very weak green | Very weak yellow | ✓ | ✕ |
| NDT24 | None | Very weak yellowish orange | Weak green | Very weak yellow | ✓ | ✕ |
| NDT25 | None | None | Very weak green | Very weak yellow | ✓ | ✕ |
| NDT26 | None | None | Weak yellowish green | Weak yellow | ✓ | ✕ |
| NDT27 | None | None | Weak green | Weak yellow | ✓ | ✕ |
| NDT28 | None | Very weak yellowish orange | Weak green | Weak yellow | ✓ | ✓ |
| NDT29 | None | None | Very weak greenish yellow | Very weak orangy yellow | ✓ | ✓ |
| NDT30 | None | None | Very weak yellow | None | ✓ | ✕ |
| NDT31 | None | None | Weak orangy yellow | Very weak Yellow | ✓ | ✕ |
| NDT32 | None | None | Weak green | Very weak yellow | ✓ | ✕ |
| NDT33 | None | None | Medium green | Medium yellow | ✓ | ✕ |
| NDT34 | None | None | None | None | ✓ | ✓ |
| NDT35 | None | None | Very weak green | Very weak yellow | ✓ | ✕ |
| NDT36 | None | None | Very weak yellowish green | Very weak yellow | ✓ | ✕ |
| NDT37 | None | Very weak yellowish orange | Very weak green | Very weak yellow | ✓ | ✕ |
| NDT38 | None | None | Very weak yellowish green | Very weak yellow | ✓ | ✕ |
| NDT39 | None | None | Very weak orangy yellow | Very weak yellow | ✓ | ✕ |
| NDT40 | None | None | Weak yellow | Weak yellow | ✓ | ✓ |
| NDT41 | None | None | Very weak greenish yellow | None | ✓ | ✕ |
| NDT42 | None | None | Medium yellowish green | Medium yellow | ✓ | ✕ |

*N/A: Not analyzed.

The phosphorescence behavior of samples NDT01–NDT42 (totaling 42) was further investigated by collecting phosphorescence spectra at room temperature following broadband illumination (215–400 nm), collecting spectra every second with 1 second integration times. All the samples emitted blue light centered at approximately 500 nm (2.5 eV), with 13 (31%) of the specimens also showing a yellow phosphorescence band centered at about 575 nm (2.1 eV), as listed in table 2. Figures 9A and B demonstrate representative spectra for samples showing phosphorescence only from the 500 nm band (NDT37) or
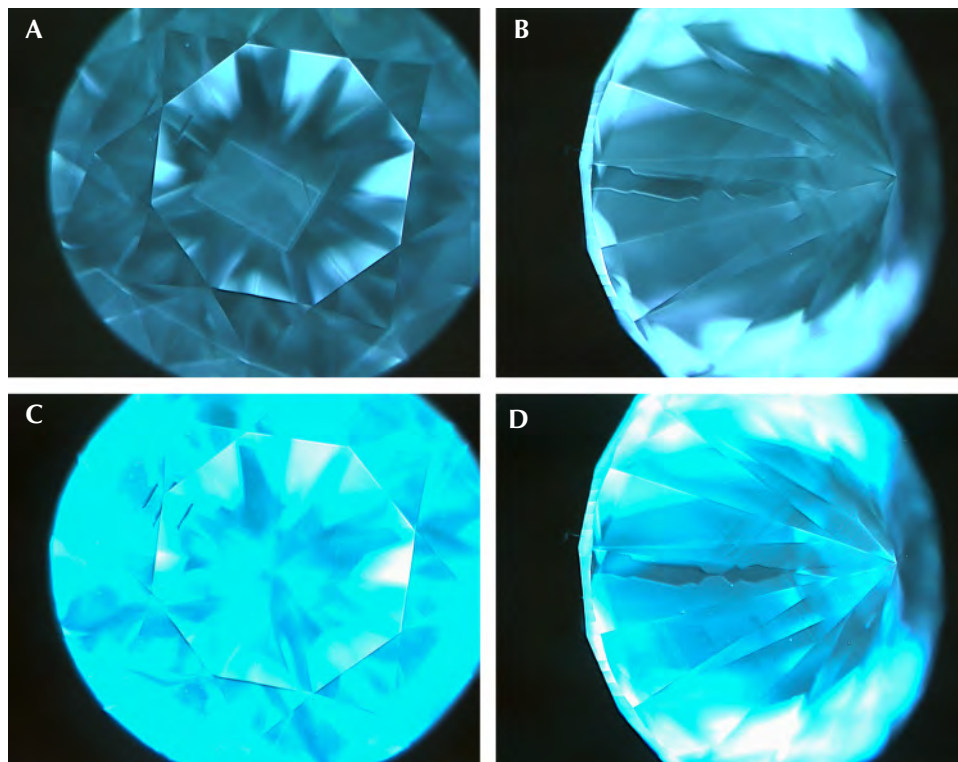
*Figure 8. Blue fluorescence (A–B) and phosphorescence (C–D) were detected for all the New Diamond Technology synthetics observed with the DiamondView. Most of the samples showed cuboctahedral growth patterns characteristic for HPHT synthetics, though they were not always easily observed. The fluorescence and phosphorescence (following a 0.10 second delay) images found here were taken for sample NDT06 with 0.12 and 1.00 second exposures, respectively. Images by Ulrika D'Haenens-Johansson.*

from both the 500 nm and 575 nm bands (NDT08). Phosphorescent emission at 500 nm is commonly observed in natural type IIb or weakly boron-containing type IIa diamonds, as well as similarly typed HPHT synthetic diamonds grown using a variety of solvent/catalyst melts (Watanabe et al., 1997; Eaton-Magaña et al., 2008; Eaton-Magaña and Lu, 2011; D'Haenens-Johansson et al., 2014), whereas the 575 nm band has been detected for HPHT synthetic type IIb diamonds grown using Co- and Ti-containing solvent/catalysts (Watanabe et al., 1997; Eaton-Magaña et al., 2008). A band at 580 nm has been observed in some natural type IIb diamonds, yet this band is generally very weak and rapidly decaying, making its observation rare. Neither of these bands have been reported for phosphorescent CVD synthetics (Wang et al., 2012). The 500 and 575 nm bands are induced following illumination with wavelengths less than approximately 400 nm (>3.1 eV) and 540 nm (>2.3 eV), respectively, and are thought to originate from donor-acceptor pair recombination between boron acceptors and donors, where the identity of the donor(s) is still being questioned (Watanabe et al., 1997). The main candidate for the 500 nm band is a nitrogen-related center, possibly isolated nitrogen, as it is likely present in all the types of natural and synthetic diamonds for which this phosphorescence is observed (Dean, 1965, 1973; Klein et al., 1995;

Watanabe et al., 1997). The donor for the 575 nm band is much less certain (Watanabe et al., 1997). If one assumes the same donor for both bands, the energy separation between the 500 nm and 575 nm bands cannot be simply explained by a distance distribution between the donors and acceptors. Instead, it is possible that the two bands involve distinct deep donors. The donor for the 575 nm band may be a different nitrogen-related center, or even a center consisting of an impurity atom with or without nitrogen. Watanabe et al. (1997) noted that the 575 nm band was mainly emitted from regions close to the seed crystal, where faster growth rates were suspected, suggesting a higher probability of incorporating impurities from the solvent/catalyst.

Comparison of the decay of the 500 nm and 575 nm bands for the NDT samples (e.g., figure 9) revealed that the latter band is longer-lived, in agreement with published results (Watanabe et al., 1997). Consequently, the samples' phosphorescence was noted to shift from blue to yellow following illumination with the spectrometer's light source. Revisiting the samples' phosphorescence behavior under the UV gem lamp (table 2), those that displayed the most intense 575 nm bands (relative to the 500 nm band) often exhibited yellowish orange phosphorescence following long-wave (365 nm) excitation. Both the long- and short-wave UV lamps generated suffi-

## PHOSPHORESCENCE SPECTRA
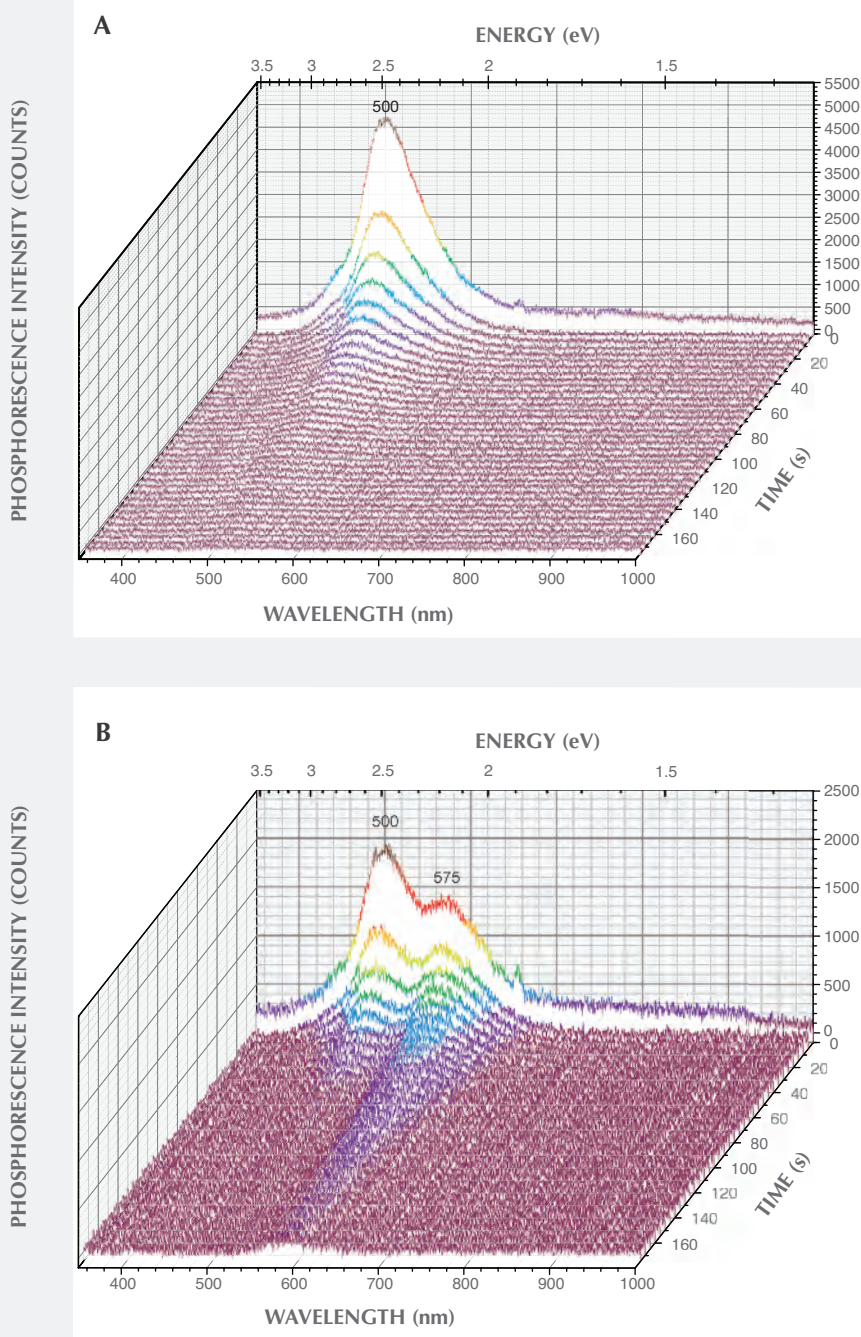


Figure 9. Room-temperature phosphorescence spectra were collected at room temperature for HPHT synthetic samples NDT01–NDT42. All 42 showed phosphorescence following illumination with broadband UV light (215–400 nm); here the spectra for the representative samples NDT37 (A) and NDT08 (B) are shown. For clarity, data is only presented for five-second intervals, even though data was collected every second. A phosphorescent emission band was detected at 500 nm for all specimens (A and B), with an additional band centered about 575 nm being observed for 13 (31%) of the samples (B). For the cases where both bands were detected, it was noted that directly following illumination, the 500 nm band dominated, with the 575 nm band displayed as a shoulder. The 575 nm band had a slower decay, and its emission could be observed even after the 500 nm emission had decayed beyond detection.

ciently high energy to induce phosphorescence from both bands (Watanabe et al., 1997).

The phosphorescence duration is affected by both the maximum phosphorescence intensity, which can be influenced by the size of the stone, and the rate of decay for the emission band(s). Since phosphorescence spectra were collected, it was possible to determine the half-life ($\tau$) of the phosphorescence, or

**PHOSPHORESCENCE DECAY**

□ 500 nm band (NDT37), τ = 9.16 ± 0.06 s

○ 500 nm band (NDT08), τ = 8.55 ± 0.07 s

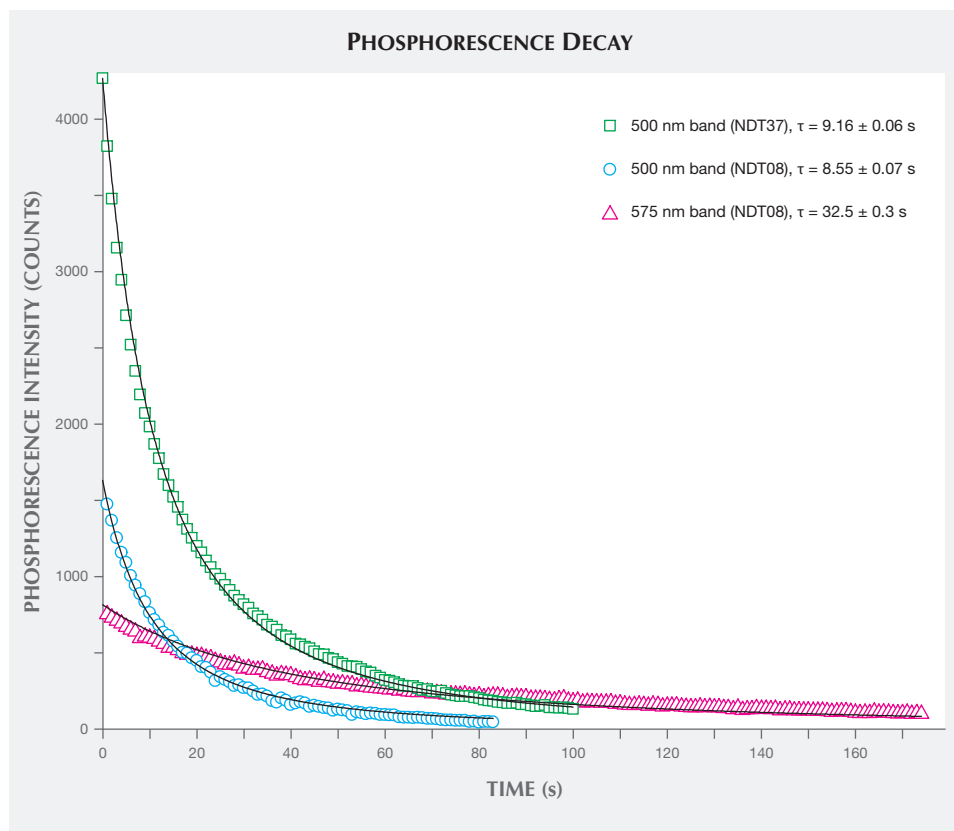△ 575 nm band (NDT08), τ = 32.5 ± 0.3 s

*Figure 10. Phosphorescence intensity as a function of time for the 500 and 575 nm bands for samples NDT37 and NDT08. The circle, square, and triangle data points were determined from the experimental data presented in figure 9. The lines illustrate the fits obtained to these data using least-squares fitting based on the hyperbolic function expressed by equation 2, from which the half-life values τ were calculated using equation 3.*

the time it took for the bands' intensities to halve. Importantly, the half-life is a measure that is independent of the initial phosphorescence intensity. The shape of the decay curve (the maximum band intensity as a function of time) can also provide information regarding the mechanism responsible for the phosphorescence. Figure 10 presents the phosphorescence decay data for the 500 and 575 nm bands for samples NDT08 and NDT37, selected for their intense phosphorescence. The bands' maximum intensities were estimated by fitting Voigt functions to the intensity data plotted as a function of energy, where energy $E$ (in eV) and the wavelength $\lambda$ (in meters) are related by

$$E = \frac{hc}{\lambda} \qquad (1)$$

where $h$ is Planck's constant ($4.13566733 \times 10^{-15}$ eVs) and $c$ is the speed of light ($2.99792458 \times 10^8$ m/s). The phosphorescence intensity as a function of time $I(t)$ was best modeled using a hyperbolic function

$$I(t) = \frac{I(0)}{(1+kt)^2} \qquad (2)$$

where $t$ is the time following the extinction of the illumination, $I(0)$ is phosphorescence intensity at $t = 0$, and $k$ parameterizes the phosphorescence recombination (Watanabe et al., 1997). The observation that a hyperbolic "bimolecular" curve fit better than an exponential decay is consistent with the donor-acceptor pair recombination mechanism that has been used to explain the phosphorescence of diamond (Watanabe et al., 1997). The least-squares fits to the data, as illustrated in figure 10, provided estimates for $k$. Setting $I(t)/I(0) = \frac{1}{2}$ and rearranging equation 2, the half-life is then defined by

$$\tau = \frac{\sqrt{2}-1}{k} \qquad (3)$$

Thus the half-life for the 500 nm phosphorescence band for sample NDT37 (one-band emission) was calculated to be 9.16 ± 0.06 s. In sample NDT08 (two-band emission), the half-life was 8.55 ± 0.07 s for the 500 nm band and 32.5 ± 0.3 s for the 575 nm band.

**FTIR Absorption Spectroscopy.** FTIR spectroscopy was used to evaluate the samples' boron- and nitro-
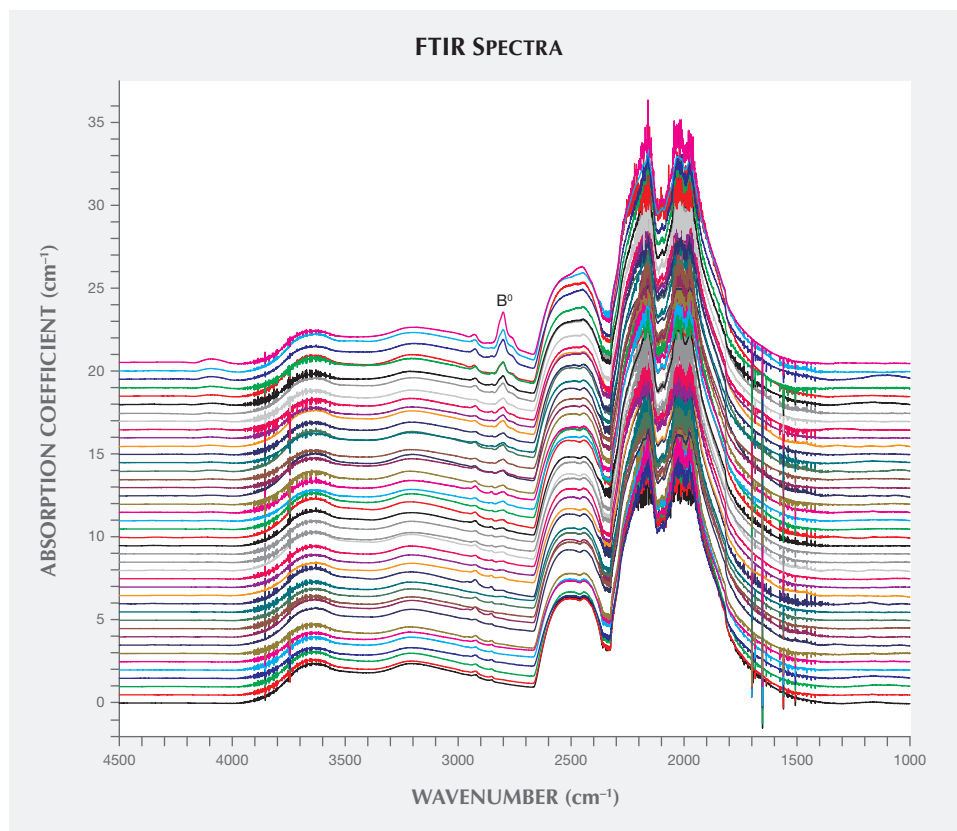
**FTIR Spectra**

*Figure 11. FTIR absorption spectroscopy revealed that 35 (80%) of the 44 synthetic diamonds contained detectable concentrations of neutral substitutional boron ($B^0$), with a characteristic absorption band centered at about 2800 cm⁻¹, and were thus classified as type IIb. Bulk $B^0$ concentrations for these synthetics are tabulated in table 1. The remaining samples did not show any boron- or nitrogen-related IR absorption and were classified as type IIa. The spectra are translated vertically for clarity. Traces for samples NDT-A and NDT-B are not shown due to poorer signal-to-noise ratio.*

gen-related impurity content, with the resulting spectra shown in figure 11. For 35 (80%) of the HPHT synthetics, the only defect-related IR absorption seen was from neutral substitutional boron defects, which create an asymmetric absorption band at approximately 2800 cm⁻¹, resulting in a type IIb classification. Boron incorporation has been found to be growth sector–dependent in HPHT synthetic diamonds, with higher concentrations observed in {111} growth sectors (Burns et al., 1990). Consequently, the boron distribution across these multi-sector samples (as seen using DiamondView imaging) was also inhomogeneous. Their faceting made it impossible to conduct FTIR absorption experiments through single growth sectors. Nevertheless, to enable semi-quantitative comparison of the boron content between samples, bulk boron concentrations across complete volumes were calculated using the integrated intensities of the 2800 cm⁻¹ band (Collins and Williams, 1971; Fisher et al., 2009). These results are tabulated in table 1, with bulk neutral boron concentrations up to 58 ± 9 ppb detected (NDT14, F color). The detection of boron is consistent with the phosphorescent behavior previously discussed. The remaining samples were assigned as type IIa because they did not

show any defect-related absorption features. As these samples also exhibited identical phosphorescence, it is suggested that they contain boron centers at concentrations below the FTIR detection limit. It is important to note that these spectra are not unique to these samples, as colorless natural diamonds and HPHT- and CVD-grown synthetics can also be type IIa or type IIb.

**Photoluminescence Spectroscopy.** Photoluminescence spectra were collected for the samples immersed in liquid nitrogen (77 K) using excitation wavelengths of 324.8, 457.0, 488.0, 514.5, 632.5, and 830.0 nm, enabling the detection of defects that emit light from within the ultraviolet to infrared range. Data using the 324.8 and 488.0 nm lasers were not collected for samples NDT-A and NDT-B. Overall, the peaks reported here were generally weak, often detected only if the laser power was high enough to saturate the diamond Raman peak. Samples NDT21, NDT26, NDT33, NDT34, and NDT42, accounting for 11% of the suite, did not reveal any defect-related photoluminescence features.

The dominant photoluminescence features observed were nickel-related, with the 830.0 nm laser
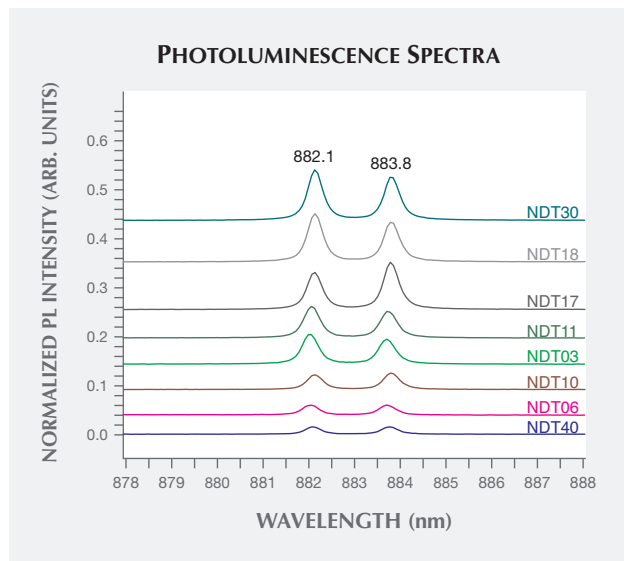
**PHOTOLUMINESCENCE SPECTRA**

*Figure 12. Representative photoluminescence spectra taken at liquid-nitrogen temperatures using 830.0 nm laser excitation revealed a Ni-related defect that produces a doublet with peaks at 882.1 and 883.8 nm in 32 (73%) of the New Diamond Technology samples. This doublet is thought to originate from the same Ni-related center that produces a doublet commonly reported at 1.4035/1.4008 eV (883.15/884.85 nm) for synthetic diamonds grown using Ni-containing solvent/catalyst melts. It is possible that the apparent energy shift resulted from an instrument calibration error. The 830.0 nm laser did not excite any other defect-related features. Once normalized to the unsaturated diamond Raman peak height, the spectra have been translated vertically for clarity.*



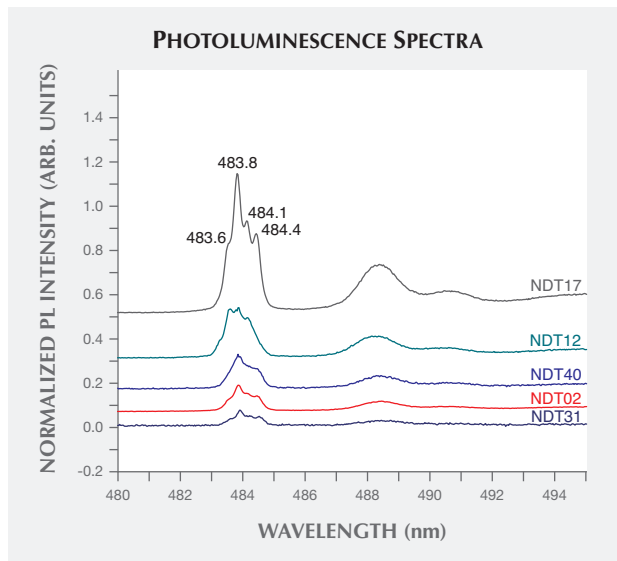**PHOTOLUMINESCENCE SPECTRA**

*Figure 13. For 27 of the 42 samples, photoluminescence spectra collected at liquid-nitrogen temperatures using excitation from a 324.8 nm laser showed a multiplet with peaks at 483.6/483.8/484.1/484.4 nm. This feature is commonly thought to originate at a Ni-related center. For clarity, the Raman-normalized spectra for only five representative samples are shown, translated vertically to avoid overlap.*

exciting a doublet at 882.1/883.8 nm (1.405/1.402 eV) in 32 samples (73%) and the 324.8 nm laser exciting a multiplet with lines at 483.6/483.8/484.1/484.4 nm (2.563/2.562/2.560/2.559 eV) in 27 samples. No comment can be made about whether samples NDT-A and NDT-B would show the latter multiplet, as no data was collected with the 324.8 nm excitation. Representative spectra, with the peak intensities normalized to the intensity of the unsaturated Raman peaks, are shown in figures 12 and 13. The 882.1/883.8 nm doublet is thought to be the one previously reported at 1.4035/1.4008 eV (883.15/884.85 nm), which is often referred to as the "1.40 eV center" (e.g., Nazaré et al., 1991; Yelisseyev and Kanda, 2007) where the shift in wavelength may be related to an instrument calibration error. The model for the 1.40 eV center is an interstitial Ni$^+$ atom distorted along a $\langle 111 \rangle$ direc-

tion (Nazaré et al., 1991). The separation of the peaks has been found to increase with increasing linewidths, suggesting that it is affected by strain levels. The 1.40 eV center is active in both photoluminescence and absorption, and is found exclusively in the {111} growth sectors in HPHT synthetic diamonds grown in the presence of Ni (Collins et al., 1990; Nazaré et al., 1991; Collins, 1992; Lawson and Kanda, 1993). Similarly, the 483.6/483.8/484.1/484.4 nm multiplet, also known as the "484 nm" or "2.56 eV" center, is commonly observed with photoluminescence in the {111} growth sectors of HPHT synthetic diamonds grown using Ni-based solvent/catalysts. Hence, it is also thought to be Ni-related, though its structure has yet to be determined (Dean, 1965; Collins et al., 1990; Collins, 1992; Nazaré et al., 1995). These nickel-related features indicate the presence of Ni in the solvent/catalyst melt used by NDT, intentional or otherwise.

Nitrogen-related features were only observed in the form of nitrogen-vacancy centers in the neutral (NV$^0$) and negative (NV$^-$) charge states with zero-phonon lines (ZPLs) at 575 (2.156 eV, not to be con-

fused with the phosphorescence band) and 637 nm (1.945 eV), respectively. These could be detected using either the 488.0 nm (not shown) or 514.5 nm lasers; figure 14 shows representative data using the latter excitation source. The features were weak, generally detectable only when the laser power was high enough to saturate the diamond Raman peak. The NV$^0$ ZPL, often more intense than that for NV$^-$, was detected in 26 (59%) of the samples. The NV$^-$ ZPL was only seen in 11 (25%) samples. These features are common in both synthetic (type IIa and IIb) and natural (type IIa) diamonds. A feature at 503.2 nm (2.463 eV), possibly the H3 (N-V-N$^0$) defect, was not detected in any of the NDT synthetics using either 457.0 or 488.0 nm lasers. This feature was previously observed in near-colorless HPHT synthetics produced by AOTC (D'Haenens-Johansson et al., 2014).

The only remaining defect-related photoluminescence feature observed was the negative charge state

Figure 14. Twenty-six of the samples showed photoluminescence features attributed to nitrogen-vacancy centers, with the neutral (575 nm) charge state more intense than the negative (637 nm) charge state. These could be detected using either 488.0 or 514.5 nm laser excitation. These selected photoluminescence spectra, taken at liquid-nitrogen temperatures using 514.5 nm excitation, have been translated vertically for clarity. R is the first-order Raman peak for diamond, the broad structure spanning 580–596 nm is the second-order Raman spectrum for diamond, and the sharp peak at 584.5 is the first-order Raman peak for liquid nitrogen, which is used to cool the samples.
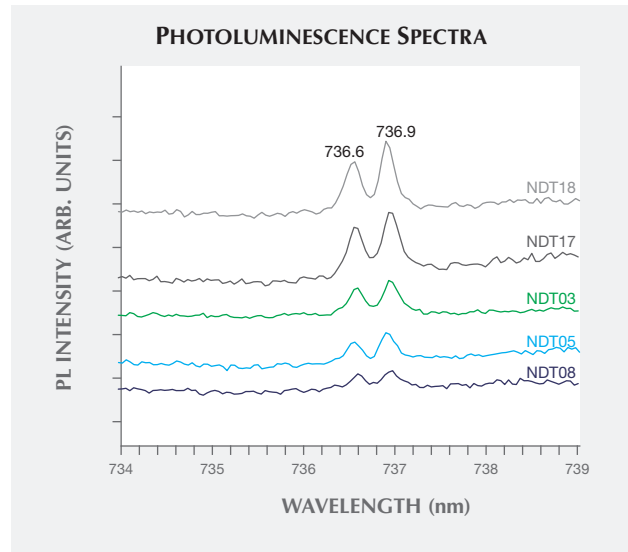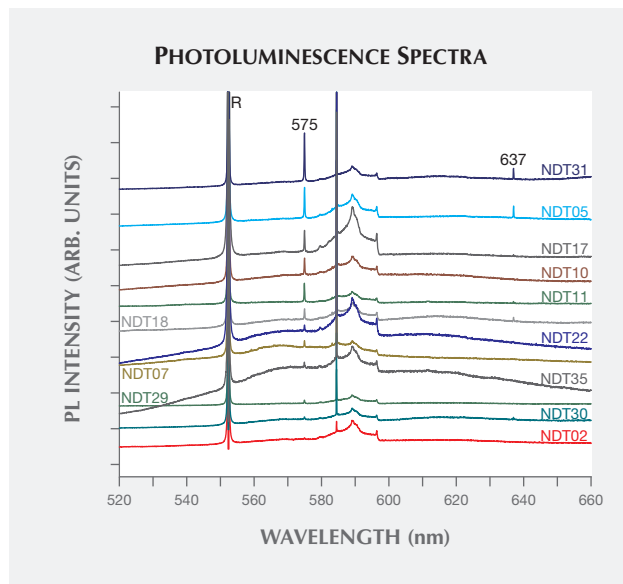


**PHOTOLUMINESCENCE SPECTRA**



Figure 15. The negatively charged silicon-vacancy center, SiV$^-$, with emission at 736.6 and 736.9 nm, was weakly detected in 18 (41%) of the New Diamond Technology samples when using either 488.0, 514.5, or 633.0 nm laser excitation at liquid-nitrogen temperatures. The selected spectra presented here have been translated vertically for clarity.

of the silicon-vacancy center, SiV$^-$, which introduced a weak doublet ZPL at 736.6/736.9 nm (1.683/1.682 eV). SiV$^-$, which could be excited by the 488.0, 514.5, or 632.5 nm lasers (figure 15), was detected in 18 (41%) of the samples. Its presence is rare in HPHT synthetic diamonds, though it has been reported in intentionally doped samples studied by Clark et al. (1995) and Sittas et al. (1996), as well as in gem-quality HPHT synthetic samples of unknown origin (Moe and Wang, 2010; Wang and Moe, 2012) and those produced by AOTC (D'Haenens-Johansson et al., 2014). The low concentrations suggest that its presence may be unintentional.

It is noteworthy that some of the PL features that were weakly detected in several of the colorless and near-colorless HPHT synthetic diamonds grown by AOTC—with peaks at 658 (1.884 eV), 675.2 (1.836 eV), 706.9 (1.753 eV), 709.1 (1.748 eV), and 712.2 nm (1.740 eV)—were not observed in the samples produced by NDT (D'Haenens-Johansson et al., 2014). For the AOTC samples, these peaks were seen for diamonds grown in either BARS or toroid presses, which used different solvent/catalyst melts and nitrogen getters.

## DISCUSSION

**Comparison with Other Gem-Quality Synthetics.**
Near-colorless and colorless synthetic diamonds of gem quality are produced using HPHT or CVD growth methods, with CVD material the most commonly encountered "white" synthetic diamond seen at GIA's laboratory. In recent years, advances in CVD growth methods and the introduction of post-growth decolorizing HPHT treatments have led to the rapid evolution of synthetic diamond quality. Production of colorless synthetics in modest sizes (approximately 0.30 ct) began around 2007 (Wang et al., 2007); by 2011, high-clarity samples weighing approximately 1 ct were widely available (Wang et al., 2012). While the size of CVD synthetics has continued to increase, the colors have been generally limited to near-colorless or faintly colored, and colorless grades are rare (Wang et al., 2013; Pure Grown Diamonds, 2015; Washington Diamonds Corp., 2013; D.NEA, 2015). The largest near-colorless CVD synthetic reported to date is a 3.16 ct sample with G color and $SI_1$ clarity, produced by Washington Diamonds Corp. (D.NEA, 2015), which was graded by a laboratory other than GIA. The record had previously been held by a 3.04 ct, I color, and $SI_1$ clarity CVD synthetic by Pure Grown Diamonds (formerly Gemesis), also graded by a non-GIA laboratory (Pure Grown Diamonds, 2014).

Conversely, HPHT growth for the gem trade was geared mainly toward fancy-color synthetic diamonds. Colorless gem-quality material has only been commercially available since 2012 (D'Haenens-Johansson et al., 2012, 2014). The main HPHT synthetic diamond producer in this sector is AOTC, whose colorless synthetics are polished to sizes up to 1 ct (AOTC, 2015). Although the D-Z diamond colors achieved by HPHT producers are typically closer to colorless than those by CVD producers, their material is generally smaller and may be visibly included. Outside of the gem industry, HPHT synthetic diamond producers such as Sumitomo Electric have reported growing 7–8 ct "rough" crystals described as "colorless" type IIa, though their material is intended for technological applications (Sumiya et al., 2002). If one further expands the search field to include unpolished colored HPHT synthetics, the largest reported in the literature is a 34.80 ct "yellow" specimen, grown solely for research purposes by De Beers (Koivula et al., 2000).

NDT's HPHT-grown synthetic gem diamonds in this investigation mark a dramatic improvement in the combination of colors and sizes attainable. Five colorless samples weighed over 2 ct, with clarities ranging from $VVS_2$ to $I_2$ (though this improved up to IF for smaller sizes). The 4.30 ct D-color, $SI_1$ clarity specimen (NDT-B) is the largest faceted laboratory-grown diamond of this color grade available to date (also reported by Poon et al., 2015), surpassing the largest CVD synthetic in both size and color known to the authors (while sharing the same clarity grade) (D.NEA, 2015). Although not studied for this investigation, a 10.02 ct E-color, $VS_1$ square-cut emerald HPHT-grown synthetic (graded by IGI), also by NDT, is so far the largest reported polished synthetic diamond grown using either HPHT or CVD technologies, of any color grade (International Gemological Institute, 2015; Wang and Moses, 2010; Poon et al., 2015; N.DEA, 2015). These results suggest that HPHT synthetic colorless gem-quality diamonds are now on a par with, and could potentially surpass, those produced by CVD methods.

Interestingly, AOTC uses both BARS and toroid presses, while NDT uses cubic presses (D'Haenens-Johansson et al., 2014). This demonstrates that different HPHT methodologies can yield comparable products, with NDT's cubic press methods currently yielding larger specimens. Like the AOTC synthetics, most of the NDT samples (80%) contained trace amounts of boron, peaking at a bulk concentration of 58 ± 9 ppb (NDT14). Meanwhile, the previously published bulk concentrations for representative AOTC samples were often higher, and in general the samples with higher boron concentrations had poorer color grades (further from colorless), introducing a blue hue that could produce grades up to Fancy Light blue, depending on the sample's size and faceting arrangement (D'Haenens-Johansson et al., 2014). DiamondView fluorescence images revealed that the intensity contrast between the different growth sectors was significantly weaker for the NDT specimens. These results may imply that the HPHT samples grown by NDT have a lower impurity content than those produced by AOTC, explaining the higher percentage of D–F color grades achieved (89% compared to 33%).

**Identification Features.** Although NDT sells its faceted synthetics with full disclosure of their origin, it is prudent to be aware of the relevant identification features in case these goods are at some point reintroduced into the gem trade without disclosure. NDT's gem-quality HPHT synthetics can be conclusively identified, though this often relies on a combination of gemological and spectroscopic observations. Sev-

eral of these characteristics are similar to those for HPHT synthetics from other sources.

Magnification may reveal the presence of metallic inclusions, which are not observed in CVD synthetic diamonds and are extremely rare, and with differing geometries, in natural diamonds (Sobolev et al., 1981). If sufficiently large or plentiful, the metallic inclusions can be confirmed by attraction to a strong magnet. Examination through crossed polarizers showed that the samples had extremely low strain levels, as indicated by low-order interference colors (blue and grays) and the inability to resolve a clear birefringence pattern. This is common for HPHT synthetics (Crowningshield, 1971) but in stark contrast to both CVD synthetic and natural stones, which show cross-hatched, mottled, or banded birefringence patterns, often in a variety of colors. The fluorescence and phosphorescence response of these HPHT synthetics was stronger to short-wave than long-wave UV, the opposite of the behavior seen in natural stones (Crowningshield, 1971; Shigley et al., 1997). Long-lasting phosphorescence, a characteristic rarely detected in natural diamonds, should be regarded with caution. If any of the above gemological observations are noted, further investigation using advanced testing techniques is crucial for conclusive origin determination.

The high-energy UV illumination from a DiamondView instrument will readily induce fluorescence in all diamonds, natural or synthetic. Inspection of the table, crown, and pavilion facets of the NDT samples revealed cuboctahedral growth sectors, which are characteristic of HPHT synthetics, though the pattern was very weak in some. Additionally, all the samples exhibited strong phosphorescence. A phosphorescence spectrometer could aid in their identification, as 13 of the 42 samples tested in this manner (31%) showed a phosphorescence band at approximately 575 nm, which has only been reported in certain HPHT-grown synthetic diamonds (Watanabe et al., 1997; Eaton-Magaña et al., 2008). Despite the similar emission wavelengths, this band should not be confused with the weak 580 nm band that has been infrequently detected for some natural type IIb diamonds. The 500 nm band, also observed, cannot be considered indicative of a synthetic origin, as it is often displayed by natural type IIb diamonds (Eaton-Magaña et al., 2007, 2008).

Further spectral analysis using FTIR absorption and PL spectroscopy may also be helpful. All the NDT samples were either type IIb or type IIa—i.e., they did not contain detectable amounts of isolated or aggregated nitrogen defects. Natural, treated, and CVD or HPHT synthetic colorless diamonds can all belong to these types. Since some 98% of natural diamonds contain A-aggregates (nitrogen pairs, which absorb at approximately 1280 cm$^{-1}$), their absence from a sample's IR spectrum would indicate a need for detailed analysis. PL, like FTIR, cannot alone conclusively identify an HPHT synthetic, yet it was effective at revealing suspicious impurities. The Ni-related features observed at 882.1/883.8 nm (1.405/1.402 eV) and at 483.6/483.8/484.1/484.4 nm (2.563/2.562/2.560/2.559 eV) are seldom detected for natural type IIa and IIb diamonds and have not been reported for CVD synthetics (Nobel et al., 1998; Chalain, 2003). The 736.6/736.9 nm (1.683/1.682 eV) SiV$^-$ feature, often used in the identification of CVD-grown samples, has been detected only rarely in natural diamonds or in other HPHT synthetics (Breeding and Wang, 2008; Moe and Wang, 2010; Wang and Moe, 2012; D'Haenens-Johansson et al., 2014). A weak SiV$^-$ feature was detected in a subset of the specimens in this study. Its presence remains a source of concern, though a stone with this feature could be either natural or CVD synthetic.

## CONCLUSIONS
New Diamond Technology's colorless HPHT-grown synthetic diamonds are being faceted into gems for the jewelry trade. This study of 44 representative samples revealed that the company can create faceted colorless and faintly colored synthetics weighing up to 4.30 ct and 5.11 ct, respectively. Although the samples spanned the full range of clarity, NDT has demonstrated the capacity to produce high clarities. One such specimen, a 1.13 ct round brilliant with a very good cut grade, characterized by D color and IF clarity, was remarkable for its quality. All indications point to high-color and high-clarity HPHT synthetics becoming more prominent in the gem trade. The colorless stones in the study are comparable to top-quality natural diamonds and surpass (for this color range) the sizes achieved by alternative producers. NDT's continued focus on expanding production and increasing the sizes of their colorless samples emphasizes the need for awareness by grading laboratories, members of the diamond trade, and consumers. Through careful analysis using gemological, fluorescence, and spectroscopic methods, these products can be confidently identified as synthetic, thus posing no threat to a well-informed, responsible, and transparent diamond trade.

# REFERENCES

AOTC (2015) Synthetic white diamonds, http://aotc.com/unique/white-diamonds [date accessed: Feb. 23, 2015].

Bates R. (2015) Company claims to have produced 5 carat synthetic diamond, *JCK Magazine*, Feb. 17, http://www.jckonline.com/2015/02/17/company-claims-to-have-produced-5-carat-synthetic-diamond.

Bovenkerk H.P., Bundy F.P., Hall H.T., Strong H.M., Wentorf R.H. (1959) Preparation of diamond. *Nature*, Vol. 194, No. 4693, pp. 1094–1098, http://dx.doi.org/10.1038/1841094a0.

Breeding C.M., Wang W. (2008) Occurrence of the Si-V defect center in natural colorless gem diamonds. *Diamond and Related Materials*, Vol. 17, Nos. 7–10, pp. 1335–1344, http://dx.doi.org/10.1016/j.diamond.2008.01.075.

Burns R.C., Cvetkovic V., Dodge C. N., Evans D.J.F., Rooney M.-L.T., Spear P.M., Welbourn C.M. (1990) Growth-sector dependence of optical features in large synthetic diamonds. *Journal of Crystal Growth*, Vol. 104, No. 2, pp. 257–279, http://dx.doi.org/10.1016/0022-0248(90)90126-6.

Chalain J.P. (2003) Gem News International: A natural yellow diamond with nickel-related optical centers. *G&G*, Vol. 39, No. 4, pp. 325–326.

Clark C.D., Kanda H., Kiflawi I., Sittas G. (1995) Silicon defects in diamond. *Physical Review B*, Vol. 51, No. 23, pp. 16681–16688, http://dx.doi.org/10.1103/PhysRevB.51.16681.

Collins A.T., Williams A.W.S. (1971) The nature of the acceptor centre in semiconducting diamond. *Journal of Physics C: Solid State Physics*, Vol. 4, pp. 1789–1800, http://dx.doi.org/10.1088/0022-3719/4/13/030.

Collins A.T., Kanda H., Burns R.C. (1990) The segregation of nickel-related optical centers in the octahedral growth sectors of synthetic diamond. *Philosophical Magazine Part B*, Vol. 61, No. 5, pp. 797–810, http://dx.doi.org/10.1080/13642819008207562.

Collins A.T. (1992) The characterisation of point defects in diamond by luminescence spectroscopy. *Diamond and Related Materials*, Vol. 1, Nos. 5–6, pp. 457–469, http://dx.doi.org/10.1016/0925-9635(92)90146-F.

Crowningshield R. (1971) General Electric's cuttable synthetic diamonds. *G&G*, Vol. 13, No. 10, pp. 302–314.

Dean P.J. (1965) Bound excitons and donor-acceptor pairs in natural and synthetic diamond. *Physical Review*, Vol. 139, No. 2A, pp. A588–A602, http://dx.doi.org/10.1103/PhysRev.139.A588.

Dean P.J. (1973) Inter-impurity recombinations in semiconductors. *Progress in Solid State Chemistry*, Vol. 8, pp. 1–126, http://dx.doi.org/10.1016/0079-6786(73)90004-6.

D'Haenens-Johansson U.F.S., Moe K.S., Johnson P., Wong S.Y., Wang W. (2012) Lab Notes: Near-colorless HPHT-grown synthetic diamonds from Advanced Optical Technology Co. *G&G*, Vol. 48, No. 2, p. 141.

D'Haenens-Johansson U.F.S., Moe K.S., Johnson P., Wong S.Y., Lu R., Wang W. (2014) Near-colorless HPHT synthetic diamonds from AOTC Group. *G&G*, Vol. 50, No. 1, pp. 30–45, http://dx.doi.org/10.5741/GEMS.50.1.30.

D.NEA (2015) 3.16 ct G color round cut created diamond, http://d.neadiamonds.com/lab-created-diamonds/WB1225.

Eaton-Magaña S., Post J.E., Heaney P.J., Walters R.A., Breeding C.M., Butler J.E. (2007) Fluorescence spectra of colored diamonds using a rapid, mobile spectrometer. *G&G*, Vol. 43, No. 4, pp. 332–351, http://dx.doi.org/10.5741/GEMS.43.4.332.

Eaton-Magaña S., Post J., Heaney P.J., Freitas J., Klein P., Walters R., Butler J.E. (2008) Using phosphorescence as a fingerprint for the Hope and other blue diamonds. *Geology*, Vol. 36, No. 1, pp. 83–86, http://dx.doi.org/10.1130/G24170A.1.

Eaton-Magaña S., Lu R. (2011) Phosphorescence in type IIb diamonds. *Diamond and Related Materials*, Vol. 20, No. 7, pp. 983–989, http://dx.doi.org/10.1016/j.diamond.2011.05.007.

Fisher D., Sibley S.J., Kelly C.J. (2009) Brown colour in natural diamond and interaction between the brown related and other colour-inducing defects. *Journal of Physics: Condensed Matter*, Vol. 21, No. 36, 364213, 10 pp., http://dx.doi.org/10.1088/0953-8984/21/36/364213.

Hall M., Lu R., Wang W. (2010) U.S. Patent No. US 2010/0220311A1. Issued September 2.

International Gemological Institute (2015) International Gemological Institute (IGI) Hong Kong certifies record-breaking, world's largest colorless grown diamond, May 26, http://igi-worldwide.com/igi-certifies-worlds-largest-colorless-grown-diamond.html.

Klein P.B., Crossfield M.D., Freitas J.A., Collins A.T. (1995) Donor-acceptor pair recombination in synthetic type-IIb semiconducting diamond. *Physical Review B*, Vol. 51, No. 15, pp. 9634–9642, http://dx.doi.org/10.1103/PhysRevB.51.9634.

Koivula J.I., Tannous M. Schmetzer K. (2000) Synthetic gem materials and simulants in the 1990s. *G&G*, Vol. 36, No. 4, pp. 360–379, http://dx.doi.org/10.5741/GEMS.36.4.360.

Lawson S.C., Kanda H. (1993) An annealing study of nickel point defects in high-pressure synthetic diamond. *Journal of Applied Physics*, Vol. 73, No. 8, pp. 3967–3973, http://dx.doi.org/10.1063/1.352861.

Martineau P.M., Lawson S.C., Taylor A.J., Quinn S.J., Evans D.J.F., Crowder M.J. (2004) Identification of synthetic diamond grown using chemical vapor deposition (CVD). *G&G*, Vol. 40, No. 1, pp. 2–25, http://dx.doi.org/10.5741/GEMS.40.1.2.

Moe K.S., Wang W. (2010) Lab Notes: Silicon-vacancy defect found in blue HPHT-grown synthetic diamond. *G&G*, Vol. 46, No. 4, p. 302.

Nazaré M.H., Neves A.J., Davies G. (1991) Optical studies of the 1.40-

eV Ni center in diamond. *Physical Review B*, Vol. 43, No. 17, pp. 14196–14205, http://dx.doi.org/10.1103/PhysRevB.43.14196.

Nazaré M.H., Mason P.W., Watkins G.D., Kanda H. (1995) Optical detection of magnetic resonance of nitrogen and nickel in high-pressure synthetic diamond. *Physical Review B*, Vol. 51, No. 23, pp. 16741–16745, http://dx.doi.org/10.1103/PhysRevB.51.16741.

Nobel C.J., Pawlik T., Spaeth J.-M. (1998) Electron paramagnetic resonance investigations of nickel defects in natural diamonds. *Journal of Condensed Matter*, Vol. 10, No. 50, pp. 11781–11794, http://dx.doi.org/10.1088/0953-8984/10/50/017.

Palik E.D. (1985) *Handbook of Optical Constants of Solids*. Academic Press, London.

Poon P.Y., Wong S.Y., Lo C. (2015) Large HPHT-grown synthetic diamonds examined in GIA's Hong Kong laboratory. *GIA Research & News*, Mar. 16, http://www.gia.edu/gia-news-research-large-hpht-grown-synthetic-diamonds-examined-in-gia-hong-kong-laboratory.

Pure Grown Diamonds (2014) World's largest laboratory pure grown diamond unveiled. *Business Wire*, Dec. 30, http://www.businesswire.com/news/home/20141229005491/en/adding-multimedia-worlds-largest-laboratory-pure-grown#.votnbs63raq.

Pure Grown Diamonds (n.d.) Lab grown diamonds, http://www.pure-growndiamonds.com/diamonds/single [date accessed: Jun. 23, 2015].

Rooney M.-L.T., Welbourn C.M., Shigley J.E., Fritsch E., Reinitz I. (1993) De Beers near colorless-to-blue experimental gem-quality synthetic diamonds. *G&G*, Vol. 29, No. 1, pp. 38–45, http://dx.doi.org/10.5741/GEMS.29.1.38.

Satoh S., Sumiya H., Tsuji K., Gouda Y. (2000) US Patent No. US006129900A. Issued October 10.

Shigley J.E., Moses T.M., Reinitz I., Elen S., McClure S.F., Fritsch E. (1997) Gemological properties of near-colorless synthetic diamonds. *G&G*, Vol. 33, No. 1, pp. 42–53, http://dx.doi.org/10.5741/GEMS.33.1.42.

Shigley J.E., McClure S.F., Breeding C.M. Shen A.H.-T., Muhlmeister M. (2004) Lab-grown colored diamonds from Chatham Created Gems. *G&G*, Vol. 40, No. 2, pp. 128–145, http://dx.doi.org/10.5741/GEMS.40.2.128.

Sittas G., Kanda H., Kiflawi I., Spear P.M. (1996) Growth and characterization of Si-doped diamond single crystals grown by the HTHP method. *Diamond and Related Materials*, Vol. 5, Nos. 6–8, pp. 866–869, http://dx.doi.org/10.1016/0925-9635(95)00449-1.

Sobolev N.V., Efimiva E.S., Pospelova L.N. (1981) Native iron in diamonds of Yakutia and its paragenesis. *Soviet Geology and Geophysics*, Vol. 22, No. 12, pp. 18–21.

Strong H.M. (1977) US Patent No. US40142673. Issued August 16.

Strong H.M., Chrenko R.M. (1971) Further studies on diamond growth rates and physical properties of laboratory-made diamond. *The Journal of Physical Chemistry*, Vol. 75, No. 12, pp. 1838–1843, http://dx.doi.org/10.1021/j100681a014.

Sumiya H. (2009) Recent advances in high pressure apparatus for diamond synthesis. *The Review of High Pressure Science and Technology*, Vol. 19, No. 4, pp. 264–269, http://dx.doi.org/10.4131/jshpreview.19.264 [in Japanese].

Sumiya H., Satoh S. (1996) High-pressure synthesis of high-purity diamond crystal. *Diamond and Related Materials*, Vol. 5, pp. 1359–1365, http://dx.doi.org/10.1016/0925-9635(96)00559-6.

Sumiya H., Toda N., Satoh S. (2002) Growth rate of high-quality large diamond crystals. *Journal of Crystal Growth*, Vol. 237–239, Part 2, pp. 1281–1285, http://dx.doi.org/10.1016/S0022-0248(01)02145-5.

Sumiya H., Toda N., Satoh S. (2005) Development of high-quality large-size synthetic diamond crystals. *SEI Technical Review*, Vol. 60, pp. 10–16.

Wang W., Moses T. (2010) Lab Notes: Large (4+ ct) yellow-orange HPHT-grown synthetic diamond. *G&G*, Vol. 46, No. 4, p. 301.

Wang W., Moe K.S. (2012) Lab Notes: Silicon-vacancy defect in HPHT-grown type IIb synthetic. *G&G*, Vol. 48, No. 4, pp. 304–305.

Wang W., Hall M.S., Moe K.S., Tower J., Moses T.M. (2007) Latest-generation CVD-grown synthetic diamonds from Apollo Diamond Inc. *G&G*, Vol. 43, No. 4, pp. 294–312, http://dx.doi.org/10.5741/GEMS.43.4.294.

Wang W., D'Haenens-Johansson U.F.S., Johnson P., Moe K.S., Emerson E., Newton M.E., Moses T.M. (2012) CVD synthetic diamonds from Gemesis Corp. *G&G*, Vol. 48, No.2, pp. 80–97, http://dx.doi.org/10.5741/GEMS.43.4.294.

Wang W., Moe K.S., Yeung S.F., D'Haenens-Johansson, U. (2013) Lab Notes: Very large CVD-grown. *G&G*, Vol. 49, No. 1, p 50.

Watanabe K., Lawson S.C., Isoya J., Kanda H., Sato Y. (1997) Phosphorescence in high-pressure synthetic diamond. *Diamond and Related Materials*, Vol. 6, No. 1, pp. 99–106 http://dx.doi.org/10.1016/S0925-9635(96)00764-9.

Washington Diamonds Corp. (2013) Going where no diamond-produing lab has gone before: A true colorless, one carat, lab grown CVD diamond, Oct. 3, http://www.washingtondiamondscorp.com/going-where-no-diamond-producing-lab-has-gone-before-a-true-colorless-one-carat-lab-grown-cvd-diamond/

Welbourn C.M., Cooper M., Spear P.M. (1996) De Beers natural versus synthetic diamond verification instruments, *G&G*, Vol. 32, No. 3, pp. 156–169, http://dx.doi.org/10.5741/GEMS.32.3.156.

Yelisseyev A., Kanda H. (2007) Optical centers related to 3d transition metals in diamond. *New Diamond and Frontier Carbon Technology*, Vol. 17, No. 3, pp. 127–178.

Zhan-Chang L., Xiao-Peng J., Guo-Feng H., Mei-Hua H. Yong L., Bing-Min Y. (2013) FEM simulations and experimental studies of the temperature field in a large diamond crystal growth cell. *Chinese Physics B*, Vol. 22, No. 1, 014701–014706, http://dx.doi.org/10.1088/1674-1056/22/1/014701.

Zhu H., Pearson K., Kim J.R. (2012) US Patent No. US2012/0192785A1. Issued August 2.

# LETŠENG'S UNIQUE DIAMOND PROPOSITION

Russell Shor, Robert Weldon, A.J.A. (Bram) Janse, Christopher M. Breeding, and Steven B. Shirey

The Letšeng-la-Terae diamond mine in Lesotho, a small nation surrounded by South Africa, is unique in that it produces some of the world's largest and highest-value diamonds from a relatively small volume of kimberlite ore. The mine, operated by De Beers during the late 1970s and early 1980s, was difficult to sustain economically because of its remoteness and very low ore grade, which made production costs very high. Since 2000, sharply rising prices for large diamonds have permitted the mine to reopen profitably as a 70/30 venture between Gem Diamonds Ltd. of South Africa and the government of Lesotho. To improve recovery of large diamonds, Letšeng's owners have implemented new processing technology that provides better identification of these crystals before processing and a crushing mechanism that reduces their potential breakage. In recent years, several important diamonds recovered from Letšeng have been sold to London luxury jeweler Laurence Graff.

While the Premier (now Cullinan) mine in South Africa is usually cited as the traditional source for very rare large diamonds, in recent years the Letšeng-la-Terae mine in Lesotho has become the major producer of such stones (figure 1). Although its total output is relatively small—about 100,000 carats yearly, compared to two million or more carats from most major diamond mines—the average value of its production in 2014 was just above US$2,500 per carat (Gem Diamonds Ltd., 2014, 2015a). This is by far the world's highest per-carat value, more than 21 times higher than the $116 average for diamonds mined worldwide, according to Kimberley Process data.

The Letšeng mine is also the world's most consistent source of type IIa diamonds (those with exceptionally low nitrogen content), which account for about one-fourth of its production (Gem Diamonds Ltd., 2014). The mine claims six of the 20 largest diamonds ever discovered—478, 493, 527, 550, 601, and 603 ct (table 1). The largest of these, the Lesotho Promise, was found in 2006 and sold to London jeweler Laurence Graff for $12.4 million. In the years since, Graff has also purchased the 493 ct Letšeng Legacy, the 478 ct Light of Letšeng, and the 550 ct Letšeng Star.

Until 2004, Letšeng had been shut down for more than 20 years because its low grade and remote location made mining unprofitable at existing diamond prices. Up until the past decade, De Beers and other mining companies typically sacrificed large crystals for the sake of rapid throughput, which maximized efficiency and reduced mining costs. Only after prices for large stones began rising sharply did the mining economics change in favor of preserving them. Because the economic viability of Letšeng

Figure 1. Rising prices and demand for large diamonds have fueled the success of the Letšeng mine in northern Lesotho. Shown here are two rough stones: a 299.35 ct slightly yellowish partial octahedron and a colorless 112.61 ct type IIa diamond. Photo by Robert Weldon/GIA; courtesy of Gem Diamonds Ltd.

Figure 2. This remote village deep in the Maloti Mountains near the Letšeng mine is primarily dedicated to agriculture and sheep herding. Villagers also form the workforce for the diamond mine. Basuto ponies such as the one seen here are esteemed for their speed and surefootedness in the steep, rocky mountain passes. Photo by Robert Weldon/GIA.

hinges on its ability to produce very large diamonds, the owners have employed new recovery processes to reduce damage and breakage of such diamonds. The mine is a major force of Lesotho's economy, employing about 1,500 workers, 90% of them locals. Letšeng accounts for 70% of the country's corporate tax revenue and 60% of its foreign exchange earnings (M. Maharasoa, pers. comm., 2014).

## BACKGROUND

The Kingdom of Lesotho is a nation of rugged mountains (figure 2) set within the boundaries of South Africa (figure 3). Its capital, Maseru, is located about 250 miles south of Johannesburg. When diamonds were discovered in South Africa in 1867, Lesotho (then known as Basutoland) was sparsely settled by agrarian villagers and shepherds living under the rule of King Moshoeshoe.

The tiny kingdom struggled to remain independent from its much larger neighbor, first resisting Zulu invasions from the south and then becoming embroiled in the growing tensions between the British and Afrikaners in southern Africa during the 1870s. The Afrikaners (descendants of early Dutch settlers) had begun to claim parts of the territory. While Basutoland's craggy mountains made for good defense, with more than 80% of the nation at least 5,000 feet above sea level, the British annexed the region in 1871. The rugged terrain also hindered exploration

for minerals, including diamonds. Large-scale agriculture was nearly impossible, which made it unattractive for colonial settlers. As a result, Basutoland remained fairly isolated from the wars and mineral rushes that shaped the southern portion of the continent during the 20th century ("Lesotho," 2014).

By road, Letšeng is located approximately 214 km

Figure 3. This map of Lesotho, formerly Basutoland, shows how the small country is completely surrounded by South Africa. The discovery of diamonds in Lesotho came 90 years after the South African finds of the 19th century.
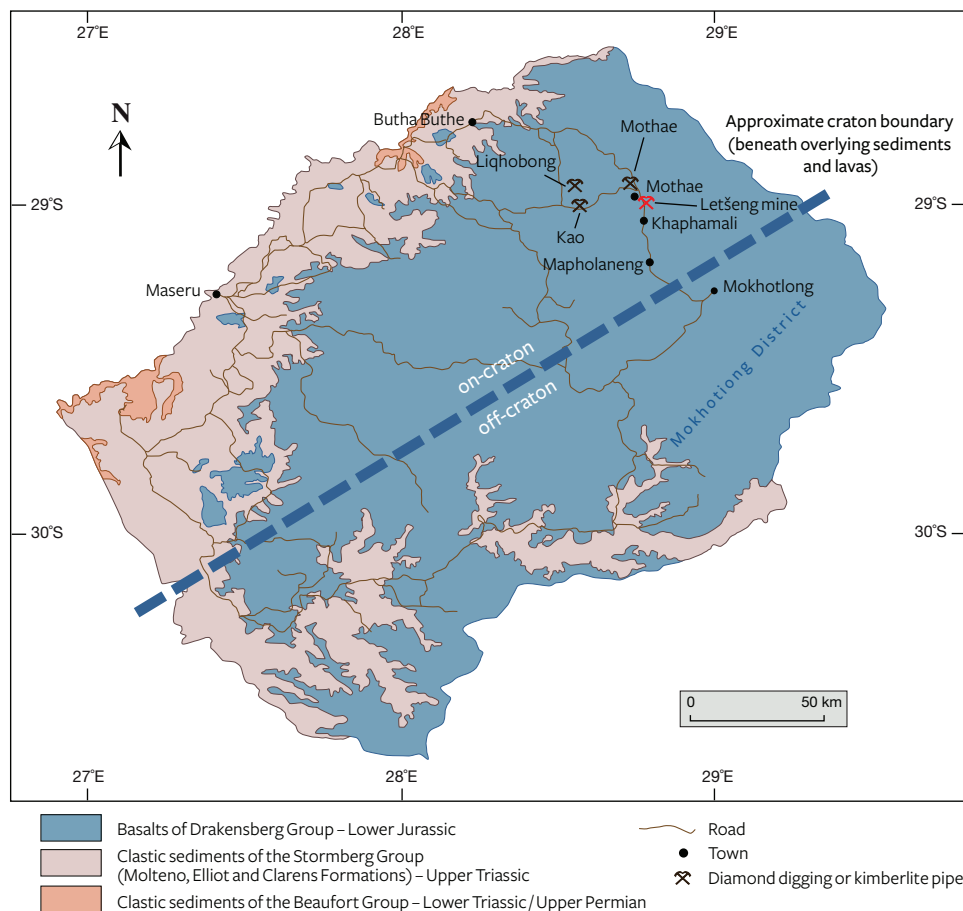
*Figure 4. This map of Lesotho shows the country's principal diamond mines within the Drakensberg basalts. Letšeng was the first diamond deposit discovered in Lesotho and remains the largest one, producing significant numbers of large diamonds. Like Letšeng, the other three mines in the area—Kao, Liqhobong, and Mothae—are all located on Archean craton underlain by older mantle at depth. There are no known primary diamond deposits in the off-craton part of the country. Map courtesy of Telfer and McKenna (2011).*

(133 miles) northeast of Maseru. The route is paved except for the last 30 km, which is a well-graded gravel road with many sharp hairpin turns. The mine's complete name is Letšeng-la-Terae (also spelled Terai), which means "the swamp at the turn," as it is located in a low saddle in the mountain range where the road makes an abrupt turn (Whitelock, 1979). The diamondiferous deposit was found in kimberlite under the superficial swamp sediment layer.

## GEOLOGICAL FRAMEWORK

Figure 4 shows that the western lowlands and parts of southern Lesotho consist of horizontally bedded sediments, whereas a thick series of flat-lying basaltic lavas form the mountains in the east. The sediments belong to the upper part of the Karoo Supergroup (late Carboniferous to mid-Jurassic, 330–180 Ma), which once covered a major portion of southern Africa. In Lesotho, these sediments form part of the Stormberg series, which are Triassic (roughly 250–200 Ma) in age and consist of pale multicolored sandstones with intercalated grits, mudstones of the Molteno (fluvial sands), Elliot (red,

green, and purple mudstones, previously called Red Beds), and Clarens (cream-colored aeolian sands, previously called Cave Sandstone) formations. These are overlain by the Early Jurassic (183 Ma) Drakensberg Beds, a monotonous series of flood basalt lava flows. The base of the lavas lies at an elevation of 1,600 meters, while the top is above 3,200 meters, for a stratigraphic thickness of more than 1,600 meters. Fine-grained basaltic dikes and sills contemporaneous with the lavas occur in the lowlands and mountains in a wide zone trending ESE-WNW. Hundreds of kimberlite pipes and dikes intruded in the Middle to Late Cretaceous (120–65 Ma) in many parts of southern Africa, and in Lesotho in the 95–85 Ma interval (Wilson et al., 2007). They occur mainly in northern and northeastern Lesotho (again, see figure 4), occupying the same ESE-WNW zone as the fine-grained basaltic dikes. Known at present are 39 pipes and 23 dike enlargements, usually called blows. Of these 62 bodies, 24 are diamondiferous. Moreover, there are more than 300 individual dikes. The age of intrusion of the Letšeng pipes has not been measured directly but is assumed to be similar to neighboring

**TABLE 1.** Largest diamonds recovered from Letšeng.

| Name | Discovered | Size (ct) | Value | Sale price per carat |
|---|---|---|---|---|
| Unnamed | 1965 | 527 | no data | no data |
| Lesotho Brown | May 1967 | 601 | US$302,400 | US$503 |
| Lesotho Promise | Oct. 2006 | 603 | US$12.4 M | US$20,564 |
| Letšeng Legacy | Sept. 2007 | 493 | US$10.4 M | US$21,095 |
| Light of Letšeng | Sept. 2008 | 478 | US$18.4 M | US$38,493 |
| Letšeng Star | Aug. 2011 | 550 | US$16.5 M | US$30,000 |

pipes. For instance, zircon from Mothae is 87 Ma (Davis, 1977), while ages of perovskite from Kao, Liqhobong, and Mothae range from 89 to 95 Ma (Lock and Dawson, 2013).

According to Clifford's Rule (as refined by Janse, 1994), the occurrence of economic diamondiferous kimberlites is restricted to the Archean (>2,500 Ma) interior of the seismically stable, erosionally flattened area of continental crust plus mantle known as a craton (see Shirey and Shigley, 2013), which is composed of a basement older than 1,800 Ma. Janse (1994) refined Clifford's Rule in stating that *economic* kimberlites occur only on archons (the Archean part of a craton) older than 2,500 Ma. As previously noted, in Lesotho this cratonic basement is hidden by overlying Triassic to Early Jurassic sediments and lavas (again, see figure 4). Archean basement must be present at depth because pieces of Archean-age mantle and crust occur in the Letšeng kimberlite pipes, showing that they fall within the window of potentially economic diamond deposits. Letšeng lies close to the eastern edge of the Kaapvaal craton, where remnants of the original Stromberg sediments and volcanics remain and the upper portions of the pipes are still preserved.

## GEOLOGY AND PETROGRAPHY OF THE LETŠENG PIPES

The high proportion of very large and type IIa diamonds in the Letšeng kimberlite has puzzled geologists. Letšeng sits near the edge of the Archean craton (see box A). In the Archean, this location might have permitted distinctive low-nitrogen, diamond-forming fluids access to the deep lithospheric mantle where the Letšeng diamonds were grown. It is possible that these diamonds did not grow in one short geologic event but slowly, over a longer geologic interval. If so, the high proportion of large diamonds could relate to especially slow growth rates from these fluids. But confirmation of these ideas would depend on detailed mineralogical studies of growth zonation and accurate age information, in particular for absolute age and/or core-to-rim ages that would reflect the duration of diamond growth. Such studies do not exist at present because of the high value of these stones—they cannot be sacrificed for research—and the exceptionally low abundance of mineral inclusions.

The Letšeng kimberlites consist of two pipes, the Main and the Satellite (figure 5), measuring 17.2 hectares (540 × 365 m) and 5.2 hectares (425 × 130 m), respectively. The pipes are carrot-shaped bodies, vertically intrusive and slightly tapering with vertical to slightly inclined walls, 83° at most. They are elongated in a northerly direction, roughly perpendicular to the general westerly trend of the fine-grained basaltic dikes, which suggests that the pipe locations

Figure 5. The Main pipe (left) and Satellite pipe (right), photographed during a 2014 visit. The larger Main pipe was originally mined by De Beers. Today both are operated by Letšeng Diamonds. The basalt raft is the circular area in the upper right portion of the Satellite pipe. Photos by Robert Weldon/GIA.

## Box A: ARCHEAN CRATONS AND THE LOCATION OF LETŠENG

The southern African continent has a fascinating geomorphological history and geology that helps explain the region's diamond distribution. In addition, the various mines across the region have taught the world's geologists many of the basic geologic principles of diamond formation and occurrence.

The basic geologic structure of the region is one where geologically old (3 to 3.7 billion years) and stable central portions of the continent known as "cratons" are surrounded by younger, deformed regions (figure A-1). Diamonds occur in primary, relatively young (often 90 million but up to 1.2 billion years in age) kimberlite volcanic pipes that have brought them from the bottom of the cratons to the surface. Kimberlites that erupt through the deformed regions off-craton are devoid of diamonds. This basic southern African fact, that the cratons are where the diamonds occur, has been applied around the world as the primary exploration approach.

Radiometric dating of mineral grains in many diamonds shows that they are old, ranging in age from about a billion years to as old as the craton itself. Since the first cratonic blocks were formed by massive continental collision and thickening, diamond formation likely occurred as part of this process. Diamond-forming fluids were carried down into the deep regions of the mantle under the continents where diamonds can grow. But given that many diamonds can be younger, later post-collision underthrusting of oceanic slabs during a process known as subduction was likely another cause of later formation.

After this long history of active continent building and modification, southern Africa was then subjected to weathering and extensive erosion. Erosion plays the major role in the genesis of secondary diamond deposits—those of alluvial (riverine) and marine derivation. Erosion is very dependent on height above sea level, and therefore uplift largely determines how much erosion will occur. Johannesburg stands a mile above sea level, while parts of Lesotho are nearly two miles above sea level. This is highly unusual for a craton. The cause of this uplift is not known, but it is relatively recent and related to hotter upwelling mantle occurring much deeper

than the bottom of the craton. A first result of this extensive erosion of major parts of the country is that the top portion of southern African kimberlites have been removed and their diamond cargo has been transported westward along the Vaal and Orange River systems to form the alluvial and marine diamond deposits of today. A second result of this erosion is that diamonds in their host kimberlites are mined today at very different levels in the volcanic pipe. Since the kimberlites were erupted through the craton before erosion took place, diamonds at Letšeng occur roughly a mile higher in the pipe than they do at other localities in South Africa such as Kimberley or Premier/Cullinan.

In some ways, every kimberlite and diamond population is unique. But Letšeng is highly unusual. Mine geologist Debbie Bowen and her colleagues have described several features that make this deposit unique: the lack of octahedral diamonds, the high percentage of resorbed and rounded dodecahedral shapes, the yield of gem-quality stones in the larger size categories, and especially the abundance of type IIa (nitrogen-free) D-color stones. She compared Letšeng diamonds to South African alluvial diamonds, whose large average stone size is a result of the destruction of the poorer, weaker diamonds during transport (Bowen et al., 2009). Circumstances that complicate our understanding of Letšeng diamonds include the extensive vertical mixing that occurs during a kimberlite eruption, the lack of control on such a chaotic process, and the inability to sample such expensive diamonds for research purposes.

The position of the Letšeng-la-Terae kimberlite pipe at the edge of the craton may or may not be partly responsible for some of the unique diamonds found there. Knowing the age of diamond growth would help place geological constraints on the types of processes that supplied the diamond-forming carbon and what its sources might have been. No definitive age studies have been carried out on Letšeng diamonds, and there have been few geochemical studies of the inclusions or the diamonds themselves. Such studies are now underway and will help us understand these questions.

were influenced by crosscutting structures. The contact between the kimberlite and the lava flows of the country rock are sharp, giving no indication of upfolding or chemical alteration. In places there is a 1 to 1.3 m marginal zone within the pipe where the kimberlite is sheared, with mud seams and calcite veins. The Letšeng kimberlites belong to the group 1 class of kimberlites, the generally non-micaceous type. Their texture is volcaniclastic.

The simple structural division into crater, diatreme, and root zones has been modified during the last decade (Scott Smith et al., 2008). Based on microscopic observation of core samples, petrographers now recognize volcaniclastic and hypabyssal kimberlite rocks instead (figure 6, top). Volcaniclastic kimberlite occurring in the crater, and layered in successive pulses, may be resedimented due to slumping. This resedimented volcaniclastic kimber-
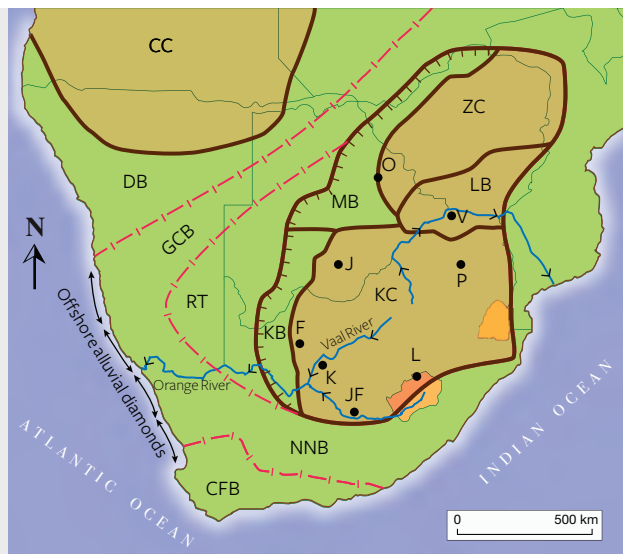
*Figure A-1. In this geologic map of southern Africa, current or recently active diamond mines (O = Orapa, V = Venetia, P = Premier/Cullinan, J = Jwaneng, F = Finsch, K = Kimberley, JF = Jagersfontein, L = Letšeng) are confined to areas of Archean crust (more than 2.5 billion years old) known as cratons, marked by long-term geological stability. These Archean cratons (CC = Congo Craton, ZC = Zimbabwe Craton, LB = Limpopo Belt, KC = Kaapvaal Craton) are shown in brown, along with two metamorphic terranes (KB = Kheis Belt, MB = Magondi Belt) suspected of containing Archean crust. The Vaal and Orange Rivers, which drain South Africa to the west, are the sources of alluvial workings along the river systems and marine deposits off the coasts of South Africa and Namibia. Relatively recent and substantial uplift of southern Africa caused these diamonds to be weathered from their original on-craton kimberlite hosts and moved westward by the rivers to the Atlantic Ocean. Note that there are no diamondiferous kimberlites in the green metamorphic mobile belts (DB = Damara Belt, GCB = Ghanzi-Chobe Belt, RT = Rehoboth Terrane, KB = Kheis Belt, MB = Magondi Belt, NNB = Namaqua-Natal Belt, CFB = Cape Fold Belt) that surround the cratons. Note the landlocked kingdoms of Swaziland and Lesotho within South Africa and the interesting location of Letšeng at the edge of the Kaapvaal Craton.*

lite becomes more massive, nonlayered kimberlite in the pipe and is often referred to as tuffisitic kimberlite breccia. This is the general kimberlite breccia present in many specimen collections. Hypabyssal kimberlite is a dense aphanitic (evenly fine-grained, non-breccia) rock occurring in the root zone. The degree of erosion in the general countryside can expose these rocks at different levels in the vertical zoning (Scott Smith et al., 2008). The Letšeng kimberlites

contain easily visible centimeter-sized olivine crystals set in a groundmass of olivine (mainly altered to serpentine), phlogopite, and calcite. Crystals of purplish to dark red pyrope, black ilmenite, and green chrome diopside can occasionally be seen in the rock or among the minerals in the surface rubble.

The Letšeng kimberlite is covered by one meter of spongy soil (primarily on the Main pipe), two meters of leached white gravel, five meters of brown basaltic gravel (mainly on the Satellite pipe), one meter of yellow ground (oxidized kimberlite), and 20 meters of soft kimberlite "blue ground" and "yellow

*Figure 6. Top: Plan view of the Main and Satellite kimberlite pipes at Letšeng, showing the location of underground tunnels within the pipes. Bottom: A cross-sectional map of the Main and Satellite kimberlite pipes. The green area in the Satellite pipe is the large basalt raft that dropped into the pipe some 90 million years ago. From Telfer and McKenna (2011).*
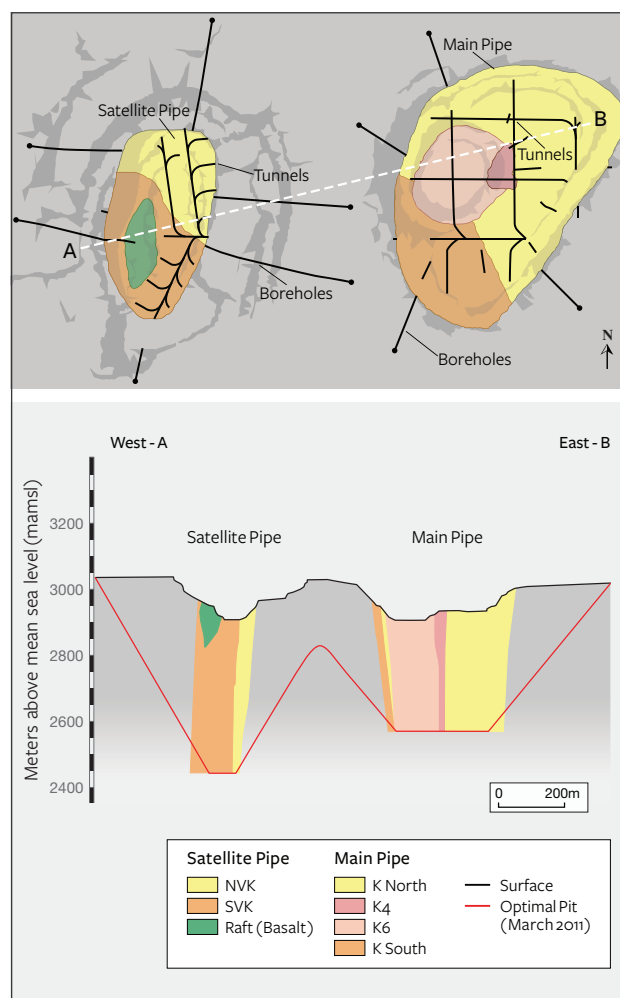
ground". Below this depth, the kimberlite becomes hard bluish grayish greenish rock descending at least 700 meters (see pipe cross-section in figure 6).

During public digging access from 1959 to 1967 (figure 7), artisanal miners occasionally recovered very large crystals from the gravels on top of the pipes and in the gravels of nearby streams that drain the Main and the Satellite pipes. Formal mining by De Beers (1977–1982), Letšeng Diamonds (Pty) Ltd. (2004–2006), and Gem Diamonds Ltd. (2007 to the present) has removed most of these near-surface deposits. Mining currently takes place in the hard kimberlite, which requires blasting and crushing.

Similar to kimberlites elsewhere, the pipes contain several pulses of kimberlite magma that are slightly different in age and, more importantly, in the size, content, and quality of the diamonds. It is therefore necessary to outline their horizontal and vertical dimensions to recover diamonds of the highest grade. Four varieties of kimberlite are recognized in the Main pipe: K North, K South, K6, and K4 (again, see figure 6, top). K6 is economically the most important, as it contains the highest diamond content. It forms a separate sharply demarcated explosive volcanic breccia pipe known as a diatreme in the western part of the kimberlite, measuring four hectares (245 ×185 m). This is the area previously mined by De Beers and now by Gem Diamonds. K6 is a soft, friable, greenish gray rock with visible crystals of olivine and occasionally orthopyroxene, set in a fine groundmass. Xenoliths of basaltic lava are abundant

*Figure 7. The informal diggings in the Maloti Mountains in 1967, at a swampy area later known as Letšeng-la-Terae. From Nixon (1973); courtesy of De Beers.*
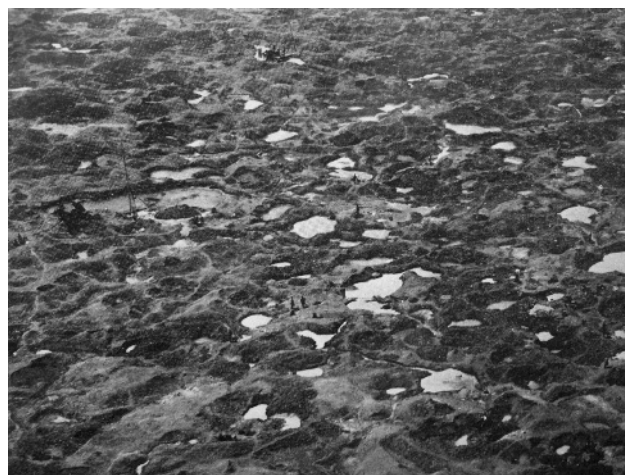


throughout and accompanied by a wide variety of basement rocks (gneisses and amphibolites) and ultramafic nodular fragments that include garnet lherzolites (Lock and Dawson, 2013). Garnet xenocrysts are also relatively abundant (Bloomer and Nixon, 1973). In the Satellite pipe two varieties are recognized: NVK and SVK (north and south volcaniclastic kimberlite), while a raft of basaltic rock occupies the upper part of the pipe (again, see figure 6).

The Main pipe accounts for 75% of the mine's output and has an average grade of 0.88 carats per hundred metric tons of material, while the Satellite

## In Brief

- Letšeng has produced some of the world's largest diamonds in the past decade, with a production value averaging more than $2,500 per carat.
- Letšeng's diamonds are unusual for their dodecahedral form and high percentage of type IIa specimens.
- The mine was sub-economic for many years because of its low ore grade, until prices for very large diamonds began rising sharply.
- To remain economically viable, the mine employs new technology to reduce breakage of large stones in the recovery process.

pipe has a yield of 2.6 carats per hundred metric tons (Gem Diamonds Ltd., 2013). Their average is by far the lowest for any diamond mine in the world, which range from 5 to 400 carats per hundred metric tons but typically from 50 to 100 carats per hundred metric tons. By comparison, De Beers's Venetia mine, located 500 miles to the north, yields about 110 carats per hundred metric tons (Krawitz, 2014).

## EXPLORATION

Stockley (1947) reported kimberlites in the Maloti Mountains of Basutoland as early as 1947, though no diamonds were found at the time (Nixon, 1973). Several additional kimberlites reported by Col. Jack Scott in 1955 added to the notion there might be diamonds, though none were discovered. Scott later got De Beers to assist him in further prospecting operations. But it was Peter H. Nixon, as a Harry Oppenheimer PhD scholar from the Research Institute of African Geology at the University of Leeds, who discovered in 1957 the two diamondiferous kimberlite pipes at Letšeng-la-Terae (Nixon, 1960). He noted that Lesotho's many kimberlite pipes are

Figure 8. Ernestine Ramaboa and husband Petrus hold up the Lesotho Brown diamond, which she discovered in 1967. At the time it was the world's seventh-largest diamond. The Ramaboas reportedly received more than $250,000 after taxes. Photo courtesy of UPI.

mostly barren of diamonds. Occasional reports of large diamond finds began to circulate nonetheless. *Lesotho Kimberlites* (1973), a book Nixon later compiled and edited as chief geologist in the country's Department of Mines and Geology, noted that some 1,200 diggers were working the area by 1965, a number that quickly swelled to some 6,000 within two years.

Figure 9. This postage stamp, issued in 1976, shows the colossal 601.26 ct Lesotho Brown diamond. The image pays homage to the Ramaboas (seen in the background) and Lesotho's King Moshoeshoe II (encircled).



The eureka moment for Lesotho came in 1967, when a digger, Ernestine Ramaboa, unearthed a brown colored diamond weighing 601.26 ct in the area of Letšeng-la-Terae. Ramaboa and her husband, Petrus, reportedly secreted the diamond away, feigning illness to avoid arousing the suspicions of fellow diggers, and then walked for four days across the mountains to the capital city of Maseru to sell their find (figure 8). News of the find spread quickly, and it was reported that the government had to step in to guarantee the Ramaboas' safety (Balfour, 1981).

At the time it was reported to be the world's eleventh-largest gem-quality diamond—and the largest reported found by an artisanal miner (Sotheby's, 2008). The diamond was named the Lesotho Brown (figure 9). The government set up a sealed tender to obtain the best possible price for the diamond. According to the September 1967 issue of *Diamond News and S.A. Jeweller*, this colossal gem was first sold for 216,300 rand (equivalent to $302,400 at the time) to South African dealer Eugene Serafini. In 1968 it was purchased, also via auction, by American jeweler Harry Winston. A fitting epilogue to the story is that Winston invited the Ramaboas to New York City for the unveiling and cleaving of the diamond. The moment was broadcast on live television across the United States (Balfour, 1981). The Lesotho Brown rough yielded 18 diamonds, including the Lesotho I, a flawless 71.73 ct diamond, and the Lesotho III (figure 10), a 40.42 ct marquise purchased by Aristotle Onassis and given to Jacqueline Kennedy as an engagement ring. In 1996 the Lesotho III ring sold at an auction of the former First Lady's estate for $2,587,500 ("Jackie O Lesotho diamond sells…", 1996).

Figure 10. The Lesotho III, a 40.42 ct marquise fashioned from the Lesotho Brown, was given by Aristotle Onassis to Jacqueline Kennedy for their engagement. Photo courtesy of Sotheby's.

## GOVERNMENT DIGGINGS

Ramaboa's discovery brought a wave of local small-scale miners to the Letšeng-la-Terae area. Despite their rudimentary tools and mining methods, they found a number of diamonds (Maleleka, 2007). In an effort to gain control over Letšeng-la-Terae, the government, through the Lesotho National Development Corporation, granted Rio Tinto Zinc (RTZ, now Rio Tinto) an exploration license in 1968. RTZ upgraded the road and airstrip in the remote area and built a sampling plant. Beginning in 1969, RTZ sampled the Main pipe to about 55 meters deep, recovering 2,635 carats over the duration of the project. The company's final report, issued in 1972, confirmed what many people suspected: that the grade was very low, though it occasionally produced unusually large diamonds. In the sampling carried out by RTZ, for example, over 90% of the value came from less than 10% of the diamonds—six stones, in fact—one of them nearly 50 ct (Chadwick, 1981). There was also the remoteness and inaccessibility of the area, which at the time made development costs uneconomically high. After RTZ declined to mine the deposit, the government granted licenses to individual diggers using limited mechanization who worked three-square-meter claims. For their part, the locals continued to find diamonds (Maleleka, 2007).

After RTZ's departure, the government of Lesotho asked De Beers in February 1975 to reevaluate the data collected by Rio Tinto. In a move that surprised some analysts, De Beers chairman Harry Oppenheimer signed an agreement with the prime minister in December 1975 to develop the mine. "De Beers will go ahead with the mine in spite of the risk—an obvious risk judged by Rio Tinto's findings against such a venture," according to one newspaper story (Payne, 1975). Even De Beers harbored some misgivings. As Oppenheimer noted, "We are certainly doing something that is pretty risky which I don't think other people would be inclined to do, and while I think that this is some way of philanthropy, we certainly were influenced by our desire to play a part in the development of Lesotho" ("Latest reports from the Lesotho Dept. of Mines," 1978; Madowe, 2013). The agreement factored in a 25% government share and a seat for the government on the board of directors of a Lesotho-based joint venture formed by De Beers. Between 600 and 900 people, mostly Basotho, were to be employed.

Diamonds would be sold through De Beers's marketing arm, then called the Central Selling Organization (CSO). The amount owed to the state from tax and dividends, once the capital had been amortized, was nearly 65% of sales. The mine's profitability was an open question, given the amount of investment needed for its infrastructure ("Onstream, upstream," 1977). Announcing the decision, a De Beers press release detailed the challenges:

> The design of the recovery plant took into consideration the particular situation of the mine—the difficulties of access, the effect of the gale force winds and the sub-zero temperatures on site. For example, gale force winds experienced at Letšeng would pose problems for conveyor scaffolds and the normal sized recovery plant buildings and the icy conditions could affect the conventional slurry and gravity circuits. The steeply sloping ground too had to be considered in relation to the pumping of slurry and gravels in the treatment plant. The plant designers, who also have to bear in mind the recovery of the larger diamonds peculiar to the main pipe at Letšeng, took the decision to excavate and locate the plant within the mountainside itself secure from the elements (De Beers Consolidated Mines Limited, 1975).

Furthermore, a road costing three million rand ($3.7 million at the time) would be built through the mountains, connecting the mine to both Johannesburg, South Africa and the country capital, Maseru. The mine officially opened in November 1977. At a cost of more than 30 million rand (US$37 million), it went at least 6 million rand ($7.4 million) over its intended budget. De Beers geared the plant to do the primary sorting and washing to identify larger gems before the ore went to the crusher. The company also installed an X-ray machine to further identify larger diamonds after the initial crushing to retrieve them before secondary crushing (Chadwick, 1981).

In 1978, a 130 ct colorless diamond was recovered, which mine manager Keith Whitelock noted would help defray operating costs for a year. Diamond prices peaked in 1980, with the high-quality stones leading the way. But prices fell sharply the following year and continued sliding. In 1982, De Beers decided to close operations (figure 11) because the cost of running Letšeng had become untenable (Blauer, 2010).

For its five years of operation, De Beers's production totaled 272,840 carats recovered from processing 9.4 million tons of kimberlite at the Main pipe, for a grade of 3.03 carats per hundred metric tons (table 2). About 65% of the output was gem quality, while 27% was industrial and 8% was bort (suited for crushing into abrasives). Only 7.6% of the production was larger than 14.7 ct, yet these accounted for 62% of the mine's revenue (Venter, 2003).

## SECOND LIFE FOR LETŠENG

After De Beers's departure, the mine was worked sporadically by artisanal diggers from 1983 to 2003, but

no formal mining was done. A second life for Letšeng began in 1999 when the Lesotho government, coming off several years of political instability and violent demonstrations in Maseru, sought help to redevelop the resource to provide sorely needed national revenue (Shor and Weldon, 2014). The result was a consortium, Letšeng Holdings SA, comprised of Matodzi Resources, Johannesburg Consolidated Investments (JCI), and Letšeng Guernsey, that took a 76% share in the venture, with the government holding the remainder. JCI, a South African gold mining firm, provided the start-up funding of approximately US$20 million (Venter, 2003). After extensive negotiations, the government and consortium agreed to a 7% royalty on diamonds sold, coupled with a 35% corporate income tax—much lower than the 15% royalty and 50% corporate tax levied on De Beers (Venter, 2003). By the time the mine was ready to begin producing, JCI had acquired a 50% share of the Letšeng Holdings consortium and commissioned a second processing plant designed to double its capacity. Mining began in May 2004, starting with the ore that De Beers had left stockpiled. The company



Figure 11. Diamonds over 3 ct, such as these two diamonds found recently at the recovery plant at Letšeng, were extracted from tailings left behind from De Beers's operation at Letšeng-la-Terae. Photo by Robert Weldon/GIA; courtesy of Letšeng Diamonds.

anticipated an annual output of 68,000 carats beginning the following year (Hill, 2006; Telfer and McKenna, 2011).

**TABLE 2.** Diamond production of Letšeng, 1955–2014.

| Period | Carats | Ore (metric tons) | Value/ct (US$) | Grade (cpht) | Operator |
|--------|--------|-------------------|----------------|--------------|----------|
| 1955–1968 | 62,070 | nd | nd | nd | artisanal |
| 1969–1972 | 2,000 | 80,000 | nd | 2.5 | RTZ |
| 1972–1976 | 43,000 | nd | nd | nd | artisanal |
| 1977–1982 | 272,840 | 9.4 M | nd | 3.03 | De Beers |
| 1983–2003 | 117,000 | nd | nd | nd | artisanal |
| 2004 | 14,000 | nd | nd | nd | Letšeng-JCI |
| 2005 | 37,000 | nd | nd | nd | Letšeng-JCI |
| 2006 | 54,677 | 2.6 M | 1,100 | 2.11 | Letšeng-JCI |
| 2007 | 73,916 | 4.0 M | 1,976 | 1.85 | Letšeng–Gem Diamonds |
| 2008 | 101,125 | 6.6 M | 2,123 | 1.53 | Letšeng–Gem Diamonds |
| 2009 | 90,878 | 7.5 M | 1,534 | 1.21 | Letšeng–Gem Diamonds |
| 2010 | 90,933 | 7.6 M | 2,149 | 2.00 | Letšeng–Gem Diamonds |
| 2011 | 112,367 | 6.8 M | 2,776 | 1.65 | Letšeng–Gem Diamonds |
| 2012 | 114,350 | 6.6 M | 1,932 | 1.75 | Letšeng–Gem Diamonds |
| 2013 | 95,053 | 6.5 M | 2,050 | 1.46 | Letšeng–Gem Diamonds |
| 2014 | 108,596 | 6.4 M | 2,540 | 1.70 | Letšeng–Gem Diamonds |

*Value in US$ per carat; cpht = carats per 100 metric tons; nd = no data*
*Sources: Bowen et al. (2009) and Gem Diamonds annual reports for 2007 to 2014*

*Figure 12. This state-of-the-art processing plant at Letšeng is designed to minimize damage to large diamonds and improve the recovery rate. The plant takes advantage of the region's mountainous topography by incorporating a gravity-fed recovery process. Photo by Robert Weldon/GIA.*

Expansion began in earnest in 2005, when Letšeng Holdings held an initial public offering (IPO) with the goal of raising $31.4 million to build the new processing plant (figure 12). The sale was buoyed by the discovery of a 186 ct diamond, quickly followed by a 72 ct stone (Zhuwakinyu, 2005).

Despite the IPO, the company fell short of the additional $26 million needed to develop the mine to full operation. As a result, JCI began negotiations to sell the Letšeng Holdings stake to Gem Diamonds, a deal that was finally signed in the fall of 2006 for $130.1 million. It resulted in a restructured ownership with a new name, Letšeng Diamonds Ltd. The government took a 6% larger stake, now totaling 30%, in exchange for a $5.54 million loan that would be repaid to the new company (Hill, 2006). Gem Diamonds owns the remaining 70% interest.

Restarting production remained a challenge because of the difficulties noted above and because the depth of the deposit was never fully sampled by Rio Tinto or De Beers (R. Burrell, pers. comm., 2014).

## MINING AND PROCESSING

When Gem Diamonds acquired the right to mine the concession in 2006, Letšeng had resumed active mining for just over a year, with an annual production of 55,000 carats. To lower costs and increase efficiency, Gem Diamonds turned to a relatively new mining method, designed for twin pipes, called split-shell open-pit mining. Traditional open-pit diamond mining involves gradual hollowing out of the entire kimberlite pipe in circular stages and, as the pit grows deeper, cutting away walls in progressively wider concentric circles. With each circle, the cut (or "waste stripping") becomes wider, so deeper mines incur increasingly higher costs as the percentage of waste to kimberlite rises. In addition, waste disposal becomes much more costly.

With the split-shell concept, the waste stripping and mining is done on one side of each pit in alternate cycles—one cycle on the northern side of each pit, then switching to the southern side. The waste is removed via a common ramp between the two pipes. The split-shell method can target higher-grade areas of each pipe and defer a large amount of waste stripping, because only part of the kimberlite is being mined at any one time. As a result, mining companies can recoup their costs much faster. A study conducted at De Beers's Venetia mine in South Africa, which converted to the split-shell method after seven years of traditional mining, found it reduced costs by 25%. Earthmoving equipment requirements were reduced by 30%, and yearly waste removal went from 32 million to 20 million metric tons, while maintaining the same level of diamond production (Gallagher and Kear, 2001).

There are risks, however. First, concentrating mining operations in the highest-grade sections of the deposit for too long can shorten the mine's life by rendering the lowest-grade areas of the pipe uneconomic. Mining operations must be carefully balanced between the sections of the pipe to ensure this does not happen. In addition, the costs will eventually rise after it becomes necessary to remove the waste from the sections of the pipe that have been deferred (Gallagher and Kear, 2001).

At Letšeng, De Beers mined a small section called K6, the highest-grade portion of the Main pipe down to 120 meters, and began working the "softer ore" section of the Satellite pipe (Telfer and McKenna, 2011). Today, most of the mining is done in the area adjacent to the section De Beers worked (K4). The Main and Satellite pipes are being worked at about 150 meters, with indicated resources (sampled with reasonable knowledge of the grade) down to 210 meters. Gem Diamonds engineers note that the mine's previous operators did not adequately sample deeper areas of the pipe. The company has recently sampled down to a depth of 476 meters at the Main pipe, still finding diamonds but uncertain of the grade. This is an inferred resource. The Satellite pipe has an in-

**TABLE 3.** Probable mining reserves as of December 31, 2010.

| Occurrence | Tonnage | Grade (cpht)[a] | Carats | Value per carat |
|---|---|---|---|---|
| Satellite pipe | 17.02 M | 2.07 | 353,000 | US$3,170 |
| Main pipe | 59.22 M | 1.46 | 867,000 | US$2,414 |
| Stockpile | 0.17 M | 0.87 | 1,500 | US$1,209 |
| Total | 76.41 M | 1.60 | 1,221,700 | US$2,631 |

[a]cpht = carats per 100 metric tons

ferred resource down to 628 meters. The company has test-bored as deep as 800 meters and is still evaluating the samples (R. Burrell, pers. comm., 2014).

A 2011 report noted that indicated resources as of December 31, 2010, were calculated at about 77 Mt (million metric tons), at a grade of 1.61 carats per hundred metric tons (cpht), yielding 1,238,000 carats worth $2,629 per carat at 2011 market prices, or roughly $33 billion. Inferred resources added another 141 Mt at a grade of 1.72 cpht, yielding 2,423,200 carats worth $2,733 per carat, or $67 billion (Telfer and McKenna, 2011). This equates to a 30-year mine life. A more immediate probable mining *reserve* is calculated at 76.4 Mt at a grade of 1.60 cpht, yielding 1,221,700 carats worth $2,631 per carat in 2011 (see also tables 3 and 4).

Letšeng is also unusual in that it yields only a small percentage of diamonds less than two millimeters. Because of this, the recovery operations do not screen for diamonds below that size (Bowen et al., 2009).

From these figures, the value of one ton of ore can be calculated as roughly $42, which is in line with other economic kimberlite mines in southern Africa. Previous and current mining has shown that the Satellite pipe has a slightly higher grade and a slightly higher content of large diamonds than the Main pipe (Telfer and McKenna, 2011).

**TABLE 4.** Probable, indicated, and inferred reserves of Letšeng, as of December 31, 2014.

| | Probable | Indicated | Inferred | Total |
|---|---|---|---|---|
| Ore (million tons) | 131.9 | 187.1 | 106.8 | 293.9 |
| Grade (ct/100 tons) | 1.71 | 1.73 | 1.67 | 1.71 |
| Carats (million) | 2.26 | 3.23 | 1.78 | 5.01 |
| Value per carat | US$2,045 | US$2,036 | US$2,051 | US$2,073 |

Source: Gem Diamonds Ltd. (2015a)

Complicating the mining of the Satellite pit is that during the kimberlite eruption 90 million years ago, an immense chunk of basalt country rock—about 1 hectare (10,000 square meters) wide and 150 meters deep—was detached into the southern section of the kimberlite pipe. This creates an immense waste expense and an obstacle to mining the pipe (see figure 6, bottom). Current plans are to mine the open pits until 2038 (Gem Diamonds Ltd., 2015b).

Letšeng produces approximately seven million metric tons of ore and 20 million metric tons of waste per year and employs local contractors for much of its mining activities, with the exception of blasting. Drilling is done with Atlas Copco Roc L8 and L6 machines. The mine employs a mixed loading and hauling fleet of Caterpillar 385C and 390D excavators, together with Caterpillar 773 (50-ton capacity) rigid-body dump trucks for hauling waste and Caterpillar 740 (40-ton capacity) articulated dump trucks hauling ore (figure 13). The mixed fleet is suited for handling different ore and waste profiles during various stages of mine development.

**IMPROVING RECOVERY AT LETŠENG**

Letšeng's financial model is dependent upon its ability to recover large stones intact. Because of this, standard diamond recovery processes, which crush the ore into small pieces for fast, efficient recovery, cannot be used without major modifications. Gem Diamonds invested $9.9 million in new diamond

*Figure 13. A 50-ton dump truck and front-end loader remove the kimberlite ore after blasting at the bottom of the Main diamond pipe. Photo by Robert Weldon/ GIA; courtesy of Letšeng Diamonds.*

processing technology to spare the large stones, all because of changes in the diamond market since the mine first operated in the 1970s and 1980s. As Gem Diamonds chief executive officer Clifford Elphick explained, prices for very large diamonds were relatively low compared to smaller stones, so it was more cost-efficient to damage such goods during processing in the name of speed. In recent years, however, the rising number of billionaires and ultra-wealthy connoisseurs has pushed prices of major diamonds to record levels. Now mines must increasingly focus on recovering these high-value stones—especially as they go deeper and mining costs rise.

After Gem Diamonds acquired a majority share of Letšeng Diamonds, the company built a second treatment plant that would double the mine's capacity. The plant's owners also introduced new technology to minimize damage to large diamonds and reduce construction and operating costs. The design of Plant 2 took advantage of the mine's topography, with the processing plant set on a 17° slope. Material would be fed from the top end, letting it flow downward stage by stage through the separating and crushing processes, reducing the need for pumps and conveyors (Bornman, 2010). Plant 2 went online in the fall of 2008. Together the two plants treat 5.7 mil-

*Figure 14. Inside Plant 2, an observation window into the conveyor belt taking the large pieces of kimberlite to the crushers. Photo by Robert Weldon/GIA; courtesy of Letšeng Diamonds.*
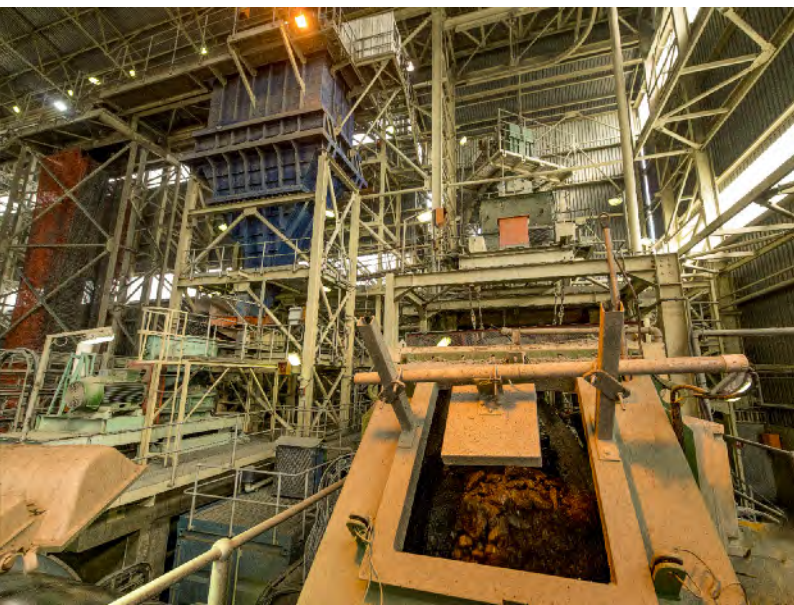


**TABLE 5.** Production of large diamonds at Letšeng, 2005–2014.

| Size (ct) | 2005 | 2006 | 2007 | 2008 | 2009 | 2010 | 2011 | 2012 | 2013 | 2014 |
|---|---|---|---|---|---|---|---|---|---|---|
| >100 | 6 | 5 | 5 | 7 | 5 | 6 | 5 | 3 | 7 | 7 |
| 60–100 | 7 | 14 | 9 | 16 | 10 | 10 | 19 | 13 | 16 | 21 |
| 30–60 | 30 | 40 | 39 | 74 | 76 | 61 | 59 | 61 | 50 | 69 |
| 20–30 | 49 | 47 | 65 | 88 | 98 | 89 | 91 | 110 | 71 | 101 |
| Total >20 ct | 92 | 106 | 118 | 185 | 189 | 166 | 174 | 187 | 144 | 198 |

*Source: Gem Diamonds annual reports*

lion metric tons of ore per year. An additional 1.3 million tons per year, mainly from waste dumps, are processed by an outside contractor, Alluvial Ventures, through their two plants.

The primary ore crushers break the large kimberlite blocks into pieces about 125 mm in diameter. From there the ore goes through a scrubbing process that uses vibration to remove excess clay, rock, and other foreign matter. In this process, the kimberlite pieces grinding together do the scrubbing without additional grinding agents that could damage the stones. From there they proceed by slurry to the coarse crushing, which sizes the material down to 45 mm diameter—a 200 ct rough is approximately 30 mm in diameter.

Although the company had recovered a number of large diamonds by 2013, executives remained concerned that major stones were not surviving the crushing process, particularly because Letšeng type IIa diamonds generally display excellent cleavage, and a significant proportion of them are cleavage fragments (Bowen et al., 2009). At the beginning of that year, the throughput of ore was deliberately slowed to allow closer observation of the conveyor to spot large stones (figure 14). After several months, though, there was still no clear correlation between processing speed and diamond damage.

In the second quarter of 2013, the company replaced the Plant 2 crushers, large steel jaws that broke the ore down to small pieces in three stages, with a cone crushing system, configured specifically for Letšeng's production (Cornish, 2013). In this new system, the ore is loaded into a receptacle and passed over a rapidly spinning cone that also oscillates side to side, crushing the ore against the sides of the passage without exerting the diamond-damaging pressure of the jaw system (Gem Diamonds Ltd., 2014). Gem Diamonds subsequently replaced the crushers in Plant 1 as well. According to Letšeng Diamonds

*Figure 15. Mazvi Maharasoa, CEO of Letšeng Diamonds, the joint venture between Gem Diamonds and the Lesotho government, photographed in front of the processing plant. Photo by Russell Shor/GIA; courtesy of Letšeng Diamonds.*

chief executive officer Mazvi Maharasoa (figure 15), the new crushers sized the kimberlite chunks into pieces roughly 50 mm (about 2 inches) in diameter, instead of 20 mm as in the past.

The result, beginning in May 2013, was an immediate improvement in the number of large diamonds recovered. From January through April 2013, Letšeng yielded one diamond over 100 carats and three diamonds between 45 and 55 carats (table 5). From May 2013 until year's end, 17 very large diamonds were recovered, including one over 150 carats, three that were approximately 100 carats, and 13 between 60 and 80 carats (Gem Diamonds Ltd., 2014).

After crushing, the kimberlite pieces are conveyed to the recovery area, where the diamonds are separated from waste rock by X-ray technology. XRL (X-ray luminescence) and XRF (X-ray fluorescence) units, developed in the 1980s, take advantage of the fact that diamonds will fluoresce when exposed to intense X-rays. The crushed kimberlite particles are dropped in a thin stream under a beam of X-rays. When a diamond fluoresces, it activates a photo-detector, triggering a jet of air that deflects the diamond into a collector box (Valbom and Dellas, 2010). Older X-ray recovery units identified diamonds by fluorescence alone, causing nonfluorescent diamonds (which include many type II) and some fancy-color diamonds to slip through to the waste piles. More recent methods adopted at Letšeng employ X-ray transmissive (XRT) technology before the crushing process to identify large rough type II crys-

tals by measuring their specific radiometric response to X-rays and eject them from further processing (Cornish, 2013). The general principle behind XRT is that diamond shows up as a much brighter image than other Si-bearing minerals. Minerals containing Fe or heavier elements will show up even darker. XRT sorting does not rely upon a diamond's transparency because it does not deal with visible light range. Even if the sample is sufficiently coated to be completely opaque, the XRT sorter will detect it. The company tested these X-ray units on tailings, recovering $12 million worth of diamonds over six months (Cornish, 2013; Gem Diamonds Ltd., 2014).

## CHARACTERISTICS AND MARKETING OF LETŠENG DIAMONDS

The Letšeng mine is famous for its very large diamonds (tables 1 and 5). The largest, the Lesotho Promise (figure 16), was discovered in 2006. At 603 ct, it surpassed the 601.26 ct Lesotho Brown. Although only marginally larger, the Lesotho Promise is a type IIa diamond, and its absence of color resulted in a stunning collection of 26 diamonds of D color and Flawless clarity (figure 17). A significant percentage of diamonds from Letšeng have exceptional clarity and transparency, no fluorescence, and

*Figure 16. The 603 ct Lesotho Promise is the fifteenth-largest rough diamond ever discovered. London luxury jeweler Laurence Graff purchased it in 2006 for $12.4 million. Photo courtesy of Laurence Graff.*

## BOX B: MORPHOLOGY OF LETŠENG DIAMONDS

Most natural gem-quality diamonds contain nitrogen impurities (type I) and grow in the form of an octahedron. A small percentage contain no measureable nitrogen impurities in their lattice (type II) and often occur as irregular, flattened, or elongate crystals. Diamonds usually crystallize in the earth's mantle in rocks known as peridotites or eclogites. These are picked up and transported to the surface by a type of molten rock called kimberlite.

Figure B-1. With increasing resorption, the morphology of a diamond crystal changes from octahedral to dodecahedral forms. From Tappert and Tappert (2011).
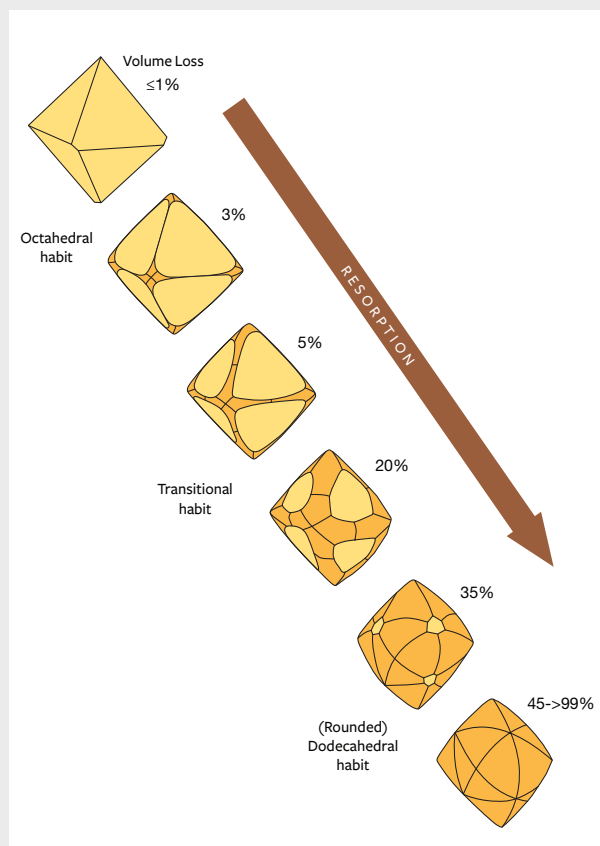




Figure B-2. These diamonds, each weighing approximately 4 ct, represent several days of mine production at Letšeng in September 2014. Most crystals show strong resorption features and dodecahedral forms. Photo by Robert Weldon/GIA.

Diamonds are chemically unstable in a kimberlite magma, and the outer surface of the diamond is often etched and partially dissolved during transport, a process known as resorption. This process causes an octahedron to lose volume and gradually convert to a dodecahedral form (figure B-1).

Several days of production at the Letšeng mine in September 2014 yielded the group of approximately 4 ct diamonds seen in figure B-2. Nearly all of them revealed strong resorption marked by smooth, rounded surfaces with indistinct features. The near-colorless and brown stones showed irregular shapes, typical of type IIa diamonds, whereas the three yellow type Ia diamonds in the center presented obvious dodecahedral forms. Of the larger stones in figure B-3 (approximately 8–10 ct range) that were available during the mine visit, all were near-

are classified as D-color and Flawless (figure 18). They are type IIa diamonds with roughly dodecahedral shapes; octahedral shapes are very rare, comprising less than 1% of the Letšeng population (Harris, 1973; Bowen et al., 2009; see box B).

In 2014, Letšeng reported that it found seven diamonds over 100 ct. By year's end it had sold five of them, which represented 14% of Letšeng's total sales

for the year. The mine recovered a record 198 diamonds larger than 20 ct, 54 more than the previous year. Letšeng's 2014 production was valued at an average of $2,540 per carat, buoyed during the final quarter by the recovery of 13 large diamonds whose price exceeded $1 million each, including a 299.3 ct yellow diamond (price undisclosed), a 112.6 ct colorless diamond that sold for $5.8 million, and a 90.4 ct

Figure B-3. Larger diamonds from Letšeng, like these crystals ranging from 8 to 10 ct, were usually type IIa with irregular forms. Photo by Robert Weldon/GIA.

colorless to slightly brownish with distinctive resorption features and irregular or elongate shapes, characteristics indicative of type IIa diamonds.

Letšeng diamonds are well known for some degree of dodecahedral form, with more than 95% of the recovered stones showing significant resorption effects (Bowen et al., 2009). The mine is also known for producing a high percentage of large type IIa diamonds of exceptional color and clarity, but with irregular crystal forms. The Letšeng mine production available to the authors was consistent on both counts.

Type IIa diamonds from Letšeng usually have irregular shapes. The 22.87 ct type IIa stone in figure B-4 (left) has excellent color and clarity but no distinct form other than a single octahedral face with visible trigons. In contrast, type Ia diamonds show more distinct forms such as the partially resorbed 32.97 ct yellow octahedron in figure B-4 (right). Octahedral forms like this are relatively rare at Letšeng.




Figure B-4. These two crystals from Letšeng illustrate the morphological differences between irregularly shaped type IIa diamonds such as the 22+ ct stone on the left and type Ia octahedral stones such as the 32+ ct stone on the right. Photos by Robert Weldon/GIA.

colorless diamond that brought $4.2 million (Max, 2015). In the first half of 2015, the average value slipped to $2,264 per carat, though 13 diamonds offered during that period sold for more than $1 million each (Gem Diamonds Ltd., 2015c).

The initial sorting and valuing is done at the mine site to satisfy the Kimberley Process (KP) requirements for export and to establish values for the gov-ernment, which receives at present a 7% royalty based on value. From the mine they are exported to Antwerp, where they undergo another KP check before proceeding to the company's sales office at Lange Herentalsestraat in the city's diamond district. At the sales office, the rough is cleaned by an acid wash to remove all surface material and then revalued and sorted for sale (C. Elphick, pers. comm., 2014). Dur-

Figure 17. Twenty-six D-Flawless diamonds of various shapes cut from the Lesotho Promise were assembled by Graff into a necklace valued at $60 million. Photo courtesy of Laurence Graff.

ing the sorting process, the Antwerp sales team first sets reserve prices on individual rough diamonds larger than 10.8 ct and then on parcels of smaller

Figure 18. This group of type IIa rough diamonds ranges from almost 14 ct to 91.07 ct. Such diamonds make Letšeng a feasible mining proposition. Photo by Robert Weldon/GIA; courtesy of Gem Diamonds Ltd.





Figure 19. This rough diamond dodecahedron from Letšeng weighs 11.14 ct. Given its rare, attractive shape and color, the stone would command a high asking price at auction. Photo by Robert Weldon/GIA; courtesy of Gem Diamonds Ltd.

goods grouped by weight, quality, and shape.

Letšeng rough is offered ten times per year in on-line auctions conducted through its Antwerp office (figure 19). Diamonds larger than 100 ct are offered individually in special sales.

Unlike other smaller diamond producers, Gem Diamonds maintains its own sales office and does not employ a contractor. Selling its own goods in this manner provides Letšeng with complete flexibility over the marketing of its rough production, said CEO Clifford Elphick (figure 20), while reducing sales and marketing costs from 2.5% to 1.5%.

"We have about 150 customers for each sale," said Elphick. "They have a ten-day viewing period to review the goods, and can bid up to the final minute."

Unlike some rough diamond auction models where high bids are averaged into across-the-board prices for a particular category, the winners buy their lots for their high bid price. "Occasionally, if a bid seems unrealistically high, we will ask the client to review it," Elphick explained. "Once in a while some people misplace a decimal point."

Elphick noted that in the eight years of selling diamonds from Letšeng, both the sales staff and clients have developed a strong understanding of the goods and their prices, so the process usually runs very smoothly.

While the very large stones capture the headlines and high price tags, most of Letšeng's earnings come from commercial goods (figure 21) and 5–15 ct goods, which actually achieve the highest per-carat prices. "We get prices over $50,000 per carat for the top qualities: type II goods of high color, which we call

Figure 20. Clifford Elphick, CEO of Gem Diamonds, emphasizes the value of large type IIa diamonds but notes that a significant portion of production includes commercial goods. Photo courtesy of Gem Diamonds Ltd.



Figure 22. These rough diamonds, a 3.72 ct faint pink and a 9.55 ct grayish blue stone, are from Letšeng's limited production of fancies. Photo by Robert Weldon/GIA; courtesy of Gem Diamonds Ltd.

'Letšeng-y,'" he said. "The cutters like these because they are easy to work, with high yields. Many of them polish to D color—perhaps a little higher than a normal D, because they are type II with very little graining."

In addition, the mine occasionally produces some fancy-color diamonds—two or three blues a year, and a larger number of pinks and yellows (figure 22).

Elphick explained that the explosion in the num-ber of ultra-wealthy individuals over the past 15 years has sparked demand for large, high-quality di-amonds, driving prices higher and making Letšeng profitable to mine again. But Elphick added that the per-carat price begins diminishing above 15 carats be-cause of the risks still inherent in diamond cutting. "If they make a mistake on a ten-carat stone, it won't put them out of business. But when millions of dol-lars are involved, they have to hedge a bit."

Lots that do not sell at the company tender auc-tions are sent to contractors for polishing. These ac-



Figure 21. During a visit to Letšeng, the authors were offered the oppor-tunity to photograph several days' worth of production. The mine produces a number of "three-grainers," such as this group of 88 stones weighing a total of 66.40 carats. Photo by Robert Weldon/GIA; courtesy of Letšeng Dia-monds.

*Figure 23. These rough diamonds (22.30, 91.07, and 23.37 ct) were auctioned through Letšeng's sales office in Antwerp. Such exceptional type IIa diamonds of unusual shape—many are cleavage fragments like these—comprise a significant part of Letšeng's production and offer the tantalizing possibility that they were once parts of larger gems. Photo by Robert Weldon/GIA; courtesy of Gem Diamonds Ltd.*

count for $15 to $20 million yearly, he said, noting that most of the buyers for polished goods are also the company's rough clients.

All of Letšeng's unsold rough is polished in Antwerp. Elphick and Maharasoa both stated that the plan is to establish a polishing operation in Maseru as part of a goal for the mine to contribute 15% of Lesotho's gross national product. Elphick said that the company already has the space to begin a small polishing operation in the capital but is awaiting permits from the government.

"It could never become a large operation that would compete with those in India," Elphick acknowledges, "but we can start small and see if we can expand later."

## CONCLUSIONS

The Letšeng mine is a unique diamond resource whose economic viability has been realized by strong increases in per-carat prices for large diamonds since 2000. While earlier attempts to mine the deposit were unsuccessful because of the low ore grade and the challenges of moving equipment to a remote location high in the mountains of Lesotho, the mine's current majority owner has invested in radically modified diamond recovery methods to greatly reduce the damage to large diamonds, particularly those above 50 ct. The company markets Letšeng's unique production through its own sales office in Antwerp (figure 23), via regularly scheduled auctions. Despite the profitability, there is concern that the mining license is finite, expiring in 2019, and that a renewal may carry more costly terms. In a 2010 paper, Mazvi Maharasoa, CEO of Letšeng Diamonds, noted that operating costs of 70 million loti per year (US$6 million) were too high given the finite nature of the lease, the fluctuating exchange rates, and the costs of building and maintaining access roads and transporting supplies. Demand for very large diamonds such as those produced at Letšeng has remained high through turbulent economic times, and the mine's operators are confident that it will continue to yield large diamonds, the sale of which will make headlines around the world.

### ABOUT THE AUTHORS
*Mr. Shor is senior industry analyst, Mr. Weldon is manager of photography and visual communications, and Dr. Breeding is a research scientist, at GIA in Carlsbad, California. Dr. Janse is a diamond exploration consultant living in Perth, Western Australia. Dr. Shirey is a senior scientist in the Department of Terrestrial Magnetism of the Carnegie Institution in Washington, DC.*

## REFERENCES

Balfour I. (1981) Famous diamonds of the world (X): the Lesotho Brown. *Indiaqua*, Vol. 29, No. 2, pp. 123–125.

Blauer E. (2010) De Beers sells historic mines. *Rapaport Diamond Report*, Vol. 33, No. 9, pp. 66–67.

Bloomer A.G., Nixon P.H. (1973) The geology of Letseng-la-terae kimberlite pipes. In P.H. Nixon, Ed., *Lesotho Kimberlites*, Lesotho National Development Corporation, Maseru, pp. 20–36.

Bornman F. (2010) Letšeng mine no. 2 plant project – A process engineering and design review. *Southern African Institute of Mining and Metallurgy: Diamonds—Source to Use 2010*, Vol. 110, No. 11 (November), pp. 271–284, http://www.saimm.co.za/Conferences/DiamondsSourceToUse2010/271-Bornman.pdf

Bowen D.C., Ferraris R.D., Palmer C.E., Ward J.D. (2009) On the unusual characteristics of the diamonds from Letšeng-la-Terae kimberlites, Lesotho. *Lithos*, Vol. 112S, pp. 767–774, http://dx.doi.org/10.1016/j.lithos.2009.04.026

Chadwick J. (1981) Big stones offset low grade at Lesotho's diamond mine. *Indiaqua*, Vol. 29, No. 2, pp. 27–33.

Cornish L. (2013) Gem Diamonds' big expansion, on a minimal budget. *Mining News*, May 16, http://www.miningne.ws/2013/05/16/a-big-expansion-on-a-minimal-budget-for-gem-diamonds/

Davis G.L. (1977) The ages and uranium content of kimberlites and associated rocks. *Carnegie Institution of Washington Yearbook 1976*, pp. 631–654.

De Beers Consolidated Mines Limited (1975) Letšeng-la-Terai. Press release, March 4.

Gallagher M.S., Kear R.M. (2001) Split shell open pit design concept applied at De Beers Venetia mine South Africa using the Whittle and Gemcom software. *Journal of the Southern African Institute of Mining and Metallurgy*, Vol. 101, No. 8, pp. 401–409, http://www.saimm.co.za/Journal/v101n08p401.pdf

Gem Diamonds Ltd. (2014) Annual report 2013, http://www.gemdiamonds.com/gem/uploads/reports/reports/Gem-Diamonds-AR.pdf

Gem Diamonds Ltd. (2015a) Annual report 2014, http://www.gemdiamonds.com/gem/uploads/reports/reports/gem-diamonds-ar-2014.pdf

Gem Diamonds Ltd. (2015b) Letšeng Mine - Life of Mine 2015, http://www.gemdiamonds.com/gem/uploads/reports/presentation/2015-05-22-letseng-life-of-mine-plan-update-presentation-may-2015.pdf

Gem Diamonds Ltd. (2015c) H1 2015 trading update, July 30, http://www.gemdiamonds.com/gem/en/media/press-releases/?ref=279

Harris J.W. (1973) Observations on Letseng-la-terae diamonds. In P.H. Nixon, Ed., *Lesotho Kimberlites*, pp. 37–38.

Hill M. (2006) Gem all set for Letseng expansion as JCI approves sale. *Mining Weekly*, September 28, http://www.miningweekly.com/article/gem-all-set-for-letseng-expansion-as-jci-approves-sale-2006-09-29

Jackie O Lesotho II diamond sells for $2.6 million at Sotheby's (1996) *Rapaport*, http://www.diamonds.net/News/NewsItem.aspx?ArticleID=1203

Janse A.J.A. (1994) Is Clifford's Rule still valid? Affirmative examples from around the world. In H.O.A. Meyer and O. Leonardos, Eds., *Proceedings of the Fifth International Kimberlite Conference 2, Diamonds: Characterization*, Genesis and Exploration, pp. 215–235. Departamento Nacional da Produção Mineral, Brasilia, 390 pp.

Krawitz A. (2014) De Beers value proposition. *Rapaport*, http://www.diamonds.net/News/NewsItem.aspx?ArticleID=48494&ArticleTitle=De+Beers+Value+Proposition

Latest reports from the Lesotho Dept. of Mines (1978) *Diamond News and S.A. Jeweller*, Vol. 40, No. 1, pp. 35–37.

Lesotho (2014) South African History Online, http://www.sahistory.org.za/places/lesotho

Lock N.P., Dawson J.B. (2013) Contrasting garnet lherzolite xenolith suites from the Letseng kimberlite pipes: inferences for the northern Lesotho geotherm. *Proceedings of the 10th International Kimberlite Conference*, Vol. 1, pp. 29–42. Bangalore. Geological Society of India, Special Issue, 350 pp.

Madowe A. (2013) The mining process for an open pit diamond mining operation — A case study on Letseng diamond mine in Lesotho. *Journal of the Southern African Institute of Mining and Metallurgy*, Vol. 113, No. 7, pp. 547–554, http://www.saimm.co.za/Journal/v113n07p547.pdf

Maharasoa M. (2010) A company perspective on mining in Lesotho. Rethinking the management of mineral resources in Lesotho. *Southern Africa Resource Watch*, No. 6, pp. 32–33, http://www.archive-org-2013.com/org/s/2013-11-23_3214541_28/Rethinking-the-Management-of-Mineral-Resources-in-Lesotho-sarwatch-org

Maleleka D. (2007) Diamond mining in Lesotho. *Southern Africa Resource Watch*, No. 4, September, http://www.resourcegovernance.org/sites/default/files/LesothoFA.pdf

Max D. (2015) Gem Diamonds' Q4 "encouraging end to positive year." *Idex*, Jan. 27, http://www.idexonline.com/FullArticle?id=40358

Nixon P.H. (1960) A mineralogical and geochemical study of kimberlites and the associated xenoliths. Unpublished PhD thesis, University of Leeds.

Nixon P.H., Ed. (1973) *Lesotho Kimberlites*. Lesotho National Development Corporation, Maseru, 350 pp.

Onstream, upstream (1977) *Indiaqua*, Vol. 15, No. 1, pp. 20–21.

Payne A. (1975) Lesotho signs up with De Beers. *Rand Daily Mail*, Feb. 5.

Scott Smith B.H., Nowicki T.E., Russell J.K., Webb K.J., Hetman C.M., Harder M., Mitchell R.H. (2008) Kimberlites: Descriptive geological nomenclature and classification. 9th International Kimberlite Conference, Extended Abstract A-00124.

Shirey S.B., Shigley J.E. (2013) Recent advances in the understanding of the geology of diamonds. *G&G*, Vol. 49, No. 4, pp. 188–222.

Shor R., Weldon R. (2014) Diamonds from the roof of the world. *GIA Research & News*, http://www.gia.edu/gia-research-news-diamonds-roof-world-shor-weldon

Sotheby's (2008) Magnificent and extremely rare diamonds to be offered in Geneva on November 19, 2008. Press release.

Stockley G.M. (1947) Report on the Geology of Basutoland. Basutoland Government, Maseru, pp. vii, 7–114.

Tappert R., Tappert M.C. (2011) *Diamonds in Nature: A Guide to Rough Diamonds*. Springer-Verlag, Berlin and Heidelberg, p. 21.

Telfer C.A., McKenna N. (2011) National Instrument NI43-101: Technical Report on the Letšeng Diamond Assets in Lesotho. Venmyn Rand, Johannesburg, pp. 21–96.

Valbom D., Dellas G. (2010) State of the art recovery plant design. *Southern African Institute of Mining and Metallurgy*, Vol. 110, No. 11, pp. 243–252, http://www.saimm.co.za/Conferences/DiamondsSourceToUse2010/243-Valbom.pdf

Venter I. (2003) Lesotho gem-mine targets full output in 2004. *Mining Weekly*, Aug. 28, http://www.miningweekly.com/article/lesotho-gemmine-targets-full-output-in-2004-2003-08-29

Whitelock K. (1979) Letseng-la-Terai: The diamond mine at the turn by the swamp on the roof of Africa. *Optima*, Vol. 28, No. 2, pp. 120–136.

Wilson M.G.C., McKenna N., Lynn M.D. (2007) *The Occurrence of Diamonds in South Africa*. Council for Geoscience, Pretoria, 104 pp.

Zhuwakinyu M. (2005) Lesotho gem-miner to be dual listed. *Mining Weekly*, May 13, http://www.miningweekly.com/article/lesotho-gemminer-to-be-duallisted-2005-05-13

# ORIGIN DETERMINATION OF DOLOMITE-RELATED WHITE NEPHRITE THROUGH ITERATIVE-BINARY LINEAR DISCRIMINANT ANALYSIS

Zemin Luo, Mingxing Yang, and Andy H. Shen

Provenance studies on nephrite jade are of gemological as well as archeological importance. Origin determination is difficult to achieve relying solely on typical gemological properties and observations. In this study, the authors present a new statistical analysis method, based on linear discriminant analysis (LDA) and trace-element data from laser ablation–inductively coupled plasma–mass spectrometry (LA-ICP-MS), to achieve significantly improved origin determination (an average of 94.4% accuracy) for eight major dolomite-related nephrite deposits in eastern Asia. As the principle is to compare one location to the rest in one round and continue such binary comparison until all possible localities are tested, the method is referred to as iterative-binary LDA (IB-LDA). Combined with trace-element composition data from LA-ICP-MS, it could prove to be a useful technique for the geographic origin determination of other gemstones.

N ephrite jade has been of great interest to East Asian cultures dating back to the Neolithic Age (Wen and Jing, 1996; Tsien et al., 1996; Wen, 2001; Harlow and Sorensen, 2005). Historically, it has been considered a symbol of wealth and power for Chinese emperors and nobility (figures 1A and 1B). Nephrite from countries such as China, Russia, and South Korea (Ling et al., 2013) continues to attract considerable attention as a gem and ornamental material, particularly in the Chinese market. Thus, geographic origin determination is important in terms of proper classification, valuation, and archaeological implications.

In Chinese culture, white is usually regarded as the color of purity and perfection (He, 2009). Due to its quality and well-established historical reputation, white nephrite from Xinjiang has maintained the highest price in the Chinese market. Xinjiang nephrite is usually translucent, with colors ranging from white and greenish white to yellow. The best material from this province is white nephrite with greasy luster, known in the trade as "mutton fat" jade. The purity, fine texture, and luster of white nephrite from Xinjiang come together to create an elegant cultural symbol (figure 1C).

White nephrite from other deposits, including Baikal (Russia), Chuncheon (South Korea), and Qinghai (China), has similar characteristics and is difficult

## In Brief

- There is no universally accepted method to determine the origin of East Asian dolomite-related nephrite.

- IB-LDA, a statistical analysis method developed by the authors, uses an algorithm based on trace-element data to determine the origin of nephrite from eight major production areas in China, Russia, and South Korea.

- This method yielded greater accuracy than the traditional LDA method, and may be useful for determining the origins of other gem materials.

to distinguish with the unaided eye or even microscopic observation (Wu et al., 2002; Ling et al., 2013). In some cases, material from other locations has been falsely represented as Xinjiang nephrite jade to fetch higher prices. A reliable quantitative method for geographic origin determination is urgently needed to protect nephrite consumers.

Nephrite is a gem-quality tremolite or actinolite polycrystalline aggregate. It is usually classified as either dolomite-related or serpentine-associated, which
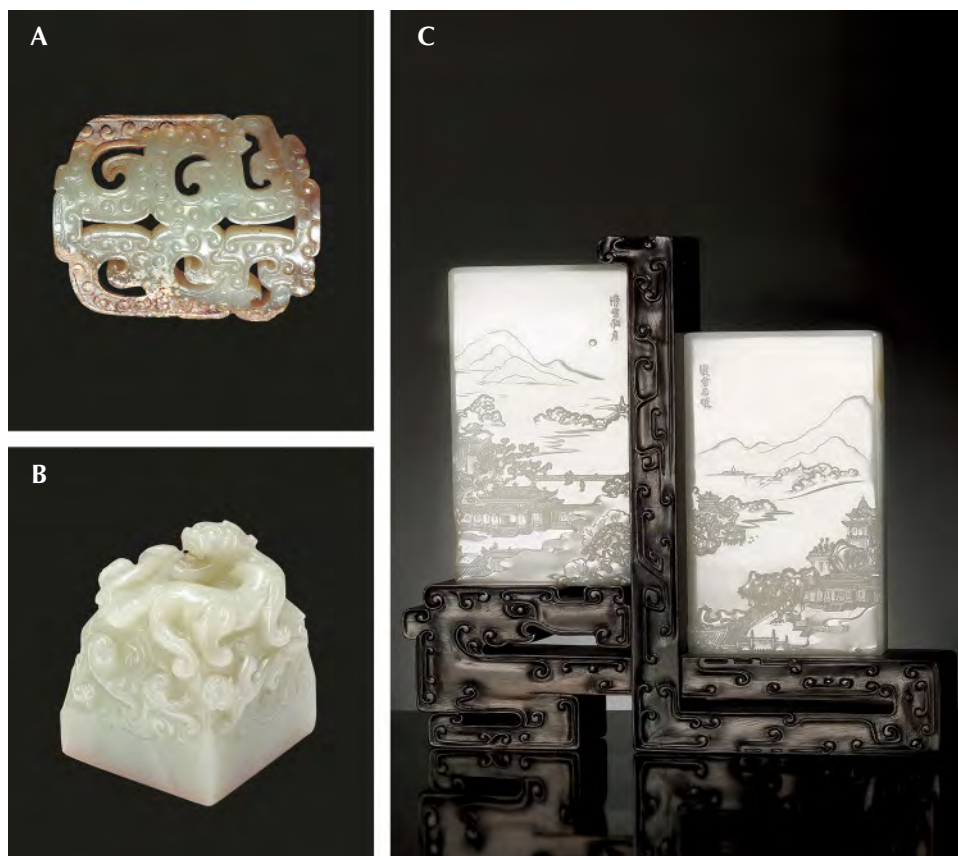
Figure 1. A: An ancient pendant discovered in the tomb of Marquis Yi, ruler of Zeng State during the Warring States period (ca. 475–221 BC). © Hubei Provincial Museum. B: The imperial seal made with white nephrite for Emperor Yongzheng during the Qing dynasty (1723–1735 AD). © Sotheby's. C: "Autumn Moon Over Han Palace" (left) and "Spring Morning Over Han Palace" (right) placed second in the Gems & Jewelry Trade Association of China's 2012 Tiangong Award for excellence in jade carving. © The Boguan Auction Company.

have different formation processes and different concentrations of Fe, Cr, Co, and Ni, as well as oxygen and deuterium isotopes (Yui and Kwon, 2002; Harlow and Sorensen, 2005; Siqin et al., 2012; Adamo and Bocchio, 2013). Dolomite-related nephrite is usually white, greenish white, yellow, or light gray, due to the relatively low concentrations of the transition metal elements listed above. Serpentine-associated nephrite is usually green. A typical example is Siberian green nephrite from Russia, known for its purity of color. The geographic sources of serpentine-associated nephrite, such as New Zealand, mainland China, and Taiwan, can be distinguished by some characteristic elements in chromite inclusions and by strontium isotopes (Adams et al., 2007; Zhang and Gan, 2011; Zhang et al., 2012).

There is no widely accepted method for distinguishing the geographic origin of dolomite-related nephrite. Two factors account for this. First, there are many sources for dolomite-related nephrite in East Asia. Eight major locations are listed in figure 2: western Xinjiang (including the famous Hetian area) and eastern Xinjiang province (China); Geermu, also known as Golmud (Qinghai province, China); Xi-

uyan (Liaoning province, China); Luodian (Guizhou province, China); Liyang (Jiangsu province, China); Baikal (Russia); and Chuncheon (South Korea). Second, because of their similar standard gemological properties, such as color, transparency, luster, refractive index, specific gravity, and major element components (Liao and Zhu, 2005; Ling et al., 2013; Liu and Cui, 2002), dolomite-related nephrite jades from these locations are very difficult to distinguish.

Geochemical research has shown that trace elements can reflect the sources of gemstones (Breeding and Shen, 2010; Blodgett and Shen, 2011; Shen et al., 2011; Zhong et al., 2013). But as the number of producing localities and the complexity of chemical composition increase, simply evaluating one or two elements cannot distinguish the different origins (Siqin et al., 2012). Multiple elements, and correlations between those elements, must be taken into account. Identifying and optimizing the variables that characterize differences among origins becomes the main focus.

Linear discriminant analysis (LDA) is a popular statistical method that can reduce the multiple dimensions of variables and provide reliable classifica-
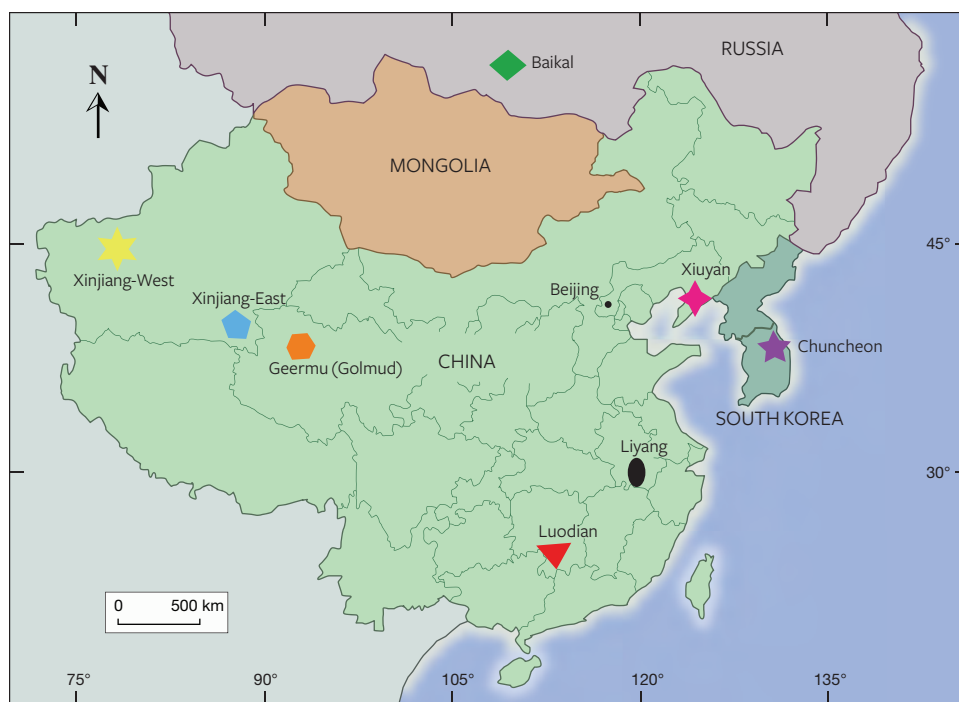
Figure 2. The eight major dolomite-related nephrite deposits in East Asia reviewed in this study. Xinjiang province has been divided into east and west regions because of their different ore-forming conditions (Tang et al., 1994). Modified from Ling et al. (2013).

tion accuracy (Fisher, 1936; Yu and Yang, 2001; McLachlan, 2004; Guo et al., 2007). Recently, this method has been used to identify the geographic origins of some single-crystal gemstones such as Paraíba tourmaline, ruby, sapphire, and peridot (Blodgett and Shen, 2011; Shen et al., 2013).

In this work, the trace-element composition and distribution of 138 dolomite-related nephrite samples from the major producing areas in East Asia have been carefully summarized. Based on the trace-element data, we propose an algorithm, which we refer to as iterative binary LDA (IB-LDA), to achieve nearly complete separation of the dolomite-related nephrite deposits. This method may have wide-ranging applications for additional mineral and gemstone origin research in the future.

## MATERIAL AND METHODS

**Sample Preparation.** All samples in this study were collected directly from the mines in eight major East Asian dolomite-related nephrite jade deposits. A total of 138 samples, with 15–19 specimens from each locality (see table 1), were chosen for LA-ICP-MS testing.

The samples were cut into blocks measuring 3.0 × 1.5 × 0.5 cm (length × width × height). The body-color ranged from white to light greenish, with scattered colors such as yellow in some samples. Samples with representative color from each deposit are shown in figure 3.

On each nephrite block, three to five points along a straight line with 5 mm intervals between each point were selected for LA-ICP-MS testing; see the "LA-ICP-MS Measurement" section below. We collected 60 test points for each origin for further statistical analysis, to be discussed in the "LDA Method" section. Due to the heterogeneous chemical composition of polycrystalline nephrite and the relatively limited number of block samples (only 15–19 per each origin), we treated each test point as an independent sample, so that each origin has a data set of 60 analyses.

**LA-ICP-MS Measurement.** Trace-element concentrations of the 138 samples were measured using an LA-ICP-MS system at the State Key Laboratory of Geological Processes and Mineral Resources, China University of Geosciences, Wuhan. The LA-ICP-MS system consisted of a GeoLas 193 nm laser and an Agilent 7500 ICP-MS. The laser fluence was set as 10 J/cm$^2$, and the ablation spot size was 32 μm. The widely used quantitative calibration standards of NIST synthetic glasses SRM610 (Pearce et al., 1997) and U.S. Geological Survey (USGS) synthetic glasses of BCR-2G, BHVO-2G, and BIR-1G (Jochum et al., 2005) were used as reference materials. Three to five spots on each sample, at approximately 5 mm intervals along a straight line, were collected for analysis. $^{29}$Si was used as an internal standard. Detailed operating conditions for the laser ablation system and the
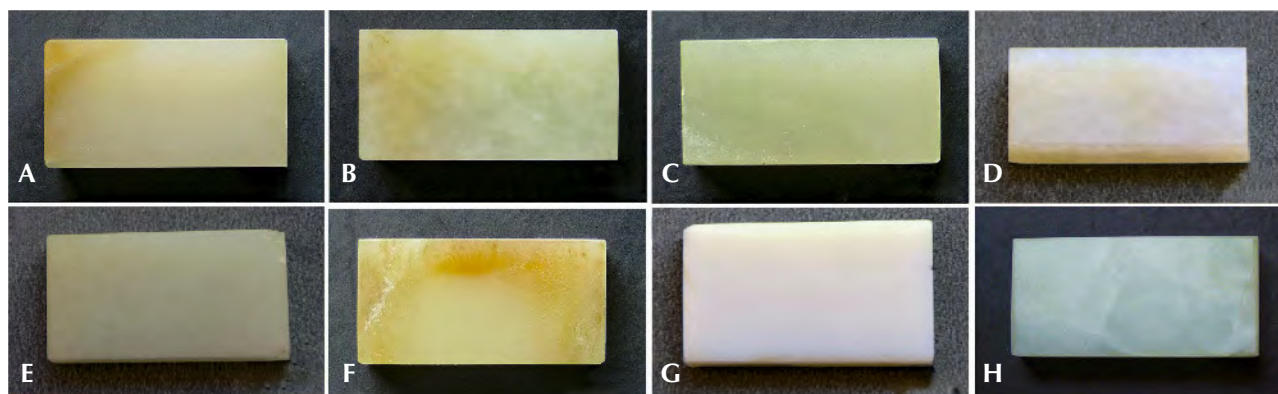
*Figure 3. Representative 3.0 × 1.5 cm nephrite samples from the eight dolomite-related deposits in this study: (A) Xinjiang-West, (B) Xinjiang-East, (C) Geermu (Golmud), (D) Baikal, (E) Chuncheon, (F) Xiuyan, (G) Luodian, and (H) Liyang. Photos by Zemin Luo.*

ICP-MS instrument and data reduction were the same as those described by Liu et al. (2008, 2010).

**LDA Method.** Linear discriminant analysis is the primary tool in this classification of nephrite from dolomite-related deposits. This method was designed for group classification, which aims to maximize between-class variance while minimizing within-class variance. Free software utilizing the statistical programming language R, version 3.1.2, was applied to this statistical analysis. Based on the trace-element concentrations collected using LA-ICP-MS, the gen-

eral procedure for LDA origin determination entailed two steps. First, original data sets of 40 independent test points for each origin except Liyang (which has a distinguishable feature, to be explored in the Discussion section), along with their trace-element information, were treated as "training sets" to build the discriminant functions (DFs) and find the best separation. The validity of the separation is characterized by the eigenvalue (EV) and total cross validation (CV); see box A for detailed definitions of EV and CV. Second, four additional samples from each origin, along with their trace-element information,

**TABLE 1.** Dolomite-related nephrite samples used in this study.

| Labeled | Locations | Mining area sources | Quantity (total 138) | LA-ICP-MS test points (total 452) | Main color |
|---|---|---|---|---|---|
| 1 | Xinjiang-West | West of Xinjiang province, China; includes Hetian, Yecheng, Xueyanuote, Xinzang 383, and Datong | 17 | 60 | White to greenish white |
| 2 | Xinjiang-East | East of Xinjiang province, China; includes Qiemo and Ruoqiang | 18 | 60 | White to light greenish white |
| 3 | Geermu (Golmud) | Qinghai province, China | 17 | 60 | White to light greenish white |
| 4 | Baikal | Russia | 17 | 60 | White |
| 5 | Chuncheon | South Korea | 21 | 60 | White |
| 6 | Xiuyan | Liaoning province, China | 17 | 60 | White to caramel |
| 7 | Luodian | Guizhou province, China | 15 | 60 | White |
| 8 | Liyang | Jiangsu province, China | 16 | 32 | Greenish white |

# BOX A: LINEAR-DISCRIMINANT ANALYSIS

## What Are DFs, EV, and CV?

In traditional LDA, each locality is classified as a group, and every trace element represents an independent variable. The combination of all these variables forms a "property space," with each variable an independent dimension. In such property space, statistical analysis assigns weight to each variable based on relative importance. The LDA designs a projection direction composed of weighted variables to achieve the best separation between groups. Along this direction, the scattered points from the same group are minimized within the group and maximized between all groups simultaneously, which can be formulated as an eigenvalue (EV), a term that will be introduced below. Such projection vectors actually are the linear discriminant functions (DFs) defined by LDA. The common mathematical expression of DF is the following:

$$\text{DF } Y_k = a_{1k}X_1 + a_{2k}X_2 + a_{3k}X_3 \ldots + a_{mk}X_m + b_k \quad (1)$$

Here $Y_k$ is the linear discriminant function score or value for a specific group K (K=1, 2,…N, where N is the number of total groups). $X_1$, $X_2$, $X_3$, … $X_m$ are characteristic variables, corresponding to the selected trace elements in our study; $a_{1k}$, $a_{2k}$, $a_{3k}$, … $a_{mk}$ are the discriminant coefficients or weights of each characteristic variable for group K; $b_k$ is the constant of linear discriminant function for group K.

EV is the key parameter for building DFs. It can be understood as the ratio of total *intergroup* deviations to the total *intragroup* deviations; the concept is defined rigorously by using covariance matrices (see Welling, 2005). In general, the DFs resulting in higher EV are chosen to build the classification model, since they can provide better separation between groups (Buyukozturk and Cokluk-Bokeoglu, 2008).

The classification accuracy and reliability of LDA can be characterized by the cross-validation (CV) accuracy rate (see Kohavi, 1995; Cawley and Talbot, 2003). The most basic mechanism for CV is:

1. Constructing a LDA model using all data points except one.

2. Using this LDA model to test the omitted data point.

3. Repeating these steps until every data point is tested.

4. The percentage of accurately classified omitted data points is the CV value. A higher CV value indicates better validity of the classification model.

Note that EV is the parameter characterizing the validity of DF in the model when building DF on training sets. On the other hand, CV is the parameter evaluating the validity of the model after it is established. These two parameters have different functions and cannot substitute for each other.

## Implementing IB-LDA

To improve the CV accuracy rate, we designed the IB-LDA method, which simplifies multiple-group comparisons into pair comparisons. In each round, the LDA process becomes a binary classification: Only the separation between one "chosen" group and the other "unchosen" groups pool is maximized by the discriminant functions. Meanwhile, the within-class variances of the chosen group and the unchosen pool are minimized respectively.

In the first round of IB-LDA, we randomly selected one of the seven localities as the "chosen" group, and the remaining six as the "unchosen" group. LDA was carried out using the statistical package for this two-group comparison. The software automatically selected various numbers of the trace elements among all input trace elements, so that the CV value corresponding to each origin in the chosen/unchosen binary classification can be achieved. Each origin is chosen to compare with the unchosen group, and the origin with the highest CV accuracy rate (versus the remaining six) is determined as the "optimal-chosen group" in this round. Hereafter, the selected trace elements and weights for the "optimal-chosen group" and "unseparated, unchosen group" will be used to build the pair of DFs for the first round of IB-LDA. The DF for the optimal-chosen group acts as the chosen sieve in this round, corresponding to the specific block box and hole in figure 4.

This process is applied to the remaining six localities, with a new set of trace elements chosen by the R software to maximize the EV and CV values. These newly selected trace elements with new weights will build a new pair of DFs for the second round of IB-LDA. Our study using this iterative-binary process identified seven origins sequentially in six rounds in the following order: Luodian, Xiuyan, Chuncheon, Xinjiang-West, Baikal, Xinjiang-East, and Geermu (Golmud). This process is shown in figure A-1.

Six pair of DFs were obtained for this classification process. The last pair of DFs separating Xinjiang-East and Geermu (training set size of 40 samples for each) was expressed as:

$$\text{DF } Y_{61(Xinjiang\text{-}East)} = -2.058\text{Li} + 1.554\text{Be} + 0.005\text{Al} + 0.012\text{K} - 9.807\text{Nb} - 0.461\text{Ba} + 6.452\text{La} - 11.891 \quad (2)$$

$$\text{DF } Y_{62(Geermu\ (Golmud))} = 0.452\text{Li} - 0.682\text{Be} + 0.001\text{Al} + 4.062\text{Nb} + 0.431\text{Ba} + 0.145\text{La} - 2.376 \quad (3)$$

Herein, we defined $CV_{orNi}$ as the CV for the origin N in the IB-LDA. It is defined as the continued multiplication of $CV_i$ from the first round to the round in which

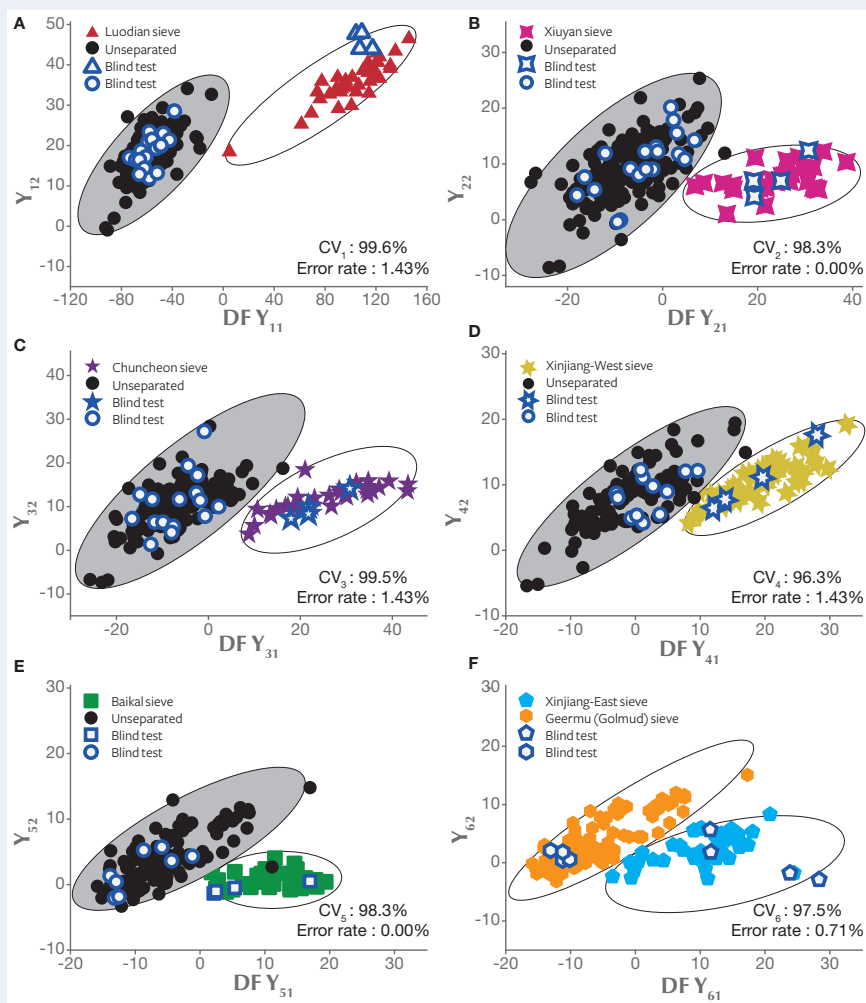**DF Value Plots for Six Rounds of IB-LDA**

*Figure A-1. This plot illustrates how six rounds of IB-LDA were used to separate seven different dolomite-related nephrite sources. The horizontal and vertical axes, named DF $Y_{i1}$ and $Y_{i2}$, were the two discriminant functions in the i round (i=1–6). The gray shaded area was the unseparated group. Luodian, Xiuyan, Chuncheon, Xinjiang-West, Baikal, Xinjiang-East, and Geermu (Golmud) were determined as the successive chosen sieves. The CV value in the bottom right of each figure corresponds to the $CV_i$ accuracy rate in each round of IB-LDA analysis. The error rate represents the probability of misclassifying the test set obtained in the blind test in each step of IB-LDA. The sum of the six error rates equals 1-AR. Solid and hollow symbols represent the training set and test set, respectively.*

the particular origin N is classified; see equation (4). $CV_i$ is the CV accuracy rate, while i is the number of iterative rounds of IB-LDA:

$$CV_{orNi(i=1,2,...N)} = CV_1 \times CV_2 \times ... \times CV_{i-1} \times CV_i \quad (4)$$

The overall CV ($CV_{total}$) for this iterative-binary classification model should be defined as the arithmetic mean value of the $CV_{orNi}$ value of each origin, as calculated in equation (5).

$$CV_{total} = \frac{\sum_{i=1}^{N} CV_{orNi(i)}}{7} \quad (5)$$

**Evaluating the Model Validity Based on EV, CV, and AR**

As a conventional method for the machine-learning model, we used two-thirds of the total data set as training sets with the remaining one-third as a test set (Kohavi, 1995). We list the EV and CV values for the training set, and the AR values for the test sets, to evaluate the validity and accuracy of the IB-LDA model. EV, CV, and AR values for traditional LDA are also presented for comparison with the IB-LDA model. In terms of both training sets (EV and CV) and test sets (AR), IB-LDA shows greater validity and accuracy than traditional LDA.

The calculated results of IB-LDA $CV_{orNi}$ for the training sets are shown in figure A-2. The overall CV ($CV_{total}$) for IB-LDA (94.4 %) was higher than that of traditional

**TABLE A-1.** EV, CV, and AR values for IB-LDA and traditional LDA

|  | EV | CV total (%) | AR (%) |
|---|---|---|---|
| IB-LDA | 6.4 | 94.4 | 95.0(±2.0) |
| Traditional LDA | 4.4 | 91.4 | 85.7(±2.5) |

*Note: 40 test points from each origin were used as training sets; the remaining 20 test points from each origin were chosen as test sets. The value in parentheses is the standard deviation of AR after five rounds of blind testing.*

LDA (91.4%). Samples outside the "expected" groups (in this case, the eight nephrite localities) in the training sets will be classified into one of the "expected" groups incorrectly according to its DF score. In machine learning and LDA, the groups "expected" in the model must all be included in the training sets to build the most comprehensive training set and DF. The solution for dealing with "unexpected" wild samples is to collect enough samples to define them as a new group within the training set. This is why all machine-learning models require larger data sets to improve their validity. We include the discussion about the "unexpected" samples in the last paragraph of box A.

**CV and EV Values Depending on the Statistical Property of Data Sets.** Our analysis was based on 60 data points in each group. To evaluate how the size of the training set

Figure A-2. The $CV_{orNi}$ for the identified origins in our IB-LDA, and CV for traditional LDA. The detailed algorithm of $CV_{orNi}$ is shown in equation 4. IB-LDA identified geographic origins with a higher CV (an average of 94.4%) than that of traditional LDA (91.4%).



can impact the validity (EV) and accuracy (CV) of the model, we conducted a series of tests by randomly removing 10 data points from each group until each training set reached 20 data points. We found that CV generally increased as each training set grew from 20 to 50. Such an increase indicates that the variance can be predicted more precisely with a larger set of samples. The variation of CV and EV with size of the training set is mainly caused by some "irregular" samples, which disturbs the variance in/between groups. We speculate that both EV and CV eventually converge to a constant value, which can only be justified with a larger total data set.

The most practical classification model needs to take into account training set size, CV, EV, and other factors, which is still a real challenge. AR values for blind testing are not included in table A-2. Because the training set is larger than 40 samples for each group, the remaining data set is too sparse to supply a test set with viable statistics. As a major difference between CV and AR in practice, CV is extracted within the training set in the building process of the classification model while AR is obtained beyond the training set after the classification model build. The AR method usually requires a larger original data set to maintain good statistics for both training sets and test sets; this requires further accumulation in the future.

We wish to emphasize that we are speculating on the accuracy and validity of both CV and AR. As the classification model deals with real "unincluded" samples without any knowledge of their origin, CV and AR can only estimate the accuracy or validity of the final analysis result. In the worst-case scenario, a nephrite sample that does not belong to any of the eight origins, it will still be (incorrectly) classified as having one of the above origins, according to its DF score. In this case, the CV and AR are meaningless for such unexpected samples. As with all machine-learning models, LDA requires that all input (the samples' trace-element information) be correctly paired with the expected output (geographic locality) at the very beginning, when the training set is built. In other words, the most practical model always requires large data sets, along with the optimization and balancing of EV, CV, and AR values.

**TABLE A-2.** CV and EV values for different training set sizes.

|  |  | Training set size 20 | 30 | 40 | 50 | 60 |
|---|---|---|---|---|---|---|
| IB-LDA | EV (mean) | 6.9 | 5.9 | 6.4 | 6.5 | 6.4 |
|  | CV total (%) | 93.2 | 93.6 | 94.4 | 95.8 | 94.2 |
| Traditional LDA | EV (mean) | 5.1 | 4.5 | 4.4 | 4.5 | 4.5 |
|  | CV total (%) | 90.0 | 88.6 | 91.4 | 94.0 | 93.3 |

| Element conc., with mean and stand. dev. | Xinjiang-West (Group 1) | Xinjiang-East (Group 2) | Geermu (Golmud) (Group 3) | Baikal (Group 4) | Chuncheon (Group 5) | Xiuyan (Group 6) | Luodian (Group 7) | Liyang (Group 8) |
|---|---|---|---|---|---|---|---|---|
| Li (ppm) | 0.082–25.097 | 0.250–28.295 | 0.358–5.435 | 1.731–20.638 | 0.100–6.875 | 0.107–1.333 | 7.857–35.066 | 14.686–56.167 |
|  | 2.075 (0.487) | 6.301 (0.888) | 2.765 (0.130) | 6.934 (0.597) | 1.058 (0.115) | 0.516 (0.037) | 22.575 (0.813) | 27.724 (1.932) |
| Be (ppm) | 1.581–51.342 | 0.740–30.731 | 0.000–1.181 | 5.140–45.301 | 11.577–28.624 | 9.058–27.810 | 0.000–7.740 | 0.045–3.771 |
|  | 26.018 (0.931) | 11.100 (1.159) | 0.380 (0.035) | 22.405 (1.613) | 19.211 (0.658) | 16.161 (0.471) | 1.035 (0.255) | 1.165 (0.134) |
| Na$_2$O (wt.%) | 0.042–0.438 | 0.021–0.182 | 0.008–0.147 | 0.056–0.133 | 0.034–0.082 | 0.024–0.067 | 0.098–0.221 | 0.457–0.913 |
|  | 0.088 (0.008) | 0.106 (0.004) | 0.081 (0.004) | 0.099 (0.003) | 0.057 (0.001) | 0.044 (0.001) | 0.179 (0.004) | 0.658 (0.019) |
| Al$_2$O$_3$ (wt.%) | 0.338–0.899 | 0.081–0.974 | 0.025–0.338 | 0.380–0.898 | 0.355–0.983 | 0.266–1.22 | 0.122–0.373 | 0.324–1.410 |
|  | 0.573 (0.021) | 0.630 (0.030) | 0.136 (0.009) | 0.621 (0.015) | 0.604 (0.015) | 0.505 (0.021) | 0.209 (0.007) | 0.550 (0.033) |
| K$_2$O (wt.%) | 0.014–0.112 | 0.025–0.231 | 0.005–0.091 | 0.028–0.193 | 0.024–0.115 | 0.019–0.078 | 0.036–0.119 | 0.116–0.294 |
|  | 0.041 (0.003) | 0.099 (0.007) | 0.049 (0.003) | 0.067 (0.003) | 0.048 (0.002) | 0.041 (0.002) | 0.092 (0.002) | 0.217 (0.007) |
| Sc (ppm) | 1.103–79.327 | 0.850–4.588 | 0.208–3.682 | 0.284–3.125 | 0.518–4.734 | 1.097–4.117 | 0.000–9.147 | 0.614–2.800 |
|  | 4.88 (1.260) | 1.893 (0.086) | 1.088 (0.087) | 1.773 (0.091) | 1.333 (0.101) | 1.960 (0.070) | 1.971 (0.197) | 1.670 (0.119) |
| Rb (ppm) | 0.295–53.317 | 0.003–52.369 | 0.000–1.302 | 1.845–9.708 | 0.421–11.329 | 0.179–3.799 | 0.000–0.662 | 0.339–28.726 |
|  | 4.840 (1.075) | 12.162 (1.589) | 0.568 (0.040) | 4.203 (0.239) | 2.679 (0.275) | 1.666 (0.125) | 0.279 (0.022) | 3.139 (1.121) |
| Sr (ppm) | 4.705–32.795 | 3.763–22.434 | 3.297–26.933 | 2.677–18.908 | 8.515–32.997 | 3.920–22.541 | 15.157–31.291 | 141.267–1272.699 |
|  | 14.721 (0.886) | 11.275 (0.477) | 16.241 (0.853) | 10.619 (0.489) | 21.268 (0.529) | 13.778 (0.591) | 20.950 (0.681) | 274.233 (21.62) |
| Y (ppm) | 1.225–18.285 | 0.159–6.479 | 0.000–1.778 | 0.294–7.185 | 0.255–10.827 | 1.032–11.420 | 3.077–29.474 | 0.361–3.772 |
|  | 4.278 (0.404) | 2.991 (0.196) | 0.514 (0.055) | 1.046 (0.147) | 0.882 (0.163) | 3.953 (0.206) | 11.138 (0.713) | 1.468 (0.143) |
| Zr (ppm) | 0.354–15.483 | 0.000–8.733 | 0.000–11.187 | 0.000–16.652 | 0.000–6.811 | 0.191–9.151 | 0.000–22.154 | 0.007–15.557 |
|  | 4.900 (0.455) | 2.739 (0.258) | 0.892 (0.207) | 1.544 (0.357) | 0.720 (0.124) | 2.420 (0.221) | 2.770 (0.459) | 3.220 (0.626) |
| Nb (ppm) | 0.189–11.698 | 0.000–3.022 | 0.000–0.322 | 0.126–1.938 | 0.033–0.566 | 0.037–0.789 | 0.173–1.096 | 0.119–0.938 |
|  | 1.441 (0.270) | 0.808 (0.113) | 0.113 (0.011) | 0.519 (0.037) | 0.208 (0.016) | 0.518 (0.022) | 0.737 (0.023) | 0.319 (0.031) |
| Mo (ppm) | 0.000–0.171 | 0.000–0.266 | 0.000–0.625 | 0.000–1.034 | 0.000–0.779 | 0.000–0.345 | 0.000–3.191 | 0.000–0.232 |
|  | 0.027 (0.006) | 0.034 (0.009) | 0.078 (0.016) | 0.055 (0.020) | 0.118 (0.021) | 0.032 (0.009) | 0.408 (0.106) | 0.041 (0.010) |
| Cs (ppm) | 0.197–13.125 | 0.071–26.950 | 0.000–1.682 | 0.401–4.311 | 0.057–1.935 | 0.069–2.447 | 0.042–0.942 | 0.000–2.395 |
|  | 3.771 (30.493) | 7.620 (0.951) | 0.718 (0.058) | 2.075 (0.139) | 0.525 (0.034) | 0.587 (0.056) | 0.412 (0.024) | 0.278 (0.095) |
| Ba (ppm) | 1.368–26.254 | 0.284–18.403 | 0.000–9.237 | 0.430–30.014 | 0.859–9.097 | 0.374–9.951 | 3.099–195.132 | 0.196–7.535 |
|  | 9.231 (0.755) | 5.887 (0.379) | 4.151 (0.251) | 7.745 (0.783) | 2.463 (0.174) | 4.159 (0.194) | 15.413 (4.120) | 2.611 (0.325) |
| La (ppm) | 0.000–39.004 | 0.040–2.282 | 0.008–0.571 | 0.011–0.523 | 0.194–1.159 | 0.000–0.887 | 0.886–18.591 | 0.277–4.565 |
|  | 2.601 (0.828) | 0.615 (0.067) | 0.286 (0.024) | 0.179 (0.017) | 0.678 (0.021) | 0.460 (0.030) | 5.083 (0.352) | 0.913 (0.138) |
| Ce (ppm) | 0.053–39.916 | 0.025–4.772 | 0.000–1.615 | 0.069–1.384 | 0.589–2.900 | 0.027–1.659 | 0.536–28.944 | 0.593–7.261 |
|  | 3.452 (0.922) | 1.400 (0.156) | 0.560 (0.049) | 0.462 (0.040) | 1.480 (0.042) | 1.001 (0.065) | 4.938 (0.543) | 1.678 (0.211) |
| Pr (ppm) | 0.000–13.764 | 0.010–0.506 | 0.000–0.283 | 0.000–0.170 | 0.056–0.302 | 0.000–0.252 | 0.256–4.649 | 0.094–1.188 |
|  | 0.997 (0.307) | 0.181 (0.019) | 0.069 (0.007) | 0.042 (0.005) | 0.157 (0.006) | 0.124 (0.008) | 1.322 (0.087) | 0.309 (0.036) |
| Nd (ppm) | 0.000–17.535 | 0.000–2.460 | 0.000–1.443 | 0.000–0.677 | 0.015–1.405 | 0.015–1.051 | 1.552–15.303 | 0.365–4.672 |
|  | 2.098 (0.477) | 0.811 (0.080) | 0.297 (0.036) | 0.266 (0.022) | 0.661 (0.036) | 0.536 (0.040) | 5.486 (0.382) | 1.238 (0.139) |
| Sm (ppm) | 0.000–14.859 | 0.000–0.707 | 0.000–0.385 | 0.000–0.393 | 0.000–0.624 | 0.000–0.395 | 0.334–3.806 | 0.000–0.773 |
|  | 1.464 (0.397) | 0.204 (0.019) | 0.079 (0.011) | 0.075 (0.009) | 0.126 (0.016) | 0.162 (0.011) | 1.176 (0.083) | 0.263 (0.029) |
| Eu (ppm) | 0.000–0.140 | 0.000–0.117 | 0.000–0.135 | 0.000–0.145 | 0.000–0.111 | 0.000–0.187 | 0.047–0.637 | 0.000–0.129 |
|  | 0.017 (0.003) | 0.019 (0.003) | 0.027 (0.004) | 0.019 (0.004) | 0.026 (0.003) | 0.076 (0.006) | 0.279 (0.016) | 0.044 (0.006) |
| Gd (ppm) | 0.072–5.373 | 0.000–0.726 | 0.000–0.430 | 0.000–0.510 | 0.000–0.367 | 0.049–0.523 | 0.000–3.222 | 0.000–0.589 |
|  | 0.768 (0.132) | 0.246 (0.019) | 0.090 (0.013) | 0.099 (0.012) | 0.148 (0.014) | 0.230 (0.013) | 1.136 (0.076) | 0.275 (0.029) |
| Tb (ppm) | 0.009–2.413 | 0.000–0.136 | 0.000–0.090 | 0.000–0.065 | 0.000–0.094 | 0.005–0.107 | 0.043–0.462 | 0.000–0.124 |
|  | 0.202 (0.049) | 0.050 (0.003) | 0.015 (0.002) | 0.008 (0.002) | 0.017 (0.002) | 0.053 (0.003) | 0.180 (0.012) | 0.038 (0.005) |
| Dy (ppm) | 0.133–8.037 | 0.011–0.731 | 0.000–0.294 | 0.000–0.429 | 0.000–1.252 | 0.117–0.957 | 0.354–2.767 | 0.027–0.596 |
|  | 0.922 (0.188) | 0.347 (0.023) | 0.084 (0.011) | 0.102 (0.012) | 0.124 (0.021) | 0.410 (0.021) | 1.145 (0.071) | 0.207 (0.023) |
| Ho (ppm) | 0.027–5.253 | 0.000–0.160 | 0.000–0.082 | 0.000–0.112 | 0.000–0.296 | 0.045–0.593 | 0.045–0.593 | 0.010–0.108 |
|  | 0.379 (0.114) | 0.083 (0.006) | 0.020 (0.002) | 0.016 (0.003) | 0.027 (0.005) | 0.023 (0.006) | 0.224 (0.018) | 0.040 (0.004) |
| Er (ppm) | 0.034–22.467 | 0.000–0.674 | 0.000–0.213 | 0.000–0.914 | 0.000–0.533 | 0.021–1.091 | 0.000–2.316 | 0.004–0.318 |
|  | 1.839 (0.558) | 0.243 (0.020) | 0.052 (0.006) | 0.095 (0.017) | 0.070 (0.011) | 0.296 (0.020) | 0.715 (0.062) | 0.114 (0.015) |
| Tm (ppm) | 0.007–4.507 | 0.000–0.100 | 0.000–0.062 | 0.000–0.083 | 0.000–0.107 | 0.006–0.180 | 0.000–0.374 | 0.000–0.034 |
|  | 0.218 (0.081) | 0.030 (0.003) | 0.010 (0.002) | 0.010 (0.002) | 0.013 (0.002) | 0.039 (0.003) | 0.091 (0.010) | 0.015 (0.002) |
| Yb (ppm) | 0.063–15.424 | 0.017–0.802 | 0.000–0.316 | 0.000–0.363 | 0.004–1.416 | 0.004–1.416 | 0.000–1.850 | 0.000–0.308 |
|  | 0.818 (0.263) | 0.204 (0.019) | 0.064 (0.010) | 0.093 (0.031) | 0.068 (0.011) | 0.234 (0.025) | 0.571 (0.055) | 0.103 (0.017) |
| Lu (ppm) | 0.003–11.295 | 0.000–0.113 | 0.000–0.047 | 0.000–0.086 | 0.000–0.103 | 0.003–0.264 | 0.000–3.899 | 0.000–0.058 |
|  | 0.378 (0.191) | 0.026 (0.003) | 0.008 (0.001) | 0.008 (0.002) | 0.014 (0.002) | 0.030 (0.004) | 0.322 (0.083) | 0.014 (0.002) |
| Hf (ppm) | 0.000–4.405 | 0.000–0.321 | 0.000–0.223 | 0.000–0.257 | 0.000–0.302 | 0.000–0.299 | 0.000–0.748 | 0.000–0.423 |
|  | 0.395 (0.102) | 0.073 (0.009) | 0.024 (0.005) | 0.025 (0.006) | 0.036 (0.006) | 0.063 (0.008) | 0.112 (0.023) | 0.096 (0.018) |
| Ta (ppm) | 0.000–8.495 | 0.000–0.188 | 0.000–0.046 | 0.000–0.090 | 0.000–0.085 | 0.000–0.108 | 0.000–0.170 | 0.000–0.157 |
|  | 0.622 (0.225) | 0.043 (0.005) | 0.007 (0.001) | 0.011 (0.002) | 0.010 (0.002) | 0.028 (0.003) | 0.039 (0.004) | 0.037 (0.005) |
| Bi (ppm) | 0.000–0.784 | 0.000–2.758 | 0.000–0.434 | 0.000–0.068 | 0.000–0.210 | 0.000–0.021 | 0.000–2.496 | 0.000–0.015 |
|  | 0.084 (0.026) | 0.076 (0.045) | 0.045 (0.010) | 0.007 (0.002) | 0.022 (0.004) | 0.007 (0.001) | 0.229 (0.056) | 0.006 (0.001) |
| Pb (ppm) | 0.293–7.710 | 0.346–10.454 | 0.055–3.691 | 0.368–17.393 | 0.925–4.882 | 0.118–3.243 | 0.271–100.569 | 0.157–5.250 |
|  | 1.195 (0.173) | 2.948 (0.228) | 1.618 (0.106) | 2.016 (0.280) | 1.895 (0.096) | 0.561 (0.059) | 3.424 (1.637) | 0.771 (0.149) |
| Th (ppm) | 0.029–5.299 | 0.036–2.406 | 0.000–0.546 | 0.000–0.983 | 0.011–0.675 | 0.005–0.620 | 0.000–1.100 | 0.074–0.892 |
|  | 0.686 (0.108) | 0.236 (0.042) | 0.074 (0.012) | 0.150 (0.025) | 0.112 (0.011) | 0.212 (0.017) | 0.254 (0.025) | 0.355 (0.034) |
| U (ppm) | 0.146–5.967 | 0.081–2.427 | 0.000–0.946 | 0.028–0.660 | 0.070–0.947 | 0.530–2.479 | 0.378–1.345 | 0.069–1.942 |
|  | 1.182 (0.154) | 1.080 (0.062) | 0.487 (0.028) | 0.179 (0.018) | 0.345 (0.018) | 1.448 (0.039) | 0.882 (0.028) | 0.304 (0.057) |

**TABLE 2.** Trace-element concentrations for eight nephrite localities, by LA-ICP-MS.

were treated as test sets. The purpose of a test set is to estimate how the classification model will deal with the data that was not included in the "training set" to build the DFs. As conventional settings for machine learning models (Kohavi, 1995), two-thirds of the total data sets (280 data points) were used as a training set, and one-third (the other 140 data points) were used as test set. This setting applies throughout the paper unless other specific modifications are mentioned. Detailed descriptions of training sets and test sets also appear in box A.

## RESULTS AND DISCUSSION

For the 138 nephrite samples from the eight locations, the concentration of elements from Li to U (45 elements total) were obtained by LA-ICP-MS measurement. To make our classification model independent of sample color, the transition metal elements (Ti, V, Cr, Mn, Fe, Co, Ni, and Cu) were excluded from further data analysis. Only 34 trace elements were involved in creating the LDA model. The mean value and standard deviation value of each trace element are calculated based on 60 detection points for each origin, as shown in table 2.

**Trace-Element Analysis to Separate Liyang from Other Origins.** As shown in table 2, the nephrite samples from Liyang (group 8) displayed much higher concentrations of Sr (>140 ppm) and $Na_2O+K_2O$ (> 0.57 wt.%) than the other seven localities (Sr<40 ppm, $Na_2O+K_2O$ < 0.56 wt.%). These results confirmed previously reported conclusions (Zhang et al., 2011; Siqin et al., 2012; Ling et al., 2013) that the distinctive Sr, Na, and K concentrations could be used as a quantitative discriminant to separate Liyang nephrite samples. These obvious diagnostic chemical signatures rendered further analysis of Liyang nephrite unnecessary. The only real challenge was to distinguish the remaining seven nephrite origins. Table 2 shows overlapping trace-element distributions. Therefore, it is important to derive effective discriminants from the trace elements to separate the origins.

**Traditional LDA in Dolomite-Related Nephrite Origin Determination.** From the outset, we attempted to use the traditional LDA method to classify the seven dolomite-related nephrite localities at once. Each nephrite locality is classified as a group, and every input trace element represents an independent variable. Seven linear discriminant functions (DFs) for seven independent nephrite groups were built simultaneously. The results showed that only the Lu-

odian samples had an isolated distribution region, while the other six localities still exhibited overlap. The full classification of all seven groups by "one-pass" LDA must balance variance among all seven groups. This may be the reason why traditional LDA presented a relatively low CV of 91.4 % and a relatively low EV of 4.48 with a training set size of 40 testing points for each group. For the details of DFs and CV, again see box A.

**IB-LDA to Optimize the Separation of Dolomite-Related Nephrite Geographic Origins.** If only aiming to distinguish one group from all the others while ignoring the differences within the remaining unclassified groups, certain group identities should be more accurate and distinguishable. Hence, we designed the "iterative-binary" LDA (IB-LDA) to optimize the separation. The procedure used to build the discriminant function and criteria database for all seven origins is described in box A.

Classifying different sources of dolomite-related nephrite by IB-LDA is analogous to sorting blocks with different shapes by putting them into the corresponding holes. As shown in figure 4, seven blocks represented seven different dolomite-related nephrite origins. The red triangle, pink four-pointed star, purple five-pointed star, yellow six-pointed star, green square, blue pentagon, and orange hexagon represented Luodian, Xiuyan, Chuncheon, Xinjiang-West, Baikal, Xinjiang-East, and Geermu (Golmud) respectively. We then needed to build corresponding blocks with differently shaped holes (named "chosen sieves" hereafter) using the training set samples. The original 280 training set samples from the seven origins were used to create seven chosen sieves in sequence after six rounds of IB-LDA processes (figure 4). The different holes represent different DFs built for each chosen sieve. The sequence of those chosen sieves directly corresponds to the six rounds of IB-LDA, which must be unchanged to maintain the validity of the classification method. We found that the IB-LDA model produces better CV and EV values than traditional LDA, as shown in table A-1, which indicates IB-LDA can effectively improve the accuracy and validity of the sieves (classification model).

Next, we evaluated the performance of the sieves built by IB-LDA on unincluded data in a blind test. Four new samples from each origin were used as a testing set to check the reliability and accuracy of the established chosen sieves (figure 5). All samples were treated as "unknown" blocks to be tested on the seven sieves in sequence. When the unknown block
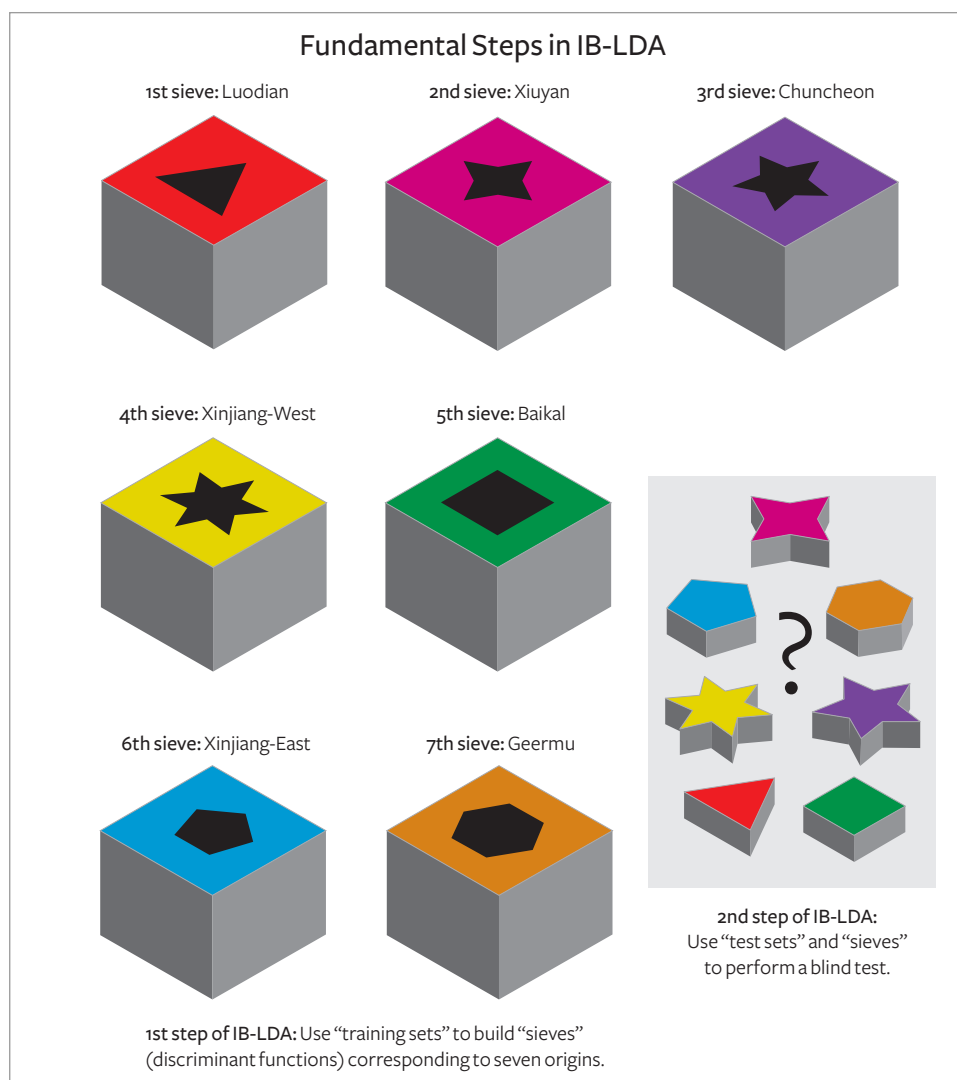
## Fundamental Steps in IB-LDA

**1st sieve:** Luodian

**2nd sieve:** Xiuyan

**3rd sieve:** Chuncheon

**4th sieve:** Xinjiang-West

**5th sieve:** Baikal

**6th sieve:** Xinjiang-East

**7th sieve:** Geermu

**1st step of IB-LDA:** Use "training sets" to build "sieves" (discriminant functions) corresponding to seven origins.

**2nd step of IB-LDA:** Use "test sets" and "sieves" to perform a blind test.

*Figure 4. These blocks illustrate the process of determining the dolomite-related nephrite origins by IB-LDA. The first step is building the "chosen sieves" sequence through six rounds of IB-LDA using the "training set" samples. The boxes had different holes corresponding to "chosen sieves" with discriminant functions in each round of IB-LDA. The second step (inset) is to use these sieves to determine the origins of testing set samples step by step in a blind test. Four test set samples from each origin were chosen randomly from the total data set, excluding the training set samples.*

fit into the correct sieve, its "shape" was identified. For example, the first chosen sieve (Luodian) allowed only the triangular blocks to be sorted out, which meant only Luodian samples could be identified and all the other samples were still in an "unseparated" status. The unseparated samples went through the second IB-LDA process, where a four-pointed star sieve representing Xiuyan was used to extract appropriately shaped blocks, and the unseparated pool was reduced once more.

This process should be repeated until all the unseparated blocks can be identified. The number of test sets with the correct classification divided by the number of the total test sets is the accuracy rate (AR) for such blind testing. The same blind test is performed five times on different test sets, and the average AR is calculated. We note that the AR value obtained is generally consistent with the CV value

calculated in the first step of IB-LDA, as shown in table A-1.

## CONCLUSIONS

We propose that an IB-LDA model, combined with trace-element information from LA-ICP-MS, is an effective method for determining the origin of dolomite-related nephrite deposits. We consider the application of IB-LDA to the quantitative classification of nephrite origin a significant improvement over the traditional method. The origin information reflected by trace-element data has been well explored and applied in nephrite origin determination. The LDA method presents obvious statistical advantages in dealing with the massive quantity of nephrite trace-element data. Finally, the successful performance of IB-LDA remarkably improved discriminant accuracy, increasing the CV accuracy rate
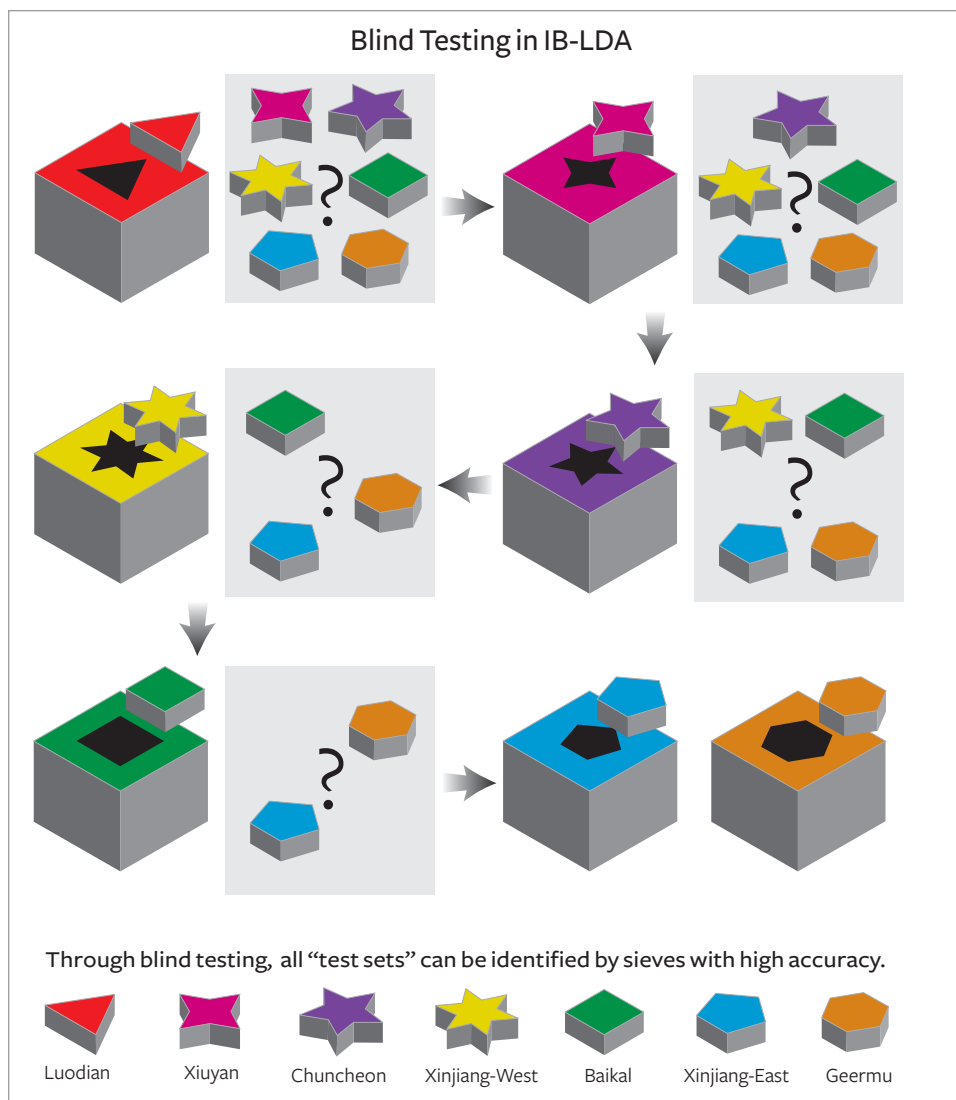
Figure 5. The schematic diagram of the blind test, the second step in IB-LDA. Only when the shape of an "unknown" block agrees with one of the sieve shapes can its origin be determined.

from 91.4% in traditional LDA to 94.4% and identifying $CV_{orNi}$ values specific to each origin. The discriminant functions database built by IB-LDA obtained a 95.0% accuracy rate in the testing of 28 unknown samples. We believe that collecting and accumulating more nephrite samples for use as training sets will further improve the reliability of the discriminant function database. The IB-LDA method should also prove useful for the origin determination of other gemstones.

ABOUT THE AUTHORS
*Dr. Zemin Luo is a member of the Center for Innovative Gem Testing Technology (CIGT), a lecturer at the Institute of Gems and Jewelry Studies (IGJS), and a fellow of the Geology Postdoctoral Research Station, at the China University of Geosciences (Wuhan). Prof. Mingxing Yang is the dean of the IGJS and leader of the classification group at CIGT. Prof. Andy H. Shen is a Hubei 100 Talent Distinguished Professor at the IGJS and the director of the CIGT.*

# REFERENCES

Adamo I., Bocchio R. (2013) Nephrite jade from Val Malenco, Italy: Review and update. *G&G*, Vol. 49, No. 2, pp. 98–106, http://dx.doi.org/10.5741/GEMS.49.2.98

Adams C.J., Beck R.J., Campbell H.J. (2007) Characterisation and origin of New Zealand nephrite jade using its strontium isotopic signature. *Lithos*, Vol. 97, Nos. 3–4, pp. 307–322, http://dx.doi.org/10.1016/j.lithos.2007.01.001

Blodgett T., Shen A.H. (2011). Application of discriminant analysis in gemology: Country-of-origin separation in colored stones and distinguishing HPHT-treated diamonds. Proceedings of the Fifth International Gemological Symposium, *G&G*, Vol. 47, No. 2, p. 145.

Breeding C.M., Shen A.H. (2010) LA-ICP-MS analysis as a tool for separating natural and synthetic malachite. *News from Research*, Oct. 11, http://www.gia.edu/gia-news-research-nr101410

Buyukozturk S., Cokluk-Bokeoglu O. (2008) Discriminant function analysis: Concept and application. *Eurasian Journal of Educational Research*, Vol. 33, pp. 73–92.

Cawley G.C., Talbot N.L.C (2003) Efficient leave-one-out cross-validation of kernel fisher discriminant classifiers. *Pattern Recognition*, Vol. 36, No. 11, pp. 2585–2592, http://dx.doi.org/10.1016/S0031-3203(03)00136-5

Fisher R.A. (1936) The use of multiple measurements in taxonomic problems. *Annals of Eugenics*, Vol. 7, pp. 179–188, doi:10.1111/j.1469-1809.1936.tb02137.x

Guo Y.Q., Hastie T., Tibshirani R. (2007) Regularized linear discriminant analysis and its application in microarrays. *Biostatistics*, Vol. 8, No. 1, pp. 86–100, http://dx.doi.org/10.1093/biostatistics/kxj035

Harlow G.E., Sorensen S.S. (2005) Jade (nephrite and jadeitite) and serpentinite: Metasomatic connections. *International Geology Review*, Vol. 47, No. 2, pp. 113–146, http://dx.doi.org/10.2747/0020-6814.47.2.113

He G.M. (2009) English and Chinese culture connotation. *Asian Social Science*, Vol. 5, No. 7, pp. 160–163, http://www.ccsenet.org/journal/index.php/ass/article/view/2985

Jochum K.P., Willbold M., Raczek I., Stoll B., Herwig K. (2005) Chemical characterization of the USGS reference glasses GSA-1G, GSC-1G, GSD-1G, GSE-1G, BCR-2G, BHVO-2G and BIR-1G using EPMA, ID-TIMS, ID-ICP-MS and LA-ICP-MS. *Geostandards and Geoanalytical Research*, Vol. 29, No. 3, pp. 285–302, http://dx.doi.org/10.1111/j.1751-908X.2005.tb00901.x

Kohavi R. (1995) A study of cross-validation and bootstrap for accuracy estimation and model selection. *Proceedings of the Fourteenth International Joint Conference on Artificial Intelligence*, Vol. 2, No. 12, pp. 1137–1143. Morgan Kaufmann, San Mateo, California.

Liao R.Q., Zhu Q.W. (2005) Chemical composition analysis of nephrites from different localities in China. *Journal of Gems and Gemmology*, Vol. 7, No. 1, pp. 25–30 [in Chinese].

Ling X.X., Schmadicke E., Wu R.H., Wang S.Q., Gose J. (2013) Composition and distinction of white nephrite from Asian deposits. *Neues Jahrbuch Mineralogie – Abhandlungen*, Vol. 190, No. 1, pp. 49–65, http://dx.doi.org/10.1127/0077-7757/2013/0229

Liu J., Cui W.Y. (2002) Study on nephrite (tremolite jade) from three localities in China. *Journal of Gems and Gemmology*, Vol. 4, No. 2, pp. 25–29 [in Chinese].

Liu Y., Hu Z., Gao S., Günther D., Xu J., Gao C., Chen H. (2008) *In situ* analysis of major and trace elements of anhydrous minerals by LA-ICP-MS without applying an internal standard. *Chemical Geology*, Vol. 257, Nos. 1–2, pp. 34–43, http://dx.doi.org/10.1016/j.chemgeo.2008.08.004

Liu Y.S., Hu Z.C., Zong K.Q., Gao C.G., Gao S., Xu J., Chen H.H. (2010) Reappraisement and refinement of zircon U-Pb isotope and trace element analyses by LA-ICP-MS. *Chinese Science Bulletin*, Vol. 55, No. 15, pp. 1535–1546.

McLachlan G.J. (2004) *Discriminant Analysis and Statistical Pattern Recognition*. John Wiley and Sons, Hoboken, New Jersey.

Pearce N.J.G., Perkins W.T., Westgate J.A., Gorton M.P., Jackson S.E., Neal C.R., Chenery S.P. (1997) A compilation of new and published major and trace element data for NIST SRM 610 and NIST SRM 612 glass reference materials. *Geostandards and Geoanalytical Research*, Vol. 21, No. 1, pp. 115–144, http://dx.doi.org/10.1111/j.1751-908X.1997.tb00538.x

Shen A.H., Koivula J.I., Shigley J.E. (2011) Identification of extra-terrestrial peridot by trace elements. *G&G*, Vol. 47, No. 3, pp. 208–213, http://dx.doi.org/10.5741/GEMS.47.3.208

Shen A.H., Blodgett T., Shigley J.E. (2013) Country-of-origin determination of modern gem peridots from LA-ICPMS trace-element chemistry and linear discriminant analysis (LDA). *Geological Society of America Abstracts with Programs*, Vol. 45, No. 7, p. 525.

Siqin B., Qian R., Zhuo S.J., Gan F.X., Dong M., Hua Y.F. (2012) Glow discharge mass spectrometry studies on nephrite minerals formed by different metallogenic mechanisms and geological environments. *International Journal of Mass Spectrometry*, Vol. 309, pp. 206–211, http://dx.doi.org/10.1016/j.ijms.2011.10.003

Tang Y.L., Chen B.Z., Jiang R.H. (1994) *Zhongguo Hetian yu (Hetian Jade of China)*. Xinjiang People's Press, Xinjiang, China, pp. 160–200 [in Chinese].

Tsien H.H., Lo H.J., Lin S.B. (1996) Crystal growth and whitening of archaic tremolite yu. *Acta Geologica Taiwanica*, Vol. 32, pp. 131–147.

Welling M. (2005) Fisher linear discriminant analysis. Department of Computer Science, University of Toronto, http://www.cs.huji.ac.il/~csip/Fisher-LDA.pdf

Wen G. (2001) Ancient Chinese jade and the jade age (translation from Zhongguo guyu yuqi shidai by E. Childs-Johnson). In E. Childs-Johnson, Ed., *Enduring Art of Jade Age China: Chinese Jades of Late Neolithic through Han Periods*, Throckmorton Fine Art, New York, pp. 31–34.

Wen G., Jing Z. (1996) Mineralogical studies of Chinese archaic jade. *Acta Geologica Taiwanica*, Vol. 32, pp. 55–83.

Wu R.H., Zhang X.H., Li W.W. (2002) Petrological characteristics of Hetian jade in Xinjiang and nephrite from Baikal area in Russia: *Acta Petrologica et Mineralogica (Sinica)*, Vol. 21, supp., pp. 134–142 [in Chinese].

Yu H., Yang J. (2001) A direct LDA algorithm for high-dimensional data - with application to face recognition. *Pattern Recognition*, Vol. 34, No. 10, pp. 2067–2069.

Yui T.F., Kwon S.T. (2002) Origin of a dolomite related jade deposit at Chuncheon, Korea. *Economic Geology*, Vol. 97, No. 3, pp. 593–601, http://dx.doi.org/10.2113/gsecongeo.97.3.593

Zhang Z.W., Gan X.F. (2011) Analysis of the chromite inclusions found in nephrite minerals obtained from different deposits using SEMEDS and LRS. *Journal of Raman Spectroscopy*, Vol. 42, pp. 1808–1811.

Zhang Z.W., Gan X.F., Cheng H.S. (2011) PIXE analysis of nephrite minerals from different deposits. *Nuclear Instruments and Methods in Physic Research B*, Vol. 269, No. 4, pp. 460–465, http://dx.doi.org/10.1016/j.nimb.2010.12.038

Zhang Z.W., Xu C.Y., Cheng H.S., Gan X.F. (2012) Comparison of trace elements analysis of nephrite samples from different deposits by PIXE and ICP-AES. *X-Ray Spectrometry*, Vol. 41, pp. 367–370.

Zhong Y.P., Qiu Z.L., Li L.F., Gu X.Z., Luo H., Chen Y., Jiang Q.Y. (2013) REE composition of nephrite jades from major mines in China and their significance for indicating origin. *Journal of the Chinese Society of Rare Earth*, Vol. 31, No. 6, pp. 738–748, http://dx.doi.org/10.11785/S1000–4343.20130615 [in Chinese].

## Unusual Graining Structure in Pink DIAMOND

Natural pink diamonds examined for origin of color determination often display visible pink coloring along planes of stress. This graining is visible at a slight angle to the plane and can occur as a single plane or multiple parallel planes. The color may be either uniform or unevenly distributed along the graining. One pink stone recently examined in the Carlsbad lab was noted to have a uniform plane of pink color with a colorless hole (figure 1, left). The diamond was graded Very Light pink, so the colored plane had low saturation, but the irregularity was impossible to miss in the microscope. When examined under polarized light, a cone of strain could be seen intersecting the plane and fitting perfectly in the colorless hole (figure 1, right).

Pink graining is the result of an unknown defect with an unknown formation mechanism (J.G. Chapman and C.J. Noble, "Studies of the pink and blue coloration in Argyle diamonds," Summer 1999 *G&G*, pp. 156–157). It seems to be related to the plastic deformation of diamond, evidenced by the color lying along planes
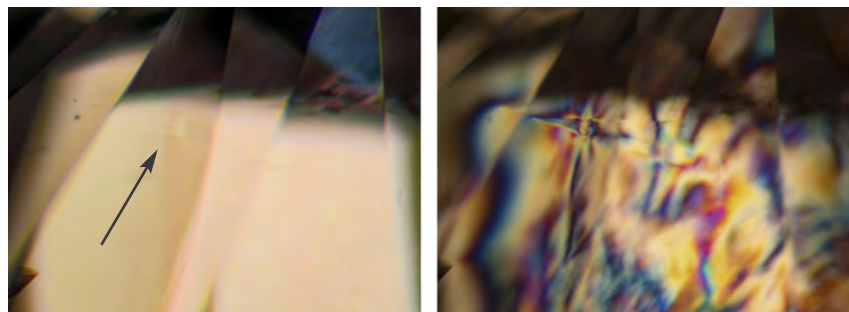
Figure 1. Left: A colorless hole within a natural pink diamond, observed with darkfield illumination. Field of view approximately 2 mm. Right: The colorless hole in polarized light, showing the cone of strain. Field of view approximately 2 mm.

of stress. Whether pink graining occurs during diamond growth or is formed after by stresses or heat from the earth (or a combination of the two) is also poorly understood. It is therefore a mystery as to whether the cone of strain formed first or concurrently and prevented the formation of pink graining at the circle of intersection, or if the cone formed afterward and destroyed the color centers associated with pink graining. Until diamond formation is more fully understood, this dynamic interplay of strain will remain a mystery.

*Troy Ardon*

## Yellow HPHT-Processed Rough Diamond

High-pressure, high-temperature (HPHT) annealing is a very effective method for changing the color of diamonds, particularly those with an undesirable brownish color. This treatment process has been practiced in the trade for more than 15 years. An important feature of this treatment is the etching often left behind on the diamond surfaces. Recently, one loose yellow diamond rough, weighing 2.47 ct and measuring 7.09 × 6.59 × 5.46 mm, was examined in the New York lab (figure 2). Without magnification, the rough had a vibrant yellow color and an overall clean-looking surface. Closer microscopic observation showed a very slightly etched surface, as well as some altered graphitized crystal inclusions in the diamond. Distinctive fluorescence reactions to long- and short-wave ultraviolet radiation similar to those of HPHT-processed material were observed, with a medium chalky bluish green under long-wave and medium to strong

Figure 2. This 2.47 ct rough diamond was HPHT processed to improve its color. Unlike conventional HPHT-treated diamonds, this stone has a natural-looking surface.
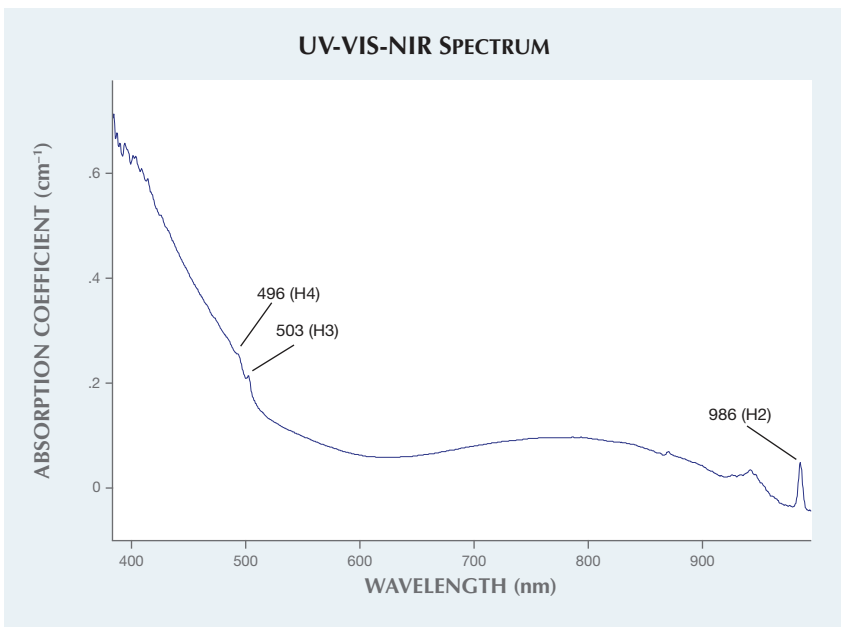


Figure 3. The yellow rough's UV-Vis-NIR spectrum, showing H2 (986 nm), H3 (503 nm), and H4 (496 nm) peaks, indicates HPHT treatment.

greenish yellow under short-wave UV. This was suspect, and further testing was needed. UV-Vis-NIR and mid-IR spectroscopy revealed the rough diamond to be HPHT processed.

The UV-Vis-NIR spectrum, seen in figure 3, showed a rise in absorption from 500 nm, associated with strong H3 (503 nm) and H4 (496 nm) peaks, along with a sharp H2 (986 nm) peak. These are indicative of HPHT treatment. Mid-IR spectroscopy (figure 4) revealed peaks at 1170 and 1332 cm$^{-1}$, indicating that the starting material of this diamond appeared to be type IaB. The high temperature and high pressure of the treatment created isolated nitrogen with a corresponding absorption peak detected at 1344 cm$^{-1}$. Occurrence of isolated nitrogen in a pure type IaB diamond is a strong indicator of HPHT treatment.

The majority of HPHT-treated rough diamonds have severely burned, etched, and pitted surfaces. This is the first time we have seen an almost eye-clean yellow rough post-HPHT treatment. With new technologies available to diamond merchants, HPHT processing techniques are becoming more

sophisticated, allowing for the retention of carat weight during the cutting process. This case serves as a clear re-minder that buying rough does not assure a lack of treatment.

*Sally Chan*

Figure 4. Mid-IR spectroscopy revealed an absorption peak at 1344 cm$^{-1}$, indicating the presence of isolated nitrogen. This occurrence and corresponding peak are characteristic of HPHT processing.
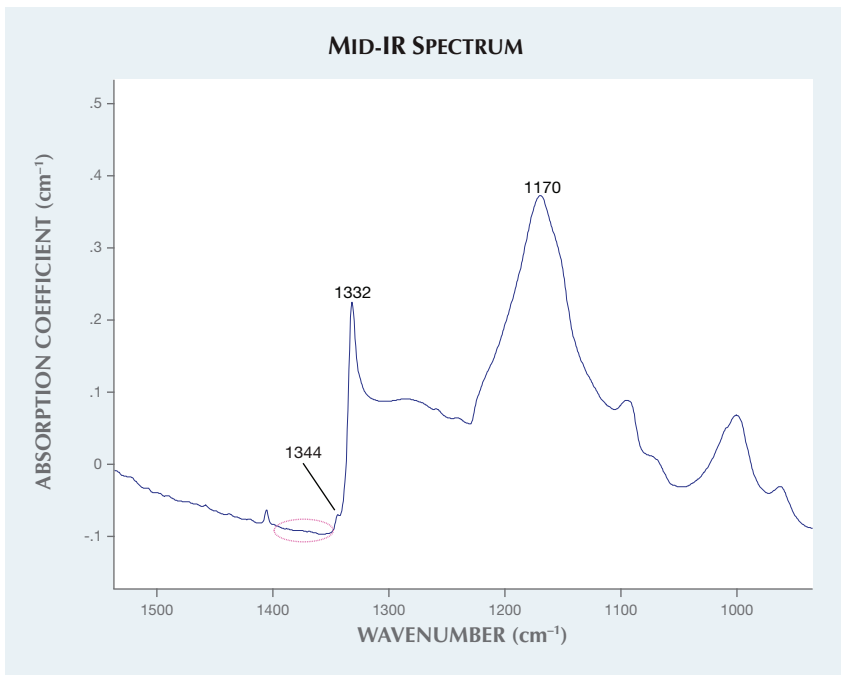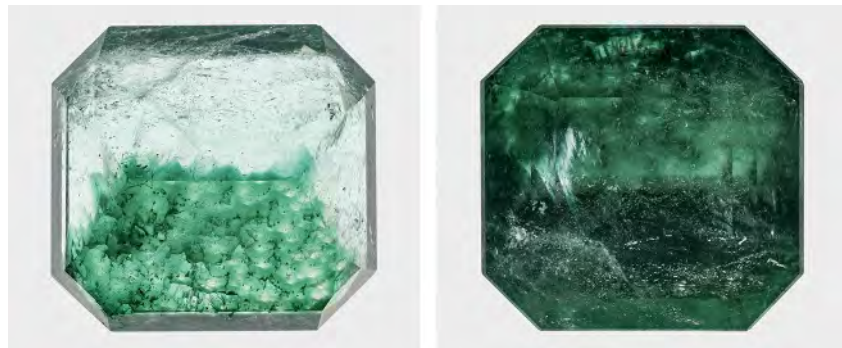
Figure 5. Left: When table-down, the stone is mainly colorless, showing some partially green overgrowth. Right: Face-up, the faceted stone displays an even and attractive dark green emerald color.

which was consistent with the observed color. Although similar zoning has been observed in emerald previously (E.J. Gübelin and J.I. Koivula, *Photoatlas of Inclusions in Gemstones, Volume 3*, Opinio Verlag, Basel, Switzerland, 2008, pp. 433–434), the zoning in this specimen was quite distinct.

This emerald demonstrates the significance of proper orientation and cutting style in fashioning high-quality gem materials.

*Jonathan Muyal, Nathan Renfro,*
*and Amy Cooper*

## Color-Zoned EMERALD

Cutting style and orientation are important considerations when cutting natural crystals with strong color zoning. Careful placement of these zones can distribute color by reflection, creating a uniformly colored finished stone when viewed face-up.

Recently, the Carlsbad laboratory received a 33.73 ct green octagonal step cut showing strong color zoning (figure 5). The gem cutter skillfully placed a thin green color zone in this emerald along the pavilion facets so that the stone would appear uniformly green when in a face-up position. Standard gemological testing revealed a refractive index (RI) of 1.571–1.578 and a specific gravity (SG) of 2.72. Chromium-related fea-

tures were observed in the red end of the spectrum when examined with a handheld spectroscope. All of these properties were consistent with emerald. During microscopic examination, minute jagged fluid inclusions and growth tubes were observed, proving the stone was of natural origin (figure 6).

Interestingly, the stone showed a strong green color zone very close to some of the pavilion facets, as well as hexagonal columnar-like growth and irregular zoning (figure 7). This type of zoning represents a late-stage influx of chromium and vanadium into the genetic environment, which were then incorporated into the crystal lattice of the beryl. EDXRF revealed high levels of Cr and V in the green color zone,

## Orange Faceted EOSPHORITE

The Carlsbad laboratory recently examined a 5.85 ct transparent orange oval mixed cut for identification services (figure 8). Standard gemological testing showed an RI of 1.640 to 1.667; the hydrostatic SG was 3.12. The stone showed yellow and reddish orange pleochroism. Fluorescence was inert to long-wave and short-wave UV radiation. The most distinctive internal characteristic, revealed by microscopic examination, was the presence of multiphase inclusions (figure 9), suggesting a formation process with the presence of water, such as pegmatitic and hydrothermal processes.

Figure 8. This 5.85 ct orange mixed cut was a rare faceted eosphorite.

Figure 6. When viewed from the side, irregular green color zoning is observed along with minute jagged fluid inclusions. Field of view 14.52 mm.



Figure 7. The colorless spots indicate parallel columnar growth of white beryl overgrown by green emerald. Field of view 19.27 mm.
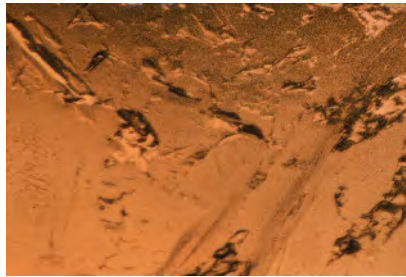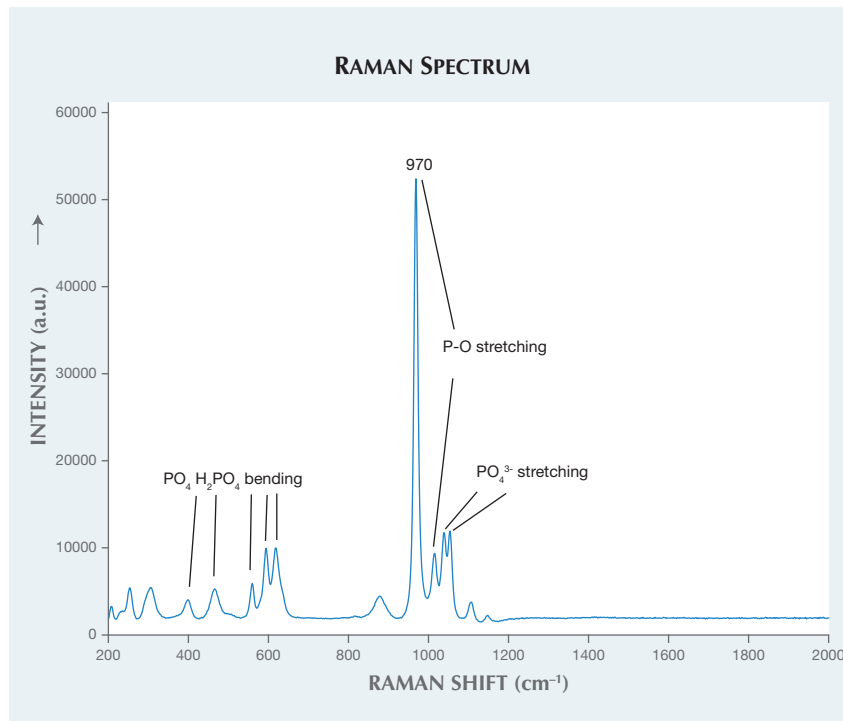
Figure 9. Multi-phase primary fluid inclusions are seen in the eosphorite, indicating a pegmatitic or hydrothermal formation process. Field of view 1.26 mm.

Raman spectroscopy confirmed that the stone belongs to the childrenite-eosphorite mineral series (figure 10), with intense peaks observed at 970 and 1011 cm$^{-1}$. These peaks are attributed to the P-O (phosphorus-oxygen) stretching vibrations (R. L. Frost et al., "Vibrational spectroscopic characterization of the phosphate mineral series eosphorite-childrenite-$(Mn,Fe)Al(PO_4)(OH)_2 \cdot (H_2O)$," *Vibrational Spectroscopy*, 2013, Vol. 67, pp. 14–21). This mineral series has a stoichiometric formula $(Mn,Fe)Al(PO_4)(OH)_2 \cdot (H_2O)$. Visible absorption spectroscopy revealed that the stone's orange color results from the combination of Fe and Mn (M.A. Hoyos et al., "New structural and spectroscopic data for eosphorite," *Mineralogical Magazine*, 1993, Vol. 57, pp. 329–336).

Energy-dispersive X-ray fluorescence (EDXRF) analysis revealed a composition of 25.10 wt.% $Al_2O_3$, 31.74 wt.% $P_2O_5$, 15.46 wt.% MnO, 11.47 wt.% $FeO_{tot}$, 0.49 wt.% MgO, 0.25 wt.% CaO, and 15.50 wt.% $H_2O$ (water weight percent is assumed from references). The stone contains 55.3 mol.% eosphorite and 40.5 mol.% childrenite. The calculated formula is $(Mn_{0.48}Fe_{0.35}Ca_{0.01}Mg_{0.03})(Al)_{1.09}(P_{0.99}O_4)(OH)_2 \cdot 0.91(H_2O)$, which indicates an intermediate member of the childrenite-eosphorite series with predominance of the Mn phase. As a result, the stone should be classified as eosphorite.

Eosphorite is the manganese-rich end member of the childrenite-eosphorite series, formed worldwide in pegmatites (T. J. Campbell and W. L. Roberts, "Phosphate minerals from the Tip Top mine, Black Hills, South Dakota," *Mineralogical Record*, 1986, Vol. 17, pp. 237–254) or by hydrothermal phosphatization of metasediments and associated with the intrusion of granites (R. S. W. Braithwaite and B. V. Cooper, "Childrenite in South-West England," *Mineralogical Magazine*, 1982, Vol. 46, pp. 119–126). This was the first faceted eosphorite examined by GIA's Carlsbad laboratory.

*Ziyin Sun, Nathan Renfro, and Amy Cooper*

Figure 10. Raman analysis of the eosphorite in the 2000–200 cm$^{-1}$ range showed a typical spectrum of phosphate oxyanions. The 970 and 1011 cm$^{-1}$ peaks are assigned to the P-O stretching vibration, while the 1038 and 1055 cm$^{-1}$ peaks are attributed to the $PO_4^{3-}$ stretching vibration. The 405, 473, 561, 595, and 618 cm$^{-1}$ peaks are associated with the $PO_4$ and $H_2PO_4$ bending modes.



RAMAN SPECTRUM

## Large Faceted HIBONITE

The Carlsbad laboratory recently examined an unusually large 134.43 ct opaque, very dark brown faceted hibonite (figure 11). Standard gemological testing gave spot RI values of 1.79 to 1.81 and a hydrostatic SG of 3.81. Hibonite, which crystallizes in the hexagonal system, has published RI values of 1.790 to 1.807, but we were unable to observe birefringence, probably due to its opacity and these values' proximity to the limits of the refractometer. The stone showed a high luster and was inert to LW and SWUV. Testing with a Geiger counter showed it was slightly radioactive. All of these features are consistent with hibonite, yet more advanced testing was needed for a positive identification of this unusual material.

Raman spectroscopy gave a spectrum consistent with hibonite. Laser ablation–inductively coupled plasma–mass spectrometry (LA-ICP-MS) analysis revealed large amounts of

*Figure 11. This 134.43 ct faceted hibonite is the largest examined by GIA to date.*

Mg, Ca, Al, Ti, and Fe; small amounts of Na, Si, Sr, La, and Ce; and traces of numerous other elements, including the radioactive elements thorium (62.62–122.60 ppma) and uranium (0.12–0.56 ppma). The presence of these elements caused the mineral to react to the Geiger counter. The thorium and REE content is consistent with samples from Madagascar (M.A.F. Rakotondrazafy et al., "Mode of formation of hibonite ($CaAl_{12}O_{19}$) within the U-Th skarns from the granulites of S-E Madagascar," *Contributions to Mineralogy and Petrology*, Vol. 123, No. 2, 1996, pp 190–201).

Microscopic examination revealed one deep green mineral inclusion breaking the surface of the table. Its Raman spectrum was consistent with spinel, a known associated mineral of hibonite. LA-ICP-MS analysis showed it was an iron-rich spinel within the hercynite($FeAl_2O_4$)-spinel ($MgAl_2O_4$) series, with almost one-third of the magnesium substituted by iron. Although difficult to see internally, other whitish mineral inclusions were visible, as well as an extensive fracture and cleavage network.

Orangy brown, transparent, and well-formed hexagonal crystals of gem-quality hibonite have been reported from Myanmar (T. Hain-

schwang et al., "Hibonite: A new gem mineral," Summer 2010 *G&G*, pp. 135–138; Summer 2012 Lab Notes, p. 136). Although not gem quality, the stone's size makes it a rare collector's mineral as well as the largest hibonite GIA has identified to date.

*Claire Ito and Ziyin Sun*

## Dyed and Natural Green JADEITE

The most coveted jadeite stones possess a deep rich green color. Lower-quality jadeite specimens are often treated with acid bleaching, polymer impregnation, and dyes to obtain this sought-after hue (E. Fritsch et al., "Identification of bleached and polymer-impregnated jadeite," Fall 1992 *G&G*, pp. 176–187). It is quite unusual to see stones with even a small amount of natural green color further altered with dyes. When this does happen, the natural properties of the untreated area can make it especially challenging to properly identify the stone as dyed.

Recently, the Carlsbad laboratory examined a carved jadeite specimen (figure 12). Standard gemological testing and Raman spectroscopy confirmed that the specimen was jadeite; infrared spectroscopy indicated the specimen had been polymer impregnated. Observation with a desktop spectroscope revealed lines at 630 and 655 nm, which are associated with chromium impurities in naturally

colored green jadeite. Observation under long-wave UV light revealed strong green-yellow fluorescence from most green areas of the stone, but not from the area where Cr lines were seen in the spectroscope. The colorless portions of the stone were also inert to UV light. Strong fluorescence in jadeite is often indicative of either polymer impregnation or a dye treatment; however, fluorescence from polymers would be evenly distributed throughout the stone due to the nature of impregnation. The fact that this stone only fluoresced from the green areas was strong evidence of dyeing rather than impregnation.

Microscopic observation (figure 13) revealed concentrations of green color in the boundary gaps in between grains, typical of dyed jadeite. The green area without fluorescence possessed a smoother, more consistent green color, which is customary for natural jadeite. Absorption spectroscopy in the UV, visible, and near-IR range confirmed that the natural area contained an absorption band from 530 to 740 nm, punctuated by natural chromium peaks at 691 and 655 nm (figure 14). The dyed green areas contained a double band around 627 and 665 nm, which is typical of dyed green jadeite.

The proper treatment identification of jadeite is essential to the consumer's confidence in this stone. Testing only a portion of this material might convince an observer that no

*Figure 12. Left: In natural light, the green band in the lower right section of the jadeite specimen is caused by natural chromium, while the other green spots are the result of a dye treatment. Right: Long-wave UV light shows a strong fluorescence from the dyed areas, with little to no fluorescence from the natural green area.*
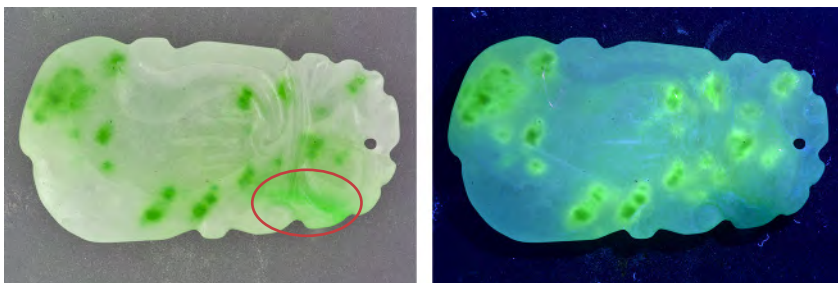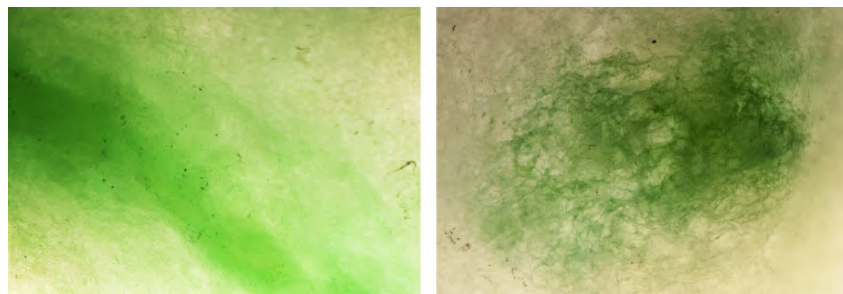
Figure 13. Left: A close-up of the natural green area shows a smooth, diffused color texture. Field of view 7.19 mm. Right: A close-up of a dyed area shows color concentrations in the thin gaps between the crystal grains of jadeite. Field of view 3.57 mm.



Figure 15. These three kornerupine beads (0.95–1.38 ct) were found to have a metallic coating.

dye had been applied. One must always expect the unexpected when attempting to determine treatments in any gemstone.

*Dylan Hand*

### Coated KORNERUPINE Beads

Three dark brown faceted beads with an unusual metallic luster were recently submitted to the Carlsbad laboratory for identification service (figure 15). The three beads ranged from 0.95 ct to 1.38 ct. Standard gemological properties revealed an RI of approximately 1.668–1.680, consistent with kornerupine. The hydrostatic SG ranged from 3.01 to 3.19. This is slightly lower than expected for kornerupine, but can be explained by air trapped in the drill holes. Raman spectroscopy confirmed that the stones were kornerupine.

All three beads exhibited a high metallic luster with silver and bronze coloration, which is not typical for kornerupine. Under microscopic examination with reflected lighting, the surfaces showed spotty luster, consistent with a surface coating (figure 16). Further evidence of coating was visible along the facet junctions, where the coating was worn away.

EDXRF chemical analysis detected large amounts of Mg, Al, and Si, consistent with kornerupine. EDXRF also revealed the presence of copper. The authors could not find documentation

Figure 14. UV-Vis-NIR spectra of the jadeite in the 250–850 nm range showed chromium lines at 655 and 691 nm in the natural green area and double broad bands around 627 and 665 nm in the dyed green area.

Figure 16. Diffused reflected light exposed spotty luster on the surface of one of the tested stones, indicating the presence of a coating. Field of view 2.17 mm.



**UV-VIS-NIR SPECTRA**

- Natural green area
- Dyed green area

Natural chromium
655  691

627
655
Dye bands

ABSORBANCE (a.u.)

WAVELENGTH (nm)

of naturally occurring copper in kornerupine, so this element may have been used to create the metallic coating. This is the first time the GIA laboratory has seen coated kornerupine.

*Amy Neurauter and
Heidi Breitzmann*

## Assembled Cultured Blister PEARL with an Unusual Component

GIA's Bangkok laboratory recently examined a blue-violet assembled cultured blister pearl (mabe) weighing 2.44 ct and measuring 10.23 × 5.86 mm (figure 17). The specimen had the appearance of a typical mabe pearl, exhibiting a boundary line between the nacre face and shell base. 2D microradiography showed a component with an unusual fluted shape, with radiotranslucency similar to that of the $CaCO_3$ nacre and the shell (figure 18).

GIA has examined the characteristics of mabe pearls used in commercial jewelry over the years (see Lab Notes: Summer 1981, pp. 104–105; Summer 1991, pp. 111–112; Fall 1991, p. 177; Summer 1992, pp. 126–127; Fall 1992, pp. 195–196; Fall 1996, p. 210), but none of these notes mentioned this unusual component. In Bangkok, this feature has
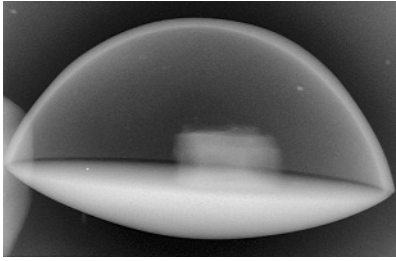


*Figure 18. A microradiograph of the intact assembled cultured blister pearl prior to sawing revealed an internal component. The radio-translucency of the object, the nacre, and the shell base are similar.*

been seen five times in mabe pearls submitted for testing since 2010; questions about its identity and purpose have been raised since the first observation.

Out of curiosity, one client decided to cut their sample in half in order to examine the interior in more detail (figure 19, left). The two halves consisted of a thin nacre dome top, which was coated with a dark layer on the inner surface; an artificial resinous material; and the white fluted object bordering the shell base. The fluted object was translucent, and a clear spiderweb structure was visible at 10× magnification. When ex-

posed to standard short-wave UV radiation (254 nm) and examined in the DiamondView, this object showed a moderate white blue reaction that followed the spiderweb pattern (figure 19, right).

Further investigation with Raman spectroscopy using a 488 nm laser revealed a calcite spectrum with peaks at 159, 285, 716, 1088, and 1750 cm⁻¹, similar to white coral (*Corallium secundum*). A small peak related to carotenoid pigments was present at 1020 cm⁻¹ (e.g., J. Urmos et al., "Characterization of some biogenic carbonates with Raman spectroscopy," *American Mineralogist*, Vol. 76, 1991, pp. 641–646).

Based on the spiderweb structure, radio-translucency, calcite spectrum, and general appearance, the object appeared to be a biogenic carbonate. White coral was the first material considered. Further research revealed accounts of sea urchin sections used in some assembled cultured blister pearls from Bali, Indonesia, in "Kuta" pearls (E. Strack, *Pearls*, Ruhle-Diebener-Verlag, Stuttgart, Germany, 2006, p. 605). Regardless of identity, the reason for including this material within some mabe pearls remains uncertain. It does not appear related to either the formation of the mabe pearl component or its weight and stability.
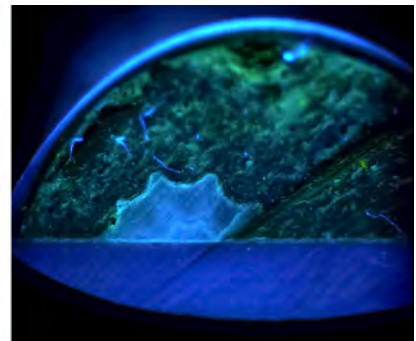
*Artitaya Homkrajae*

*Figure 17. This blue-violet assembled cultured blister pearl (mabe) weighed 2.44 carats and measured 10.23 × 5.86 mm.*



*Figure 19. Left: The cross-section revealed the white fluted object with a spiderweb structure bordering the shell base. Right: DiamondView imaging showed a moderate white blue reaction following the spiderweb pattern.*

*Figure 20. Three unique abalone pearls are shown alongside a typical 12 mm golden South Sea bead-cultured pearl for comparison.*

### Three Unique Large Natural Pearls from *Haliotis* (Abalone) Species

Natural abalone pearls are produced by many species of the *Haliotis* genus, which are ear-shaped saltwater univalve gastropods. They may form in many different sizes and shapes, though they are commonly encountered in baroque shapes, often taking the form of elongated "horns" and "teeth." The pearls are also notable for their high luster and attractive multicolored appearance, which is usually dominated by blue, green, or yellowish green bodycolors. GIA has reported on many *Haliotis* pearls in previous Lab Notes over the years (Fall 1984, p. 169; Spring 1996, pp. 47–49; Fall 2004, pp. 259–260; Spring 1993, p. 51).

Three large and unique abalone pearls from a client's collection were recently submitted to the New York laboratory (figure 20). Each piece was remarkable in its own right. A button-shaped pearl, measuring approximately 26 × 24 mm with impressive vivid "peacock" blue and green hues, was set in a yellow metal brooch. The second piece, seen in figure 20 on the far right, was a loose abalone pearl weighing 66.83 ct and measuring approximately 42 × 26 × 19 mm with a striking resemblance to a fish's head. The eye, mouth, and gill features were clearly outlined in the specimen, which possessed a smooth surface and subtle array of iridescent greenish yellow colors. The third piece, weighing 113.58 ct and measuring approximately 62 × 29 × 16 mm, was also loose and resembled the head of a snake. It exhibited strong iridescence with mottled patches of various colors

*Figure 21. All three specimens from figure 20 showed concentric and void-related internal structures typical of abalone pearls.*
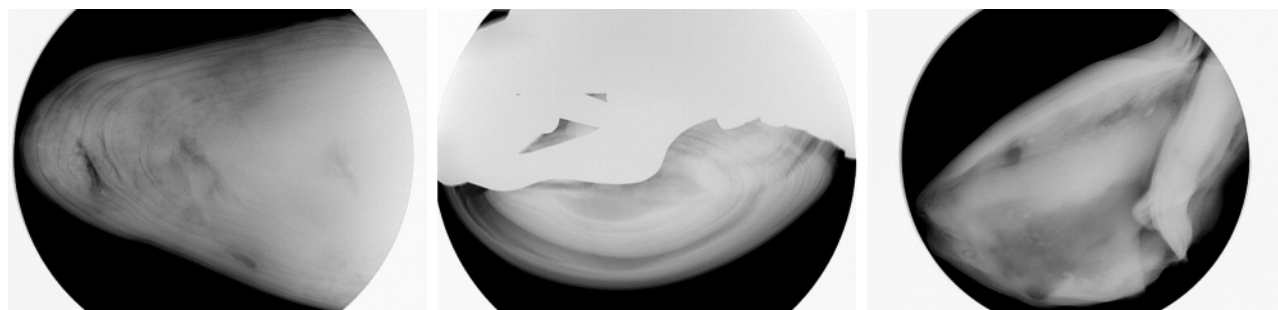
*Figure 22. This photomicrograph shows the patches of color and botryoidal-like subsurface structure characteristic of abalone pearls. Field of view 3.9 mm.*



*Figure 23. These intensely colored CVD synthetic diamonds, weighing 0.64 ct (left) and 0.43 ct (right), are color graded as Fancy Deep green-blue and Fancy Deep greenish blue, respectively.*

similar to the pattern observed on the scaly skin of snakes.

Microradiography revealed characteristic *Haliotis*-related voids with concentric growth structures in all three pearls (figure 21). Two of the pearls also revealed an iodine-rich composition, which GIA has noted is a fairly consistent property of abalone pearls. Such internal structures, along with their distinctive multicolored orient, bubble-like (botryoidal) subsurface structure (figure 22), interesting chemical composition, and chalky greenish yellow fluorescence under long-wave UV are all characteristic of abalone pearls.

The various shapes are determined by where the pearls are formed within the body of the mollusk, and often mirror the form of the gonad (E. Strack, *Pearls*, Ruhle-Diebener-Verlag GmbH & Co. KG, Stuttgart, 2006). Examining all three specimens at the same time allowed us to see a range of colors and shapes possible in abalone pearls. We look forward to encountering more of these unusual pearls.

*Joyce Wing Yan Ho and Surjit Dillon Wong*

---

### Irradiated Green-Blue CVD SYNTHETIC DIAMONDS

As-grown CVD synthetic diamonds are routinely treated in order to create attractive colors. Irradiated CVD synthetic diamonds without a multi-step treatment process are rarely seen in the lab, though an irradiated Fancy Deep gray-blue CVD synthetic has been reported (Fall 2014 Lab Notes, pp. 240–241). The New York lab recently examined two such examples: a 0.64 ct Fancy Deep green-blue and a 0.43 ct Fancy Deep greenish blue specimen (figure 23).

Dark inclusions, faint color bands, and chips on the girdle were observed in both specimens under the microscope. Tatami-like strain was also seen in both diamonds under cross-polarized light. DiamondView images revealed parallel green linear

*Figure 24. DiamondView images reveal linear striations in the pavilions of the 0.64 ct (left) and 0.43 ct (middle) specimens. A face-up image of the 0.43 ct synthetic shows a yellowish green zone of growth interruption (right).*

**UV-VIS-NIR SPECTRA**

393.5
594.2
666.5
741.2
737.0
735.8
469.9
464.3
0.64ct
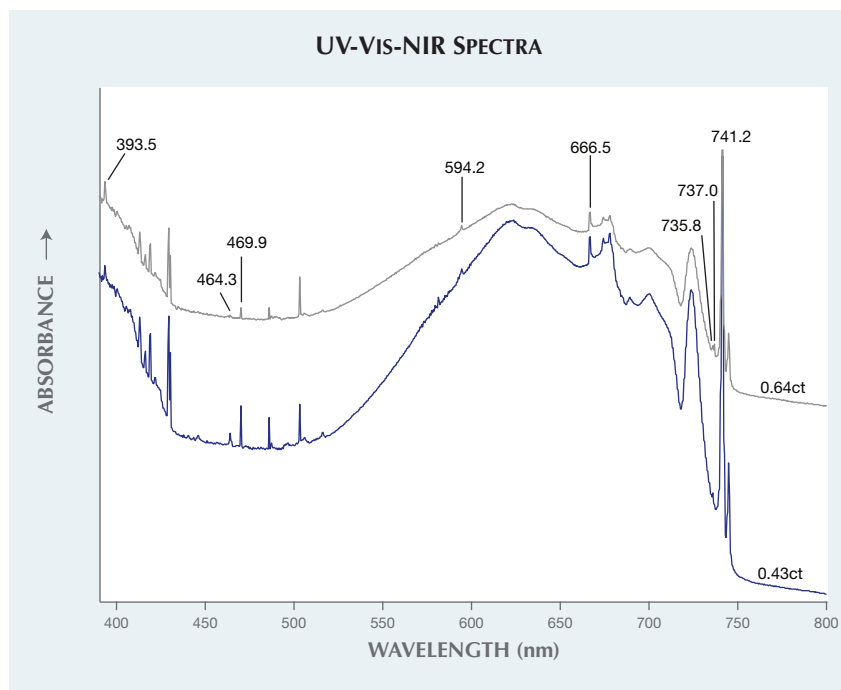0.43ct

ABSORBANCE →

WAVELENGTH (nm)
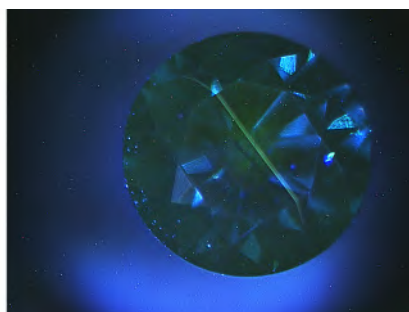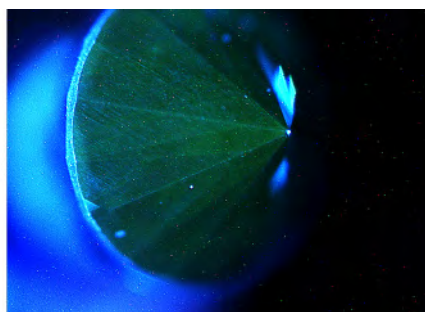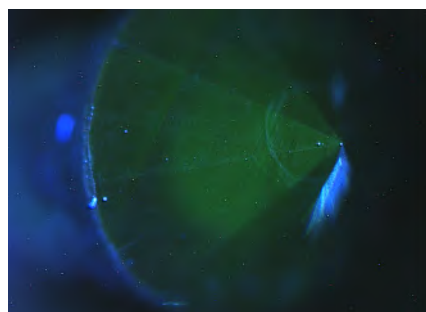
*Figure 25. Absorption spectra of the two green-blue CVD synthetics at liquid nitrogen temperature revealed radiation-related peaks. The peaks at 666.5 and 735.8 (both neutral self-interstitial defects) indicate that these samples were annealed at lower temperatures or irradiated without annealing. The Si-V center defect (737.0 nm center) can also be observed at the 736.5–736.9 nm doublet. Many unknown absorption bands (unlabeled in this spectra) are also detected.*

striations in the pavilions (figure 24). Face-up DiamondView images also showed yellowish green zones, which were formed by growth interruptions (again, see figure 24). Both stones were pure type IIa diamonds with no other defects in the IR spectra. High-resolution UV-Vis-NIR absorption spectra detected Si-V center defects at the 736.5–736.9 doublet (737 nm center, (V-Si-V)⁻); the spectra also revealed radiation-related peaks at 393.5, 464.3, 469.9, 594.2, 666.5, 735.8, and 741.2 nm (figure 25). The 393.5 band is from the ND1 center, a negatively charged vacancy (V⁻). An intrinsic radiation center (TR12) was detected at 469.9 nm. The TR13 center at the 464.3 peak is a local vibrational mode associated with the TR12 center, and the 594.2 band (595 nm center) is a typical radiation-induced center. The 666.5 peak is attributed to a neutral self-interstitial ($I^0$) defect. The 735.8 band, also caused by the $I^0$ defect, is

related to the 666.5 band. Strong absorption from the GR1 center, which contains neutral vacancies ($V^0$), was detected at 741.2 nm. All these radiation-related peaks can be destroyed by HPHT treatment, while peaks at 666.5 and 735.8 nm can be annealed out at temperatures ranging from 420° to 540°C (see A.T. Collins, "Spectroscopy of defects and transition metals in diamond," *Diamond and Related Materials*, Vol. 9, Nos. 3–6, 2000, pp. 417–423). The presence of these peaks indicates that these CVD synthetics were either annealed at lower temperatures (<420° to 540°C) or irradiated without annealing.

Although microscopic features such as strain pattern can be helpful in the identification of CVD synthetics, they are not conclusive. DiamondView imaging is very useful for this purpose due to its ability to detect linear striations. As CVD growth techniques continue to improve, we

anticipate that intensely colored, high-quality CVD synthetic diamonds will become more prevalent in the trade.

*Kyaw Soe Moe, Ulrika D'Haenens-Johansson, and Wuyi Wang*

## Polished Freeform TOPAZ Imitating Diamond Rough

Topaz is one of many near-colorless diamond simulant materials that may be faceted to bear a closer resemblance to diamond. Although most diamond simulants in the marketplace are faceted, every now and then, one comes across what appears to be a near-colorless octahedron diamond rough (see Lab Notes: Fall 1996, p. 205; Fall 1997, pp. 217–218; Fall 2007, p. 250; Fall 2009, pp. 230–231). A near-colorless 13.70 ct stone (figure 26) was recently submitted to the New York laboratory as a rough diamond from an alluvial source. At first glance, even with a well-trained eye, this stone could easily be misidentified. It bore a striking resemblance to diamond rough, with a "well-formed" octahedral shape and trigon-like formations on the surface

*Figure 26. The 13.70 ct topaz under daylight-equivalent light. Note the triangular features on each of the octahedral faces.*
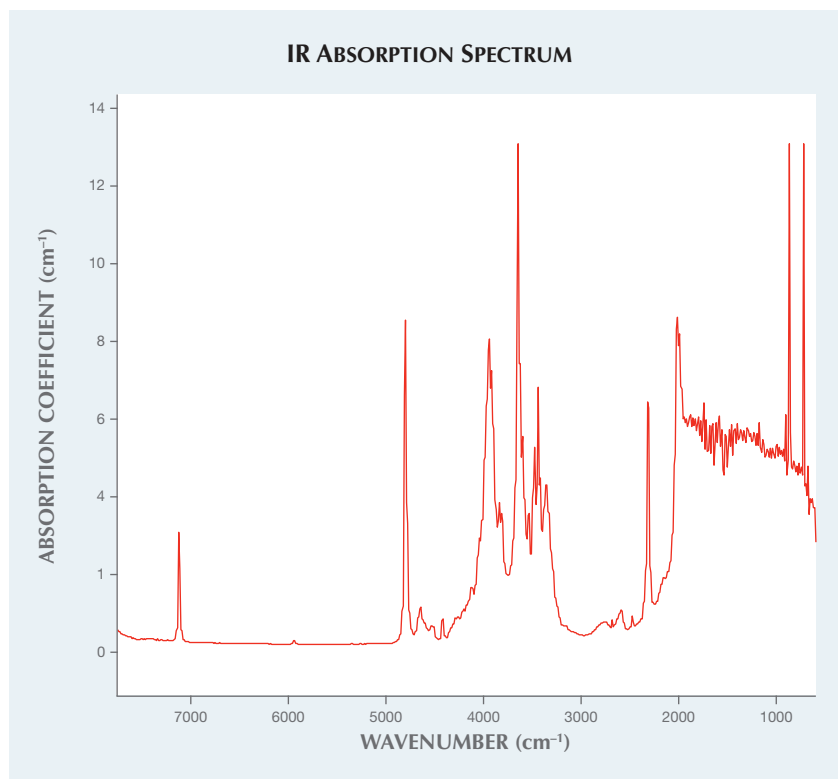
## IR ABSORPTION SPECTRUM



*Figure 27. Many absorption peaks related to the hydroxide ion in the crystal structure of topaz are detected in this infrared absorption spectrum, including those at 4802 and 3650 cm⁻¹. These have never been documented in any diamond absorption spectrum.*

(FTIR) spectroscopy, which revealed the distinctive topaz absorption spectrum shown in figure 27, with peaks at 4802 and 3650 cm$^{-1}$ (K. Shinoda and N. Aikawa, "IR active orientation of OH bending mode in topaz," *Physics and Chemistry of Minerals*, Vol. 24, No. 8, 1997, pp. 551–554).

Although topaz can be easily shaped and polished into an octahedral shape, the trigon-like figures observed on the surface require an additional fabrication step and are not typically seen in octahedral-shaped simulants. Intentional material processing steps to mask a stone's identity remind gemologists of the caution and care that need to be taken when dealing with gemstone identification—even when the identity of the material initially seems obvious.

*Akhil Sehgal and Riccardo Befi*

of each of the faces. To further complicate the identification of this stone, topaz and diamond have the same heft due to overlapping specific gravities: 3.52 (+/-0.10) for diamond,

3.53 (+/-0.04) for topaz. The material was doubly refractive, with a spot RI reading of 1.61, properties consistent with topaz. Final confirmation came from Fourier-transform infrared

For online access to all issues of GEMS & GEMOLOGY from 1934 to the present, visit:

**gia.edu/gems-gemology**

# GEMS & GEMOLOGY

# CONGRATULATIONS

This year, hundreds of readers participated in the 2015 *Gems & Gemology* Challenge. Entries arrived from around the world, as readers tested their gemological knowledge by answering questions listed in the Spring 2015 issue. Those who earned a score of 75% or better received a GIA Certificate of Completion recognizing their achievement. The participants who scored a perfect 100% are listed below.

## G&G Challenge Winners

### Australia
Barbara Wodecki

### Belgium
Sheila Sylvester

### Canada
Diane Gauthier

### Italy
Chiara Piussi

### United Kingdom
Francesca Lawley

### United States
Andrea Blake

Beverly Brannan

Thaïs Anne Lumpp-Lamkie

Lisa Marsh–Vetter

Paul Mattlin

Daniel Novak

Lydia Pringle

Jana Smith

Ric Taylor

Colleen Walsh

Flora Walters

Glenn Wargo

## Answers
See pages 56–57 of the Spring 2015 issue for the questions.

1 (d), 2 (b), 3 (a), 4 (b), 5 (a), 6 (d), 7 (a), 8 (c), 9 (*), 10 (a), 11 (b), 12 (d), 13 (c), 14 (c), 15 (d), 16 (d), 17 (c), 18 (b), 19 (a), 20 (b), 21 (a), 22 (a), 23 (c), 24 (a), 25 (d)

* Question withdrawn

## Cleavage System in Pink Diamond

A 0.29 ct natural Fancy Intense purplish pink diamond with a microscopically interesting geometric feature (figure 1) was recently examined at GIA's Carlsbad laboratory. A network of planar cracks, oriented in three octahedral directions, was observed at the surface of a pavilion facet (figure 2). These linear cleavage cracks were caused by localized strain on an octahedral plane.

The octahedral plane in diamond has the weakest atomic bonding, which means that when a diamond is strained, this is the direction that will be most affected. This stone offers the perfect example of strain products in



Figure 2. Three directions of cleavage along octahedral planes are seen in this pink diamond. Photomicrograph by Jonathan Muyal; field of view 1.22 mm.

Figure 1. This Fancy Intense purplish pink 0.29 ct diamond was host to a complex cleavage network. Photo by Robison McMurtry.



pink diamond. The purplish pink color results from plastic deformation along octahedral planes. Also present along the octahedral plane is a zone where the strain was so great that it was relieved by cracking, creating the cleavage network seen in figures 2 and 3.

The cleavage network in this diamond is the most aesthetic one encountered by the author to date due to its finely textured geometric pattern. Interestingly, the clue to
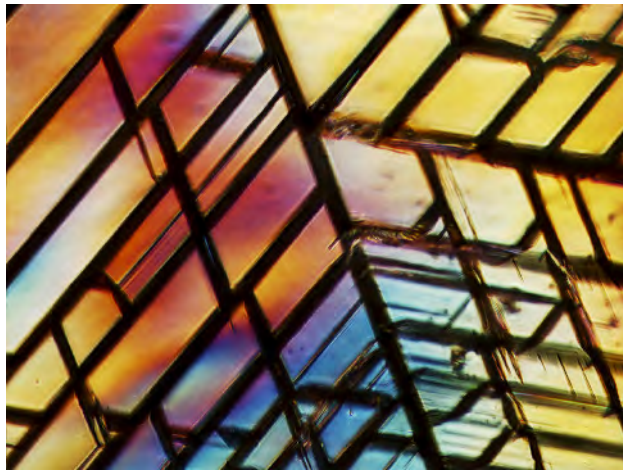
Figure 3. Between crossed polars the diamond shows high-order interference colors consistent with the strain causing the cleavage network along the octahedral planes. Photomicrograph by Jonathan Muyal; field of view 0.62 mm.

the planar cleavage network lies in the bodycolor of the stone, which indicates significant strain. This high-order strain is easily revealed between crossed polars. If a cleavage network is present in a diamond such as this, it may have a strain-induced bodycolor as well.

*Jonathan Muyal*
*GIA, Carlsbad*

### Rough Diamond Fragment with a Large Green Cleavage Surface

A colorless 2.02 ct flattened diamond crystal fragment (figure 4), from Rowan Beach of San Francisco, was examined at GIA's Carlsbad lab. The fragment exhibited a large bluish green internal surface that was readily visible without magnification. Initially thought to be a colorful mineral inclusion, it proved to be a radiation-induced coloration along the internal surface. When a diamond is irradiated (during laboratory color treatment or occasionally in nature), carbon atoms are removed from their normal position in the diamond lattice; this creates what scientists call the "GR1" optical defect (i.e., a vacant atom position in the lattice). The presence of this defect causes the diamond to selectively absorb light toward the red end of the visible spectrum, while the remaining portions are transmitted through the diamond and, when recombined, seen as a green or bluish green color. The GR1 optical defect can be removed in the lab by heating the diamond to over 600°C; this heating changes the green color to yellowish brown. The added energy allows a carbon atom to again occupy the vacant lattice position.

Green or bluish green color in diamonds is most often the result of exposure to a source of radiation in a geologic environment near the earth's surface. The source of exposure could be a nearby grain of a radioactive mineral that gives rise to a small "radiation spot" on the outer surface.

Conversely, the source could be a radioactive solution that was able to penetrate surface-reaching cleavages in the diamond. In both cases, the source produced alpha-particle radiation, which has a limited penetrating distance in diamond. As a result, the radiation spot or stain is confined to a zone close to the radioactive material. Such radiation stains are not uncommon in diamonds, though they are often removed by the faceting process.

The presence of a large green internal radiation stain indicates that this diamond was irradiated in a near-surface geological environment where temperatures high enough to modify the GR1 were unlikely. This means that the irradiation took place in the crust after the diamond was transported up from the mantle by the kimberlite magma eruption. Although the geographic origin of this rough diamond is uncertain, it is one of the more intriguing examples of a natural "radiation-stained" diamond we have seen.

*James Shigley*
*GIA, Carlsbad*

### Blue Gahnite Inclusions in Cat's-Eye Heliodor

Four golden oval cabochons (figure 5) were submitted to the Carlsbad laboratory by L. Allen Brown (All That Glitters, Methuen, Massachusetts) for scientific examination. Standard gemological testing revealed that the stones were beryl. Under incandescent fiber-optic illumination, the stones showed a very sharp cat's eye, caused by growth

Figure 4. This 2.02 ct rough diamond displays prominent green coloration along an internal cleavage surface. Such coloration is thought to result from the presence of a natural radioactive solution within the cleavage. Photo by James Shigley.
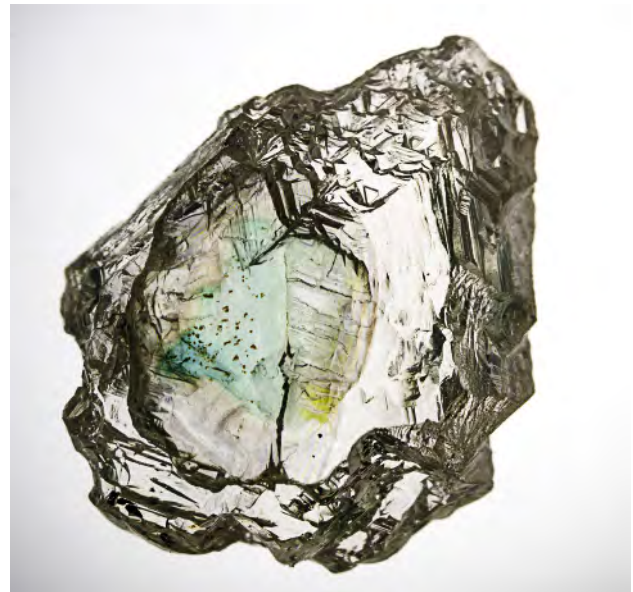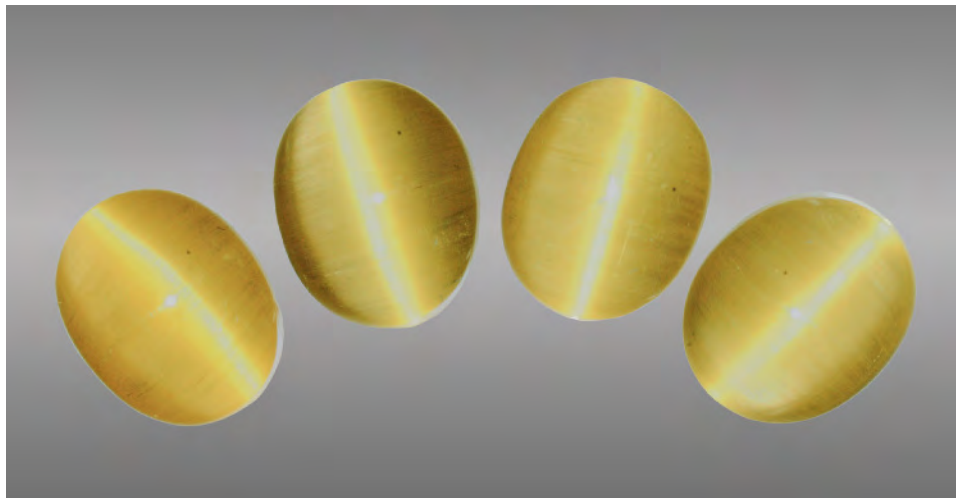
*Figure 5. These four heliodor cabochons display sharp eyes under incandescent fiber-optic illumination. Photo by C.D. Mengason.*

tubes and fine needle-like inclusions oriented parallel to the c-axis. Under magnification, blue crystals with octahedral morphology (figure 6) were the most distinctive internal characteristic.

Raman microspectroscopy was used to identify the blue octahedral inclusions as gahnite, a zinc-rich end member of the spinel group with the general formula $ZnAl_2O_4$. It occurs most commonly as an accessory mineral in granitic pegmatites, usually associated with almandine-spessartine garnet, muscovite, beryl, tourmaline, and nigerite (D.R. Soares, et al., "Chemical composition of gahnite and degree of pegmatitic fractionation in the Borborema Pegmatitic Province, northeastern Brazil," *Anais da Academia Brasileira de Ciências*, 2007, Vol. 79, No. 3, pp. 395-404). According to Brown, the stones were purchased in Tucson in 2010 and were represented as being from Brazil. These are the first beryls with gahnite inclusions that GIA has examined to date. Since gahnite is a diagnostic inclusion in sapphires

*Figure 6. Diffused fiber-optic illumination reveals well-formed blue octahedral crystals in addition to the hollow tubes that cause the chatoyancy. The black needle-like inclusions may be hematite. Photomicrograph by Nathan Renfro; field of view 1.10 mm.*
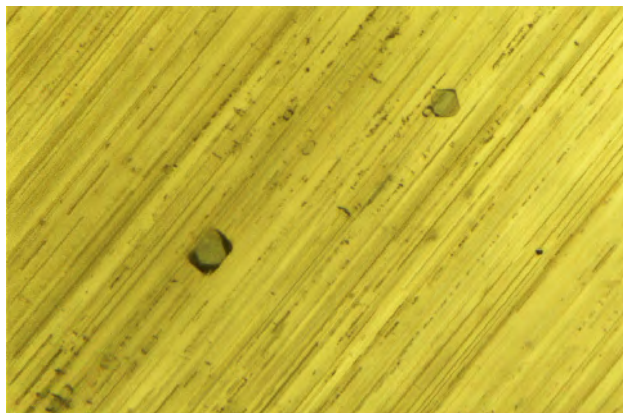


from Sri Lanka (E.J. Gübelin and J.I. Koivula, *Photoatlas of Inclusions in Gemstones*, Vol. 3, Opinio Verlag, Basel, Switzerland, 2008, p. 290), detailed study of gahnite may also provide some indication of the geographic origin of heliodor.

*Ziyin Sun, Nathan Renfro,*
*Jonathan Muyal, and Adam Steenbock*
*GIA, Carlsbad*

## Pezzottaite Debuts as the Newest Trapiche Gem Mineral

Since the first enigmatic six-spoked emeralds were sent to GIA in the mid-1960s for analysis (H.L. McKague, "Trapiche emeralds from Colombia," Fall 1964 *G&G*, pp. 210–213, 223), the family of trapiche-type gem minerals has grown to include a variety of species and morphologies. One of the latest mineral varieties to exhibit the rare trapiche form is a relatively new and rare mineral itself: pezzottaite.

Following its appearance at the 2003 gem shows in Tucson, pezzottaite has quickly become an item coveted by gem and mineral collectors around the world. A member of the beryl group and with trigonal symmetry (the beryl *species* has hexagonal symmetry), it was approved by the International Mineralogical Association in September 2003 as a unique species and named after mineralogist Dr. Frederico Pezzotta (see B.M. Laurs et al., "Pezzottaite from Ambatovita, Madagascar: A new gem mineral," Winter 2003 *G&G*, pp. 284–301).

In 2004, while working in the gem markets of Mae Sai and Mae Sot along the border of Thailand and Myanmar, Elaine Rohrbach of Gem-Fare obtained a small collection of pale pink trapiche crystals and crystal fragments reported to be of Burmese origin. Laboratory analysis later proved these crystals to be the cesium-containing mineral pezzottaite (previously confirmed localities include Madagascar and Afghanistan).

A doubly terminated, well-developed crystal obtained by one of the authors (JIK) exhibits the tabular prismatic habit characteristic of the species, but with a complete six-

Figure 7. As viewed through the pinacoid face, strong oblique fiber-optic lighting illuminates the six-legged trapiche structure emanating from the c-axis of this doubly terminated 2.33 ct pezzottaite crystal. Photo by Kevin Schumacher.
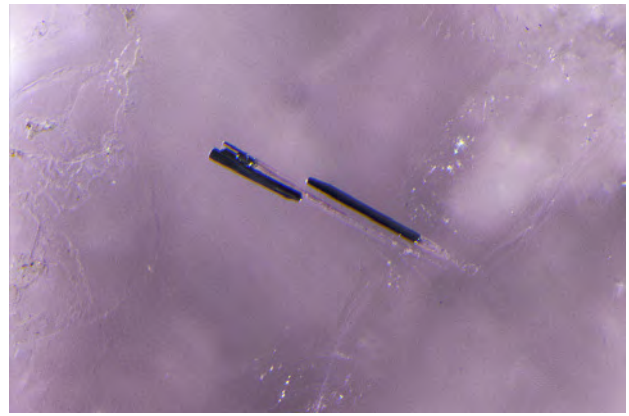


Figure 9. Eye-visible dark needles were seen throughout the pezzottaite crystal with diffused transmitted illumination. Despite a clear Raman signal, the features could not be conclusively identified. Photomicrograph by Nathan Renfro; field of view 1.10 mm.

spoke trapiche structure that is clearly visible in both reflected and transmitted light (figure 7). Another doubly ter-

Figure 8. Another well-developed, doubly terminated pezzottaite crystal from the same locality, weighing 6.17 ct and measuring 11.19 × 10.71 × 8.61 mm, has separate crystals growing at random angles on each pinacoid face. Each of these smaller crystals also exhibits trapiche growth. The white trapiche growth reaches all six prism faces in both of the tabular crystals, as well as those faces on the secondary growth crystals. Photo by Elise A. Skalwold.



minated crystal obtained by author EAS from the same parcel shows secondary crystals growing out of each pinacoid face, each of which are also trapiche crystals (figure 8). Similar to trapiche crystals of other mineral species, each of the spokes radiates from the central c-axis toward the prism faces and in a plane parallel to the basal pinacoid. Exploring the former crystal's inner world revealed not only the details of the white spokes and a spray of golden brown needles and eye-visible black needles, but also a delightful surprise: minute euhedral blue crystals (figures 9 and 10). Unfortunately, the black needles were not identifiable despite their distinct Raman spectrum. Due to their depth within the host, the brown needles and blue crystals remain mysteries as well. Let this be a lesson that nondestructive

Figure 10. Using diffused transmitted and oblique fiber-optic illumination, a golden-brown spray of needles is shown deep in the crystal, along with a bright blue crystal to its right. Their depth precluded analysis by Raman spectroscopy. Photomicrograph by Nathan Renfro; field of view 0.91 mm.
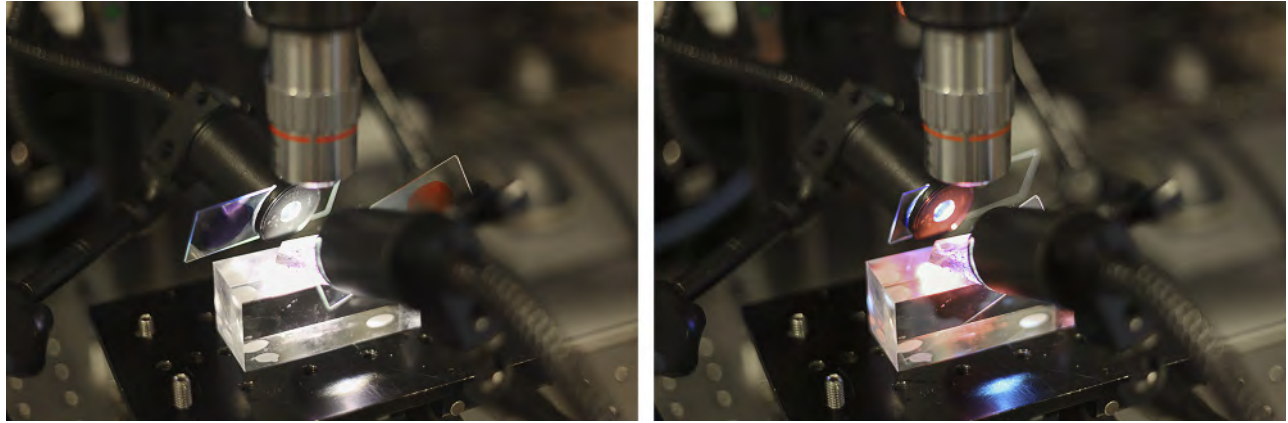
*Figure 11. In one method of applying Rheinberg-type illumination, glass slides are fitted to the end of two fiber-optic illuminators and painted with red and blue ink (left) to create a filter that is easily positioned by moving the colored portion of the glass slide into the light path (right). Photos by Danny J. Sanchez.*

testing cannot always provide answers, but we can be content with exploring the beauty of the micro-world while leaving some mysteries for the future.

*Elise A. Skalwold*
*Ithaca, New York*

*John I. Koivula*
*GIA, Carlsbad*

### Modified Rheinberg Illumination
Lighting control is one of the most important considerations for maximizing the use of the gemological microscope; with greater control over illumination sources, more information may be gathered from observing a specimen.

An interesting technique that gives the microscopist another lighting tool is modified Rheinberg illumination, also known as differential color illumination (M. Pluta, *Advanced Light Microscopy: Specialized Methods*, Vol. 2, PWN-Polish Scientific Publishers, Warsaw, 1989, pp. 113). This method, as modified for gemological microscopy, employs the use of a contrasting color filter between each illumination source and the subject (figure 11) to achieve an "optical staining" effect (figure 12). When viewing crystallographically aligned subjects such as negative crystals or inclusions with well-defined, reflective crystal faces, each illumination source highlights areas that have the same crystallographic orientation (figure 13). This provides dramatic false-color contrast to an otherwise low-contrast

*Figure 12. This silvery metal sulfide inclusion in fluorite shows angular crystal faces, but the low contrast in the image on the left makes it difficult to resolve the orientation of the faces from different sections of the inclusion. Rheinberg illumination provides stark contrast between differently oriented regions by using two colored illumination sources that reflect their independent color off of crystallographically aligned crystal faces, as seen in the center and right images. This allows the microscopist to easily observe the different orientations of the crystal faces in the metal sulfide inclusion, as evidenced by the dramatic boundary of the two contrasting colors. Photomicrographs by Danny J. Sanchez; field of view 1.66 mm.*
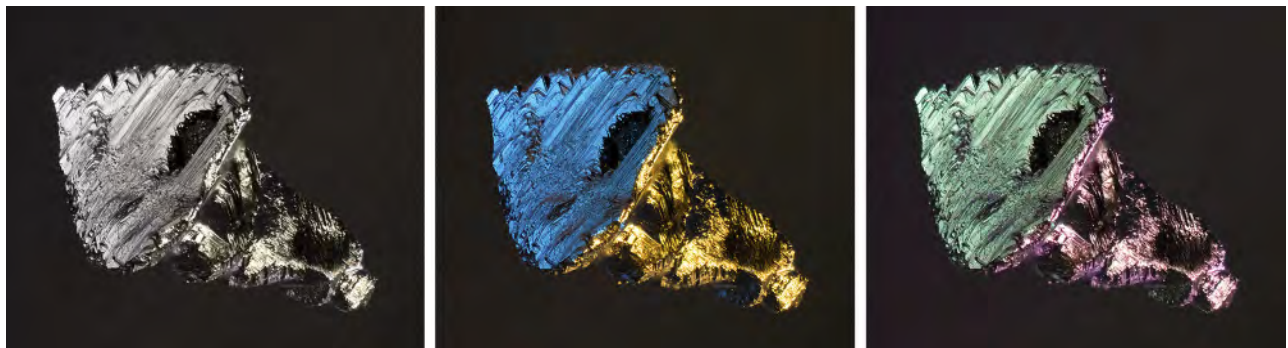
Figure 13. With modified Rheinberg illumination to impart contrasting color on some of the crystal faces, the negative crystals in the rock crystal quartz (left) prove to be crystallographically aligned (right). Photomicrographs by Nathan Renfro; field of view 7.34 mm.

subject. This enhanced contrast makes it easier to observe the relationship between areas in an inclusion scene with identical and also differing crystallographic orientations.

*Nathan Renfro*
*GIA, Carlsbad*

*Danny J. Sanchez*
*Los Angeles*

### Glassy Melt Inclusions in Sapphires from Montana

Two-phase inclusions are common in many sapphires. Physical and chemical analysis of the gas and liquid phases present in these inclusions can shed light on the formation conditions of alluvial sapphires, even in the absence of evidence of source rock lithology. We report here some initial observations of a different type of two-phase inclusion, seen in alluvial sapphires from the Rock Creek and Missouri River deposits in the state of Montana.

At first glance, these inclusions appeared to be ordinary gas-liquid inclusions (figure 14, left); however, polishing through the inclusions demonstrated that the "liquid" component was actually a glassy solid. The identification of the solid as a glass rested with the phase's optically isotropic nature and the lack of an identifiable Raman spectroscopic signal attributable to any crystalline phase. Glassy melt inclusions in Montana sapphires were previously documented by John Koivula (R.W. Hughes, *Ruby & Sapphire*, RWH Publishing, Boulder, Colorado, 2007, pp. 468–469). Electron microprobe analysis (EPMA) of glass inclusions from several samples showed them to be dacitic to trachydacitic in composition. In this sense the inclusions are ordinary two-phase inclusions in which the original liquid phase was a silicic magma that quenched to form a silicate glass. The gas phase is presumed to have originally been dissolved in the silicate magma. Later exsolution produced a separate gas phase as volatile solubility

Figure 14. Left: A two-phase glassy melt and gas inclusion and a glass-filled discoid fracture in a sapphire from the Rock Creek deposit in Montana. Center: A two-phase glassy melt and gas inclusion and a glass-filled discoid fracture in a sapphire from the Rock Creek deposit. Right: A two-phase glassy melt and gas inclusion, in a sapphire also from the Missouri River, showing the surrounding discoid fracture. This fracture presumably filled with a silicate liquid and partially healed, leaving an impression in some places of the corundum host's trigonal crystallographic orientation. Photomicrographs by Aaron Palke; field of view 1.24 mm (left) and 0.62 mm (center and right).

*Figure 15. This 4.71 ct Brazilian colorless topaz hosts a cluster of hexagonal molybdenite crystals. Photo by Kevin Schumacher.*

in the magma decreased due to falling pressure and/or temperature. Volatile exsolution likely also led to the discoid fractures commonly seen around melt inclusions, which are filled with silicate liquid and/or the volatiles themselves (again, see figure 14, left). Figure 14 (center) captures a snapshot of the process of volatile exsolution and the "bursting" of the two-phase inclusions, in which multiple gas bubbles seem to have precipitated instantaneously as the inclusion exploded out into the surrounding corundum. Due to the high relief of the silicate glass, these dis-

coid fractures often have a "flux"-like appearance. In some cases, the fractures seem to have partially healed, leaving hexagonal geometric patterns as evidence of the crystallographic orientation of the sapphire host (figure 14, right). Further work is being carried out to characterize these inclusions and to decipher the story they have to tell about the genesis of alluvial Montana sapphires.

*Aaron Palke and Nathan Renfro*
*GIA, Carlsbad*

*Richard B. Berg*
*Montana Tech of the University of Montana*
*Butte, Montana*

## Molybdenite in Topaz

A photogenic cluster of hexagonal molybdenite crystals ($MoS_2$) was recently discovered in a 4.71 ct transparent colorless hexagonal step-cut topaz (figure 15). The topaz host was identified using traditional gemological testing, and the molybdenite cluster (figure 16) was identified through its metallic luster, morphology, and the presence of molybdenum, which was detected using focused EDXRF analysis.

This gem, which came from Luciana Barbosa of the Gemological Center in Ashville, North Carolina, is from Seridó, Rio Grande do Norte, Brazil. We have never seen this inclusion-host association before, and it is not previously recorded in the literature. This elegant gem is a perfect micromount of molybdenite in a faceted showcase.

*John I. Koivula*

*Figure 16. It was a surprise to discover molybdenite crystal inclusions in topaz. Shadowed lighting reveals iridescence and surface details on the cluster, which measures 2.82 mm in length. Photomicrograph by Nathan Renfro.*

# LETTERS

## NATURAL DIAMONDS MISTAKENLY IDENTIFIED AS NPD SYNTHETIC DIAMONDS

We have read with much interest and surprise the recent *G&G* lab notes on two purported synthetic nano-polycrystalline diamonds, or NPD (Spring 2014, pp. 69–71; Winter 2014, pp. 300–301). Looking at the data presented in these reports, it appears unlikely to us that the analyzed samples are indeed NPD synthetic diamonds.

In the infrared spectrum shown in the first lab note, the authors did not mention the presence of strong, distinct absorptions at approximately 2460 and 660 $cm^{-1}$; only two bands at 3611 and 3727 $cm^{-1}$ were described. These four bands are well known and correspond with some deviation to vibrations of molecular $CO_2$: $v_2$ is the angular bend at about 667 $cm^{-1}$, $v_3$ is the asymmetric stretch at about 2349 $cm^{-1}$, and the two other bands are combinations of the fundamentals: $v_3 + 2v_2$ near 3683 $cm^{-1}$, and $v_3 + v_1$ near 3686 $cm^{-1}$ (Schrauder and Navon, 1993). Note that Schrauder and Navon describe a natural diamond, not a synthetic one—the presence of $CO_2$-like features is a relatively rare feature of natural diamond but has never been described for any type of synthetic diamond. This oversight of $CO_2$-rich diamonds is even more puzzling as GIA scientists have participated in our publications on this variety of diamonds (Hainschwang et al., 2006; Hainschwang et al., 2008), or published their own work on the subject (Wang et al., 2005), including a lab note by the authors on a natural black $CO_2$-rich diamond (Johnson and Moe, 2010).

Then the interpretation of the dominant one-phonon absorption band at 1220 $cm^{-1}$ is missing. Interestingly, it is also missing in previous papers on NPD (Skalwold, 2012; Skalwold et al., 2012), even though the band was first documented in the 1980s for natural and synthetic polycrystalline diamond. This band has been attributed to absorption of the diamond lattice distorted by inclusions of lonsdaleite; EPR spectroscopy has identified a very high concentration of broken C-C bonds due to interconnected textures of diamond (111) and lonsdaleite ($10\bar{1}0$) (Bokii et al., 1986). Lonsdaleite has been known since the early 1960s (Ergun and Alexander, 1962), but its existence as a discrete material has been questioned recently (Németh et al., 2014). Instead, faulted and twinned cubic diamond has been suggested as responsible for the unusual properties of so-called lonsdaleite-rich diamonds. Since additional research is clearly required to confirm or deny the existence of lonsdaleite, we will continue to call these diamonds "lonsdaleite-rich" for simplicity's sake. Yet the presence of lonsdaleite in the diamonds described, even if found in NPD, is certainly not proof of synthetic origin.

Another point it seems the authors did not consider is the presence of large quantities of inclusions, especially "graphite" crystals (more correctly nanocrystalline carbon, as there are no Raman bands of highly crystalline graphite), and hence the samples' low clarity/transparency. The authors note that "unlike natural diamond, the stone in question was heavily included with graphite crystals." Yet their morphology and distribution is not unlike that seen in many natural diamonds, and it is not documented to our knowledge in synthetic diamonds, and certainly not in NPD. Note also the murky yellowish bodycolor, which is different from the yellow to brown color previously described for NPD.

But most importantly, there are natural diamonds with the same properties as synthetic NPD. We encountered such stones while studying the separation of natural-color from treated-color black diamonds around 1998–1999. The samples we acquired as faceted stones had been taken out of the ground even earlier. Sumitomo did not officially produce NPD until 2012. We have been working for many years on the topic of "$CO_2$-rich diamonds" and have 20 faceted samples of natural polycrystalline black "$CO_2$-rich" and "lonsdaleite-rich" diamonds in our laboratory collections that were acquired from large parcels of natural-color, natural black diamond prior to 1999. Additionally, we own an impact diamond from the Popigai meteorite crater (see Yelisseyev et al., 2013). These 21 diamonds have optical and spectroscopic properties similar to those of the diamonds described in both lab notes., and vary only by the intensity of the "$CO_2$-like" and one-phonon absorptions. They all contain distinct amounts of nanocrystalline carbon inclu-

*Figure 1. Two large indented naturals observed in a pair of natural lonsdaleite-rich diamonds offer strong evidence of their natural origin. Photos by Thomas Hainschwang.*
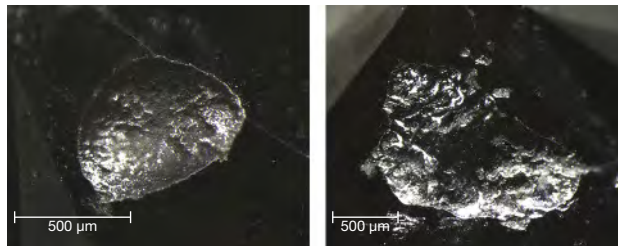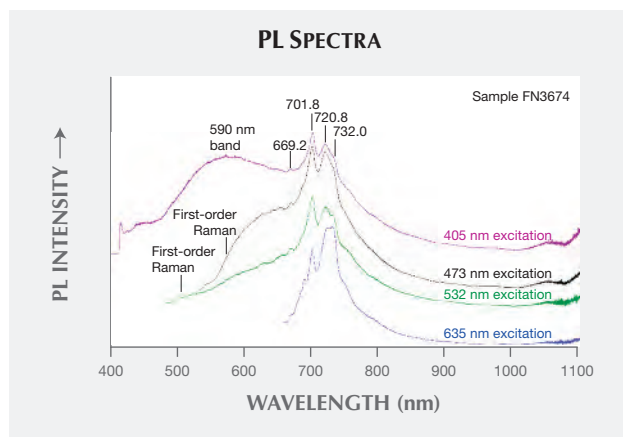
## PL SPECTRA



*Figure 2. The photoluminescence spectra of a natural polycrystalline lonsdaleite- and "CO₂-rich" diamond recorded using four different laser excitations. These spectra differ distinctly from the spectra of the NPD synthetic samples.*

sions and are heavily strained due to their apparent polycrystalline structure, just like NPD. We have several samples with naturals on their surface that are undoubtedly remnants of the etched surface of natural crystals and not of NPD blocks (figure 1).

Additionally, some of these faceted diamonds contain fissures lined with iron oxide, plus solid unidentified inclusions other than graphite. These features are unambiguous proof of natural origin. On top of this, the photoluminescence spectroscopy data of the natural samples varies distinctly from what is published in Skalwold et al. (2012): The spectra excited by 405, 473, 532, and 635 nm lasers are characterized by very broad bands, always with three somewhat less broad bands superimposed at 701.8, 720.8, and 732.0 nm (figure 2), a signature very different from the broad band with relatively sharp bands at 612 and 667 nm described by Skalwold et al. (2012). Thus, they are natural diamonds with properties close to NPD.

Looking at the similarities between our reference samples of natural, apparently polycrystalline "lonsdaleite-rich" diamonds and the samples described in the two recent *G&G* lab notes, the weight of the evidence strongly indicates that the specimens examined by GIA are not synthetic NPD but natural black diamonds.

*Thomas Hainschwang (thomas.hainschwang@ggtl-lab.org)*
*GGTL Laboratories – GEMLAB (Liechtenstein)*
*Balzers, Liechtenstein*

*Franck Notari*
*GGTL Laboratories – Gemtechlab*
*Geneva, Switzerland*

*Emmanuel Fritsch*
*University of Nantes, CNRS, Institut des Matériaux*
*Jean Rouxel (IMN)*
*Nantes, France*

## REFERENCES

Bokii G.B., Bezrukov G.N., Klyuev Y.A., Naletov A.M., Nepsha V.I. (1986) *Natural and Synthetic Diamonds*. Nauka Press, Moscow (in Russian).

Ergun S., Alexander L.E. (1962) Crystalline forms of carbon: a possible hexagonal polymorph of diamond. *Nature*, Vol. 195, No. 4843, pp. 765–767, http://dx.doi.org/10.1038/195765a0

Hainschwang T., Notari F., Fritsch E., Massi L., Breeding C.M., Rondeau B. (2006) Natural "CO₂-rich" colored diamonds. *G&G*, Vol. 42, No. 3, p. 97.

Hainschwang T., Notari F., Fritsch E., Massi L., Rondeau B., Breeding C.M., Vollstaedt H. (2008) HPHT treatment of CO₂ containing and CO₂-related brown diamonds. *Diamond and Related Materials*, Vol. 17, No. 3, pp. 340–351, http://dx.doi.org/10.1016/j.diamond.2008.01.022

Johnson P., Moe K.S. (2010) Lab Notes: Black diamond with solid CO₂ micro-inclusions and phosphorescent *zones.* G&G, Vol. 46, No. 2. pp. 140–141.

Németh P., Garvie L.A., Aoki T., Dubrovinskaia N., Dubrovinsky L., Buseck P.R. (2014) Lonsdaleite is faulted and twinned cubic diamond and does not exist as a discrete material. *Nature Communications* 5, article no. 5447, http://dx.doi.org/10.1038/ncomms6447

Schrauder M., Navon O. (1993) Solid carbon dioxide in a natural diamond. *Nature*, Vol. 365, No. 6441, pp. 42–44, http://dx.doi.org/10.1038/365042a0

Skalwold E.A. (2012) Spotlight: Nano-polycrystalline diamond sphere: A gemologist's perspective. *G&G*, Vol. 48, No. 2, pp. 128–131, http://dx.doi.org/10.5741/GEMS.48.2.128

Skalwold E.A., Renfro N., Shigley J.E., Breeding C.M. (2012) Characterization of a synthetic nano-polycrystalline diamond gemstone. *G&G*, Vol. 48, No. 3, pp. 188–192, http://dx.doi.org/10.5741/GEMS.48.3.188

Wang W., Moses T., Moe K.S., Shen A.H.-T. (2005) Lab Notes: Large diamond with micro-inclusions of carbonates and solid CO₂. *G&G*, Vol. 41, No. 2, pp. 165–167.

Yelisseyev A., Meng G.S., Afanasyev V., Pokhilenko N., Pustovarov V., Isakova A., Lin Z.S., Lin H.Q. (2013) Optical properties of impact diamonds from the Popigai astrobleme. *Diamond and Related Materials*, Vol. 37, pp. 8–16,

## REPLY

We appreciate the letter from Thomas Hainschwang and his colleagues related to our two nano-polycrystalline diamond (NPD) lab notes from 2014. We identified the samples as NPD primarily using FTIR spectroscopy and DiamondView images, as performed by Skalwold et al. (2012). We also confirmed our identification using XRD analysis, though these results were not included in the short lab notes.

A broad peak at 1220 cm⁻¹ in the mid-IR spectrum is typical of NPD samples (figure 3; see also Skalwold et al., 2012). Solid sintered NPD (i.e., cubic diamond) can be achieved by growth conditions of ≥15 GPa and ≥2,200°C (Sumiya, 2012). However, this *P-T* condition varies depending on the graphite starting material's grain size and crystalline nature. Consequently, a hexagonal diamond structure can also be observed in NPD, in addition to cubic diamond. The broad band at 1220 cm⁻¹ in our samples is most likely attributed to the structure of 6H hexagonal di-

amond (Wu, 2007). In the one-phonon region (400–1332 cm$^{-1}$), 2H hexagonal diamond (lonsdaleite) and 3C cubic diamond are *not* IR active. A 6H diamond of natural origin has never been reported. Sumiya (2012) confirmed that NPD contains 50 to 100 ppm of nitrogen, mostly aggregated as A, B, and N3 center with less than 1 ppm of single nitrogen. Thus, the 1220 cm$^{-1}$ peak, which is located well within nitrogen spectral region, can probably be enhanced by nitrogen A and B aggregates.

NPD contains oxygen from 10 to 30 ppm (Skalwold, 2012). Thus, the $CO_2$-related features could be observed in these samples. Although peaks at 3727 and 3611 cm$^{-1}$ (stated) and 2358 and 735 cm$^{-1}$ (not stated) in the Spring 2014 lab note are similar to solid $CO_2$ features, their positions are not quite matched with established peaks. The XRD pattern of our samples shows two sharp peaks at 44 and 75 degrees (2θ), consistent with NPD grown at 15 GPa and 2500°C (Sumiya, 2008). We felt that a detailed discussion of IR and XRD analyses was beyond the scope of our lab notes.

DiamondView images of NPD usually show a distinct, mottled fluorescence pattern (figure 4). This typical pattern has been observed in all NPDs we have examined at GIA's New York laboratory.

Every stone submitted to GIA is carefully examined using a gemological microscope and tested using standard and advanced gemological techniques before we make any
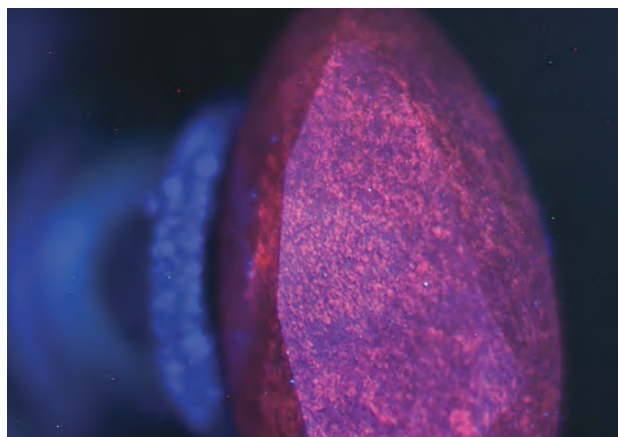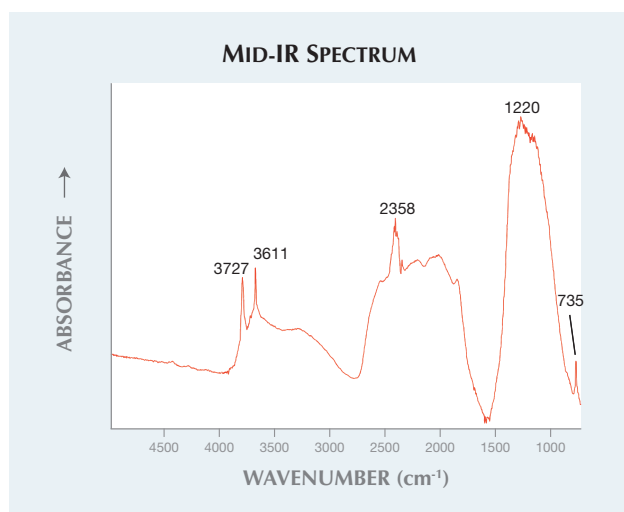


Figure 4. This DiamondView image of the 0.90 ct sample shows the typical fluorescence pattern observed in every NPD sample examined by GIA. Image by Paul Johnson.

comments or conclusions. The letter from Dr. Hainschwang and his colleagues showed photos of lonsdaleite-rich diamonds. Since we have not seen these samples, however, a comparison cannot be made. For a true comparison, we would need IR spectra and DiamondView images, as these are key identification tools for NPD synthetics. Polycrystalline diamonds (e.g., carbonado and framesite) can be found in nature (Harlow and Davies, 2005), but these are extremely small and would not reach the sizes of the specimens examined in the lab notes.

We respect Dr. Hainschwang's concerns but feel confident in our identification.

*Kyaw Soe Moe and Paul Johnson*
*GIA, New York*

Figure 3. This mid-IR spectrum of a 0.90 ct sample is figure 14 from the Spring 2014 lab note. The four peaks at 3727, 3611, 2358, and 735 cm$^{-1}$ are similar to established solid $CO_2$ peaks. But the peak positions are somewhat different, and they could be of different assignment. The broad peak at 1220 cm$^{-1}$ is most likely attributed to the structure of 6H hexagonal diamond, which has never been reported in natural diamond.



**MID-IR SPECTRUM**

ABSORBANCE →

WAVENUMBER (cm$^{-1}$)

## REFERENCES

Harlow G.E., Davies R.M. (2005) Diamonds. *Elements*, Vol. 1, No. 2, pp. 67–70, http://dx.doi.org/10.2113/gselements.1.2.67

Skalwold E.A. (2012) Nano-polycrystalline diamond sphere: A gemologist's perspective. *G&G*, Vol. 48, No. 2, pp. 128–131, http://dx.doi.org/10.5741/GEMS.48.2.128.

Skalwold E.A., Renfro N., Breeding C.M., Shigley J. (2012) Transparent, faceted nano-polycrystalline synthetic diamond. *News from Research*, http://www.gia.edu/ongoing-research/transparent-faceted-nano-polycrystalline-synthetic-diamond

Sumiya H. (2012) Novel development of high-pressure synthetic diamonds "ultra-hard nano-polycrystalline diamonds." *SEI Technical Review*, No. 74, pp. 15–23, http://global-sei.com/technology/tr/bn74/pdf/74-03.pdf

Sumiya H., Irifune T. (2008) Microstructure and mechanical properties of high-hardness nano-polycrystalline diamonds. *SEI Technical Review*, No. 66, pp. 85–92, http://global-sei.com/technology/tr/bn66/pdf/66-11.pdf

Wu B.R. (2007) Structural and vibrational properties of the 6H diamond: First-principles study. *Diamond and Related Materials*, Vol. 16, No. 1, pp. 21–28, http://dx.doi.org/10.1016/j.diamond.2006.03.013

# G&G

## Gem News International

**Contributing Editors**

Emmanuel Fritsch, *University of Nantes, CNRS, Team 6502, Institut des Matériaux Jean Rouxel (IMN), Nantes, France* (fritsch@cnrs-imn.fr)

Gagan Choudhary *Gem Testing Laboratory, Jaipur, India* (gagan@gjepcindia.com)

Christopher M. Breeding, *GIA, Carlsbad* (christopher.breeding@gia.edu)

## COLORED STONES AND ORGANIC MATERIALS

**Large star emerald.** Star emeralds are rare specimens, and most are found in either Brazil or Madagascar. In 1999, Manuel Marcial de Gomar (Key West, Florida) purchased a 1,000-carat parcel of rough emeralds from Diallo Mahmoud, an independent emerald dealer based in Africa. Mahmoud noted that the parcel came from Madagascar. Marcial de Gomar later noticed that some crystals showed indications of chatoyancy. He chose this particular piece thinking it could be cut to produce a cat's-eye emerald. Miami-based cutter Jone Ribeiro cut the stone into a 25.86 ct double cabochon (figure 1). Marcial de Gomar put the stone into his personal collection, where it stayed for 13 years, until independent gemologist and appraiser Martin Fuller examined Marcial de Gomar's collection in 2013. Both experts recognized that this emerald was a star and not a cat's eye. It was subsequently sent to GIA's Carlsbad laboratory for an identification report.

The stone is described as an oval double cabochon natural star emerald. The asterism was caused by minute
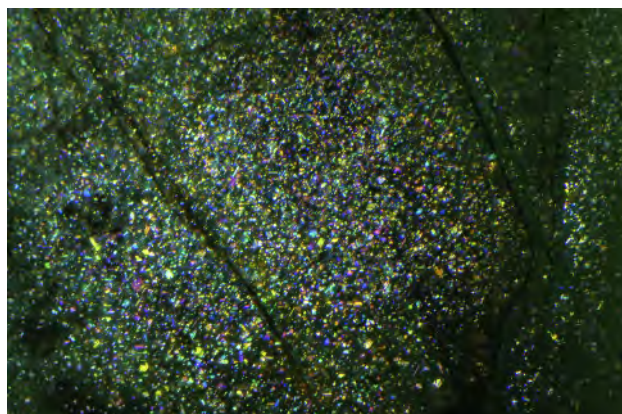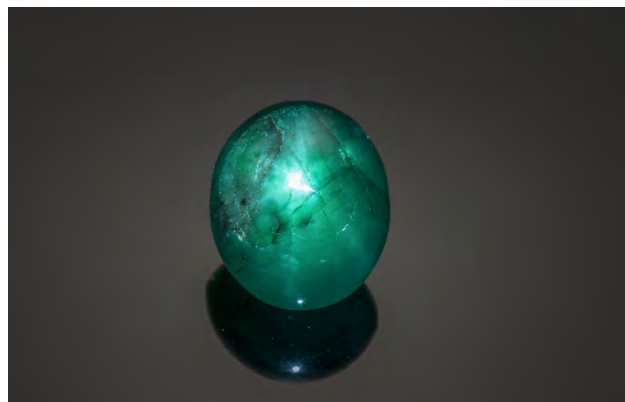


*Figure 2. Minute fluid inclusions oriented parallel to the basal plane of the crystal are the cause of this emerald's asterism. The inclusions exhibit thin-film interference, causing rainbow colors that are visible at high magnification. Photo by Nathan Renfro; field of view 1.8 mm. Courtesy of Manuel Marcial de Gomar.*

*Figure 1. A weak, six-rayed star is visible in this 25.86 ct emerald cabochon. Photo by Robert Weldon/GIA, courtesy of Manuel Marcial de Gomar.*



hexagonal fluid inclusions oriented parallel to the basal plane of the crystal (e.g., Spring 2004 GNI, p. 104; K. Schmetzer, et al., "Asterism in beryl, aquamarine, and emerald—an update," *Journal of Gemmology*, Vol. 29, No. 2, 2004, pp. 66–71). They exhibit thin film interference with direct, pinpointed light that caused the asterism, as well as rainbow colors seen at high magnification (figure 2). Prior to this report, very few asteriated emeralds were recorded (e.g. Fall 1995 GNI, p. 206; Spring 1995 GNI, pp.
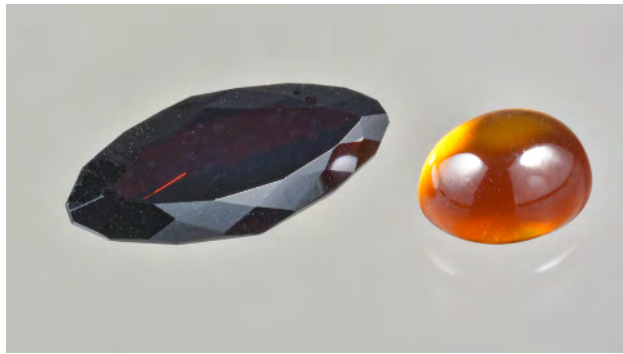
Figure 3. The 4.40 ct natural red rutile on the left was compared with a 4.47 ct orange flame-fusion synthetic rutile. Photo by C.D. Mengason.
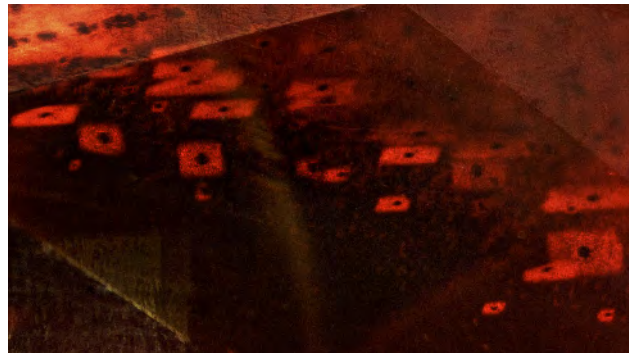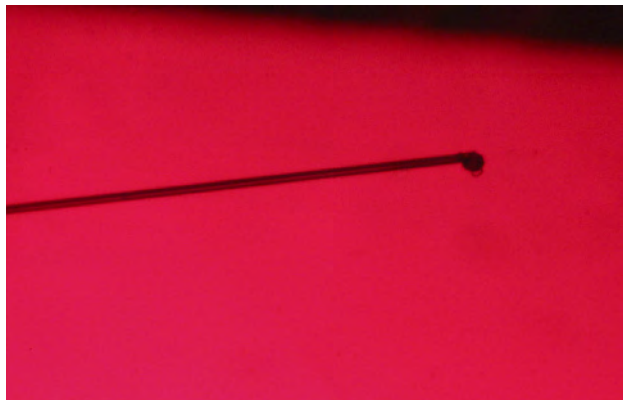


Figure 5. Near the girdle, rectangular tabular inclusions are observed under fiber-optic illumination. Photomicrograph by Ziyin Sun; field of view 2.43 mm.

60–61; Spring 2002 GNI, p. 104; Summer 2006 GNI, pp. 171–172). This is the eleventh, and largest, star emerald known to date.

*Carl Chilstrom*
*GIA, Carlsbad*

**Natural faceted red rutile.** The Carlsbad laboratory recently received a 4.40 ct dark red marquise brilliant (figure 3, left) for examination. Standard gemological testing revealed a refractive index that was over the limit of the RI liquid, as well as a hydrostatic specific gravity (SG) of 4.27. The specimen was inert to both long-wave (LW) and short-wave (SW) UV. Under reflected light, it showed a metallic luster. Raman testing identified the material as rutile. To distinguish it as natural or synthetic rutile, we compared it with a known flame-fusion orange synthetic rutile sample (figure 3, right).

Under magnification, the most distinctive internal characteristic of the dark red specimen was an octagonal blockage with a long growth tube extending to the surface

(figure 4). Near the girdle, some unknown rectangular tabular inclusions were also observed, which were not identified by Raman spectroscopy (figure 5). Both internal features indicated the specimen was natural rutile. Straight and angular growth banding was also observed (figure 6). Raman spectroscopy for both the red sample and the orange synthetic revealed major peaks at 610, 446, and 242 $cm^{-1}$ and minor peaks at 818, 707, and 319 $cm^{-1}$, confirming their identity as rutile (see the RRUFF database at rruff.info).

Laser ablation–inductively coupled plasma–mass spectrometry (LA-ICP-MS) revealed that the dark red rutile had a composition of 98.2% $TiO_2$ and 1.5% $Fe_2O_3$ by weight, with traces of Mg, Al, Si, Ca, Sc, V, Cr, Cu, Zn, Zr, Nb, Cd, In, Sn, Sb, Hf, Ta, W, Pb, and U. The presence of Nb (176.81–296.93 ppmw), Ta (15.13–25.81 ppmw), Hf (0.15–0.40 ppmw), Zr (3.29–4.84 ppmw), Pb (0.01–0.56 ppmw), and U (0.07–0.27 ppmw) suggested a natural origin. The orange synthetic rutile contained 99.9% $TiO_2$, plus traces of Mg, Si, Cr, Co, Cu, and Zn. Traces of iron (1.66 ppmw, 0.0238% $Fe_2O_3$ by weight) were also detected. Synthetic

Figure 4. In this natural red rutile, an octagonal blockage is capped at the end of the growth tube. Photomicrograph by Ziyin Sun; field of view 1.40 mm.



Figure 6. The natural rutile shows straight and angular growth banding. Photomicrograph by Ziyin Sun; field of view 4.92 mm.
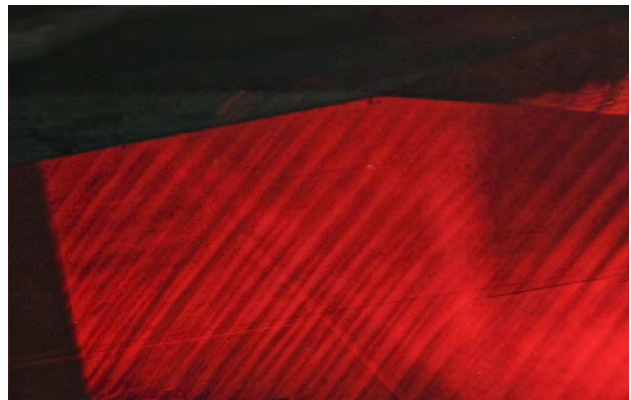
Figure 7. Face-up view of two quartz cabochons from Brazil, weighing 116.95 ct (left) and 44.12 ct (right) with cross-like quartz inclusions. Photo by Jaroslav Hyršl.
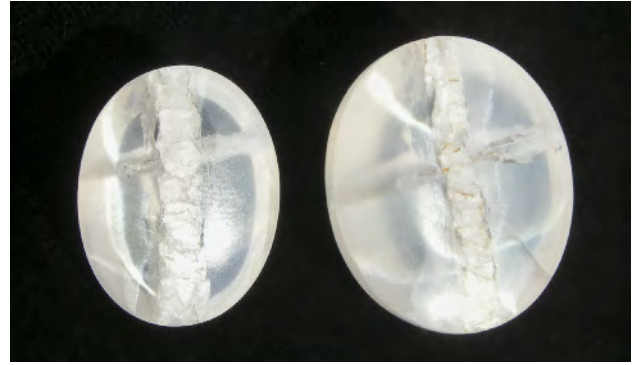


Figure 8. The stars in the quartz samples, seen from the base, are eye-visible in sunlight. Photo by Jaroslav Hyršl.

rutile boules created by the Verneuil process have an orange color with 0.04% $Fe_2O_3$ and a clear reddish color with 0.2% $Fe_2O_3$ (C.H. Moore, Jr. and R. Dahlstrom, "Synthetic rutile crystal and method for making same," U.S. Patent 2792287). The red specimen's lower chemical purity indicates natural origin.

Visible spectra of both stones were taken. The red bodycolor of the natural rutile matched the transmission window between 650 and 700 nm in the red portion of the spectrum, which was likely caused by iron.

Although rutile is a common inclusion in many minerals, the few crystals that are faceted usually weigh less than 1 ct. This faceted stone was very rare because of its large size. It was the first faceted natural rutile examined by GIA's Carlsbad laboratory.

*Ziyin Sun (zsun@gia.edu), Amy Cooper, and*
*Adam Steenbock*
*GIA, Carlsbad*

**Rare "star and cross" quartz from Brazil.** The author purchased two very unusual quartz samples (figure 7) in Brazil in 2015. Both were cut as cabochons with a slightly curved bottom; one weighed 116.95 ct (35.0 × 30.3 × 15.6 mm), while the other weighed 44.12 ct (28.3 × 22.3 × 10.0 mm). The larger cabochon was slightly milky, while the smaller one was almost clear. Both showed a strong six-rayed star when illuminated (figure 8). The stars were centered on the top of the cabochons, which indicates that both were cut perpendicular to the c-axis. The most unusual feature was a cross-like inclusion in both stones. It was white and coarse-grained, only slightly translucent. The longer part of both crosses measured about 4 mm wide. The shorter part had a thickness 1.5 to 2 mm and the angle of the intersection was about 85 degrees in both cabochons, which meant that the two specimens were probably cut from the same crystal. RI results and Raman analysis showed the cross to be quartz, rather than a foreign mineral. The origin of the cross inclu-

sions is uncertain, but they are strong evidence of nature's ability to produce rarities.

*Jaroslav Hyršl (hyrsl@hotmail.com)*
*Prague*

**Serpentine cabochon with unusual olive green color.** Serpentine is a common ornamental stone in the jewelry trade. With colors ranging from yellowish green to deep green, it is commonly used as an imitation of jadeite or nephrite.

Recently, the Gem Testing Laboratory at the Shijiazhuang University of Economics in Hebei, China, examined an olive green cabochon (figure 9) weighing 4.05 ct and measuring approximately 12 × 8 × 6 mm, reportedly purchased from China's Shandong province. The sample was relatively clean, with a vitreous luster and without any eye-visible inclusions. Without magnification, it resembled high-quality jadeite jade. Standard gemological testing gave

Figure 9. This 4.05 ct translucent serpentine is unusual for its olive green color and lack of impurities. Photo by Yanjun Song.
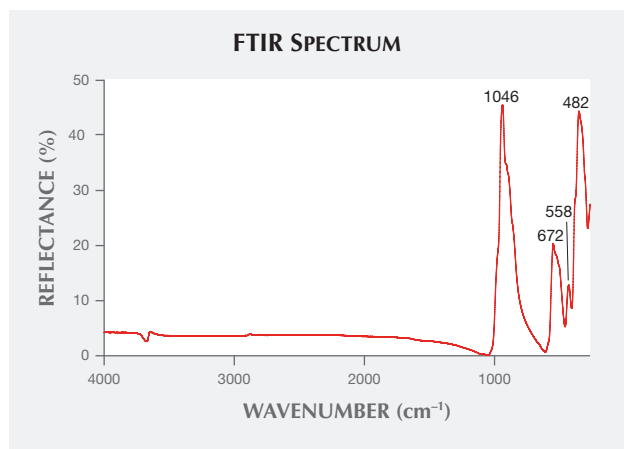
**FTIR SPECTRUM**

*Figure 10. The FTIR spectrum of the 4.05 ct emerald-green cabochon sample exhibits characteristic peaks at 1046, 672 and 482 cm⁻¹, all consistent with serpentine.*

a spot RI of 1.56 and a hydrostatic SG of approximately 2.56; the sample was inert to both LW and SWUV. These properties are consistent with serpentine. Four main peaks were observed in the 1100–400 $cm^{-1}$ region of the infrared reflectance spectrum (figure 10). The two peaks at about 1046 and 482 $cm^{-1}$ were related to the fundamental Si-O vibrations. The remaining two peaks at 672 and 558 $cm^{-1}$ are attributed to the $OH^-$ and Mg-O vibrations, respectively, confirming the sample's identity as antigorite, a species in the serpentine family.

EDXRF was used to differentiate the sample from the common "Xiuyu" variety of serpentine, from China's Liaoning province. Testing revealed that both Cr and Ni were significantly higher in this material than in serpen-

tine from Liaoning, indicating that the specimen may have formed from the serpentinization of mafic-ultramafic rocks. We suspect it may have originated in Taian City in Shandong province, which is famous for "Taishan jade," a newfound variety of serpentine.

Although serpentine is common in the Chinese market, this was the first time our researchers have encountered a sample of such high quality.

*Yanjun Song and Lu Zhang*
*Shijiazhuang University of Economics, Hebei, China*

**Thai-Myanmar petrified woods.** Petrified woods (figure 11, left) have long been used as a gem and ornamental material due to their beauty, luster, durability, and relative rarity. Certain minerals (mainly quartz, opal, or moganite) crystallize or precipitate in the hollow cavities and cells of the woods in a fossilization process. Fossil trading is government regulated in some countries, and gemologists should know the useful identifying characteristics of petrified woods, which can be misidentified as jasper and agate. With this in mind, the author examined Thai-Myanmar petrified wood samples, fashioned as cabochons (figure 11, right), for gemological characterization.

More than 100 Thai samples were collected from the four localities shown in figure 12: Tak, in Ban Tak-Oke (TAK); Khon Kaen, in Ban Hin Khao (BHK); Chaiyaphum, in Noen Sa Nga (CYP); and Nakhonratchasima, in Kroke Duan Ha (KDH). About 100 Burmese samples were donated by carvers from Mae Sai in Chiang Rai province (MYR), near the border of Thailand and Myanmar. Thai specimens were collected from either Quaternary gravel beds of fluvial deposits or the high-terrace sands and grav-




*Figure 11. Left: Petrified woods are carved and sold as ornamental gem materials, such as these specimens from the Mae Sai market near the Thai-Myanmar border. Right: A few of the cabochons from this study. Photos by Seriwat Saminpanya.*

*Figure 12. A map showing the localities in Thailand and Myanmar where the petrified wood samples originated. Adapted from Saminpanya and Sutherland, 2013.*

els of paleorivers. Tektite grains found in the sediments date back 700,000 to 900,000 years (P. W. Haines et al., "Flood deposits penecontemporaneous with ~0.8 Ma tektite fall in NE Thailand: Impact-induced environmental effects?" *Earth and Planetary Science Letters*, Vol. 225, 2004, pp. 19–28).

Thirty-eight samples (all but seven from Thailand) were tested by standard gemological methods, Raman spectroscopy, and X-ray diffraction (XRD). Thirty-seven of these came from dicotyledonous plants, indicated by vascular bundles concentrated in an outer ring of active growth. Periods of slow (winter) and fast (summer) growth create the growth rings in the trunk. One sample came from a palm tree, and had vascular bundles dispersed throughout the trunk.

The rough surfaces may have been altered and stained by soil or iron oxides, resulting in black, brown, cream, white, and red coloration. Colorless areas and different shades of brown, black, gray, white, cream, yellow, orange, and red appeared below the surface. Some samples exhibited color banding. Most Thai samples were opaque or nearly opaque; those from Myanmar were translucent and lighter in tone. The surfaces showed varying degrees of luster and fracturing. RI ranged from 1.425 to 1.543 (tested at the flat polished base of the cabochon), and SG ranged from 1.963 to 2.616. Most samples fluoresced weak to moderate chalky white under LWUV, but some were inert or showed very weak white fluorescence.

A gemological microscope can often reveal a well-preserved wood grain structure in petrified wood samples.

Studies of wood structure generally involve the transverse, tangential, and radial sections of the trunk (R.F. Evert, *Esau's Plant Anatomy: Meristems, Cells, and Tissues of the Plant Body: Their Structure, Function, and Development*, 3rd ed., John Wiley & Sons, Hoboken, New Jersey, 2006, pp. 203, 292–296). A transverse section of one of the samples (figure 13) showed several tiny oval-shaped pores filled with quartz or opal (e.g., S. Saminpanya and F.L. Sutherland, "Silica phase-transformations during diagenesis within petrified woods found in fluvial deposits from Thailand-Myanmar," *Sedimentary Geology*, Vol. 290, 2013, pp. 15–26). The samples also showed thin parallel rays, groups of cells oriented perpendicular to the trunk's main axis. In some samples, the parenchyma (the most common plant tissue cells) consisted of pale lines or bands running across the rays. Others showed parenchyma surrounding a pore on the long and parallel wood grains of the tangential section, or dark-colored pores extending the length of the trunk. On the radial section, the pores ran the length of the trunk, with wood grains perpendicular to the pores.

Raman spectra were characteristic of opal (according to the RRUFF database, rruff.info), quartz, and moganite (K.J. Kingma and R.J. Hemley, "Raman spectroscopic study of microcrystalline silica," *American Mineralogist*, Vol. 79, 1994, pp. 269–273). Figure 14 shows the peaks for the TAK, BHK, and CYP samples; peaks for KDH (which included opal) and MYR samples were previously presented (Saminpanya and Sutherland, 2013). Most of the quartz material displayed peaks at 354, 395–397, and 464–466 cm$^{-1}$, with different colors within a sample exhibiting different peak intensities. Some samples showed only major peaks of quartz at 464–466 cm$^{-1}$. Moganite was mixed with quartz in one sample apiece from CYP, KDH, and MYR, indicated



Figure 14. Raman spectra of petrified wood samples from Chyaphum (CYP), Tak (TAK), and Khon Kaen (BHK) with quartz (Q) peaks at 465 cm$^{-1}$. Samples from Chyaphum show a moganite (M) peak at 503–506 cm$^{-1}$.

Figure 13. Oval pores and rays (wavy white lines) are seen on a transverse section of this petrified wood sample, and the growth rings are visible as two lines crossing the image. Photomicrograph by Seriwat Saminpanya; field of view 10 mm.
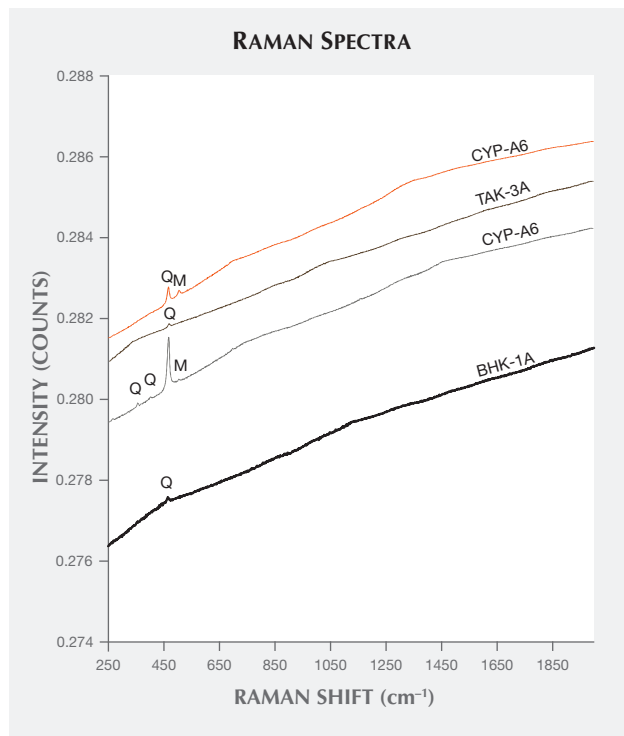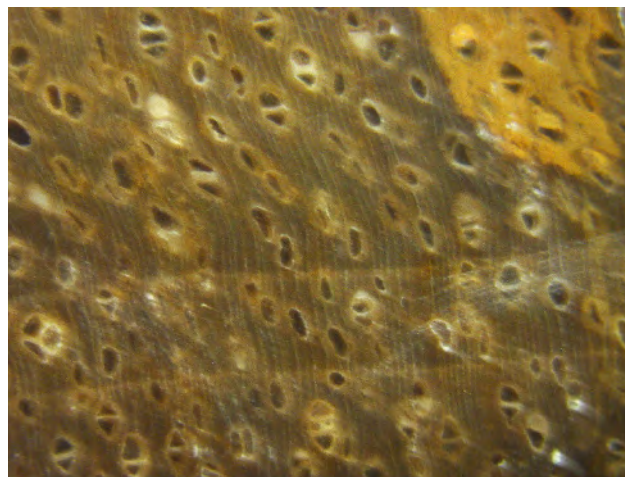


by peaks at 503–506 cm$^{-1}$, close to the reference peak of 501 cm$^{-1}$ (Kingma and Hemley, 1994). Two KDH samples showed bands centered at 1587 and 1607 cm$^{-1}$, characteristic of opal (Saminpanya and Sutherland, 2013), which was probably responsible for the weak to moderate chalky white fluorescence in some of the samples.

XRD showed that the quartz peaks had an average 2Θ of 21.0, 26.7, 36.6, 39.6, 40.4, 42.5, 45.9, 50.2, and 55.0 degrees; the opal-CT peaks had an average 2Θ of 20.7, 21.7, 36.0, 44.0, and 56.9 degrees (again, see rruff.info). Quartz appeared in the XRD peaks of samples from all localities, but the opal-CT was found only in samples from KDH and MYR. The diffractogram of opal-CT in one sample from KDH appeared noisy. This may be due to its amorphous nature, though extending the XRD scan times may improve the resolution of the peaks. At this stage, XRD can only detect quartz and opal from these samples.

*Seriwat Saminpanya*
*Srinakharinwirot University, Bangkok*

## SYNTHETICS AND SIMULANTS

**Coated rock crystal imitation of ruby.** Recently the Dubai Central Laboratory received for identification a rough stone

*Figure 15. This coated rock crystal imitation of ruby has a brown skin. Photo by Nazar Ahmed Ambalathveettil, Dubai Central Laboratory.*



*Figure 16. The rock crystal shows dark red under transmitted light to imitate ruby. Photo by Nazar Ahmed Ambalathveettil, Dubai Central Laboratory.*

weighing 616.93 g and measuring approximately 114.3 × 65.8 × 53.0 mm (figure 15). Most of it was covered by a brown skin, while other parts were transparent. Viewed through one of the transparent areas, the stone showed a red color. Under oblique light, the stone appeared dark red, with some areas that were colorless (figure 16).

Microscopic examination with transmitted light revealed negative crystals, fingerprints, and two-phase inclusions. Observation of the transparent and opaque areas on the surface showed red, green, and blue areas of coating that could be removed using sharp needles. These coated areas gave the stone a purplish red color overall, but some transparent areas appeared colorless under transmitted light and no coating was observed there. The stone's SG was 2.60. The coated area gave a patchy chalky blue and purple reaction under LWUV and was inert to SWUV. Specific gravity and inclusions indicated a rock crystal; this was confirmed by Raman spectroscopy.

This was the first time the Dubai Central Laboratory had identified such a large coated rough stone imitating ruby.

*Nazar Ahmed Ambalathveettil (nanezar@dm.gov.ae)*
*and Mohamed Karam*
*Gemstone Unit, Dubai Central Laboratory*
*Dubai, United Arab Emirates*

**Color-change synthetic cubic zirconia as peridot imitation.** Peridot is a common gemstone in the jewelry industry; however, it is rarely simulated using substances other than glass (Summer 2004 Lab Notes, p. 165). The State Gemological Centre of Ukraine recently received for identification an



*Figure 17. This synthetic cubic zirconia imitation of peridot, with an estimated weight of 4.50 ct, is shown in daylight (left) and incandescent light (right). Photos by Igor Iemelianov; field of view 13.20 mm.*

oval-cut gemstone, with an estimated weight of 4.50 ct, set in a ring. The stone was greenish yellow in daylight (figure 17, left) and orangy yellow in incandescent light (figure 17, right). The client who submitted the ring specifically wished to know if the center stone was peridot. The sample was transparent and isotropic, with an RI of 2.150 (measured by a refractive index meter) and was inert to both SW and LWUV radiation. Microscopic examination revealed no inclusions. The measured relative reflectivity (RR 65–67), obtained using a Presidium DuoTester, clearly matched that of cubic zirconia, a result in line with the other gemological observations. This allowed us to identify the stone as cubic zirconia. Chemical analysis with EDXRF showed Zr and Y, with minor Pr and Nd. These impurities can cause color change in this stone. Using fiber-optic light with the spectroscope, we observed a complex set of absorption lines in both the orange and green-blue regions (the same measurement can be seen at http://www.gemlab.co.uk/peridot.html). This study shows the importance of studying a variety of simulants, even those for less-expensive gems such as peridot.

*Iurii Gaievskyi (gaevsky@hotmail.com)*
*and Igor Iemelianov*
*State Gemological Centre of Ukraine, Kiev*

**Coral inclusions in plastic.** Composites assembled from opaque-to-translucent and transparent gem materials such as turquoise, chalcedony, opal, chrysocolla, tourmaline, and peridot have become popular over the past few years, as evidenced by the number of samples received for identification at the Gem Testing Laboratory in Jaipur, India. Recently, we examined an orangy red bead of plastic (figure 18) with embedded fragments of coral.

The round bead weighed 37.50 ct and measured 20.62 × 20.57 × 14.02 mm. The bead was represented as coral, but its smooth texture along with the luster was sufficient



*Figure 18. This 37.50 ct plastic bead contained visible fragments of carbonate-type coral (the lighter spots). Photo by Gagan Choudhary.*

enough to rule out that possibility. A few spots of lighter color (again, see figure 18), visible to the unaided eye, made it more interesting. Under strong fiber-optic light, minute transparency was observed, while microscopic examination revealed numerous gas bubbles scattered throughout the bead. Sharp boundaries between the lighter spots and the host bead suggested that these spots of lighter color were actually fragments of some other material. These randomly oriented fragments also displayed some concentric radiating structures (figure 19, left), typically seen in carbonate-type corals. Some chips also showed elongated sections (figure 19, right), along with some whitish to faintly colored areas.

Although the bead was obviously an artificial product, its major component was still to be identified. A spot RI of

*Figure 19. Some of the fragments embedded in the plastic bead displayed concentric radiating structures (left), typically seen in carbonate-type coral, while others show elongated sections (right). Also note the sharp edges and whitish to faintly colored areas of the fragments. Photomicrographs by Gagan Choudhary; field of view 5.08 mm.*
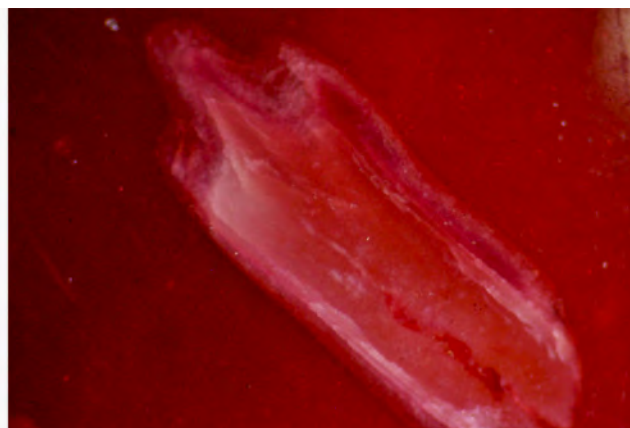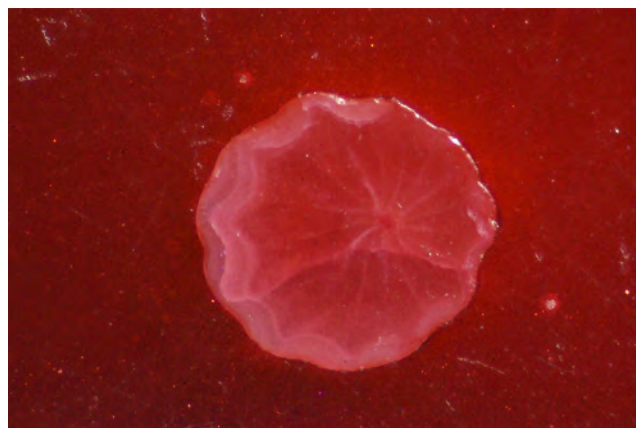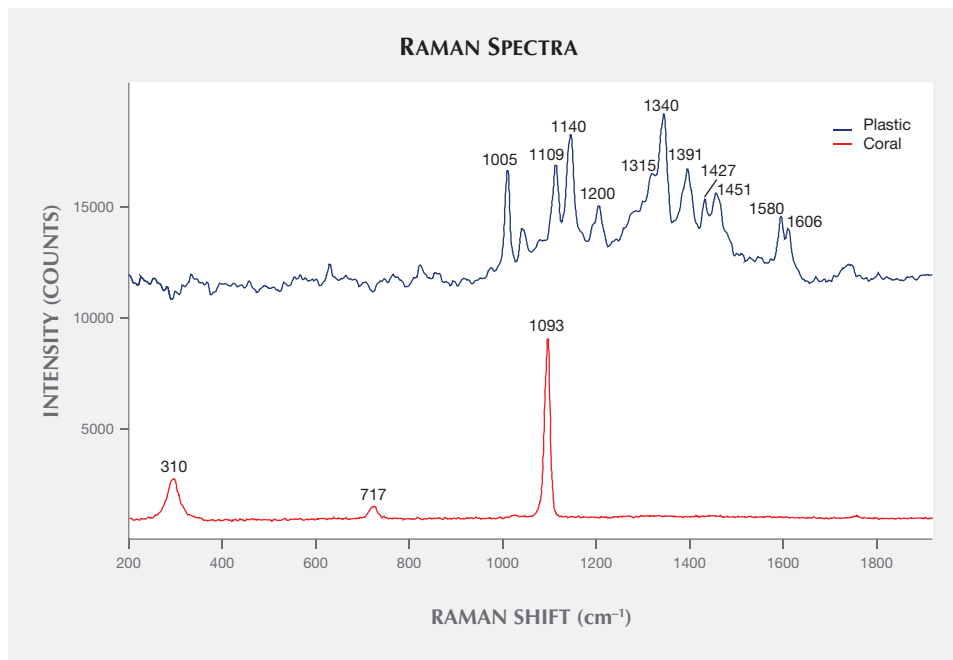
**RAMAN SPECTRA**

*Figure 20. Raman spectra using 785 nm laser confirm that the major component of the bead is plastic (blue trace), while the grains are a carbonate such as calcite (red trace). The lack of carotenoid-related peaks suggests the use of white coral fragments.*

approximately 1.53 and hydrostatic SG of 1.97 were obtained. Under UV light, the bead fluoresced orange, with a stronger reaction to SW than LW; a desk-model spectroscope revealed a broad absorption band from the violet to yellow-orange region. Raman spectroscopy (figure 20) confirmed the major component of the bead as plastic, while the grains were identified as carbonate. We did not detect any carotenoid-related peaks, which have been suggested as the cause of color in pink-to red-coral (C.P. Smith et al., "Pink-to-red coral: A guide to determining origin of color,"Spring 2007 *G&G*, pp. 4–15). On the basis of Raman spectra and concentric radiating structure, the sharp fragments were identified as white coral.

Coral-plastic composites have been reported previously (e.g., Fall 2008 Lab Notes, p. 253). Further, orange-red plas-

tics have also been known as coral imitations for decades. This specimen turned out to be notable because of the use of coral fragments as inclusions; however, we could not clearly understand its purpose.

*Gagan Choudhary (gagan@gjepcindia.com)*
*Gem Testing Laboratory, Jaipur, India*

**A jadeite bangle simulant: Hydrogrossular garnet.** Jadeite, a material significant within Chinese culture, is often submitted to the Lai Tai-An Gem Laboratory for identification.

Historically, the name "jade" has been applied to either nephrite or jadeite. Nephrite has been used for adornment and ornamentation for thousands of years in China, and nephrite objects from many dynasties are found in muse-

*Figure 21. The photo on the left shows a jadeite jade bangle. The photo on the right shows two hydrogrossular garnet bangles that were claimed to be jadeite. Photos by Lai Tai-An Gem Lab.*
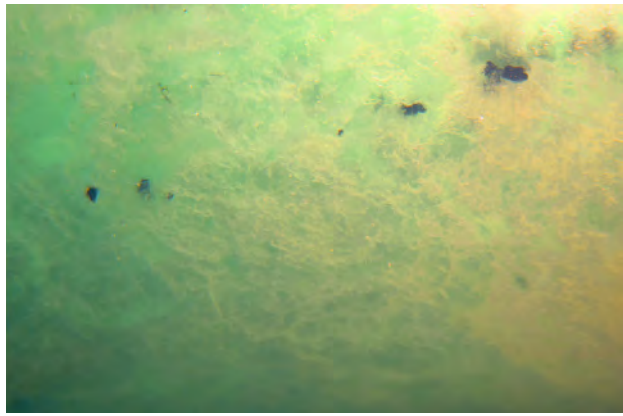
Figure 22. These hydrogrossular garnet bangles exhibit the black pepper-like inclusions that are sometimes found in this material. Photo by Lai Tai-An Gem Lab, field of view 8.20 mm.
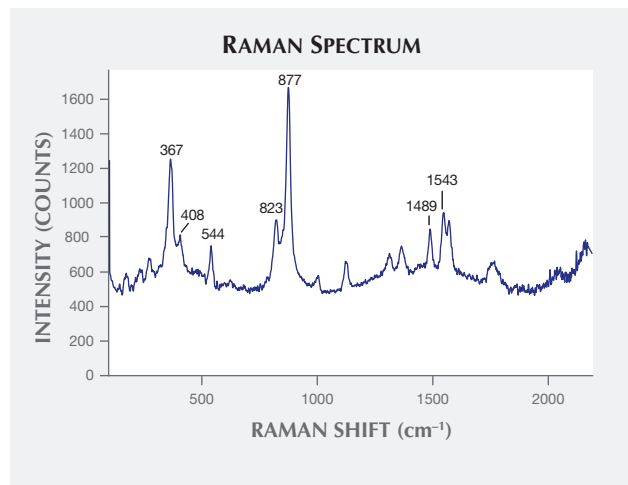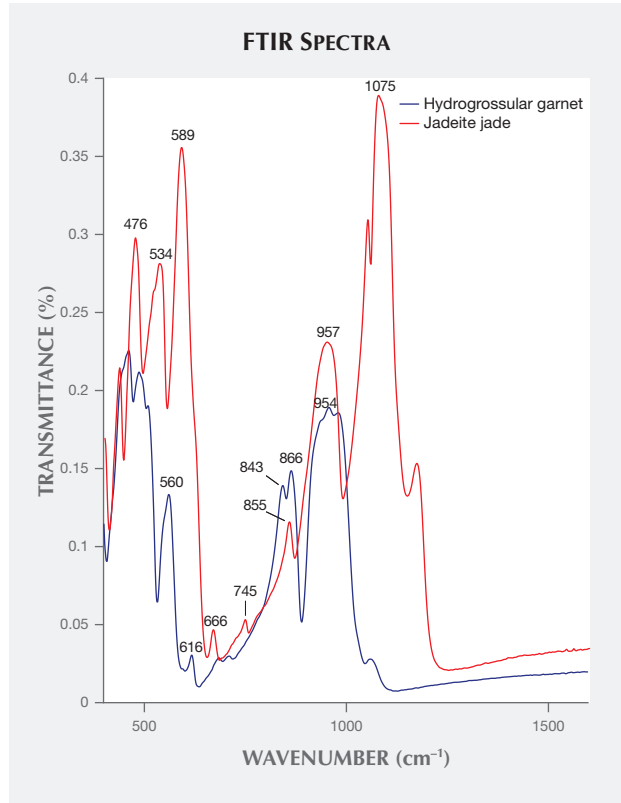


Figure 24. Raman analysis of one of the client's bangles, using a near-infrared wavelength of 785 nm, confirms its hydrogrossular garnet identity.

ums, auctions, and antique shops around the world. While newer to the Chinese market, jadeite jade is becoming increasingly important. Jadeite bangles (figure 21, left) the re-

Figure 23. FTIR spectra reveal the difference between jadeite jade (red line, peaks at 1175, 1075, 1051, 957, 855, 745, 666, 589, 534, 476, and 435 cm⁻¹) and hydrogrossular garnet (blue line, peaks at 954, 866, 843, 616, 560, 488, and 458 cm⁻¹).



quire more rough than cabochons or fashioned stones, resulting in a larger amount of waste. Consequently, the value placed on good-quality pieces is higher, and jadeite bangles with fine textures and brilliant colors continue to set new records in auction houses.

We recently received two similar-looking bangles (figure 21, right) for identification. The client claimed the pieces were jadeite, but we determined them to be hydrogrossular garnet. This jadeite simulant is rarely seen in bangle form; it is more likely encountered as carvings or cabochons. In this particular case, the similarity to jadeite was extremely convincing.

The two translucent, light to strongly saturated green and white hydrogrossular garnet bangles weighed 339.55 ct and 400.03 ct, and measured 75 × 11 mm and 77 × 12 mm, respectively. Both exhibited a spot RI of 1.72, SG of 3.42/3.45, inert reaction to both SW and LWUV, and a light pink reaction through the Chelsea color filter. The absorption spectrum showed a cutoff below 460 nm, and the material exhibited black pepper-like inclusions (figure 22); these characteristics suggest that the color of the garnet is natural.

The identification was confirmed by FTIR and Raman analysis. Peaks at 954, 866, 843, 616, 560, 488, and 458 cm⁻¹ in the infrared spectra (figure 23), and peaks at 367, 408, 544, 823, 877, 1489, and 1543 cm⁻¹ (figure 24) in the Raman spectrum are indicative of hydrogrossular garnet. The similarity to jadeite could lead to a costly error, so those in the trade must be aware of such imitations.

*Larry Tai-An Lai (service@laitaian.com.tw)*
*Lai Tai-An Gem Laboratory, Taipei*

## TREATMENTS

**Impregnated and dyed turquoise.** Turquoise has a cryptocrystalline structure, which gives rise to the gem's porosity. Its vulnerability to body oils, ordinary solvents, and dirt can induce variation of color. This porous gemstone's ap-

Figure 25. Spectroscopic analysis of this 15.21 gram turquoise reveals that the material has been both impregnated and dyed. Photo by Wen Han.



Figure 26. Some lines, along with the cavity, fluoresce white when exposed to long-wave UV radiation, indicating the presence of filling material. Photo by Wen Han.

pearance and durability can be enhanced by various treatment techniques, such as dyeing, impregnation (with polymer, wax, or plastic), and the proprietary Zachery process (E. Fritsch et al., "The identification of Zachery-treated turquoise," Spring 1999 *G&G*, pp. 4–16).

Turquoise, often featured in vintage jewelry pieces, is becoming increasingly popular in the Chinese market. Recently, the NGTC Beijing lab received for identification a 15.21 gram turquoise sphere with green color (figure 25). The specimen measured approximately 3.5 cm in diameter; its spot RI value was 1.59 and its hydrostatic SG value was 2.58. The test sample was inert, except for several lines and a cavity with moderate white fluorescence under both LW

and SWUV radiation (figure 26), suggesting impregnation. Magnification showed some filling material were also present in the cavities. Additionally, green color concentration was observed in the material's cavities and cracks.

Infrared reflectance spectroscopy revealed complicated peaks containing turquoise and impregnated materials. The bands at 1118 and 1050 $cm^{-1}$ were assigned to the asymmetric stretching vibrations of phosphate units, while the 835 $cm^{-1}$ was caused by the bending vibration of OH units. Other features from approximately 647 to 482 $cm^{-1}$ were due to the phosphate bending modes of turquoise. The 2918 and 2850 $cm^{-1}$ peaks were attributed to wax; additionally, a series of small peaks from 1800 to 1350 $cm^{-1}$ indicated the
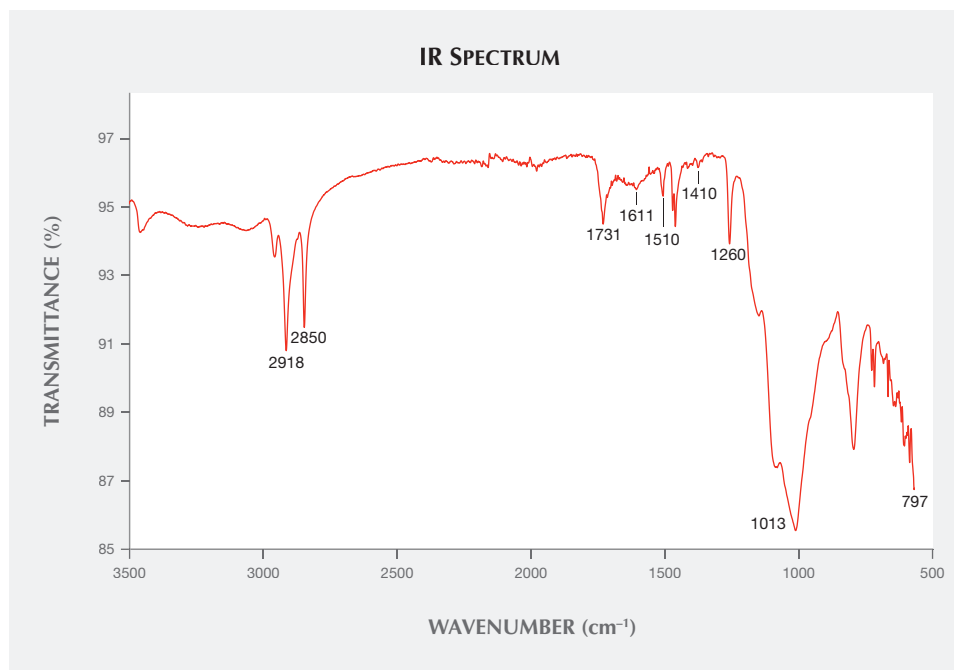


**IR SPECTRUM**

Figure 27. The infrared transmittance spectrum of small amounts of powder scraped from the sample shows that the turquoise was impregnated with three components: epoxy resin, acrylic polymer, and silicone.
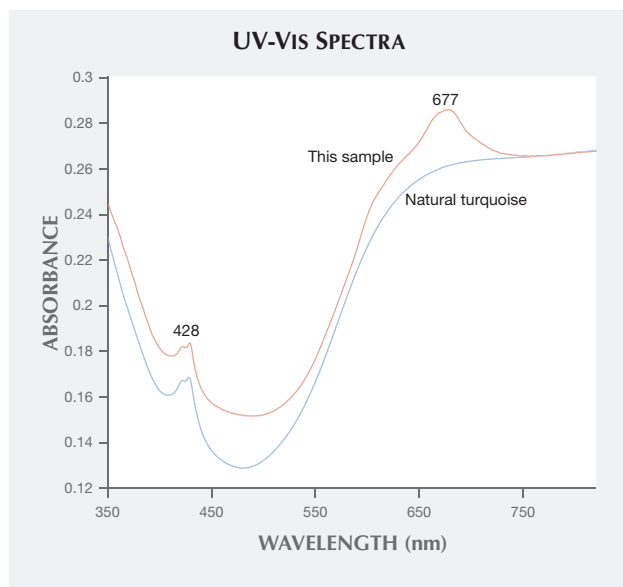
## UV-VIS SPECTRA



*Figure 28. When compared with the spectrum of a known natural turquoise sample, the 677 nm band of the UV-VIS spectrum indicates that the sample in this study was dyed.*

presence of organic matter. To identify this organic material, we scraped off some powder from the edge of one of the cavities with a blade. The resulting infrared transmittance spectrum indicated the presence of three kinds of polymer (figure 27). The 1731 and 1013 cm⁻¹ peaks were attributed to acrylic polymer, and the 1611 and 1510 cm⁻¹ peaks were due to epoxy resin; both are commonly applied to various gem materials for impregnation. Peaks at 1410, 1260, and 797 cm⁻¹ were characteristic absorption features of silicone. Silicones are polymers consisting of repeating units of siloxane (a functional group composed of two silicon atoms and one oxygen atom, often combined with carbon and hydrogen). The 1410 and 1260 cm⁻¹ peaks were caused by asymmetric and symmetric deformation vibrations of $Si-CH_3$,

respectively, and the 797 cm⁻¹ was assigned to the Si-C stretching vibrations of the silicones.

EDXRF chemical analysis detected mainly P, Al, Cu, Fe, and Si. The first four are consistent with the chemical composition of turquoise, while Si was suspected to be a byproduct of silicone impregnation. The UV-Vis spectrum showed two absorption bands: a band centered at about 428 nm caused by $Fe^{3+}$ d-d electronic transition, and a sharp band centered at approximately 677 nm (figure 28). Natural-color turquoise does not show the 677 nm band; many Chinese labs consider this feature characteristic of dyed material.

Turquoise is usually impregnated with acrylic polymer or epoxy resin for stabilization in addition to the dyeing process to change its color. This is the first time we have encountered turquoise that was dyed and impregnated with three components. Our investigation reinforces the need to identify any and all treatments.

*Wen Han (winnerzx@126.com), Taijin Lu, Huiru Dai, and Jun Su*
*National Gems & Jewelry Technology Administrative Center (NGTC)*
*Beijing*

*Hui Dai*
*Institute of Geological Experiment of Anhui Province*
*Hefei, China*

## ERRATA

1. In the Summer 2015 article by E. Sorokina et al., "Rubies and Sapphires from Snezhnoe, Tajikistan," coauthor Dr. Andrey K. Litvinenko was incorrectly listed as director of GIA Moscow.

2. In the Summer 2015 GNI entry "Crimson Prince ruby from Namya" (pp. 214–215), the location of Namya was incorrectly shown on the map. The location has been corrected in the online versions (HTML and PDF) of the Summer 2015 issue.

---

### IN MEMORIAM
### TINO HAMMID (1952–2015)

*Gems & Gemology* mourns the loss of acclaimed gem and jewelry photographer Tino Hammid, who died July 11 at the age of 63 after a two-year battle with cancer. Mr. Hammid is widely remembered throughout the industry for his kindness and his passion for the craft.

The son of Academy Award–winning filmmaker Alexander Hammid, the New York native established his career in Los Angeles. From 1980 to 1982, he served as a staff photographer at GIA's Santa Monica campus. Upon leaving GIA, he became a successful freelance photographer, capturing some of the world's most remarkable gems.

In 1983, he began photographing gemstones for David Federman's popular Gem Profile column in each monthly

issue of *Modern Jeweler*. Their 25-year collaboration yielded two Jesse H. Neal awards for business journalism and a pair of Gem Profile hardcover volumes: *The First 60* (1988) and *The Second 60* (1992). Mr. Hammid's work appeared in countless other books, and starting in 1987 he photographed more than 100 Christie's jewelry auction catalogs.

*G&G* has been privileged to showcase Mr. Hammid's talents for over 30 years. Longtime readers of the journal will recognize his distinctive backgrounds and use of light and shadow. Through his style and technique, he exerted a lasting influence on gem photography. Tino Hammid is survived by his wife, Petra, and three children. We extend our deepest condolences to his family and friends.